CHALMERS
UNIVERSITY OF TECHNOLOGY

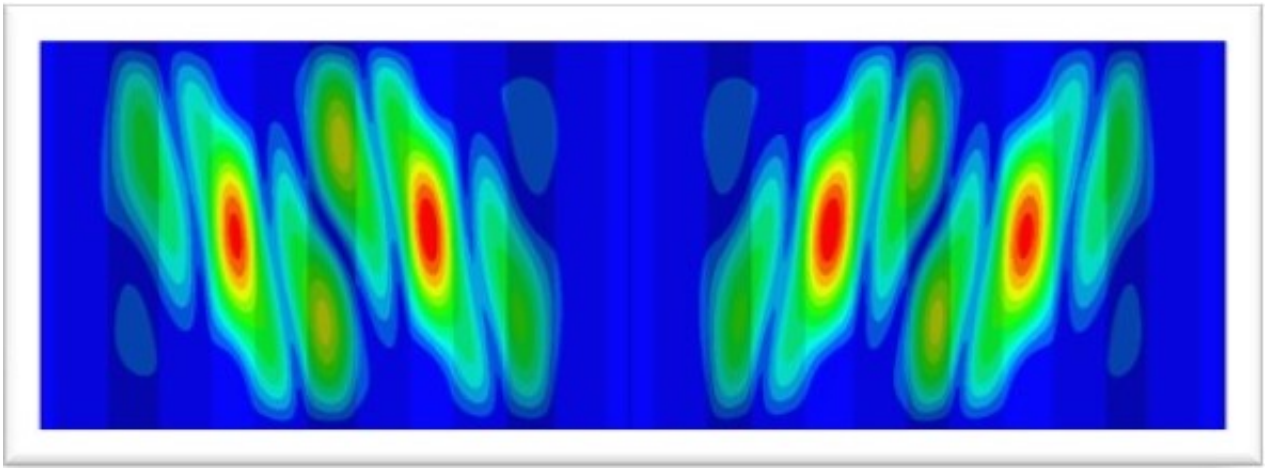

Shear behavior and imperfection sensitivity analysis of Stainless Steel girders with corrugated web plates

A parametric study to investigate the sensitivity of Stainless steel bridge girders' shear behavior to initial imperfection

Master's thesis in Master Program Structural engineering and building technology

Fatima Hlal

Naheel Mohra

Department of Architecture and Civil Engineering
Chalmers University of Technology
Master's thesis ACEX30-18-84
Gothenburg, Sweden 2018

Master's thesis ACEX30-18-84

Shear behavior and imperfection sensitivity analysis of stainless steel girders with corrugated web plates

A parametric study to investigate the sensitivity of Stainless steel bridge girders' shear behavior to initial imperfection

Fatima Hlal and Naheel Mohra

CHALMERS
UNIVERSITY OF TECHNOLOGY

Department of Architecture and Civil Engineering
Division of Structural Engineering
Chalmers University of Technology
Gothenburg, Sweden 2021

Shear behavior and imperfection sensitivity analysis of stainless steel girders with corrugated web plates

A parametric study to investigate the sensitivity of Stainless steel bridge girders' shear behavior to initial imperfection

Fatima Hlal
Naheel Mohra

Supervisors:
Farshid Zamiri, Teknisk specialist / Broinspektör, AFRY
Professor Mohammad Al-Emrani, Department of Architecture and Civil Engineering, CHALMERS

Examiner:
Mozdheh Amani, Department of Architecture and Civil Engineering

Department of Architecture and Civil Engineering
Division of Structural Engineering
Lightweight structures
Chalmers University of Technology
SE-412 96 Gothenburg
Telephone: + 46 (0)31-772 1000

Cover: Interactive buckling mode for a corrugated web obtained from FE-simulation.

Department of Architecture and Civil Engineering
Gothenburg, Sweden 2018

Stainless Steel Bridge Girders with Corrugated Webs
A parametric study to investigate the sensitivity of Stainless steel girder's shear behaviour to initial imperfection
Fatima Hlal and Naheel Mohra
Department of Architecture and Civil Engineering
Division of Structural Engineering, Lightweight Structures
Chalmers University of Technology

Abstract

Steel bridges are prone to corrosion, and over the lifetime of the bridge, corrosion is likely to necessitate maintenance work, re-painting, and inspections. Stainless steel, on the other hand, is more corrosion-resistant material and can help to reduce the problem's negative impacts. Moreover, as these structures are deep in web height, it is common to use thin webs in steel bridges to prevent utilizing a lot of material and get the highest strength out of the material with a minimal amount of weight. The method of manufacturing, however, is complicated due to the thin thickness. To overcome this problem, corrugated webs, which are lighter than traditional flat web steel girders, are used. This kind of Thin shell element, on the other hand, is susceptible to initial imperfection.
The aim of this master's thesis is to research the shear behavior of bridge girders with stainless steel corrugated webs and their sensitivity to initial imperfection. This is done by, firstly, a literature review to decide the most influential parameters on the shear capacity of bridge girders with corrugated webs. Secondly, using ABAQUS software, a sensitivity analysis to initial imperfection is investigated by varying the shape and amplitude of initial imperfection on three different girders. Single eigen shapes and various combinations of eigen shapes have been considered as the shape of the initial imperfection. Hw/400, Hw/300, Hw/200, and Hw/100 are used to estimate the amplitude. Thirdly, a limited parametric study, by changing one-factor-at-a-time, has then been performed to see the effect of each dimensional parameter on the girder's shear capacity. Finally, the shear capacity of the investigated girders has been compared to the shear capacity provided by Eurocode equations.
The results show that the shear capacity of bridge girders with stainless steel corrugated webs is sensitive to both initial imperfection shape and amplitude. The shear capacity decreases significantly with increasing initial imperfection amplitude. In addition, the most critical initial imperfection shape is a single-mode shape of Eigen shapes and not the first positive mode shape. Web height, web thickness and corrugation depth significantly increase the shear capacity. Flat fold length decreases the shear capacity. However, the shear span has a negligible effect. Finally, using the design curve of Eurocode with the first buckling mode and initial imperfection amplitude of Hw/200 is on the safe side.

Keywords: Corrugated web, Shear capacity, Stainless steel, , Steel bridges, Initial imperfection, Sensitivity analysis, Parametric study.

Rostfria brobalkar med korrugerade liv
En parametrisk studie för att undersöka känsligheten hos balkens tvärkraftsbeteende i rostfritt stål för initial imperfektion
Fatima Hlal and Naheel Mohra

Sammanfattning

Stålbroar har en benägenhet att korrodera, och under bronslivstid kommer korrosion sannolikt att kräva underhållsarbete, ommålning och inspektioner. Rostfritt stål är å andra sidan ett mer korrosionsbeständigt material och kan hjälpa till att minska problemets negativa inverkan. Eftersom dessa strukturer är djupa i balkhöjd, är det vanligt att använda tunna balkar i stålbroar för att förhindra att mycket material används och få högsta styrka ut ur materialet med en minimal vikt. Metoden för tillverkning är emellertid komplicerad på grund av den tunna tjockleken. För att lösa detta problem används korrugerade liv, som är lättare än traditionella plattbalkar. Denna typ av tunt skalelement är å andra sidan mottagligt för initiala imperfektioner.

Syftet med detta examensarbete är att undersöka tvärkraftsbeteende hos brobalkar med korrugerade liv av rostfritt stål och deras känslighet för initial imperfektion. Detta görs först genom en litteraturöversikt för att bestämma de mest inflytelserika parametrarna för tvärkraftkapacitet med korrugerade liv. För det andra, med hjälp av ABAQUS-program, undersöks en känslighetsanalys för initial imperfektion genom att variera formen och amplituden hos den initiala imperfektionen på tre olika balkar. Enstaka egenformer och olika kombinationer av egenformer har använts som utformning av den initiala imperfektionen. Hw / 400, Hw / 300, Hw / 200 och Hw / 100 är de procentsatser av banhöjd som används för att uppskatta amplituden. För det tredje har sedan en begränsad parametrisk studie genom att ändra en faktor åt gången utförts för att se effekten av varje dimensionsparameter på balkens tvärkraftkapacitet. Slutligen har tvärkraftkapacitet hos de undersökta balkarna jämförts med den tvärkraftkapacitet som tillhandahålls av Eurocode-ekvationer.

Resultaten visar att tvärkraftkapacitet hos balkar med korrugerade rostfria stålliv är känslig för både formen och amplituden hos en initial imperfektion. Tvärkraftkapacitet minskar avsevärt med ökande initial imperfektionsamplitud. Dessutom är den mest kritiska initiala imperfektionsformen av en enkel-mod-form av egenformer och inte den första positiva lägesformen. Banhöjd, bantjocklek och korrugeringsdjup ökar avsevärt tvärkraftkapacitet. Platt vikningslängd minskar tvärkraftkapacitet. Tvärkraftspänning har dock en försumbar effekt. Slutligen är det på den säkra sidan att använda Eurocode-designkurva med första knäckningsläge och initiala imperfektionsamplitud på Hw/200.

Nyckelord: Korrugerade liv, Tvärkraftkapacitet, Rostfritt stål, Stålbroar, Initial imperfektion, Känslighetsanalys, Parametrisk studie.

Preface

This Master's thesis was initiated at the Chalmers University of Technology's Department of Architecture and Civil Engineering and performed at the AFRY's Bridge and Infrastructure department in Gothenburg between January and June 2021.

First and foremost, we would like to express our gratitude to our AFRY supervisor Farshid Zamiri for his unquestioning support and considerable expertise in a variety of engineering and programming areas, which are both critical to the success of our project. Having you as a supervisor has been a great honour.

Mohammad Al-Emrani, it was unfortunate that you were unable to engage from the beginning, but once you arrived, you were a huge assistance.. We are really grateful for your prompt aid, generosity of time, and most important, your kindness.

We'd also like to extend our thanks to our examiner Mozdheh Amani for her constant support and valuable comments during the work. Our sincere thanks for your guidance and commitment throughout the research.

Finally, we'd like to thank Saad Almeri for his constant support and assistance throughout the project, particularly his programming aid.

Gothenburg, June 2021, Fatima Hlal and Naheel Mohra

Contents

List of Figures

List of Tables

List of Symbols

Roman upper-case letters

D_x	The transverse bending stiffness per unit length
D_y	The longitudinal bending stiffness per unit length
E	Modulus of elasticity
E_y	Tangent modulus of the stress-strain curve at yield strength
G_e	Elastic shear modulus
I_y	Second moment of inertia around the strong axis
K_G	Global buckling coefficient.
K_L	Local buckling coefficient.
F_y	The uniaxial yield strength of the web material
$R_{p0.05}$	Proof stress for stainless steel
$V_{bw,Rd}$	Web contribution to shear strength

Roman lower-case letters

a	Shear span
b	Flat fold length in corrugation
b_f	Flange width
c	Inclined fold length in corrugation
d	Projection of inclined fold c
f_u	Ultimate strength
f_y	Yield strength
f_{yw}	Yield stress limit in web
h_r	Corrugation depth
h_w	Web height
s	Unfolded length of one half corrugated web wave
t_f	Flange thickness
t_w	Web thickness
w	Length of one half corrugated wave

Greek letters

α	Flat fold length in corrugation
β	Ratio of the longitudinal fold width, b, to the inclined fold width, c.
ε	Engineering strain
σ	Engineering stress
σ_{true}	True stress
ε_{true}	True strain
ε_{true}^{pl}	Plastic part of the true strain
$\varepsilon_u l$	Ultimate strain
γ_{M0}	Safety factor
γ_{M1}	Safety factor
$\tau_{cr,G}$	Global critical shear buckling stress for a corrugated web
$\tau_{cr,I}$	Interactive critical shear buckling stress for a corrugated web
$\tau_{cr,L}$	Local critical shear buckling stress for a corrugated web
τ_y	Shear yielding stress for a corrugated web
υ	Poisons ratio
χ_c	Reduction factor for out of plane buckling
$\chi_{c,l}$	Reduction factor due to local buckling
$\chi_{c,g}$	Reduction factor due to global buckling
$\chi_{c,i}$	Reduction factor due to interactive buckling
λ	Eigenvalue regarding buckling
$\lambda_{c,L}$	Slenderness regarding local buckling
$\lambda_{c,G}$	Slenderness regarding global buckling
$\lambda_{c,I}$	Slenderness regarding interactive buckling
ρ	Normalized shear strength

1
Introduction

Steel bridges are susceptible to corrosion, requiring regular repairs, re-painting, and audits during their lifetimes, which is expensive. Using stainless steel, on the other hand, may help to mitigate the problem's negative implications.

Because the beams are deep in web height, it is usual in steel bridges to employ thin webs to prevent wasting a lot of material and to get the most strength out of the material with the least amount of weight. However, such thicknesses make the manufacturing process extremely complex. This challenge was handled by using corrugated webs instead of very thin flat plates. Steel Corrugated webs in [CWGs] are attached to the two flanges by welding [14] resulting in corrugated web steel girders being lighter than flat web steel girders [30].

1.1 Background

Since the early 1960s, corrugated web beams have been used for steel buildings in Europe and since the 1980s for highway bridges in Europe and Japan. Standard corrugated steel I-beam consists of two steel flanges welded to a corrugated steel web. The most commonly used corrugation profile is the trapezoidal profile, although other web profiles have been used, such as sinusoidal. Many studies and researches have been performed on the corrugated web and have shown that they have more stability, improved shear behavior, and better fatigue resistance.[7]

The use of corrugated webs has been proposed for a long time to improve the buckling strength and rigidity out of the plane and replace the use of vertical stiffeners. It was first used with very thin web panels in aircraft structures and was then applied for applications in civil engineering in buildings and bridges. It was realized that corrugated web beams are economical to use and can improve the aesthetics of the structure.[25]. It was also demonstrated by Li et al. [14] that the corrugated web steel beams have 1.5 - 2 times more resistance for a shear than the conventional flat web beams.

The first research to perform the subject of shear buckling behavior was by Easley and McFarland. Subsequently, several theoretical and experimental studies have been performed on the buckling behavior and strength of corrugated steel webs, such as Elgaaly et al. and Abbas et al. in USA, Luo and Edlund in Sweden and Yoda et al. and Yamazaki in Japan and many other studies. [19]

Until the mid-1990s, shear buckling modes were only known as local and global buckling in corrugated steel web girders. Local buckling shows failure in a subpanel, while global buckling represents a failure of several folds on the entire web. Later on, experimental specimens indicated that the failure of some of them was initially shown in one fold and then spread to others. This mode was categorized and considered a local buckling mode. But after that, this mode of buckling has been defined by detailed experimental observations as an interactive buckling mode.[25]

The use of high-strength steels (HSSs) in buildings and bridges have numerous advantages such as eliminating the use of substantially thick steel plates which cause a lot of problem in the different stages of building. High-strength steels offer designers the ability to build structures using slender members and more weight-efficient elements than the normal strength steel (NSSs). That is related to their high strength, excellent durability, and strong weldability and corrosion resistance. [24]

Currently, stainless steel is not widely used in structures since it is more costly than standard carbon steel. However, the characteristics of stainless steel, such as corrosion resistance and high strength, make it more sustainable to be used in structural bridge girders in the long run, taking the life cycle cost of LCC into account.

The usage of both solutions, stainless steel bridges with corrugated webs, is expected to improve the mechanical properties of the bridges and provide lower life cycle costs.

A lot of researches on shear buckling resistance of corrugated web girders can be found in international literature, but it is still unknown how the changes in geometric imperfections and the different influential imperfection parameters due to the manufacturing process and their effect on the shear capacity have not been studied and explained yet.[26].

The Chalmers University of Technology initiated this master's thesis and conducted it at the Department of Bridges at AFRY in Gothenburg.

1.2 Scope

The aim of this project is to prove the shear buckling performance of the corrugated web using stainless steel and to identify the most influential imperfection parameters and their effect on the shear behavior. The shear buckling occurs in three different modes: local, global and interactive. Results from past tests and from FEM analysis will be provided and compared with a new FEM modeling wherein all three modes will be included and observed. Moreover, It has been observed that the shear buckling behavior is sensitive to the initial imperfections of the corrugated web in conventional steel, but it is still unknown how it will be effected using a new steel material, so the objectives of this thesis can be summarized in three goals.

The first objective is a literature study to identify the most critical parameters that influence the shear behavior of the steel girders with the corrugated web.

The second objective is to study the sensitivity of stainless steel bridge girders with corrugated webs to unavoided initial imperfections. The effect of both shape and amplitude of initial imperfection will be investigated.

The third objective is to assess the effect of corrugation configurations on the ultimate shear capacity of the stainless steel bridge girders with the corrugated web.

The final goal is to see if the Eurocode design equations can be used to determine the ultimate shear capacity of the stainless steel bridge girders with the corrugated web.

1.3 Limitations

1- In this master's thesis, just the steel girder of a bridge will be researched, especially shear buckling behavior, with the rest of the bridge components such as the deck, stiffeners, and non-steel components left out..

2- Only a single-span, simply-supported beam will be examined..

3- The influence of the corrugation bend radius on shear behavior will not be taken into account..

4- In this thesis, the girder's behavior after buckling will not be explored in depth..

5- Only one type of stainless steel will be investigated, and it will not be utilized as a study variable.

6- To avoid any unusual load routes, the span ratio will be kept less or near to 3.

7- Only trapezoidal corrugations will be investigated.

8- The ratio of flange thickness to web thickness will be considered equal to or larger than 3 to ensure shear failure and avoid failure due to flange deformation.

2

Literature Review

2.1 Bridge girders with corrugated webs

A bridge girder with a corrugated web varies from the conventional I-beam with a flat web in many ways. As per [14], there are many advantages to using corrugated web girders (CWGs). Firstly, shear buckling strength is enhanced in the CWGs over the conventional flat web girders. Secondly, CWGs have shown 1.5-2 times more shear resistance than the conventional flat web girders [14].

Moreover, the webs are typically thin corrugated steel plates varying in thickness from 1 mm to several millimeters. Thus, because of the weight reduction, CWGs are considered a more economic option compared to flat web girders. Corrugated web girders are 9-13 percent lighter than stiffened flat web girders.[14]. And according to [30], the weight of CWGs can be nearly 20 percent less than the conventional flat web girders if there is no minimum limit for the web thickness. It is also known that the CWGs with deeper webs are more economically efficient.

Also, the out-of-plane stiffness of corrugated webs provides high stability to the webs, thus, eliminate the need for transverse stiffeners that are commonly used in flat web girders [30], and that leads to better fatigue resistance [7]

2.1.1 Corrugation Shapes

There are several shapes of the CWGs. The trapezoidal shape is the most common. However, there are other corrugation shapes like sinusoidal, triangular, and rectangular, as shown in figure 2.1 and figure 2.2.

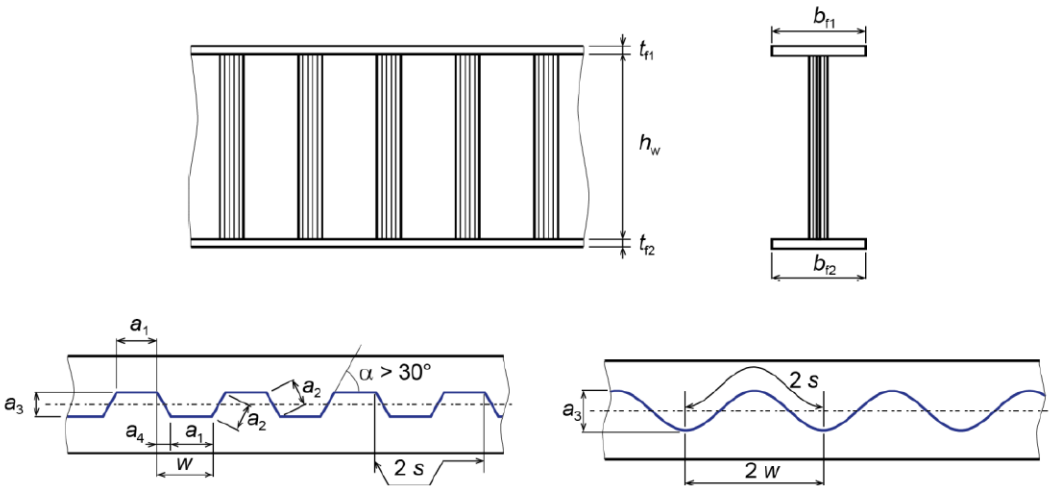

Figure 2.1: Typical geometric notations for corrugated web girder from Eurocode [8]

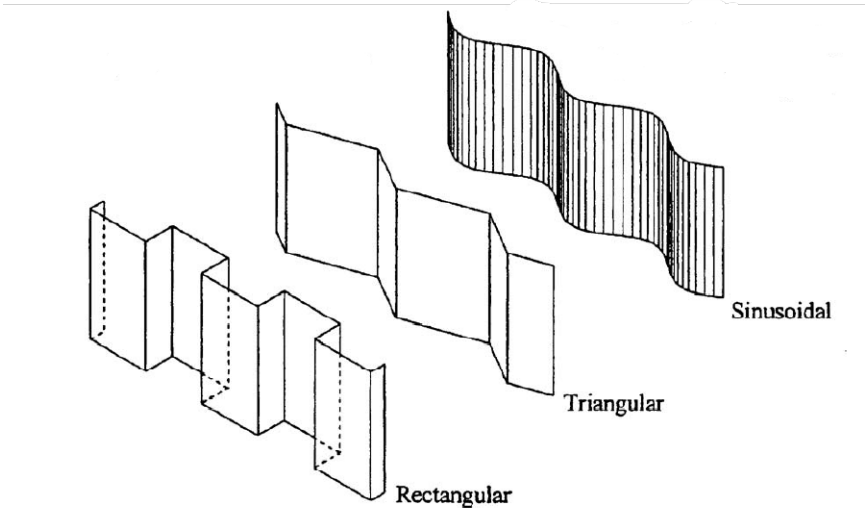

Figure 2.2: Different shapes of web corrugation [7]

According to Sauce et al. [30], sinusoidal web girders require thicker webs due to global buckling. But at the same time, it gives less weight due to shorter lengths. If the web's minimum required thickness is not considered, the sinusoidal web girders can give up to 14 percent weight reduction than the trapezoidal web girders. However, This percentage decreases if there is a minimum limit for the web thickness.

Even though sinusoidal web girders may save some weight, the trapezoidal web girders are more common due to the ease of fabrication, as stated by Sauce et al. [30]

2.1.2 Shear behaviour differences between flat and corrugated web bridge girders

Many differences can be observed in the shear behavior of flat and corrugated webs.

2.1.2.1 Shear stress distribution

Corrugated webs do not carry bending stresses as flat webs. The ratio between the corrugation depth and the web thickness is typically between (10- 30), which gives flexibility of several hundred to several thousand. This phenomenon is known as the accordion effect. For this reason, the corrugated webs can not carry significant axial loads like flat webs subjected to the same loading. [7]
Due to the accordion effect, the bending stresses in girders with corrugated webs are carried mainly by the flanges. On the other hand, the shear stresses are carried totally by the corrugated webs, and consequently, the shear stress along the web height is constant.[24]

2.1.2.2 Manufacturing-induced residual stresses

The residual stress distribution in CWGs differs from conventional I-girders due to the accordion effect and different welding paths. Membrane residual stresses are main for flat web girders while it is bending stresses in CWGs. [28]

Compressive stresses in flanges of CWGs increase due to the transverse bending moment induced by the manufacturing process. Whereas the tensile residual stresses' magnitude in the web and the flange of CWGs is similar to the girders with flat webs. Moreover, increasing or decreasing the corrugation angle has no effect on the width of the tensile zone of the web in CWGs. [28]

Conventional I-girders, except at the ends, can be distinguished by quasi-stationary residual stress distribution induced by the manufacturing process. Stresses are virtually equal on the top and bottom surfaces of the flanges and on both sides of the web. Whereas due to the negligible axial stiffness of corrugated webs due to the "accordion effect," quasi-zero residual stresses emerge in the corrugated webs. [28]

2.1.2.3 Elastic buckling

Conventional I-girder web plates supported by the flange, and the vertical stiffeners show the well-known local buckling mode. At the same time, the girders with corrugated webs may show three different buckling modes as shown in figure 2.3. The local buckling in one fold and the global buckling mode in many folds extended through the web height. The last mode, which is called interactive buckling mode,

is in-between the previous two modes. In this mode, the buckle extends over few folds.[24]

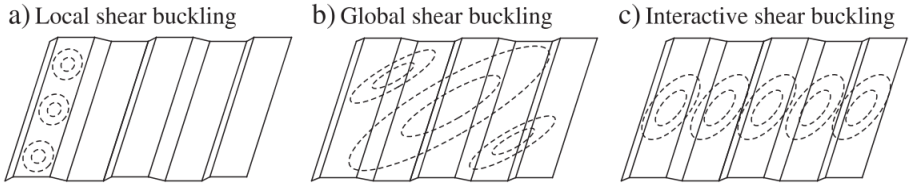

Figure 2.3: Different buckling modes of trapezoidal corrugated webs [18]

2.1.2.4 Shear failure mechanism

In general, the webs in the girders with corrugated webs fail under shear due to buckling or yielding. Moreover, pure shear along the height of these webs is noticed in the shear tests and no interaction between the shear and bending [15]. However, from a study performed by Zhang et al. on large-scale specimens, the flange carries about 7% of the shear capacity, which shouldn't be neglected [20].

The previous studies have shown different results regarding stocky webs. Hassanein et al. showed that stocky corrugated webs do not reach yielding, while others proposed that the stocky webs may reach yielding [15].

Referring to [24] the conventional I-girders show the formation of plastic hinges in shear failure. These hinges take place due to the difference in upper and lower flange movements that end with the plastic hinge formation. But CWGs don't exhibit such plastic hinges when there are local or interactive buckling modes.

However, recently Zhang et al. pointed out that in the girders with corrugated webs, plastic hinges may develop, in such cases the shear failure mechanism can be divided into three types, quasi-mid section mechanism when the girders are narrow and flexible, girder mechanism for deep and rigid girders, and finally mid-section mechanism for the girders in between the two previous cases [32]. The three failure mechanisms are shown in figure 2.4

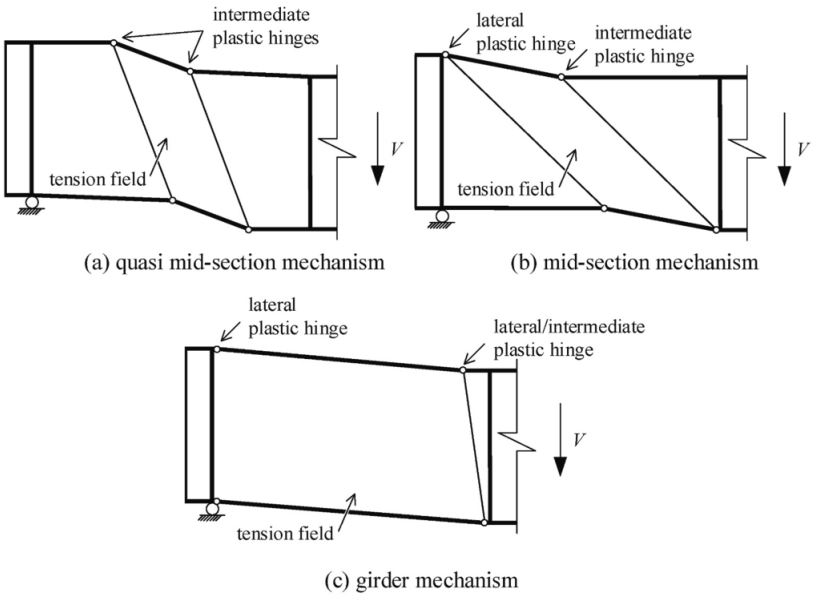

Figure 2.4: Different shear failure mechanisms of corrugated webs [32]

2.2 Shear strength of normal-strength carbon steel girders

It has been observed that girders with corrugated webs fail mostly due to buckling. The shear buckling resistance researches started in 1969 [27]. In the beginning, only global buckling was considered with considering the corrugated web as an orthotropic plate. Many types of research followed, and it was observed that the shear buckling can be governed by local buckling considering isotropic plate or global buckling considering orthotropic plate. Thereafter, numerous investigations have been done, and the shear buckling then divided into three different modes of local, global and interactive[27].

The basic theory behind these researches is using isotropic plate buckling theory for local buckling and orthotropic plate buckling theory for global buckling[27]. Also, the basic equation for the interaction of local and global buckling is firstly proposed by Lindner, and Aschinger [25]. It is shown below in equation 2.1. Changing the value of n gives the order of the interaction, which means that n=1 gives a first-order interaction.

$$\left(\frac{1}{\tau_{cr,i}}\right)^n = \left(\frac{1}{\tau_{cr,l}}\right)^n + \left(\frac{1}{\tau_{cr,g}}\right)^n \tag{2.1}$$

Table 2.1: Order of interactive mode from different authors[25]

Author	**Bergfelt and Leiva**	**Yi et al.**	**El-Metwally**	**Abbas et al.**	**Hiroshi**	**Sayed-Ahmed**
n	1	1	2	2	4	3

It is worth pointing out that the different authors considered different orders of interaction as shown in the table 2.1 [25]. In addition to other interaction orders, there might be different local and global buckling factors (kL and kG). The local buckling coefficient, which is related to the buckling within one fold, depends on the aspect ratio of the fold (w/hw) and the boundary condition between the folds and between the fold and the flanges [30]. However, the global buckling coefficient depends on the boundary conditions of the web [30].
The annotations used in the following equations are illustrated in figure 2.5

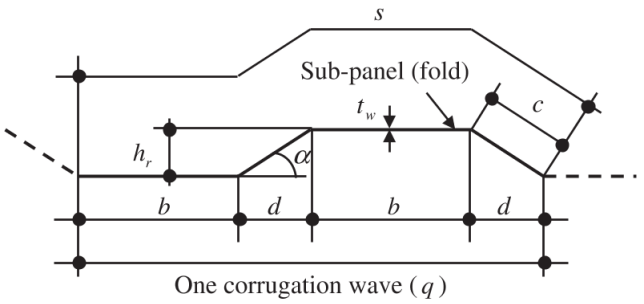

Figure 2.5: Geometric notation of one wave of corrugation [23]

2.2.1 Design shear buckling strength according to Moon et al. [17]

According to Moon [17], the the design shear buckling strength can be calculated directly from equation 2.2 and no need to calculate local and global buckling separately. This formula is based on a first-order interactive buckling.[17]

The shear strength of the corrugated web according to Moon[17]

$$\frac{\tau_{cr}}{\tau_y} = \begin{cases} 1.0 & : \lambda_s \leqslant 0.6 \\ 1 - 0.614\,(\lambda_s - 0.6) & : 0.6 < \lambda_s \leqslant \sqrt{2} \\ \frac{1}{\lambda_s^2} & : \sqrt{2} < \lambda_s \end{cases} \tag{2.2}$$

where λ_s is Shear buckling parameter of corrugated web and is defined in equation 2.3

$$\lambda_s = 1.05\sqrt{\frac{\tau_y}{k_l E}}\left(\frac{h_w}{t_w}\right) \tag{2.3}$$

k_I is The interactive shear buckling coefficient and defined in equation 2.4

$$k_I = \frac{30.54}{5.34\left(h_r/t_w\right)^{-1.5} + 5.72\left(w/h_w\right)^2} \tag{2.4}$$

τ_y is the shear yielding stress; τ_{cr} is the critical shear buckling stress.

2.2.2 Design shear buckling strength according to Driver et al. [23]

Driver et al. [12] propose one formula, 2.6, that include the interaction between local and global buckling. This formula is also applicable when inelastic buckling or yielding is dominated.

They also recommend lower bound values for the local and global buckling coefficients considering a simply supported juncture.[23]. The value of 5.34 for the local buckling coefficient and the value of 31.6 for the global buckling coefficient are suggested.

Other recommendations for global buckling coefficients are also suggested[23] when the web length is relatively large in comparison with the web height. Elgaaly et al. considered that the web is quite long in comparison with its height and proposed the value of 31.6 for a simple support and the value of 59.2 for a fixed support. Also, Easely, consider the values 36 for simple support and 68.4 for a fixed support condition respectively [23].

Worth mentioning here that the local buckling coefficient is related to the aspect ratio of the fold and the boundary condition at the juncture with flange. However, the global buckling coefficient is related to boundary conditions, e.g., for long webs lead to smaller global buckling coefficient, and the boundary condition at the juncture with flange [30].
In Driver et al. only elastic buckling is considered. However, if the shear stress is larger than $0.8\tau_y$, the inelastic shear buckling coefficient from Elgaaly et al. which is equal to 2.5 [30], should be used,[23].

The inelastic shear buckling stress, according to Elgaaly et al. [30] for both local and global buckling is as follows.

$$\left(\tau_{cr}\right)_{\text{inel}} = \sqrt{0.8\tau_y\left(\tau_{cr}\right)_{el}} \leq \tau_y \tag{2.5}$$

where shear yielding strength by the von Mises yield criterion is defined as:

$$\tau_y = \frac{F_y}{\sqrt{3}}$$

F_y is the uniaxial yield strength of the web material.

The shear strength of the corrugated web according to Driver et al.[23] is as follows.

$$\tau_{nD} = \sqrt{\frac{(\tau_{crL} \cdot \tau_{cr.G})^2}{(\tau_{cr,L})^2 + (\tau_{cr,G})^2}} \tag{2.6}$$

In which the elastic local buckling stress is calculated as follows.

$$\tau_{cr,L} = k_L \frac{\pi^2 E}{12\,(1-v^2)} \left(\frac{t_w}{w}\right)^2 \tag{2.7}$$

ν is Poison's ratio
E is Young's modulus of elasticity
w is the maximum of the flat fold width and inclined fold width

The elastic global buckling stress is calculated according to equation 2.8

$$\tau_{cr,G} = k_G F(\alpha, \beta) \frac{E t_w^{0.5} b^{1.5}}{12 h_w^2} \tag{2.8}$$

In which $F(\alpha, \beta)$, the geometric coefficient, is

$$F(\alpha, \beta) = \sqrt{\frac{(1+\beta)\sin^3\alpha}{\beta + \cos\alpha}} \cdot \left(\frac{3\beta + 1}{\beta^2(\beta+1)}\right)^{0.75} \tag{2.9}$$

where α is the corrugation angle and β is the ratio of the longitudinal fold width
To reach shear yielding capacity, Driver et al. [12] recommended the following limit on the slenderness (h_w/t_w) where h_w is web depth and t_w is web thickness.

$$\frac{h_w}{t_w} \leqslant 1.91\psi \sqrt{\frac{E}{F_y} \left(\frac{b}{t_w}\right)^{1.5} F(\alpha, \beta)} \tag{2.10}$$

Moreover, to maximize the shear capacity assuming (b/c>1) the ratio of longitudinal fold to web thickness, the ratio of the longitudinal fold width to the web thickness

must be satisfied as follows: [12].

$$\frac{b}{t_w} \leqslant 2.586\sqrt{\frac{E}{F_y}} \tag{2.11}$$

2.2.3 Design shear buckling strength according to Sause and Braxtan. [23]

Sause and Braxtan [23] suggest value 36 for global buckling coefficient kG with simple boundary conditions and the value 68.4 for fixed boundary conditions.

Worth mentioning that these equations are derived on the basis of small-scale girders with very thin webs (smaller than 1mm). Meaning that the stress-strain relation and the initial imperfections due to the fabrication and welding process could be considerably different from real bridge girders[23].

The shear strength of corrugated web according to Sause and Braxtan [23] is given in equation 2.12.

$$\tau_{n,s} = \tau_y \left(\frac{1}{(\lambda_{I,3})^6 + 2} \right)^{1/3} \tag{2.12}$$

The interactive slenderness parameter can be calculated from the equation below using n=3 is given as

$$\lambda_{I,n} = \lambda_L \lambda_G \left(\left(\frac{1}{\lambda_L} \right)^{2n} + \left(\frac{1}{\lambda_G} \right)^{2n} \right)^{1/2n} \tag{2.13}$$

The local slenderness parameter is calculated as follows

$$\lambda_L = \sqrt{\frac{12\,(1-v^2)\,\tau_y}{k_L \pi^2 E}} \frac{w}{t_w} \tag{2.14}$$

The global slenderness parameter

$$\lambda_G = \sqrt{\frac{12 h_w^2 \tau_y}{k_G F(\alpha,\beta) E t_w^{0.5} b^{1.5}}} \tag{2.15}$$

β is the ratio between longitudinal fold width to inclined fold width. Values of 1 to 2 are commonly used [30]. α is the corrugation angle. Values of 30 and 45 degrees are commonly used [30].

2.2.4 Design shear buckling strength according to Hassanein et al. [23]

Hassanein et al. proposed an interaction formula between local and global buckling considering a fixed juncture between the flange and the web with n=0.6.
They recommended the value of 8.98 for the local buckling coefficient and the value of 59.2 for the global buckling coefficient. These values are the upper bound since the juncture is considered to be fixed.

It is worth to point out that Hassanein et al. concluded that the juncture between the web and flange can be considered fixed if ($t_f/t_w > 3.0$). However, if ($t_f/t_w < 3.0$), a simply supported juncture should be considered with changing the interactive formula with n=0.6 to a first order interaction with n=1 [27]. Also, the value of 5.34 for the local buckling coefficient and the value of 31.6 for the global buckling coefficient[30] should be taken into account.

The elastic local buckling stress is calculated Same to equation 2.7

The elastic global buckling stress is calculated as follows

$$\tau_{cr,G} = k_G \frac{D_x^{0.25} D_y^{0.75}}{t_w h_w^2} \tag{2.16}$$

The transverse bending stiffness per unit length is calculated as follows

$$D_x = \frac{q}{S} \cdot \frac{E t_w^3}{12} \tag{2.17}$$

The longitudinal bending stiffness per unit length is calculated as follows

$$D_y = \frac{E I_y}{q} \tag{2.18}$$

The second moment of area is defined as

$$I_y = 2bt_w \left(\frac{h_r}{2}\right)^2 + \frac{t_w h_r^3}{6 \sin\alpha} \tag{2.19}$$

The shear strength of the corrugated web according to Hassanein et al.[23] is defined as

$$\tau_{cr,I,0.6} = \frac{\tau_{cr,L} \cdot \tau_{cr,G}}{\left((\tau_{cr,L})^{0.6} + (\tau_{cr,G})^{0.6} \right)^{\frac{1}{0.6}}} \tag{2.20}$$

2.2.5 Hassanein et al. also proposed interactive equations for Driver and Sause equations [23]

The shear strength of the corrugated web proposed by Hassanein et al. based on Driver equation[23] is defined as the following equation.

$$\tau_{n,D,0.6} = \tau_{cr,I,0.6} \tag{2.21}$$

The shear strength of the corrugated web proposed by Hassanein et al. on Sause and Braxtan equation[23] is defined as follows.

$$\tau_{n,S,0.6} = \tau_y \left(\frac{1}{(\lambda_{I,0.6})^6 + 2} \right)^{1/3} \tag{2.22}$$

The proposed interactive slenderness factor for Moon equation is calculated as below[23]

$$\lambda_{I,0.6} = \sqrt{\frac{\tau_y}{\tau_{cr,I,0.6}}} \tag{2.23}$$

2.2.6 Shear resistance for plate girders with corrugated web according to Nie et al.[18]

Recently Nie et al. performed a shear test on eight steel H-shape girders with corrugated web and derived a new equation for elastic shear buckling strength through an extensive parametric study[18]. Then nonlinear buckling analysis is performed to assess the effect of initial imperfection on shear strength, and a proposed relation between the normalized shear strength ρ with shear buckling slenderness ratio λ_s is established[18].

Elastic shear buckling strength according to Nie et al.[18] is calculated as follows.

$$\tau_{\mathrm{el}} = \begin{cases} B\left(\tau_{\mathrm{L,el}}, \tau_{\mathrm{G,el}}, f\right) - 0.109\tau_{\mathrm{L,el}} + \frac{0.0229\tau_{\mathrm{L,el}}^2}{B\left(\tau_{\mathrm{L,el}}, \tau_{\mathrm{G,el}}, f\right)} \leq \tau_{\mathrm{L,el}} & \tau_{\mathrm{L,el}} < 11.09 f \tau_{\mathrm{G,el}} \\ 1.5\tau_{\mathrm{G,el}} & \tau_{\mathrm{Lel}} \geq 11.09 f \tau_{\mathrm{G,el}} \end{cases} \tag{2.24}$$

$$f\left(b/h, h_{\mathrm{r}}/t\right) = \left[0.06\left(h_{\mathrm{r}}/t\right) + 0.68\right]\left[9.28(b/h)^2 - 5.95(b/h) + 1.63\right] \tag{2.25}$$

$$B\left(\tau_{\mathrm{L,el}}, \tau_{\mathrm{G,el}}, f\right) = \sqrt[3]{A\left(\tau_{\mathrm{L,el}}, \tau_{\mathrm{G,el}}, f\right) - 0.0031\tau_{\mathrm{Lel}}^3 + 0.0728 f \tau_{\mathrm{G,el}} \tau_{\mathrm{L,el}}^2} \tag{2.26}$$

$$A\left(\tau_{\mathrm{L,el}}, \tau_{\mathrm{G,el}}, f\right) = \sqrt{\left(0.0031\tau_{\mathrm{L,el}}^3 - 0.0728 f \tau_{\mathrm{G,el}} \tau_{\mathrm{L,el}}^2\right)^2 - 1.2 \times 10^{-5} \tau_{\mathrm{L,el}}^6} \tag{2.27}$$

The shear strength for the corrugated web proposed by Nie et al. The three buckling modes are considered in the equation 2.28.

$$\rho = \begin{cases} 1 - 0.328\lambda_{\mathrm{s}}^2 & \lambda_{\mathrm{s}} \leq 0.75 \\ -0.137\lambda_{\mathrm{s}}^3 + 0.912\lambda_{\mathrm{s}}^2 - 2.11\lambda_{\mathrm{s}} + 1.94 & 0.75 < \lambda_{\mathrm{s}} \leq 1.87 \\ \frac{1}{\lambda_{\mathrm{s}}^2} & \lambda_{\mathrm{s}} > 1.87 \end{cases} \tag{2.28}$$

Where the normalized shear strength is calculated as follows.

$$\rho = \frac{\tau_{\mathrm{cr}}}{\tau_{\mathrm{y}}} \tag{2.29}$$

And the shear buckling slenderness ratio

$$\lambda_{\mathrm{s}} = \sqrt{\frac{\tau_{\mathrm{y}}}{\tau_{\mathrm{el}}}} \tag{2.30}$$

Due to the corrugation, the shear modulus needs to be modified to consider the reduction of shear stiffness [24]. The elastic shear modulus suggested by Johnson and Kaffola for corrugated webs gives good agreement with the test results [18].

$$G_e = \frac{E}{2(1+v)} \cdot \left(\frac{b+d}{b+c}\right) \tag{2.31}$$

Where b, c, d are shown in figure 2.5
The local elastic buckling shear stress is defined as follows.

$$\tau_{\mathrm{L,el}} = k_{\mathrm{L}} \frac{\pi^2 E}{12\left(1-v^2\right)(w/t)^2} \tag{2.32}$$

The global elastic buckling shear stress is defined as follows.

$$\tau_{\mathrm{G,el}} = k_{\mathrm{G}} \frac{E t^{1/2} h_{\mathrm{r}}^{3/2}}{12h^2} \left(\frac{b+d}{b+c}\right)^{1/4} \left(\frac{3b+c}{b+d}\right)^{3/4} \tag{2.33}$$

The local buckling coefficient for simple juncture is defined as follows.

$$k_{\mathrm{L,s}} = 5.34 + 4.0(\ \mathrm{h/w})^2 \tag{2.34}$$

The local buckling coefficient for fixed juncture is calculated as follows.

$$k_{\mathrm{L,f}} = 8.98 + 5.6(\ \mathrm{h/w})^2 \tag{2.35}$$

The global buckling coefficient for simple juncture is calculated as follows.

$$k_{\mathrm{G,s}} = 1.2747(\ \mathrm{h/a})^2 + 0.7603(\ \mathrm{h/a}) + 34.176 \tag{2.36}$$

The global buckling coefficient for fixed juncture is defined as follows.

$$k_{G,f} = 3.0545(h/a)^2 - 0.0231(h/a) + 64.195. \tag{2.37}$$

2.2.7 Shear resistance for plate girders with corrugated web according to Leblouba et al.[13]

The shear strength proposed by Leblouba et al. , using Richard's equation, is based on a statistical study of 125 previous tests with twelve new conducted experiments [13].

The shear strength of the corrugated web proposed by Leblouba et al. [13]

$$\rho_{M-1} = \frac{1}{\left(1 + \left(\frac{\lambda_{I,4}}{1.58}\right)^{1.6}\right)^{1.15}} \tag{2.38}$$

Where the slenderness ratio

$$\lambda_{I,n} = \sqrt{\frac{\tau_y}{\tau_{I,n}}} \tag{2.39}$$

The interactive shear buckling is shown in equation 2.40. The factor u is equal to zero when considering local and global buckling only and equal to an integer value when shear yield stress is also involved [13].

$$\frac{1}{(\tau_I)^n} = \frac{1}{(\tau_L)^n} + \frac{1}{(\tau_G)^n} + \frac{u}{(\tau_y)^n} \tag{2.40}$$

The model has been adjusted by Leblouba et al. according to 2.41 using Hill's hyperbolic equation. The improved model gives better prediction to shear strength comparing to the collected test data [16].

$$\rho_{M-2} = \frac{1}{1 + \left(\frac{\lambda_{I,3}}{1.4}\right)^{1.7}} \tag{2.41}$$

2.2.8 Shear resistance for plate girders with corrugated web in Eurocode [8]

. The basis of the Eurocode equation is Höglund's work [14]. Höglund suggests that the interaction between the local and global buckling is weak, and considering them separately is sufficient[14]. Thus, Eurocode consider two separate checks for local and global buckling and select the minimum of them.

Kövesdi and Kollar [27] mentioned that Leblouba et al. [14] who compared the models from the existing analytical model that estimated the shear strength and a database of 125 test results and found that the formula EN 1993-1-5 is conservative and accurate regarding local and global shear buckling design of girders with corrugated webs.

The design rules of sinusoidal and trapezoidal corrugated web girders are given in section 13 EN 1993-1-5 [8]

The notations in Eurocode equation is shown in figure 2.6

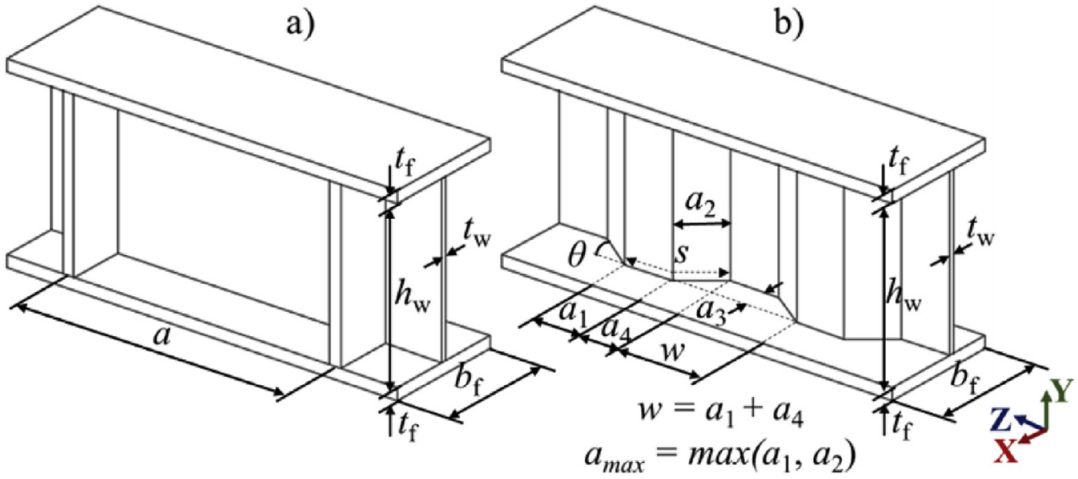

Figure 2.6: Geometric notation of a. Flat web b. Corrugated web [27]

The shear buckling resistance of corrugated web girders according to Eurocode [8] is defined as follows.

$$V_{bw,Rd} = \frac{\chi_c f_{yw} h_w t_w}{\sqrt{3}\gamma_{M1}} \tag{2.42}$$

$$\text{where the reduction factor } \chi_c = \min\left(\chi_{c,l}, \chi_{c,g}\right) \tag{2.43}$$

The local reduction factor is defined as follows.

$$\chi_{c,\ell} = \frac{1,15}{0,9 + \bar{\lambda}_{c,\ell}} \leq 1,0 \tag{2.44}$$

where local slenderness factor is defined as follows.

$$\overline{\lambda_{c,l}} = \sqrt{\frac{f_{yw}}{\sqrt{3}\tau_{cr,l}}} \tag{2.45}$$

The global reduction factor is defined as follows.

$$\chi_{\mathrm{c,g}} = \frac{1.5}{0.5 + \bar{\lambda}^2_{\mathrm{c},g}} \leq 1.0 \tag{2.46}$$

Where global slenderness factor

$$\bar{\lambda}_{c,g} = \sqrt{\frac{f_{yw}}{\tau_{cr,g}\sqrt{3}}} \tag{2.47}$$

The critical local shear stress is defined as follows.

$$\tau_{cr,\ell} = 4,83E\left[\frac{t_w}{a_{\max}}\right]^2 \tag{2.48}$$

The critical global shear stress is defined as follows.

$$\tau_{cr,g} = \frac{32,4}{t_w h_w^2}\sqrt[4]{D_x D_z^3} \tag{2.49}$$

For sinusoidal corrugated webs $\tau_{\mathrm{cr},\ell}$ should be calculated from

$$\tau_{cr,\ell} = \left(5,34 + \frac{a_3 \cdot 5/6 \cdot s}{h_w t_w}\right)\frac{\pi^2 E}{12\left(1-v^2\right)}\left[\frac{t_w}{s}\right]^2 \tag{2.50}$$

The longitudinal bending stiffness per unit length is defined as follows.

$$D_x = \frac{Et_w^3}{12\left(1-v^2\right)}\frac{w}{s} \tag{2.51}$$

Where w is the length of one half wave.
s is the unfolded length of one half wave.

The transverse bending stiffness per unit length is defined as follows.

$$D_y = \frac{EI_z}{w} = \frac{E \cdot t_w a_3^2}{12} \cdot \frac{3 \cdot a_1 + a_2}{a_1 + a_4} \tag{2.52}$$

2.3 The parameters that affect shear buckling strength

The shear buckling strength of the bridge girders with corrugated webs is affected by many parameters like the geometry of the corrugations like the depth and the width of the folds, the boundary conditions between the fold and between the web and the

flanges, the aspect ratio of the web and the aspect ratio of the fold, the thickness of the web and finally the inevitable initial imperfection due to the manufacturing process.

2.3.1 Corrugated web configuration

According to Nie et al. the the shear strength is not related to the corrugated configuration when the inclined and flat folds are equal and the parameters that affect elastic shear buckling are $\frac{b}{h}$, $\frac{h_r}{t}$, $\tau_{G,el}$, $\tau_{local,el}$ [18] where b is flat fold length in corrugation, h is trapezoidal corrugated web height, t is trapezoidal corrugated web thickness, h_r is the corrugation depth, $\tau_{local,el}$ and $\tau_{G,el}$ is the the elastic local and global shear buckling strength respectively.

2.3.2 Corrugation depth (corrugation angle α)

According to the parametric study that has been done by Hassanein et al. on HSSs for small corrugation depths (50 to 100mm) the ultimate shear capacity increases significantly [24]. However, with larger corrugation depths (150 to 300mm) the increase in ultimate shear capacity becomes insignificant and can be neglected [24].

It is been observed that increasing the corrugation depth decreases the possibility to form shear plastic hinges in HSSs. That is due to the increase of the flange rigidity and larger shear capacity, which prevent any difference in the deflection between lower and upper flanges, which is the main cause for forming plastic hinges in the flat web girders[24].

Pointing out that for HSSs and NSSs, using corrugation angle less than 30 degrees where the web is closer to flat are results in global buckling mode. To avoid the global buckling mode, an increase in the corrugation angle is suggested. That will change the buckling mode to interactive and local buckling mode.[24] and [30].

To point out here that the global buckling governs the shear failure only in deep, thin webs with small corrugation depths. Otherwise, the shear yielding is dominaterd[30]. The girders with trapezoidal corrugated webs have residual shear strength about half of their capacity[14]. Hassanein demonstrated that increasing the depth of the corrugations in HSSs also results in a higher residual shear capacity beyond failure. However, initial stiffness is not affected by increasing the corrugation depth[24].

2.3.3 Web height

According to the parametric study that has been done by Hassanein et al.[24] on HSSs, the increase in web depth increases the ultimate shear strength significantly. However, that is accompanied by a decrease in the ultimate shear stress. Thus the smaller depth is more efficient in terms of material usage. Moreover, the corrugated webs fail suddenly under buckling; however, it is observed that a considerable residual shear strength after buckling. This can improve the brittle failure after buckling.

The post-buckling residual strength increases with decreasing the web height also [24].

Worth mentioning here that the parametric study by Hassanein et al. [24] on HSSs considered each parameter at a time and did not take into account the interaction.

2.3.4 Web thickness

From the parametric study provided by Hassanein et al. on HSSs considering one parameter at a time, the increase in the web thickness increases the ultimate shear load as in increasing the height. However, increasing web thickness means to increase the web area, and through a comparison of the efficiency of using many thicknesses, it was observed that the efficiency decreases with larger web thicknesses. Thus, smaller web thicknesses give higher shear capacity, but less economical solutions [24].

2.3.5 Flange width and flange thickness

Hassanein et al. [25] investigated the effect of flange width and founded that the flange width has a negligible effect on shear behavior of girders with corrugated webs [25].
To add here that increasing the flange thickness increases the flange stiffness and thus increases the residual shear capacity [32]

2.3.6 Initial imperfection

Bridge girders with corrugated webs are usually designed in a conservative way, and that is due to the lack of data about the real initial imperfection of the folds, imperfection in the geometry of the corrugated webs, the radius of the bend between the fold, and also the imperfection due to residual stresses [23]
The amplitude and shape of the initial geometric web imperfections play a major role in the shear strength and behavior of corrugated web steel girders. For example, it was observed that the FE results obtained by hassanein et al. [23] are higher than the corresponding experimental ones conducted by Elgaaly et al. to study the behavior of steel beams with corrugated webs under shear [23]. The existence of inevitable out-of-plane initial imperfections in the specimens was the reason for this difference.

Furthermore, in the experiments performed to analyze the shear behavior and strength of corrugated steel webs, Moon et al. [23] calculated the initial imperfection magnitude. It was observed that the initial imperfection had a maximum magnitude of 17.9 mm. Although the experiments were carried out using large-scale specimens, it was reported that the web thickness of the test specimen (4 mm) was comparatively smaller than that used for the real bridges[23].

This is one of the reasons for the extensive study of initial imperfection. Also, the extent of the real bridges' initial imperfections could be smaller than that of their study. Therefore, it is concluded that further analysis should be carried out on the initial imperfections of actual corrugated web bridges [23].

In addition, the results of FE studies performed by Driver et al. [23], showed that considering the lower bound assumption of simply supported edges at the web panel boundaries, the shear strength is overestimated, at least in one part of the web folds, due to the sensitivity of the shear behavior to the existence of initial imperfections in the web.

2.3.6.1 Imperfection amplitude

Sause et al. [30] studied the change in the normalised shear strength with the normalised amplitude of the out-o-plane imperfection. An imperfection amplitude up to 10% of t_w the shear buckling capacity reaches yielding shear strength. However, increasing the imperfection amplitude decrease the shear buckling strength significantly[30].

Hassanein et al. suggested that an imperfection magnitude equal to the corrugated web thickness (t_w) is realistic considering the size of the panels in the webs of bridge girders[23].

An amplitude of (hw/200) is suggested by Yi et al. [27] as a realistic amplitude for the imperfection considering the interaction order of n=0.7. It is observed that when shear buckling controls, the effect of the amplitude of initial geometric imperfection can be neglected on the post-buckling behavior. However, the geometric initial imperfection amplitude becomes critical on the post-buckling behavior when the yielding controls [27].

From a study performed by Kollár and Kövesdi [26], providing virtual manufacturing to verify the deformation and residual stresses with the test results and use them welding as input for virtual testing to find the resulted shear buckling resistance, the imperfection amplitude suggested by EN 1993-1-5:2006 (hw/200) to calculate the shear buckling strength is applicable but needs more investigation [26].

On the other hand, Kollár and Kövesdi [27] applied virtual manufacturing techniques to simulate the residual stresses and deformation due to the manufacturing process, considering different web thicknesses (3mm, 2mm, and 1.2mm), presented that the residual stress in the corrugated webs can be neglected and the realistic imperfection amplitude is much smaller than $h_w/200$ suggested by EN 1993-1-5:2006 [27]. Thus, Kollár and Kövesdi suggested a more advanced modeling that takes into account the real initial imperfection [27].

To point out here that, according to Kollár's virtual simulation of the manufacturing process, with increasing the corrugation angle (from 30 to 45 to 60 degrees) the

imperfection amplitude of (hw/200) gives very close load-displacement curves from virtual manufacturing and equivalent amplitude of (hw/200) [26].

2.3.6.2 Imperfection Shape

The shape of imperfection has a considerable effect on shear buckling strength. Sause et al. [30] performed a parametric study for the effect of the shape of imperfection where the imperfection amplitude is kept constant (0.1 *tw) and the shear strength is compared with different buckling mode shapes. It is observed that the shear capacity increases with the buckling mode number. Meaning that the first mode gives the lowest capacity [30]. The same conclusion has been reached by Driver et al. that the most critical mode is the first mode [12].

The shape of deformation after the manufacturing process was observed to be a sine wave function [27]. However, the location of the maximum deflection between the experiment or real bridges can be different from what to be modeled in numerical analysis, and also the shape of out-of-flatness could be different from simulated eigenshapes, which could lead to some deviations [12].

2.3.6.3 Shear buckling strength and shear yielding strength as a function shear slenderness

According to Nie et al., the shear strength of trapezoidal corrugated webs is correlated to the shear buckling strength and shear yielding strength [18]. Moreover, referring to EN 1993-1-5, Johansson et al. propose that with a slenderness ratio lower than 0.25, the girder's web can reach yielding shear strength (stocky) [14].

When the shear buckling strength less than the shear yield strength i.e. the shear slenderness is high (e.g. a=h=20q, figure 2.5), the shear strength after buckling becomes less sensitive to the existence of initial imperfection. Due to the stability of the boundary conditions, the membrane effect of the web is fully established, meaning that after the shear buckling strength of the web is reached, the shear loading capacity will also continually increase.

However, when the shear buckling strength is higher than the shear yield strength (e.g. a=h=8q), the shear strength becomes more sensitive to the existence of initial imperfection [18].

2.3.6.4 Imperfections configuration

To propose a design formula for shear buckling, a parametric study should be performed base on linear buckling analysis to find a suitable elastic buckling strength. Thereafter, a nonlinear buckling analysis should be performed to assess the sensitivity of shear strength to unavoidable initial imperfection and propose a safe design

formula [18].

Material and geometric nonlinear analysis associated with defining the imperfection should be performed to analyze the bridge girder with corrugated web, especially when the buckling controls the design[27].
According to Kollár and Kövesdi there are many possibilities to define the imperfection in the analysis [27] as shown below:

1- Defining sine wave function as observed after manufacturing process and include the initial imperfection as an equivalent amplitude for the geometric and residual stresses due to manufacturing.[27]

2- Considering suitable eigenshapes as buckling shapes and implementing an equivalent amplitude for geometric and residual stresses due to manufacturing. This method usually gives safe results.[27]

3- Using the conception of Collapse-affine, where a collapse mechanism is defined on the basis of experimental results or previous analysis to define the shape of the collapse. Then updating the initial geometry depending on the defined imperfect shape.[27]

4- Considering suitable eigenshapes with amplitude of 80% of experiment imperfection measurements accompanied with mean values of residual stresses as stress pattern.[27]

5- Performing a numerical fabrication simulation to extract the exact displacement with exact residual stresses (as performed by Kollár and Kövesdi [28] . Then implementing the real values of manufacturing imperfection in the analyzing model.[27]

2.3.7 Combined parameters

Previous parameters were considering one dimension at a time. However, Hassanein et al. [23] proposes four combined parameters and suggest that these parameters are the most effective parameters on the shear strength of corrugated web girders [23].

1- Corrugation depth to web thickness ratio (h_r/t_w)
The ratio has value of (14.58 to 29.17) [23]. Hassanein et al. proposed that decreasing h_r/t_w associated with low h_w/t_w ratio results in global buckling[25]. However, the interactive buckling mode was mainly affected by the ratio h_r/t_w and b/h_w. It is observed that the interactive buckling mode was associated with large values of b/h_w (around 0.203) and various values for h_r/t_w [25].

To point out here that the minimum value for the ratio h_r/t_w is 10 in order to satisfy the geometric stiffness that are recommended by Easley for girders with corrugated

webs [25].

For small values of the ratio h_r/t_w as 10, decreasing the web height results in a considerable increase in critical shear stress. However, with large values for the ratio h_r/t_w like 30, the difference in critical shear stress is negligible for different web depths [25].

2- Width of the flat panel to web depth ratio (b/h_w)
The ratio has value of (0.135 to 0.2) [23]
Hassanein et al. found that an increase in the ratio b/h_w results in an increase of the critical shear stress, and this increase becomes larger with thicker webs [25]. However, it is suggested that the ratio b/h_w should be less or equal to 0.2, and that is applicable for boundary conditions that are fixed or simply supported[25].

3- Aspect ratio of the web panel (a/h_w)
The ratio has value of (2 to 3) [23]
This is also called the "Shear span ratio" a/h_w, and it resembles the ratio between the shear span and the web height. While Hassanein [23] considers it as one of the most effective parameters, Nie et al. suggest that the shear strength is not related to the shear span ratio[18].

Hassanein et al. found that increase the ratio a/h_w results in an increase of the critical shear stress for the same **a**. Meaning that the most critical case is where this ratio equal to unity[25].

4- Web plate slenderness (h_w/t_w)
The ratio has value of 133 to 400 [23]. Hassanein et al. observed that increasing the plate slenderness lead to a reduction in critical shear stress for various web thicknesses [25]. It is also observed that there is a limit (hw/tw=150) beyond which the reduction of critical shear stress becomes negligible[25].
It is noticed by Hassanein [25] that local buckling takes place when the ratio h_w/t_w > 250 associated with the plate width to thickness of b/t_w=54.

5- Flange thickness to web thickness ratio
According to Hassanein et al. [25], the ratio between the flange thickness and the web thickness plays a major role in the failure mechanism of the girder. It is proposed that the girder fails under shear when the thickness of the flange to the thickness of the web is larger than three, where the flange provides support that rigid enough to fix the juncture between the flange and the web. On the contrary, when the mentioned ratio is less than three, the girder will exhibit a failure due to flange deformation, and the juncture is close to simple support. [25]

2.3.8 Corrugation geometry

Parameters influencing interactive shear buckling need to be identified to predict interactive shear buckling behaviour. As seen in figure 2.7, the geometric parameters

of a corrugated web are a, d, t, h, c, and α. In the bridge structure, the width of the flat panel(a) is nearly equal to the width of the inclined panel (c). With taking an equal to c, the geometric parameters are reduced to just five a or c, d, t, h and α. In this case, The critical stress for a wider variety of steel is similar to the yield stress. The local buckling strength stated in equation 2.7 suggests that all the sides of the panels are simply supported[19]. It is possible to rewrite that equation as follows:

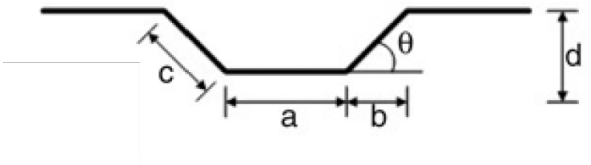

Figure 2.7: Notations used by Yi et al. [19]

$$\tau_{\mathrm{cr},L}^{E} = \left[5.34 + 4\left(\frac{a}{h}\right)^2\right] \frac{\pi^2 E}{12\left(1-v^2\right)} \left(\frac{t}{a}\right)^2 \tag{2.53}$$

Since a/h is a very small ratio for a typical corrugated web, 0.1-0.2, so it can be neglected in the equation 2.53 and it becomes:

$$\tau_{\mathrm{cr},L}^{E} = \frac{5.34\pi^2 E}{12\left(1-v^2\right)} \left(\frac{t}{a}\right)^2 \tag{2.54}$$

The elastic global buckling stress given in Equation 2.16 can be expressed as follows:

$$\tau_{\mathrm{cr},G}^{E} = 36\beta E \frac{1}{\left[12\left(1-v^2\right)\right]^{1/4}} \left[\frac{(d/t)^2+1}{6\eta}\right]^{3/4} \left(\frac{t}{h}\right)^2 \tag{2.55}$$

where

$$\eta = \frac{a+b}{a+c} \tag{2.56}$$

The corrugation angle α is between 25°-35°and in case a=c, the variable η can be account as a constant due to the very small changes which are less than 5 percent. The theoretical global shear buckling strength can be simplified with less than 1 percent difference if d/t is greater than 8.66, as given below:

$$\tau_{\mathrm{cr},G}^{E} = C_G \left(\frac{d}{t}\right)^{1.5} \left(\frac{t}{h}\right)^{2} \tag{2.57}$$

Where C_G is constant and it is equal to

$$C_G = \frac{5.045\beta E}{\left(1-v^2\right)^{1/4} (\eta)^{3/4}} \tag{2.58}$$

Previous experiments have shown that the ratio between elastic local and global buckling strengths influences interactive shear buckling. The ratio can be expressed as follows:

$$\frac{\tau_{\mathrm{cr},G}^{E}}{\tau_{\mathrm{cr},L}^{E}} = C_I \left(\frac{a}{h}\right)^{2} \left(\frac{d}{t}\right)^{1.5} \tag{2.59}$$

where:

$$C_I = \frac{C_G}{C_L} = \frac{36\beta E \frac{1}{[12(1-v^2)]^{1/4}} \frac{1}{(6\eta)^{3/4}}}{5.34 \frac{\pi^2 E}{12(1-v^2)}} = 0.6813\beta \left[\frac{2\left(1-v^2\right)}{\eta}\right]^{3/4} \tag{2.60}$$

As seen earlier, the coefficient, C_I, has only one geometric parameter η which is almost constant. Therefore, it can be get that only the geometrical parameters a/h and d/t influence the interactive shear buckling strength. [19]

2.3.9 Recommendation from literature

According to the static analysis that has been done by Leblouba et al. on a wide range of dimensions of corrugated web girders, there are some limits where the parameter has no effect on shear strength [15] illustrated below.
1- E in range (190 to 210 GPa) has no influence on shear strength.
2- Fy (360 to 490)
3- hw (1080 to 1315)
4- β (1.51 to 2.21)
5- Corrugation angle α (33 to 45)

Also, Leblouba et al. point out some geometrical recommendations for the corrugation as shown below [14].
1- $\alpha < 22$ degrees. However, Lindner and Huang suggestion is α should not be less than 30 degrees.
2 – Adjacent folds must adequately support each other along the fold line to fully mobilize the local buckling shear strength $\beta > 1.13$
3 – When $\beta > 1$, the longitudinal folds are wider and more likely to local shear buckling.

2.3.10 Summary

The previous sections provide a review of shear buckling behavior for stocky and slender girders from different sources, including numerical and practical tests, and a summary of the studied parameters with their effect on shear buckling behavior is presented below. Due to the complexity of defining the interaction between the various affecting factors besides the exact value for the initial imperfection amplitude, a numerical parametric study is the most efficient way. Referring to the annotations in figure 2.5

2.4 Stainless steel

Stainless steel is an effective alternative to traditional carbon steel if there are criteria for corrosion resistance, as it was invented more than 100 years ago. Stainless steel has been widely used in steel bridges.[3] More attention has been paid to life cycle costs in recent years, not just concentrating on investment costs. Stainless steel is more expensive than carbon steel, but it is still a decent choice with lower prices for possible repairs and renovations. In addition, stainless steel at the end of its life cycle is entirely recyclable, creating a new demand for civilian structures [3].

The strength properties of stainless steels are strong, such as carbon steels, see section 2.4.2 which indicates that their use in bridge construction is acceptable.[3] The steel is classified as stainless steel if the chromium content is at least 10.5 %. Due to their transparent passive surface of chromium oxides which are formed on the surface when oxygen is present, stainless steels are self-healing in several respects. With increased chromium content, its protection against corrosion improves.[3]
Four major steel types are subcategorized in the material; ferritic, martensitic, austenitic, and duplex (Stålbyggnadsinstitutet, 2017). Due to their high resistance to corrosion, formability, and high strength, Duplex and Austenitic are more suitable for bridge applications.[3] The chromium content, which determines the corrosion resistance, is one of the differences between the four types of stainless steel. The choice of steel depends on the setting in which the structure will be installed, the investment cost, and the strength needed.[3]

Table 2.2: Summary of the most influencing parameters of bridge girder on shear behavior

Ref.	**Method**	**Parameter(s)**	**Parametric study**	**Result Effect**
Hassan Abbas and Driver	Experiment	Imperfection amplitude	Initial imperfection has significant influence.	Significant effect on shear strength
	FEM	Imperfection amplitude	Increasing the imperfection amplitude decrease the shear buckling strength significantly	Significant effect on shear strength
Nie et al.	Experiment	Shear span (a) and corrugation configuration (q)	(τ_{cr}/τ_y) relationship is unrelated to the corrugated configuration (q) and shear span ratio (a/h_w)	Unrelated to shear strength
	FEM	1) Initial imperfection 2) (a/ q)	The ultimate loading capacity decreases significantly at the descending stage where shear buckling occurs after yielding (a=h=8q)	Significant effect on shear strength
		1) b/h_w 2) h_r/t_w	Increasing b/h_w change the mode from global to local. Increasing h_r/t_w change the mode from global to local. Increasing both parameters together fasten the change of mode from global to local.	Change buckling mode
		1) t_w 2) q	λ_ρ relationship is unrelated to the corrugated configuration (q)	Unrelated to shear strength
		Initial imperfection	is insensitive to initial imperfection when $\lambda > 2,3 duetomembrane$ effect. (represents shear strength) decreases fast when Λ between 0,75 and 2,3. In this range there is the largest effect of initial imperfection on shear strength.	Significant effect on shear strength
		Shear Span	and relationship is unrelated to shear span ratio	Unrelated to shear strength

Ref.	Method	Parameter(s)	Parametric study	Result Effect
Kollar and Kövesdi 2018	Experiment and FEM	Alpha on initial imperfection	The maximum difference is observed for corrugation angle of 60°, which is 80 m/m and it is within the tolerance according to the sensitivity analysis. The virtual testing and the experiment give good agreement with the three angles, so initial imperfection is not related to the angle, Imperfection of hw/200 is applicable but needs more research	Alpha unrelated to initial imperfection
	FEM	Alpha	Shear strength increases with increasing of Alpha	Normal effect on shear strength
Hassanein et al. 2017	FEM	1) tw 2) hw	1) Increasing web thickness and height leads to significant increase in yielding region in the Web, thus raises the strength of the girders. 2) Small web thicknesses are more economical, 3) smaller web heights have higher post buckling strength 4) Smaller hw is more efficient	Significant effect on shear strength
		hr (Alpha)	Increasing corrugation depth (hr) decrease the possibility of PHs which only become visible in global shear failure due to increased rigidity of flanges besides the higher shear strength that does not result in differential deflection between upper and bottom flange to form PHs. Increasing hr increases shear strength considerably.	Significant effect on shear strength
Jongwon Yi, Heungbae Gilb	FEM	1) b/hw 2) hr/tw	1) When b/hw ratio increases, t.global/t.local increase which means local buckling (Not mentioned in the paper). 2) When hr/t ratio increases, t.global/t.local increase which means local buckling (Not mentioned in the paper). 3) The elastic buckling analysis results showed that the interactive shear buckling mode and strength was not influenced by material in elasticity or yielding, but rather by the geometry of the corrugated plate.	Change buckling mode

Ref.	Method	Parameter(s)	Parametric Study	Result Effect
Moussa Leblouba, Samer Barakat, 2019	Expirement	1) Shear span (a) 2) hw 3) Alpha	1) Increasing Alpha leads to increasing shear strength and better usage of material strength and shear capacity. 2) shear span doesn't have an effect the shear strength	Normal effect on shear strength
Hassanein and Kharoob 2013	FEM	1) hr/tw 2) b/hw 3) a/hw 4) hw/tw	Decrease thickness result in web initial stiffens decrease, initial imperfection=tw	Normal effect on shear strength
Moussa Leblouba, Samer Barakat, 2019	Expirement	1) Shear span 2) hw 3) Alpha	1- b and tw are mostly affect then hw 2- E in range (190 to 210 GPa) has no influence 3- Suggested ranges where the parameters has no effect Fy (360 to 490) hw (1080 to 1315) beta (1.51 to 2.21) Alpha (33 to 45)	Significant effect on shear strength
Moussa Leblouba, Samer Barakat and Zaid Al-Saadon	Experiment and FEM	hw	Longitudinal fold b and tw are the most influential, followed by hw, then the rest of the parameters; the modulus of elasticity E is noninfluential within the range [190–210] GPa	Significant effect on shear strength

2.4.1 History of stainless steel in general

In the 19th century, many researchers in many countries worldwide, such as England, Germany, and the United States, conducted studies and experiments on iron alloys and various amounts of chromium, nickel, and carbon. Under certain conditions, alloys with more chromium often proved to be much more resistant to corrosion than carbon steel.[10]

Harry Brearley from Sheffield, UK, developed the basic concepts of what would become known in 1926 in Canton, Ohio, as the stainless steel method. It was a method of making stainless steel with low carbon chromium that seemed to be much cheaper than the current process of making the material to be used with low carbon ferrochrome. The term stainless iron at that time applied to what is now called ferritic stainless steel. [10]

Until 1930, martensitic, ferritic, and austenitic were the three grades of stainless steel. For various factors, the austenitic grades, such as 18-8, became the most popular: their ease of processing, manufacturing, and welding and their superior corrosion resistance in most environments. On the other hand, the austenitic alloys were significantly more expensive and vulnerable to intergranular corrosion and stress corrosion cracking than the martensitic and ferritic grades.[10]

Further changes in stainless steel occurred at a relatively rapid rate after the first discovery. Elwood Haynes received a patent for martensitic stainless steel in 1919. William J. Kroll from Luxembourg was the first to discover precipitation hardening stainless steel in 1929, and Avesta Ironworks first manufactured duplex stainless steel in Sweden in 1930. [10]

Avesta Ironworks developed two ferritic-austenitic alloys in Sweden to reduce the intergranular corrosion problem that was common with the austenitic alloys. Grade 453E, which was a chromium-nickel alloy, and grade 453S, which was the same as grade 453E but also included 1.5% molybdenum, were developed by Avesta.[10]. These alloys had about the same carbon content (0.1 %) as the austenitic grades but show improved corrosion resistance between the borders. They also had equivalent or greater resistance than the austenitic grades to uniform corrosion.[10].

Payson and Harrison documented the positive effect of duplex microstructure concerning intergranular corrosion in 1932 and Lindh in 1934. For all corrosion-resistant materials, duplex stainless steels have some of the highest strength levels. The mechanical properties are strengthened by balancing the structure to be about half ferrite and half austenite, with the improved mechanical properties contributing to the ferrite. These new alloys have been the subject of a lot of recent research..[10].

By the time, just as various structural and engineering carbon steels meet different criteria for strength, weldability, and hardness, there has also been a large variety of stainless steels with varying levels of resistance and strength to corrosion.[31] The properties of stainless steel are the result of controlled alloying element additions,

each of which affects mechanical properties and the ability to withstand various corrosive conditions. Choosing stainless steel that is adequate for the application without being overly heavily alloyed and expensive is essential.[31]. A clear and strongly adherent coating of chromium-rich oxide spontaneously forms on the surface of stainless steel with a combination of a chromium content above 10.5%, a clean surface, and exposure to air or some other oxidizing environment[31]

In the presence of oxygen, if scratching or cutting damages the surface, it reforms instantly. Although the surface is very thin, it is both stable and non-porous, around 5x10-6 mm.[31] As long as the stainless steel is adequately corrosion resistant for the service environment, the atmosphere will not respond further. It is called a passive film for this purpose. The structure determines this passive layer's stability, the surface treatment of the stainless steel, and the corrosiveness of its surroundings. If the chromium content increases and is further strengthened by alloying molybdenum and nitrogen additions, its stability increases.[31]

2.4.2 Mechanical properties

2.4.2.1 Stress-strain behaviour

For stainless steels, the stress-strain curves differ from traditional carbon steels. In carbon steel, there is a linear elastic behavior to the yield strength where plastic deformation occurs [3]. As shown in figure 2.8, the change for stainless steel is smoother, and due to strain hardening, stainless steel deviates earlier from the linear elastic behavior with no defined yield strength.[3]. The stress-strain curve has a constant slope. Until the yield point for standard hot-rolled carbon steels, the slope gradually decreases for cold-formed carbon steels and stainless steels after the stress of proportionality are reached and yielding starts, as seen in figure 2.8. [3].

For stainless steel, the yield strength is generally determined by the stress corresponding to 0.2 % of the permanent strain but also depending on the element thickness. The nominal values for test strength and final strength are given in table 2.3. According to the recommendations from the Swedish Transport Administration, the proposed steel qualities are based on recommendations for corrosivity class C4. [3]

2.4.2.2 Factors affecting the stress-strain behaviour

Stainless steel is more complicated than carbon steel, and the production process has an influence on its properties. Many factors affect the curve of stainless steel.[31]. Cold working Stainless steel resides in the annealed condition, i.e., it has been heated up, maintained for some time at that temperature, and then quickly quenched. The material is given back to a soft and workable state by Annealing. Cold working improves stainless steel's strength grades during fabrication, especially austenitic, by increasing the strength of the stainless steel, a reduction in the ductility happens. However, due to the initial high ductility values, especially for austenitic stainless

steels, this usually has a slight effect. Material can be purchased in a cold-working condition.[31]
As stainless steel is cold-worked, tensile and compressive behavior and anisotropy tend to exhibit increasing non-symmetry. The longitudinal direction's compression strength is lower than the tensile strength in both the transverse and longitudinal directions for cold-worked material. Therefore, in the choice of design strength for cold-worked material, care is required. Stainless steels can be purchased in a cold-working condition (see table 2.4).[31].

2.4.2.3 Strain-rate sensitivity

Strain-rate sensitivity in stainless steel is more obvious than in carbon steel. At rapid strain rates, a proportionally higher strength can be achieved for stainless steel than for carbon steel.[31]

2.4.2.4 Strength of stainless steel

The characteristic yield strength fy and characteristic ultimate strength fu are taken in design calculations as the minimum values for the 0,2% test strength and tensile strength (Rm) specified in EN 10088-4 and 5 as shown in table 2.3. These values apply in the annealed state for stainless steel.[31]

With cold forming, both austenitic steel and duplex steel have higher strength properties, even if some ductility is lost. However, stainless steel is a ductile material, so there is no concern about the potential lack of ductility. In addition, the cold forming of the substance is reversible at some point in its service life. The original properties can be restored by annealing.[3]

2.4.2.5 Modulus of elasticity

The young's modulus of elasticity E is the slope of the initial portion of the stress-strain curve and a key parameter determining the deformation of the structural members of stainless steel and the stiffness of the stainless steel frameworks, as well as their strength when modes of instability control failure. [3].

A value of 200 kN/mm2 for the modulus of elasticity of all stainless steels is recommended for structural design. The Secant module is more suitable for estimating deflections. For Poisson's ratio, a value of 0,3 can be taken, and 76,9 kN/mm2 for the shear modulus, G.[31]

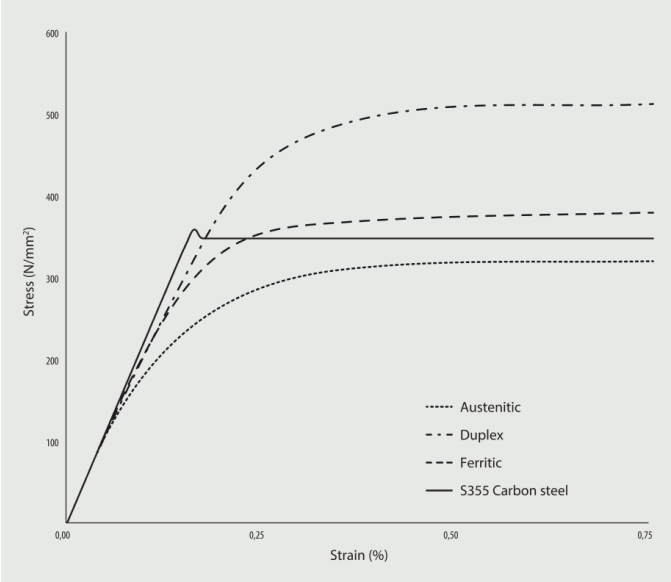

Figure 2.8: Stress-strain curves for different stainless steels and Carbon steel[31]

2.4.3 Suitable stainless steel for structural applications

Stainless steel is classified into the following five basic classes: Austenitic, Ferritic, Duplex, Martensitic, and Precipitation hardening, each category offering unique properties and several different degrees of corrosion resistance. According to SCI, Steel Construction Institute, the Austenitic, duplex, and ferritic stainless steels are most commonly used in structural applications. In table 2.3, the strengths of specific grades suitable for structural applications are given.[31]

2.4.3.1 Austenitic stainless steels

Austenitic stainless steels have a face-centered cubic atomic structure compared to structural carbon steels, which have a body-centered cubic atomic (crystal) structure. As a result, in addition to their corrosion resistance, austenitic stainless steels have high ductility, are readily cold-formed, and are readily weldable.[31]
Austenitic stainless steels also have considerably greater durability over a wide range of temperatures than structural carbon steels. They can be reinforced by operating in cold environments but not by heat treatment. Their corrosion efficiency can be further increased by higher chromium levels and molybdenum and nitrogen additions. In design and construction, they are by far the most commonly used stainless steel.[31]

For structural applications that need a combination of good strength, corrosion resistance, formability, excellent field and shop weldability, and, for seismic applications,

Table 2.3: Nominal values of the yield strength [fy] and the ultimate strength [fu] for common stainless steels to [EN 10088 (N/mm2)[31]]

	Grade	Product form							
		Cold rolled strip		Hot rolled strip		Hot rolled plate		Bars, rods & sections	
		Nominal thickness t							
		t $\leq 8mm$		t $\leq 13,5mm$		t $\leq 75mm$		For $\varnothing \leq 250mm$	
		fy	***fu***	***fy***	***fu***	***fy***	***fu***	***fy***	***fu***
Austenitic	1.4301	230	540	210	520	210	520	190	500
	1.4307	220	520	200	520	200	500	175	500
	1.4318	350	650	330	650	330	630	-	-
	1.4401	240	530	220	530	220	520	200	500
	1.4404	240	530	220	530	220	520	200	500
	1.4541	220	520	200	520	200	500	190	500
	1.4571	240	540	220	540	220	520	200	500
Duplex	1.4062	530 (1)*	700 (1)*	480 (2)*	680 (2)*	450	650	380 (3)*	650 (3)*
	1.4162	530 (1)*	700 (1)*	480 (2)*	680 (2)*	450	650	450 (3)*	650 (3)*
	1.4362	450	650	400	650	400	630	400 (3)*	600 (3)*
	1.4462	500	700	460	700	460	640	450 (3)*	650 (3)*
	1.4482	500 (1)*	700 (1)*	480 (2)*	660 (2)*	450	650	400 (3)*	650 (3)*
	1.4662	550 (1)*	750 (1)*	550 (4)*	750 (4)*	480	680	450 (3)*	650 (3)*
Ferritic	1.4003	280	450	280	450	250 (5)*	450 (5)*	260 (6)*	450 (6)*
	1.4016	260	450	240	450	240 (5)*	430 (5)*	240 (6)*	400 (6)*
	1.4509	230	430	-	-	-	-	200 (7)*	420 (3)*
	1.4521	300	420	280	400	280 (8)*	420 (8)*	-	-
	1.4621	230 (5)*	400 (9)*	230 (8)*	400 (8)*	-	-	240 (7)*	420 (7)*

Note:
The nominal values of fy and fu given in this table may be used in design without taking special account of anisotropy or strain hardening effects.
For ferritic stainless steel, EN 10088-4 gives fy values in the longitudinal and transvers direction. This table gives the longitudinal values which are generally about 20 N/mm2 lower than the transverse values.
1.4621, 1.4482, 1.4062 and 1.4662 are only covered in EN 10088-2 and 3. 1.4509 bar is only covered in EN 10088-3.
(1) t $\leq 6,4mm$
(2) t $\leq 10mm$
(3) t or $\leq 160mm$
(4) t $\leq 13mm$
(5) t $\leq 25mm$
(6) t or $\varnothing \leq 100mm$
(7) t or $\varnothing \leq 50mm$
(8) t $\leq 12mm$
(9) t $\leq 6mm$

Table 2.4: Nominal values of the yield strength [fy] and the ultimate strength [fu] for structural stainless steels to [EN 10088] in the cold worked condition[31]

	Cold Worked Condition			
	CP350		**CP500**	
	fy	**fu**	**fy**	**fu**
Grade	N/mm2	N/mm2	N/mm2	N/mm2
1.4301	350	600	460	650
1.4318	2	2	460	650
1.4541	350	600	460	650
1.4401	350	600	460	650
1.4571	350	600	460	650
Note:				
1 According to EN 10088, the CP classification defines only the required 0,2% proof strength, fy. The steels used should have declared properties that meet the conservative tabulated values for ultimate strength, fu, unless type testing is used to demonstrate the acceptability of lower values.				
2 Grade 1.4318 develops a 0,2% proof strength of 350 N/mm2 in the annealed condition.				

very good elongation before fracture, Austenitic stainless steels areThe most commonly used regular austenitic stainless steels are grades 1.4301 (known as 304) and 1.4307 (304L) and contain 17.5 to 20% chromium and 8 to 11% nickel. They are ideal for industrial sites that are agricultural, urban, and light.[31].
Grades 1.4401 (316) and 1.4404 (316L) can be used in marine and industrial areas. They contain around 16 to 18% chromium, 10 to 14% nickel, and 2 to 3% molybdenum addition, which increases corrosion resistance.[31]

2.4.3.2 Duplex stainless steels

Duplex stainless steels have a mixed austenite and ferrite microstructure, so they are also called austenitic-ferritic steels. Usually, they contain 20 to 26% chromium, 1 to 8% nickel, 0.05 to 5% molybdenum and 0.05 to 0.3% nitrogen. Since they contain less nickel than the austenitic grades, they are cheaper than other types. [31]. In the annealed state, they are around twice as strong as austenitic steels that can make section size reduction possible - in weight-sensitive structures such as bridges or offshore topsides, and this can be very useful. They are acceptable for a wide variety of corrosive conditions.[31]. Compared to austenitic, Duplex stainless steels' higher strength results in more limited formability since they have good ductility. They can also be improved by working in the cold, but not by treating them with heat. They have outstanding weldability and good cracking resistance to stress corrosion. As they are more likely to be found in heavier gauges, they can be seen as complementary to ferritic stainless steel.[31].

1.4462 is a duplex grade that is highly resistant to corrosion, ideal for the marine and other hostile conditions. Increased use of stainless steels for load-bearing applications has led to increased demand for duplex steels, and new 'lean' duplex grades have been produced. Due to the reduced alloy content of nickel and molybdenum, these grades are defined as lean, making the grades significantly more cost-efficient.[31].

2.4.3.3 Ferritic stainless steels

Ferritic stainless steels have chromium content between 10.5% and 18%. There are either no or very minimal nickel additions in ferritic stainless steels, and their body-centered atomic composition is the same as that of structural carbon steels. They cost less and exhibit less market volatility than the austenitic grades with equal corrosion resistance.[31]. Generally, they are less ductile than austenitic stainless steel and less weldable. Ferritic stainless steel's shaping and machining properties are identical to those of structural carbon steel S355. They can be reinforced, but to a more limited degree than the austenitic stainless steels, by cold working. They can not be improved, like the austenitic grades, by heat treatment.[31]. Typical uses are atmospheric conditions in the interior and mild exterior. They have good resistance to cracking stress corrosion, and their corrosion efficiency can be further improved by molybdenum additions. For several light gauges galvanized steel applications, they provide a corrosion-resistant substitute. In gauges of 4 mm and below, ferritic grades are commonly used.[31]
1.4003 (containing about 11 percent chromium) and 1.4016 (containing approximately 16,5 percent chromium, with higher corrosion resistance than 1.4003) are the two 'ordinary' ferritic grades appropriate for structural applications and widely available. Welding significantly impairs grade 1.4016's corrosion resistance and durability.[31].

2.4.4 Application of stainless steel in bridge structures

Stainless steel can be used in various ways like household goods, food processing machinery, large appliances, medical equipment, and automotive equipment. In several architectural projects and monuments, steel is also featured.[10] In the transport industry, where both cutlery martensitic and chromium-nickel austenitic stainless steels have been used, many of the most significant stainless steel applications can be found.[10]
In many other necessary fields, such as infrastructure, architecture, water applications, etc., stainless steel is used. Below are some examples of existing bridges of stainless steel and a short review in tables 2.6 and 2.7 of these examples:

Table 2.6: Examples of stainless steel bridges, a [1][6][5][4]

Bridge name	Location	Crosses	Inauguration	Span
Garrison Crossing (Fort York)	Toronto, Canada	Rail corridors	2019	52 m
Helix bridge	Singapore	Marina Bay	2010	285 m
Story bridge	Brisbane, Australia	Brisbane river	2015	777 m
Söderström bridge	Sweden, Stockholm	River	1957 Renovated: 2017	174 m
Folke Bernadotte bridge	Sweden, Stockholm	Djurgårdsbrunn Bay	2019	98 m

Table 2.7: Examples of stainless steel bridges, b [1][6][5][4]

Bridge name	Type	Stainless steel products	Materials
Garrison Crossing	Arch bridge for pedestrian	All stainless steel	UR 2205 Duplex
Helix bridge	Bridge for pedestrians	All stainless steel	Forta DX 2205 (plate and tubular)
Story bridge	Cantilever bridge for roadway	Mesh, I-beam, angle bar, polished tube, coupling cable	316/316L, Atlas steels, Anzor Fasteners, Ronstan tensile
Söderström bridge	Bridge for railway	The whole supporting structure	Forta LDX 2404 plate
Folke Bernadotte bridge	Bridge for pedestrians	All stainless steel	Forta LDX 2101

2.4.4.1 Garrison Crossing (Fort York pedestrian and cycle bridge)- Canada

Garrison Bridge is the first stainless steel built-in Canada and designed by Pedelta Canada Inc. Garrison Crossing consists of two main bridges connecting two rail corridors. The overall form resembles a Yin Yang shape, expressing a modern, understated and elegant aesthetic.[6]. From the south extension of Stanley Park, one bridge structure stretches across the Kitchener rail corridor and falls on the north side of Ordnance Triangle Park. On the south side of Ordnance Triangle Park, the second bridge structure starts and stretches across the Lakeshore West rail corridor, landing on the grounds of Fort York.[6]

Because of its excellent mechanical properties, duplex stainless steel was chosen: it has a distinctive and beautiful look, has high durability, lightweight and resistant to corrosion and weather, needs less maintenance, and offers reduced life-cycle costs. Garrison Crossing is composed entirely of stainless steel, apart from the concrete

deck and wood handrails.[6]

Figure 2.9: Picture of Garrison Crossing, photo: courtesy of PEDELTA [6]

2.4.4.2 Helix bridge - Singapore

The Helix Pedestrian Bridge, which opens into Marina Bay in 2010, crosses the mouth of the Singapore River. It links the Raffles Avenue district to the new Bay district, which includes the Sands Resort and Gardens By The Bay and the CBD Financial District. The bridge is 285 meters long, with three spans of 65 meters and two spans of 45 meters. The bridge elements are all built from stainless steel.[1]
The DNA molecule was the source of inspiration for the structure. It offered a disappointingly lightweight solution for a bridge that curves in plan and is tubular in section, designed to incorporate structure, deck, and canopy within its 10.8-meter diameter overall. The Singapore Urban Development Authority was prompted to have the bridge constructed of duplex stainless steel by the economy of materials encouraged by the DNA-based structure.[1]. A structure with improved mechanical properties compared to austenitic steels was produced using duplex stainless steel grade Forta DX 2205. It also quickly met the criteria for corrosion resistance, reducing the risk of cracking stress corrosion while also providing high fatigue strength. The high strength of duplex stainless steel for the Helix Bridge resulted in material savings that meant that the cost of the material was equal to the use of carbon steel.[1]. In addition, over the structure's 100-year design life, the research found that stainless steel would offer a lower cost alternative than using carbon steel because of maintenance savings and frequent inspections and repainting. Naturally,

stainless steel is corrosion resistant and does not require regular maintenance.[1].

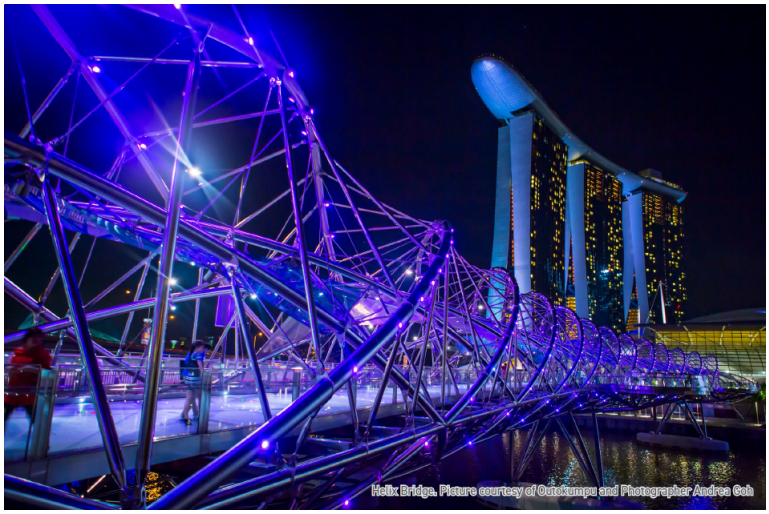

Figure 2.10: Picture of Helix bridge, photo: Andrea Goh [1]

2.4.4.3 Story bridge - Australia

With advanced stainless steel materials and laser-fusion technology, Brisbane's iconic Story Bridge offers enhanced safety measures. As a result of an excellent partnership between various project stakeholders, the 76-year old heritage-listed cantilever bridge now features three-meter high, stainless steel protective barriers on its pedestrian walkways. The bridge cost 8.4 $ and opened in 2015. [5].
Firstly, The idea was to design an anti-climb structure that was functional and aesthetically attractive while maintaining the bridge's heritage values. This gave the engineers a big challenge, including the fixation of the barrier structure without permanent attachment methods, such as welding or other damaging techniques, to the existing heritage-listed bridge. There was also a crucial design necessity to ensure the protection of pedestrian views of the river, Brisbane and surrounding areas, and the Story Bridge.[5]. A dynamic structural design that met the exacting demands of the specification was the concept solution given. The concept evolved to use laser-fused open section beams of stainless steel for the posts, placed with a blackened Carl Stahl X-TEND stainless steel mesh barrier approximately three meters apart. The structure is a crucial safety addition to the Story Bridge and, in its outstanding and unique engineered design, exudes functionality. Stainless steel is unmatched for providing durability, structural performance, low maintenance, corrosion resistance, and aesthetics in selecting materials.[5]

Figure 2.11: Picture of Story bridge, photo courtesy of Atlas steel [5]

2.4.4.4 Söderström bridge - Sweden

Four 174-meter long railway bridges form the Söderström Bridge network. It first opened in 1957. It links the Old Town of Stockholm with its district of Södermalm. It is essential for the city's subway traffic to southern Sweden OS, enabling over 330,000 regular passenger journeys, equivalent to one train every three minutes. In 2017, the bridges requested repairs. Not only is the renovated Söderström Bridge complex more potent, but it is also capable of handling even higher traffic volumes. And since the carrying capacity of the bridge is essential for freight and commuter trains entering and leaving Stockholm, this increased ability to handle high volumes of traffic will provide the city and its inhabitants with a significant advantage for decades to come.[4].
Carbon steel was used in the original bridge. Although it is robust and durable - both attributes desirable in a bridge - but it is also susceptible to corrosion. Forta LDX 2404 duplex stainless steel beams, which would minimize potential maintenance needs, were recommended for the material. This new steel gives more resistance against corrosion and high durability with low maintenance.[4].

c

Figure 2.12: Picture of Söderström bridge, photo courtesy of Stål and Rörmontage
[4]

2.4.4.5 Folke Bernadotte bridge - Sweden

The new bridge adds characteristics to the continued growth of Stockholm's walking city and enhances mobility for both pedestrians and cyclists. In northern Djurgården, the stainless steel bridge connects the museum park with Rosendal in southern Djurgården. The bridge's new location gives Gärdet and the new Djurgårdsstaden a great link to Djurgården and the green oasis of the Swedish capital, the Royal National City Park. The Folke Bernadotte Bridge was opened by King Carl XVI Gustaf and Queen Silvia of Sweden in Stockholm on 17 September 2019. The new bridge is named after Count Folke Bernadotte of Wisborg (1895-1948), the king, diplomat, and mediator of the Red Cross.[2].
The pedestrian and bicycle bridge, 98 meters long, is constructed from duplex steel and assembled by Stål och Rörmontage. Then the bridge pieces were transported for assembly to Stockholm. A steel bridge offers good possibilities for a high degree of prefabrication which minimizes the on-site environmental effect and offers many other benefits as a more significant part of the development can take place in a regulated and secure environment. Duplex steel contributes deficient levels of metal ions to the atmosphere, and no environmentally harmful coating is needed for bridges made of it.[2]

Figure 2.13: Picture of Folke Bernadotte bridge, photo courtesy of Stål and Rörmontage
[2]

3

Parametric design and Numerical Study

A numerical model using ABAQUS software is employed to predict the influence of various parameters on shear behaviour of corrugated web girders. The model was developed to represent the girder's shear behavior when subjected to pure shear stress.

The FE-model is then validated by the analysis of two specimens exist in literature, One of High-performance steel (G7A), of grade HPS485W, tested by Driver et al. [24] and one of Normal strength steel (M12) tested by Moon [24].

Thereafter, a Comparison of HPS485W and normal strength steel shear behaviour with stainless steel (Duplex 1.4162) has been performed.

After that, a sensitivity analysis for initial imperfection (shape and amplitude) has been performed on three different girders: M12 girder tested by Moon [24], Specimen S2 presented by Nie et al.[18] and one with inelastic buckling, Matsnoki girder[24].

3.1 The software

ABAQUS-2019 was employed in this investigation. Both material and geometrical non-linearity were considered, and the FE-model was validated using existing experimental data.

3.2 Mesh setting

The girder was initially modeled with first-order structural elements (S4R), a four-node thin-shell structural element with reduced integration points that accounts for finite strains and may be defined by the thickness as a section property, and then with second-order structural elements (S8R), which has additional degrees of freedom (three displacement components and three rotation components) which can also be used to describe finite strains. This type of element describes behavior with a coarser mesh and is utilized in parametric studies to reduce computing time.

A mesh type convergence between the two meshes (S8R and S4R) has been performed for each case.

Five-degree-of-freedom elements (S8R5) can be more effective. However, it is not recommended for finite-strain applications.

3.3 Loading and boundary conditions

A concentrated load is applied on the girder at the center of the top flange. Depending on the experiment, this load can be applied at different span locations. In Zhang's specimen, for example, the load was subjected at a distance of 4000 mm [20], and in Abbas's specimen (G7A) [11], the load was subjected at a distance of 4500 mm from the support, while in Hassanein's FEM-model [24] the load is applied in the middle of the span.

To ensure a constant stress distribution on the girder and prevent any local buckling, transverse stiffeners were added under the point load and over the supports. When simulating the entire loading process, including the post-critical equilibrium, the load applied in steps with the modified RIKS method available in the ABAQUS software. In both snap-through and snap-back buckling problems, this method is successful. Instead of the displacement control system, the RIKS method uses the arc control system, which capture snap-back instabilities in buckling problems.

To handle the large displacement analysis, the non-linear geometry parameter (NLGEOM) is currently included. The models were simply supported (roller support) at nodes on the bottom flange. To prevent lateral torsional buckling, the load point was limited in the z-direction, while the symmetrical point in the bottom flange was limited in the longitudinal direction to give the girder stability. The boundary condition is illustrated in figure 3.1

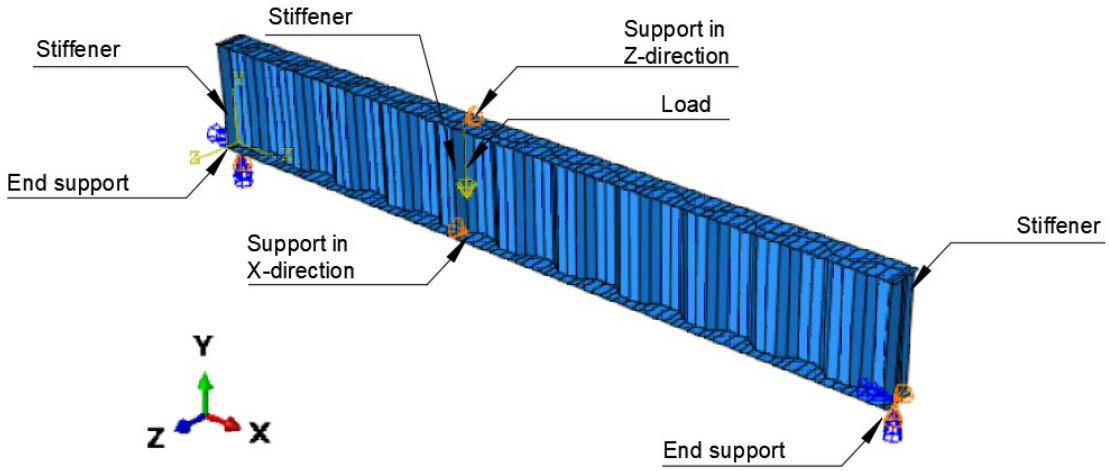

Figure 3.1: Boundary conditions and loading point for girder G7A (Test specimen performed by Driver et al., dimensions are illustrated in section 3.6.1)

3.4 Material model

3.4.1 Material model for carbon steel

According to Hassanein et al. [24] the three different constitutive models for steel material are elastic-perfect plastic, elastic-plastic with hardening, and tri-linear curve gives close results with a maximum difference of 3.5%. In the verification of specimen G7A, an elastic-perfectly plastic is used. Poisson's ratio has been taken equal to 0.3, and the modulus of elasticity is considered 200 GPa. However, for stainless steel, a new constitutive material model will consider the true stress-true plastic strain.

3.4.2 Material model for stainless steel

Stainless steel has different behavior compared to carbon steel, and the material must be treated as elastic-plastic in non-linear analysis. Thus according to the [31], the stress-strain curve of stainless steel are modified using Equations 3.1 and 3.2 [31].

$$\varepsilon = \frac{\sigma}{E} + 0.002\left(\frac{\sigma}{E}\right)^{n} \quad \text{for } \sigma \leq f_y \tag{3.1}$$

$$\varepsilon = 0.002 + \frac{f_y}{E} + \frac{\sigma - f_y}{E_y} + \varepsilon_u\left(\frac{\sigma - f_y}{f_u - f_y}\right)^{m} \quad \text{for } f_y < \sigma \leq f_u \tag{3.2}$$

where:
σ is the engineering stress
ε is the engineering strain
E, f_y and f_u are given in the table
n, m are coefficients calculated from Equations 3.3 and 3.4.

$$n = \frac{\ln(4)}{\ln\left[\frac{f_y}{R_{p0.05}}\right]} \tag{3.3}$$

$$m = 1 + 2.8\frac{f_y}{f_u} \tag{3.4}$$

in which:
$R_{p0.05}$ is the 0.05% proof stress
E_y is the tangent modulus of the stress-strain curve at yield strength, calculated from Equation 3.5.

$$E_y = \frac{E}{1 + 0.002n\left[\frac{E}{fy}\right]} \tag{3.5}$$

ε_u is the ultimate strain, corresponding to the ultimate strength f_y, calculated from Equation 3.6.

$$\varepsilon_u = 1 - \frac{f_y}{f_u} \tag{3.6}$$

The values used to modify the stress-strain curve and to use it in FE simulation are σ_{true} and $\varepsilon^{pl}_{\text{true}}$. These values are calculated from Equations 3.7 and 3.9

$$\sigma_{\text{true}} = \sigma(1+\varepsilon) \tag{3.7}$$

$$\varepsilon_{\text{true}} = \ln(1+\varepsilon) \tag{3.8}$$

$$\varepsilon^{pl}_{\text{true}} = \varepsilon_{\text{true}} - \frac{f_y}{E} \tag{3.9}$$

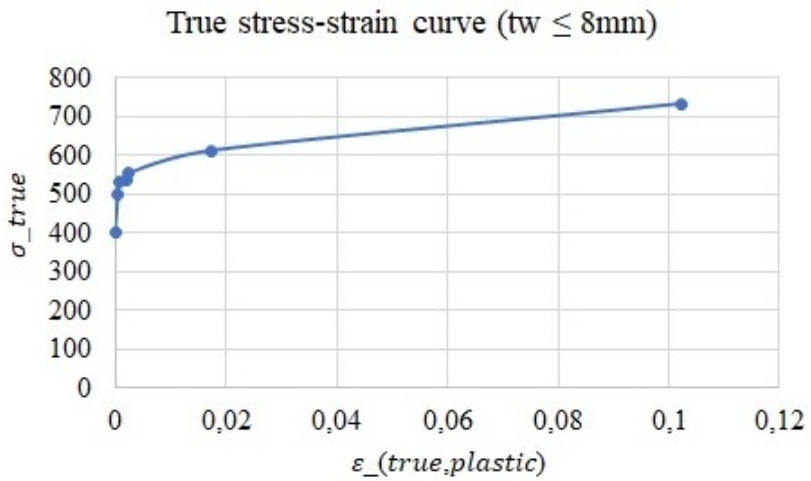

Figure 3.2: True stress-strain curve for stainless steel 1.4162 for web and flanges tw $\leq 8mm$

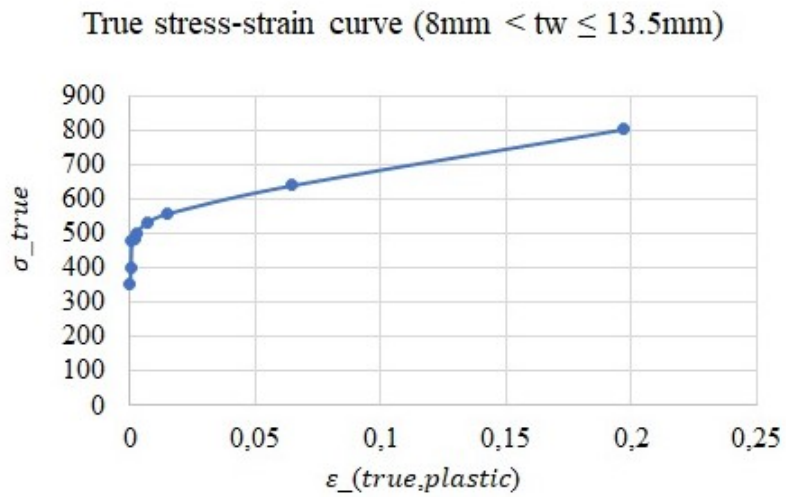

Figure 3.3: True stress-strain curve for stainless steel 1.4162 for web and flanges tw $\leq 13.5mm$

Table 3.1: Input parameters for true stress-strain curve

True stress-strain Stainless steel 1.4162					
FE simulation					
tw $\leq 8mm$			8mm <tw $\leq 13.5mm$		
Stress_ true	Strain true	Strain_ true_pl	Stress_ true	Strain true	Strain_ true_pl
402,0623	0,00265	0	355,8538	0,0024	0
501,5853	0,00317	0,00052	401,0575	0,00264	0,00024
531,7637	0,00332	0,00067	481,4715	0,00306	0,00066
534,48	0,00465	0,002	487,1504	0,00442	0,00202
552,7883	0,00506	0,00241	502,4129	0,00481	0,00241
612,1744	0,02009	0,01744	535,0011	0,00939	0,00699
732,9631	0,10486	0,10221	559,7509	0,01757	0,01517
873,9319	0,22192	0,21927	641,6333	0,06709	0,06469
			805,4513	0,19916	0,19676

The strength of stainless steel varies depending on the thickness of the steel plate. As shown in table 2.3, stainless steels have different values of the ultimate yield strength and the ultimate strength. This is because there are greater possibilities of deformation and instability in a thicker steel plate.

Duplex steel grade 1.4162 has good mechanical properties and corrosion resistance, so this type will be used in this thesis. See table 2.3 for specific mechanical properties relating to this type of stainless-steel.

Depending on the material thickness, the true stress-strain curves for 1.4162 stainless steel vary. The plastic behaviour of the material used in this project is shown in Figures 3.2, 3.3 and table 3.1.

3.5 Initial imperfection modeling

When buckling occurs, a significant drop in shear capacity is observed, making the post-buckling behavior complex to be studied. Additionally, it has been evidenced that introducing the initial imperfection to the perfect geometry can decrease the discrepancies between the experiment data and FEM modeling [25]. In the current simulation, an elastic buckling analysis has been performed on perfect geometry then the shape of the first positive mode is considered as the initial imperfection shape with the measured amplitude from test results. For Example, the reported initial imperfection in girder G7A is 4.06 mm.

3.6 Validation of FEM Modelling

Validation of the current FEM has been done by the analysis of two previous test specimens, One of High-performance steel (G7A), of grade HPS485W, tested by Driver et al. [24] and one of Normal strength steel (M12) tested by Moon [24].

3.6.1 Girder of Driver et al., G7A

3.6.1.1 Girder description

Girder G7A was designed with a trapezoidal corrugation profile. The wavelength is about 1m and the steel is of grade HPS485W according to ASTM standards [11]. The bend radius was chosen of 120 mm for better fatigue life. However, in this study, the radius has not been considered. The effective simply supported span is 11 m. To ensure shear failure, the concentrated load was applied one meter away from the mid-span, so the shear failure happens in the shorter span. The shear span ratio was (4.5/1.5=3) to reduce the potential of creating a tension field that carries more shear[11]. Also, stiffeners were added under the load point and at supports to avoid any local failure or web crippling. Additionally, the dimensions of the flange were chosen to ensure failure under shear in the web[11].
The dimensions of G7A are illustrated in figures 3.4 and 3.5

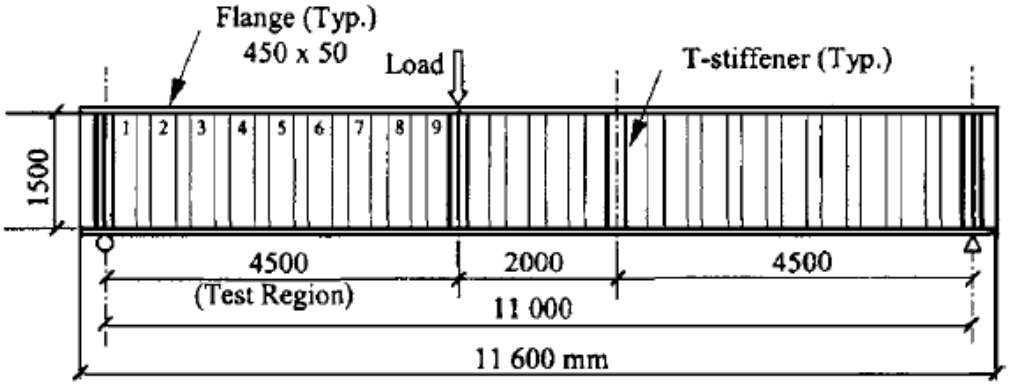

Figure 3.4: G7A girder dimensions [11]

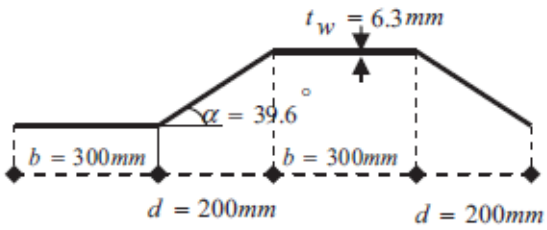

Figure 3.5: G7A girder corrugation details [24]

3.6.1.2 Material model

An elastic-perfectly plastic material model is used in this section, refer to figure 3.6. Poisson's ratio has been taken equal to 0.3, and the modulus of elasticity is considered 200 GPa.

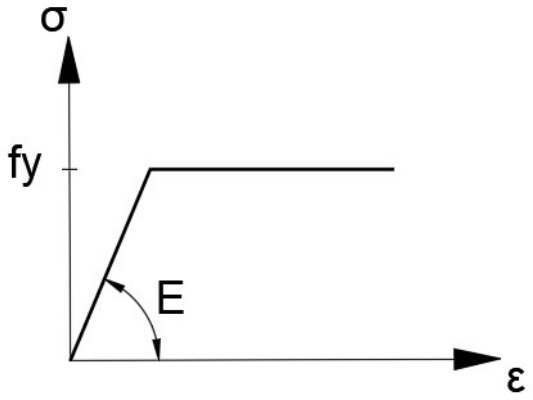

Figure 3.6: Nonlinear material model used in FE-simulation, G7A

3.6.1.3 Mesh convergence

To assess the accuracy of mesh size, a convergence study has been provided using five different element sizes with the two mentioned types of mesh (S4R and S8R) and the verification has been done comparing eigenvalues for different mesh sizes. The convergence study is illustrated in table 3.2 and figures 3.7 and 3.8

Table 3.2: Mesh convergence study for G7A

S8R		
Mesh size	**Mesh size [mm]**	**Eigen value**
Hw/15	100	11.305
Hw/20	75	9.4837
Hw/30	50	9.1285
Hw/60	25	9.0987
Hw/120	12.5	9.087
S4R		
Mesh size	**Mesh size [mm]**	**Eigen value**
Hw/15	100	21.318
Hw/20	75	14.12
Hw/30	50	10.868
Hw/60	25	9.49
Hw/120	12.5	9.2

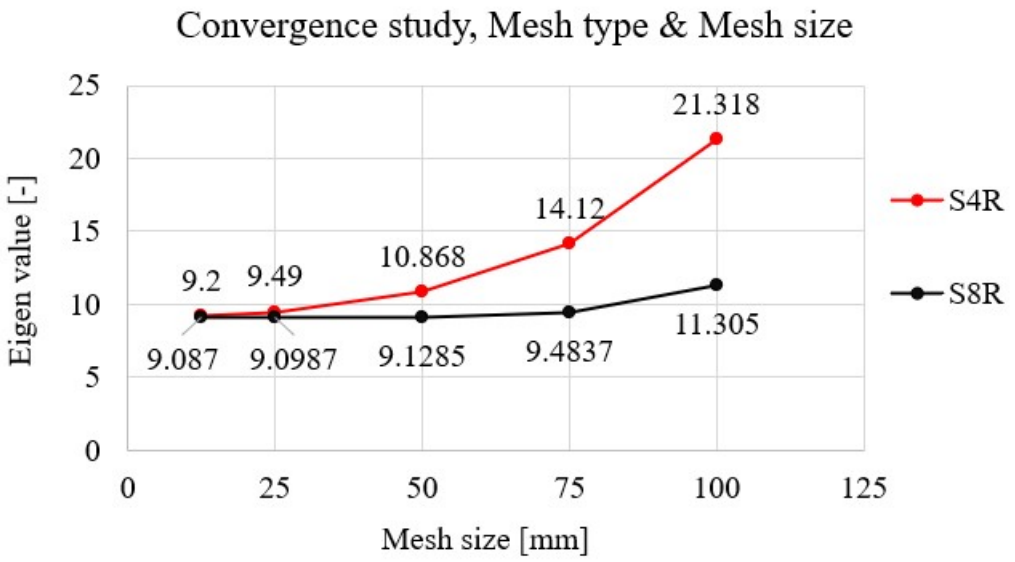

Figure 3.7: Mesh convergence study for G7A

It is seen that with mesh (S4R), the element size of 25 mm and 12.5 mm give close eigenvalues with a difference of 3%. On the other hand, mesh of 75 mm and 50 mm give eigenvalues with a difference of 3.6%, so an element of size 75 mm and type S8R gives good accuracy to proceed with it.

The shear stress versus mid span displacement has been compared for the two mesh types, S8R and S4R, and the results are presented in figure 3.8. The two types of mesh give same initial stiffness. The behaviour after ultimate load is different. However, the post buckling residual stresses are similar.

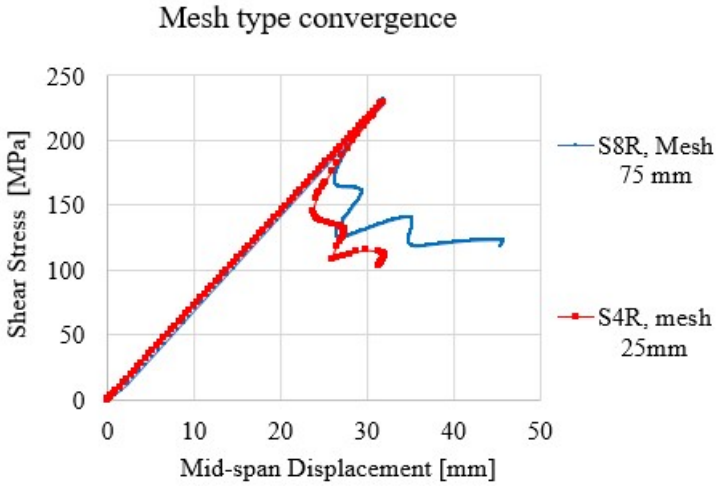

Figure 3.8: Mesh type convergence, G7A

The mesh configuration is shown in the figure 3.9.

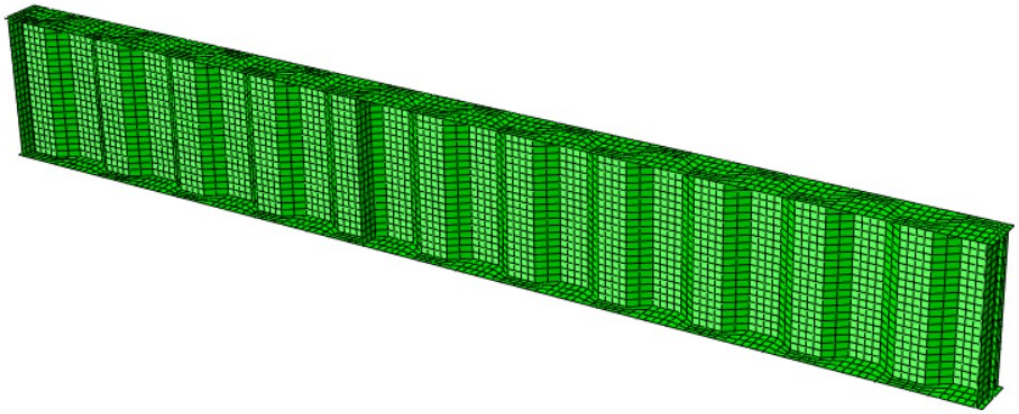

Figure 3.9: Mesh configuration, G7A

3.6.1.4 Results of FEM simulation

The first buckling mode from linear buckling analysis is presented in figure 3.10. The results of the ultimate shear capacity and the buckling load are presented in table 3.3. The dimensional notations are illustrated in figure 3.11. Also, the buckling stress from FEM has been compared to the buckling stress according to the Eurocode. Shear behaviour of the girder is described in figure 3.13. Finally, the load versus deflection is presented in figure 3.12

Figure 3.10: First buckling mode for girder G7A

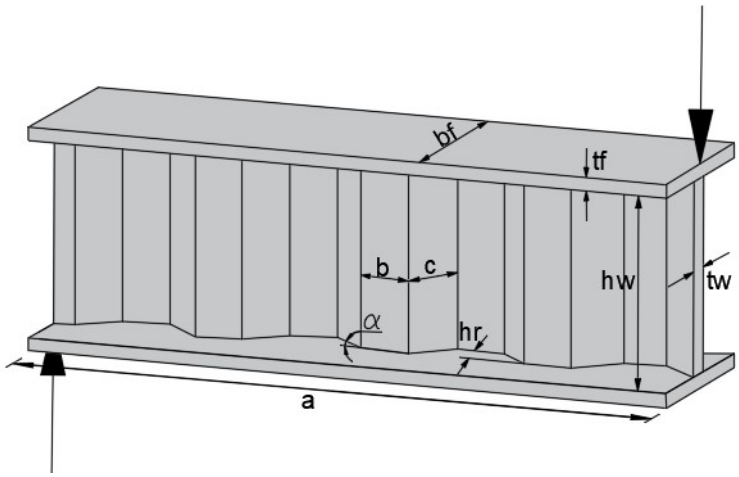

Figure 3.11: Notations of trapezoidal corrugated web girders

Table 3.3: Verification of FEM-model, G7A

Dimension					
b_f **(mm)**	t_f **(mm)**	h_w **(mm)**	t_w **(mm)**	**Imperfection (mm)**	α **(degrees)**
450	50	1500	6.3	4.06	36.9
h_r **(mm)**	**b (mm)**	**c (mm)**	**d (mm)**	**a (mm)**	**Length (mm)**
150	300	250.04	200	4500	11000
Material model					
E (Gpa)	F_y **(MPa)**	**Plastic Strain at** F_y	F_u **(MPa)**	**Plastic Strain at** F_u	**Poisson ratio**
200	465	0	540	Perfectly plastic	0.3
Results					
τ_y **(MPa)**	τ_{ult_FE} **(MPa)**	τ_e **(MPa)**	**Difference**	τ_{ult_FE}/τ_y	τ_e/τ_y
268.47	232.43	244.00	4.7%	0.87	0.91
Eigen value	τ_{cr} **(MPa)**	τ_{cr_EU} **(MPa)**	**Difference**	τ_{ult_EU}	
9.48	487.3	426	0.14	182.27	

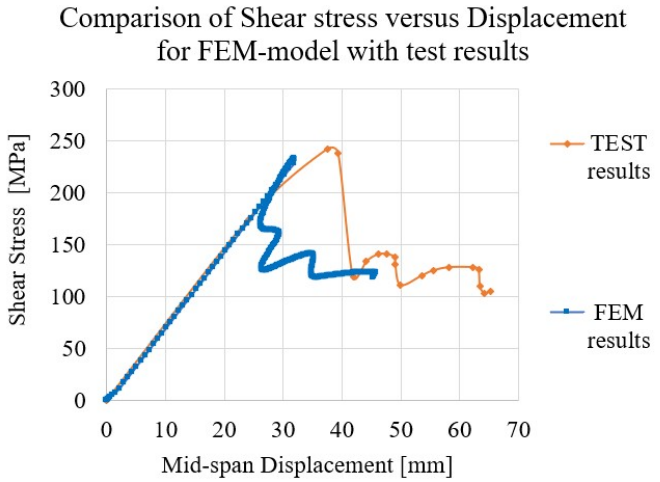

Figure 3.12: Shear stress versus mid-span deflection for specimen G7A with test results

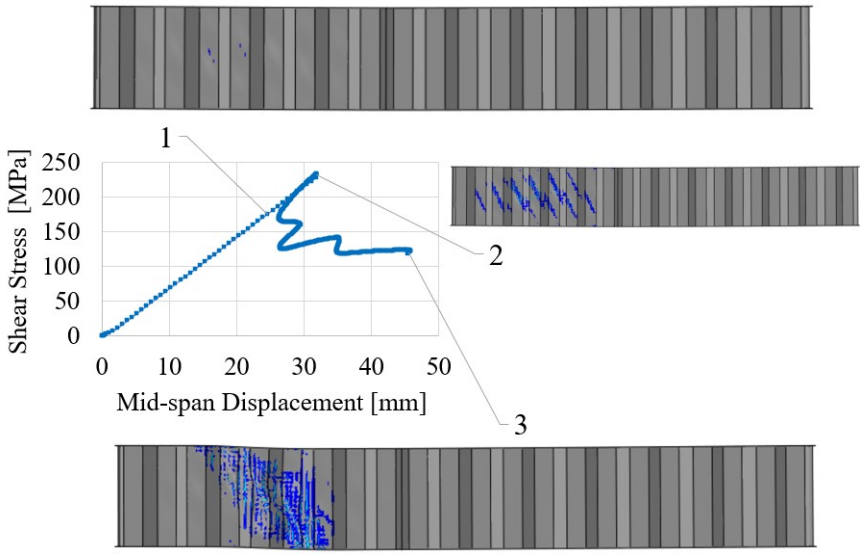

Figure 3.13: Shear behaviour of girder G7A

Referring to figure 3.13, Von Mises stresses reach yielding firstly in the middle of the web (1) where the buckling is largest as seen in the first buckling mode in figure 3.10. Thereafter, the yielding extends diagonally within the web (2) until it reaches the ultimate capacity. After that, a sudden drop in the capacity is observed after point (2). Point (3) shows the yielded area in the web due to shear stresses extends diagonally.

Referring to figure 3.12, the ultimate load from the FEM simulation for specimen G7A is in good agreement with the experiment data. The ultimate load reported from the experiment is 244 MPa, and the ultimate load from FEM is 232.43 MPa with a difference of around 4.7%.

Also, initial stiffness is identical for the experiment and FEM-model. Some difference in mid-span deflection is noticed, 31.89 mm and 37.5 mm from FEM and experiment, respectively. Adding here that the ultimate load is reported while the other values of load-displacement curve for the test results is extracted using AutoCAD since no detailed data is reported.

Moreover, the reserved capacity after buckling, reported from the test is around 120 MPa, is well described in FE-model, and it is in good agreement with the test results.

Comparing the shear buckling stress calculated according to Eurocode mentioned in section 2.2.8 and from FE-simulation, Eurocode considers the local buckling to be critical in this case which is seen in the FE-model and from the experiment's results. However, the value of the local buckling stress and the ultimate load capacity are underestimated by the Eurocode.

3.6.2 Girder of Moon et al., M12

3.6.2.1 Girder description

Girder M12 was designed with a trapezoidal corrugated web with conventional steel S296. The load was applied in the mid-span. Bearing stiffeners with a thickness of 25 mm was attached at the supports and loading points to prevent web bearing failure due to concentrated loads. A 15 mm plate was installed between the loading stiffeners to induce shear deformation of the corrugated steel plate [24]. The geometric corrugation properties of the girder and the material properties are presented in Table 3.6 and the dimensions of M12 corrugation are illustrated in figure 3.14. The maximum initial imperfection is reported as 17.9 mm measured near the top flange on the right side.

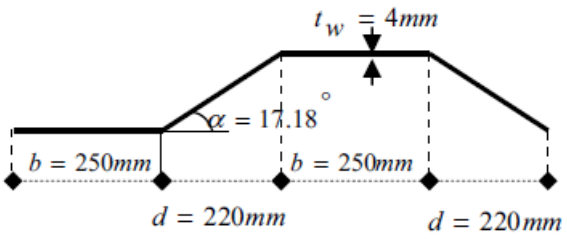

Figure 3.14: M12 girder Corrugation details[24]

3.6.2.2 Material model

An elastic-plastic with E/100 hardening material model is used in this section, refer to figure 3.15. Poisson's ratio has been taken equal to 0.3, and the modulus of elasticity is considered 200 GPa.

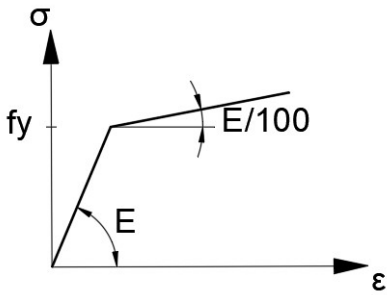

Figure 3.15: Nonlinear material model used in FE-simulation, M12

3.6.2.3 Mesh convergence

A mesh convergence study is carried out to determine whether a particular mesh size is suitable for FE-simulations. In ABAQUS, several mesh sizes are tested, and the study is converging when the eigenvalue is converging. The elements are organized freely. To minimise computation time, Quadratic S8R element type is used here

since it gives same behaviour with coarser mesh. Results are presented in Table 3.4 and in figure 3.16.

Table 3.4: Mesh convergence study for M12, Mesh type [S8R]

Mesh size	Mesh size (mm)	Eigen value for first mode
hw/20	100	3.9076
hw/26.667	75	3.7667
hw/40	50	3.7552
hw/80	25	3.7503
hw/160	12.5	3.7498

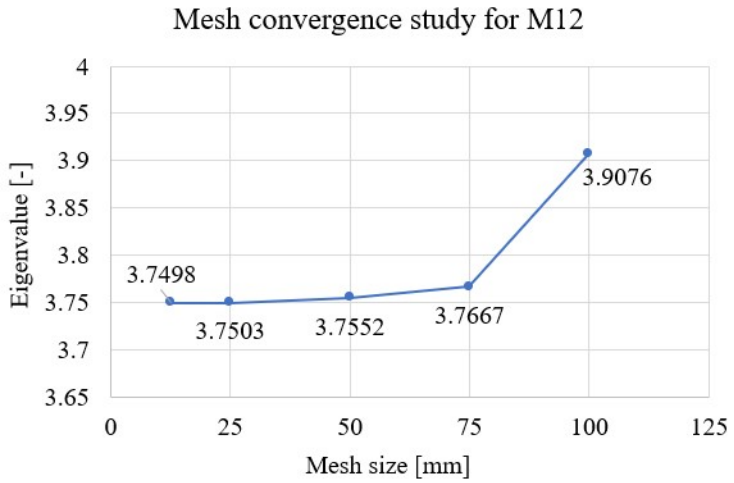

Figure 3.16: Convergence study for M12

It is concluded from the convergence study that element size of 75mm, 50 mm, 25 mm, and 12.5 mm with Quad element type (S8R) give close values of Eigen values with a difference of 3% so an element of size 75 mm gives good accuracy to proceed with.

3.6.2.4 Results of FEM simulation

The girder M12 has been simulated with the same settings mentioned in girder G7A. The maximum initial imperfection is reported as 17.9 mm measured near the top flange on the right side, which is similar to the second eigenshape. This imperfection is around hw/100 which is quite large compared to the conventional girders' imperfection. The girder may be forced to buckle in this situation with the shape of the imperfection, which is similar to mode 2. For this reason, the real imperfection has been simulated with the second eigenshape.

Moreover, the method suggested by Eurocode considering amplitude as hw/200 with the first eigen buckling shape has been used [24]. The first buckling mode from linear

buckling analysis is presented in figure 3.17. The second buckling mode from linear buckling analysis is presented in figure 3.18. The imperfection shape reported from the real test is presented in figure 3.19.

The two simulations have been compared to a perfect girder where no imperfection is imposed and the results are presented in figure 3.21. The dimensions of the girder with the results of the ultimate shear capacity and the buckling load are presented in table 3.6. The dimensional notations are illustrated in figure 6.1. Also, the buckling stress from FEM has been compared to the buckling stress according to the Eurocode. Shear behaviour of the girder is described in figure 3.22. Finally, the load versus deflection (for mode 2) is presented in figure 3.20

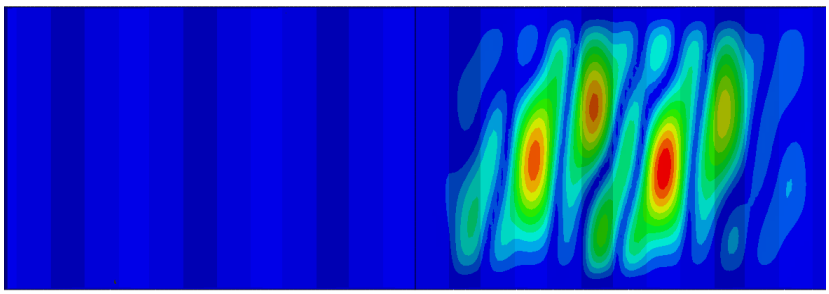

Figure 3.17: First Buckling mode for girder M12

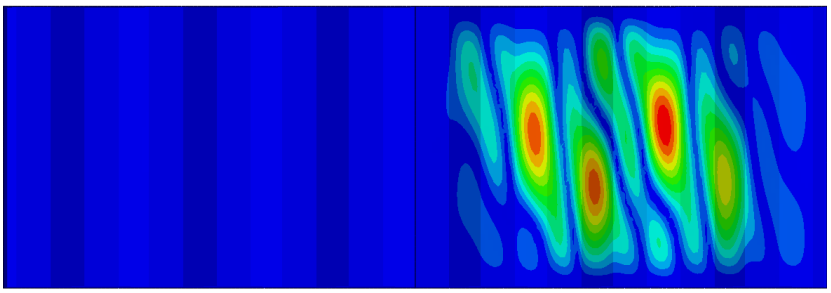

Figure 3.18: Second Buckling mode for girder M12

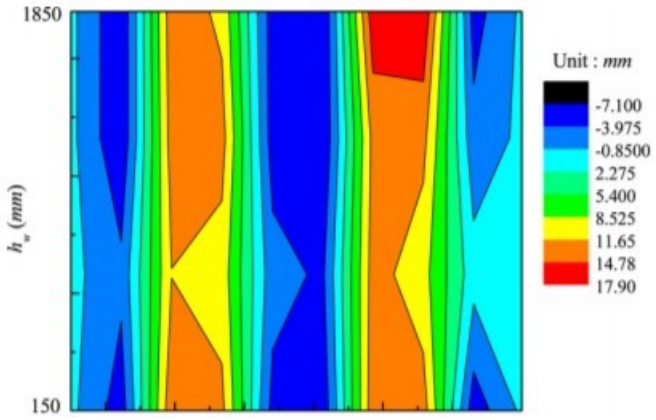

Figure 3.19: Real imperfection shape reported from experiment [17]

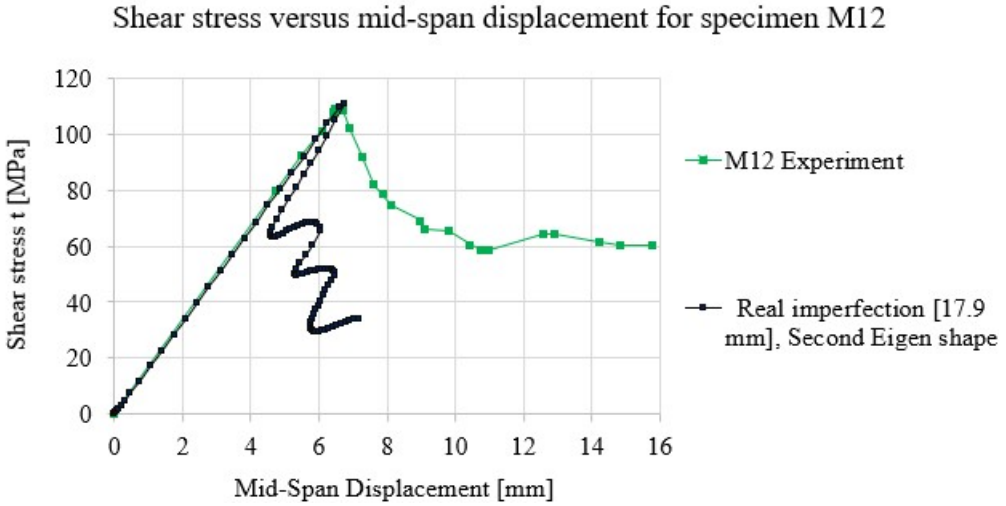

Figure 3.20: Shear stress versus deflection for specimen M12 for FEM simulation and test results, Mode2, Real imperfection

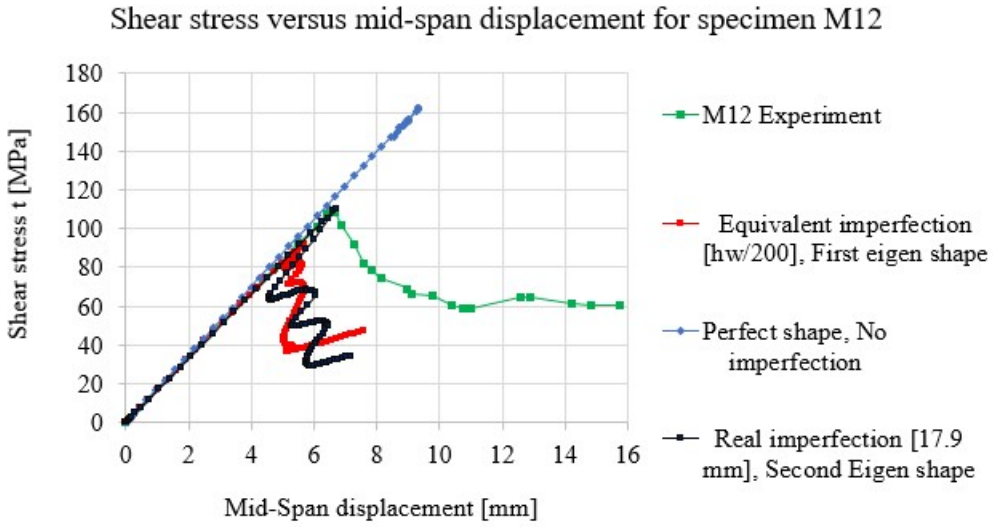

Figure 3.21: Shear stress versus deflection for specimen M12 for FEM simulation, First mode with equivalent imperfection, Second mode with real imperfection magnitude, perfect shape and test results.

Comparing the test results with the simulation of the second mode with real imperfection, which gives the closest values, the FEM analysis shows good agreement with the test results. The reserved capacities after buckling are close (around 60 MPa). The ratio ($\frac{\tau_{ult-FE}}{\tau_{ult-e}} = 0.65$) in FEM simulation and 0.64 reported in experiment. The ultimate capacity is 110.46 MPa and 109 MPa from FEM and experiment, respectively. Also, mid-span deflection is 6.73 mm and 6.67 mm from FEM and experiment, respectively.

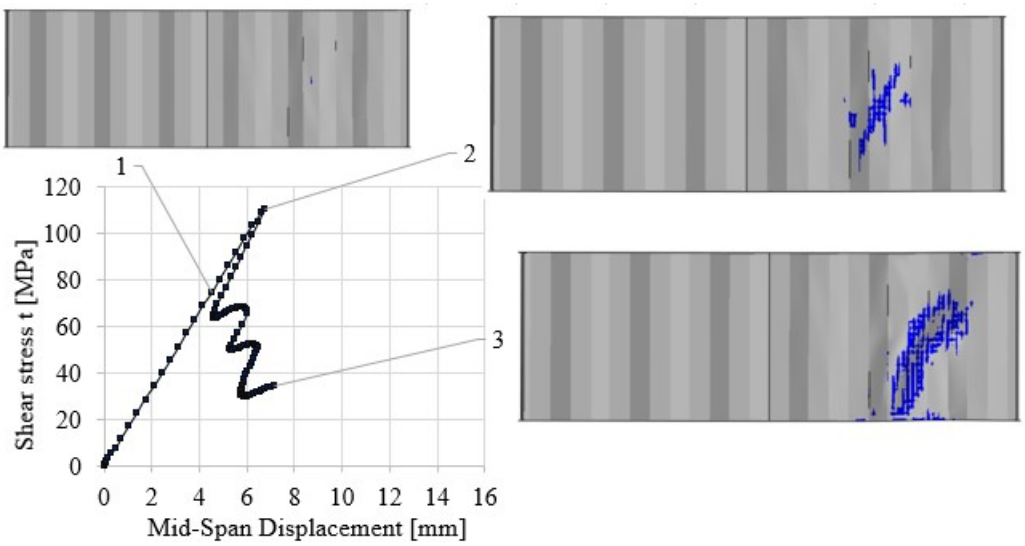

Figure 3.22: Shear behaviour of girder M12, second buckling mode, real imperfection amplitude=17.9 mm.

Referring to figure 3.22, Von Mises stresses reach yielding firstly in the top right of the web (1) where the buckling is largest as seen in the second buckling mode in figure 3.18. Thereafter, the yielding extends diagonally within the web (2) until it reaches the ultimate capacity. After that, a sudden drop in the capacity is observed after point (2). Point (3) shows the yielded area in the web after failure. The shear failure obtained from FEM shows a similar shape to the one reported from the experiment, see figure 3.23

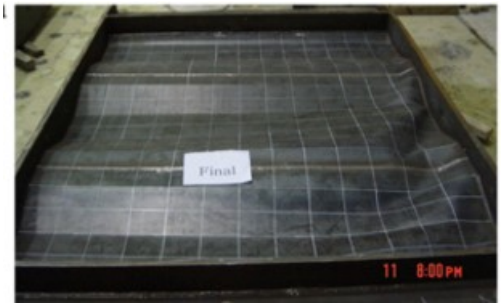

Figure 3.23: Reported shear failure of girder M12 [17]

Comparing the test results with the simulation of the first mode with equivalent imperfection, see figure 3.21, the discrepancies here are much higher. FEM-simulation gives a capacity of 91.57 MPa with a difference of 16% from the test results. Also, mid-span deflection is 5.76 mm and 6.67 mm from FEM and experiment, respectively. Also, the shear failure resulted from first mode as imperfection, see figure 3.24, shows the yielded area in the middle of the web which is not the case in real test.

Table 3.6: Verification of FEM-model, M12

Dimension					
b_f **(mm)**	t_f **(mm)**	h_w **(mm)**	t_w **(mm)**	**Imperfection (mm)**	α **(degrees)**
300	30	2000	4	17.9	17.18
h_r **(mm)**	**b (mm)**	**c (mm)**	**d (mm)**	**a (mm)**	**Length (mm)**
68.2	300	220.06	210.25	3000	6000
Material model					
E (Gpa)	F_y **(MPa)**	**Plastic Strain at** F_y	F_u **(MPa)**	**Plastic Strain at** F_u	**Poisson ratio**
200	296	0	496	0.099	0.3
Results					
τ_y **(MPa)**	τ_{ult_FE} **(MPa)**	τ_e **(MPa)**	**Difference**	τ_{ult_FE}/τ_y	τ_e/τ_y
170.9	110.5	109	1.376%	0.65	0.64
Eigen value	τ_{cr} **(MPa)**	τ_{cr_EU} **(MPa)**	**Difference**		
3.7667	199.63	247.296	19%		

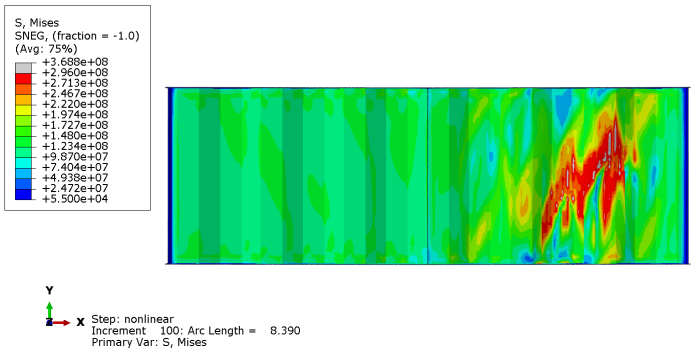

Figure 3.24: Shear failure of girder M12, first buckling mode, Imperfection hw/200

4

Comparison of Duplex 1.4162 and carbon steel shear behavior

The two verified specimens G7A and M12 has been investigated using stainless steel material, Duplex 1.4162, and the results are shown in figure 4.1 for girder M12 and in figure 4.3 for girder G7A .These figures illustrate the behavior of the girder when it is made of Duplex 1.4162 comparing to carbon steel and it can be observed that the behavior is similar to a large extent. The initial stiffness is identical. However, stainless steel girder shows larger capacity and higher residual shear capacity.

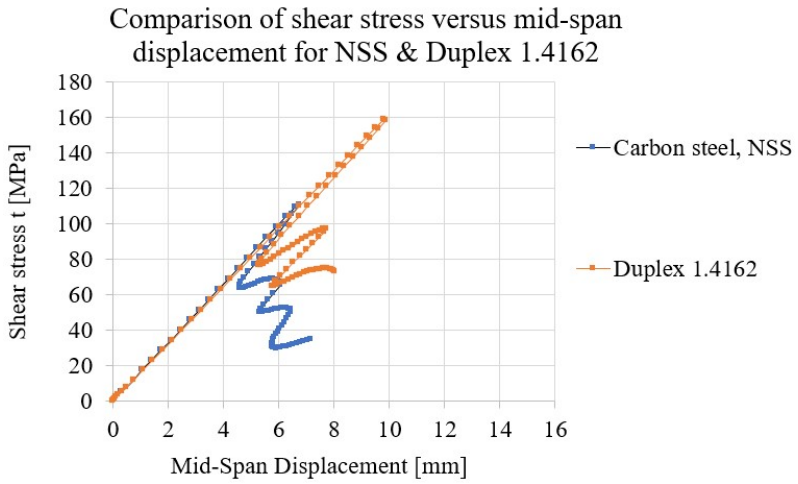

Figure 4.1: Shear stress versus displacement of girder M12 for Carbon steel and stainless steel

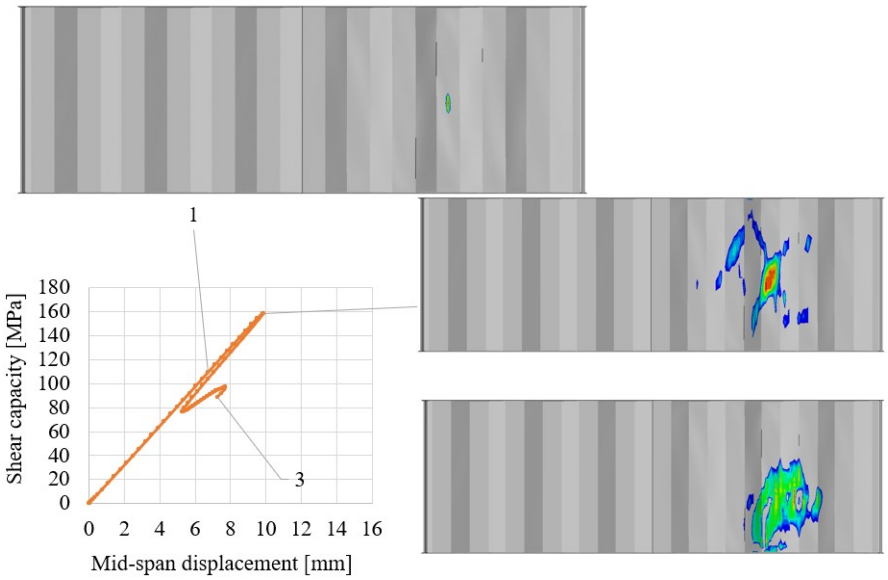

Figure 4.2: Shear behavior of girder M12, Duplex 1.4162

The variation in behavior between normal strength steel and Duplex 1.4162 is more significant and that can be seen in figure 4.1. The yielding in normal strength steel starts earlier, at around 4.5 mm in normal strength steel and around 7 mm in stainless steel, see figure 4.2 and figure 3.22 . Referring to table 4.1, in the case of normal strength steel, the increase in capacity is about 43%, owing to the higher yielding strength of stainless steel, and even the hardening effect.

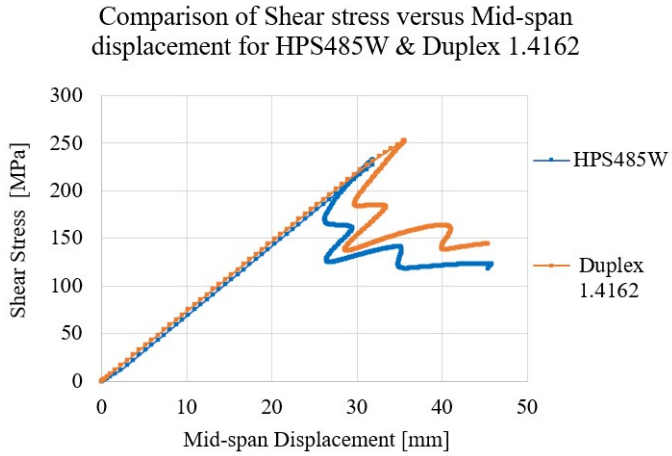

Figure 4.3: Shear stress versus displacement of girder G7A for Carbon steel and stainless steel

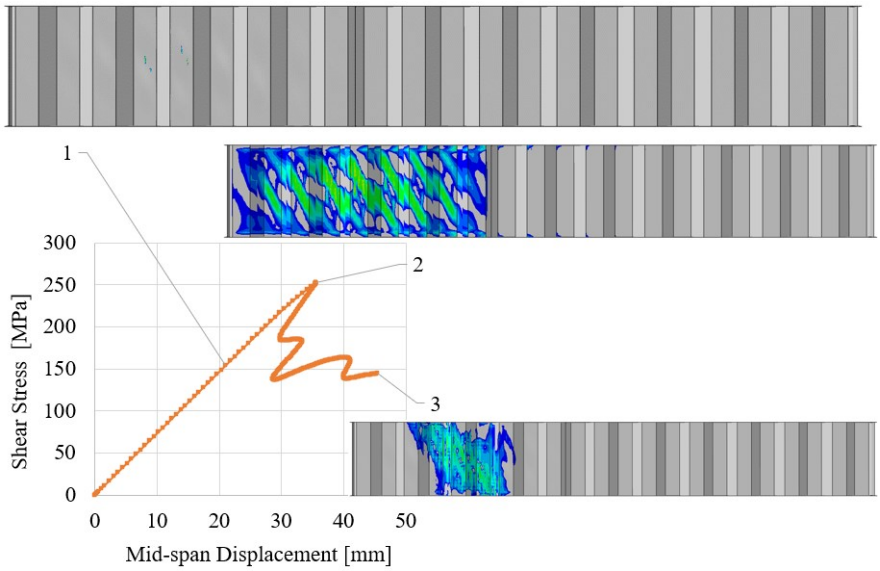

Figure 4.4: Shear behavior of girder G7A, Duplex 1.4162

The variation in behavior between High Performance Steel, which was simulated with material model elastic-perfectly plastic, and Duplex 1.4162, which was simulated with material model true stress-true strain, can be seen after yielding . The yielding in stainless steel starts earlier (at around 22 mm in stainless steel and 25 mm in high performance steel) because the yield stress used in ABAQUS is smaller. However, due to the hardening effect, stainless steel girders give higher capacity after yielding. Referring to table 4.1, from HPSW485 to Duplex 1.4162, the shear capacity of girder G7A increases by 9%.

Table 4.1: Comparison of shear capacity for carbon steel and stainless steel

G7A		
HPSW485	**Duplex 1.4162**	**Difference**
232.44	252.335	9%
M12		
NSS	**Duplex 1.4162**	**Difference**
110.47	158.29	43%

5

Imperfection sensitivity

Previous research on corrugated webs made of carbon steel has shown that the initial imperfection has a significant effect on ultimate shear capacity. However, since there is no literature on this subject in stainless steel, this study will concentrate on stainless steel. For this purpose, two prominent cases have been distinguished. The first case is a slender web where the shear buckling strength is close or lower than the shear yielding strength (Moon girder (M12) and S2 presented by Nie et al.[18]) and the second case is a stiff girder where the shear buckling strength is larger than the shear yielding strength (Matsnoki girder[24]). The corrugation configurations of Moon girders has been illustrated earlier 3.14, and the corrugation configuration for S2 and Matsnoki girders are presented in figure 5.1 and figure 5.2 for S2 and Matsnoki, respectively. Moreover, different amplitudes and shapes for initial imperfection have been considered for each case.

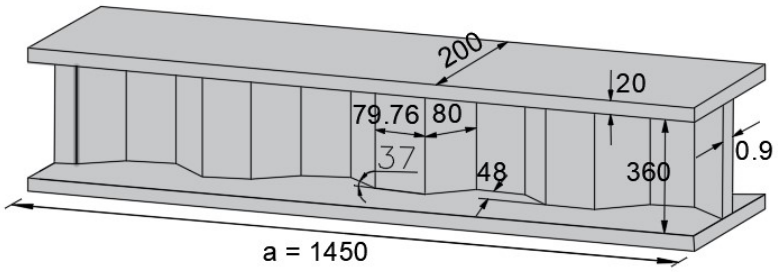

Figure 5.1: S2 girder's details

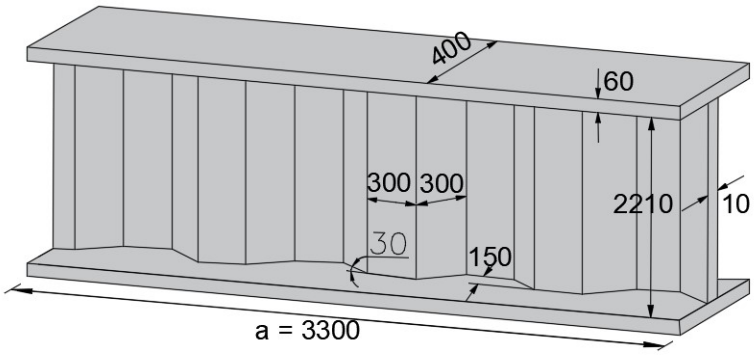

Figure 5.2: Matsnoki girder's details

According to Chen, [9] the imperfection shape can be modeled based on the eigen

buckling shapes, a combination of several modes, modeling the post-buckling mode, or by modeling the actual measured imperfection shape. In this study, firstly, the single buckling shapes will be simulated to find the most critical mode. After that, many mode combinations will also be investigated to assess the possibility of having more critical cases than the individual modes.

Negative eigenshapes can be ignored if the capacity results from positive and negative eigenvalues are the same, according to [21]. As a consideration, in this study, both positive and negative eigenshapes would be considered initially. Furthermore, the eigenvalues have very close values, indicating that the corrugated web is extremely sensitive to initial imperfection [9].

A probability method would be used here due to the variability of shear capacity. According to Chen [9], an arbitrary number of modes may be considered, and the difference between the last mode and the first mode is a percentage change. In this study, the percentage change between the last investigated mode and the first mode is chosen to be 20%, and so the modes to be considered are the ones in a range of the first eigenvalue to 1.2*first eigenvalue. $\Delta\lambda_{\mathrm{cr}} = 20\%$.

$$\Delta\lambda_{\mathrm{cr}} = \frac{\lambda_{\mathrm{cr}}^{m} - \lambda_{\mathrm{cr}}^{1}}{\lambda_{\mathrm{cr}}^{1}} \tag{5.1}$$

5.1 Shear buckling strength is close to shear yield strength, Specimen M12

The specimen (M12) studied earlier has also been studied for different shapes and amplitudes using stainless steel material (Duplex 1.4162). A linear buckling analysis has been performed to define the number of modes considered in the study. The convergence study has been conducted earlier, and a mesh of size 75mm is used here. The number of eigenmodes that fulfill the condition of 20% in 50 Modes. The modes are presented in figures 5.3, 5.5, 5.6, 5.7. The eigenvalues for the fifty modes are presented in table 5.1

Table 5.1: The modes considered in the study with range of 20% from first mode, M12

Eigen Shapes	**Eigen value**	**ABS**	τ_{cr} **[MPa]**		**Eigen Shapes**	**Eigen value**	**ABS**	τ_{cr} **[MPa]**	
1	3.7667	3.7667	199.64	***	29	4.3554	4.3554	230.84	***
2	-3.7694	3.7694	199.78	***	30	4.358	4.358	230.97	***
3	3.7742	3.7742	200.03	***	31	-4.3629	4.3629	231.23	***
4	3.7765	3.7765	200.15	***	32	-4.3638	4.3638	231.28	***
5	-3.7771	3.7771	200.19	***	33	4.3767	4.3767	231.97	***
6	-3.7778	3.7778	200.22	***	34	-4.3847	4.3847	232.39	***
7	3.7897	3.7897	200.85	***	35	4.3892	4.3892	232.63	***
8	-3.79	3.79	200.87	***	36	-4.3924	4.3924	232.80	***
9	4.0661	4.0661	215.50	***	37	4.3957	4.3957	232.97	***
10	-4.0753	4.0753	215.99	***	38	4.3993	4.3993	233.16	***
11	4.0829	4.0829	216.39	***	39	-4.4011	4.4011	233.26	***
12	4.0853	4.0853	216.52	***	40	-4.4045	4.4045	233.44	***
13	-4.0898	4.0898	216.76	***	41	4.437	4.437	235.16	***
14	-4.0917	4.0917	216.86	***	42	-4.4496	4.4496	235.83	***
15	4.1352	4.1352	219.17	***	43	4.45	4.45	235.85	***
16	-4.1401	4.1401	219.43	***	44	4.4572	4.4572	236.23	***
17	4.2389	4.2389	224.66	***	45	4.461	4.461	236.43	***
18	4.2393	4.2393	224.68	***	46	-4.4758	4.4758	237.22	***
19	4.2411	4.2411	224.78	***	47	-4.4768	4.4768	237.27	***
20	4.2421	4.2421	224.83	***	48	-4.4837	4.4837	237.64	***
21	-4.2423	4.2423	224.84	***	49	4.4894	4.4894	237.94	***
22	-4.2432	4.2432	224.89	***	50	-4.5077	4.5077	238.91	***
23	-4.2438	4.2438	224.92	***	51	4.526	4.526	239.88	
24	-4.2459	4.2459	225.03	***	52	-4.5469	4.5469	240.99	
25	4.3423	4.3423	230.14	***	53	4.5834	4.5834	242.92	
26	4.3428	4.3428	230.17	***	54	-4.6289	4.6289	245.33	
27	-4.3495	4.3495	230.52	***	55	4.6468	4.6468	246.28	
28	-4.35	4.35	230.55	***					
*** Eigenvalues in the studied range, 1.2*first eigenvalue									

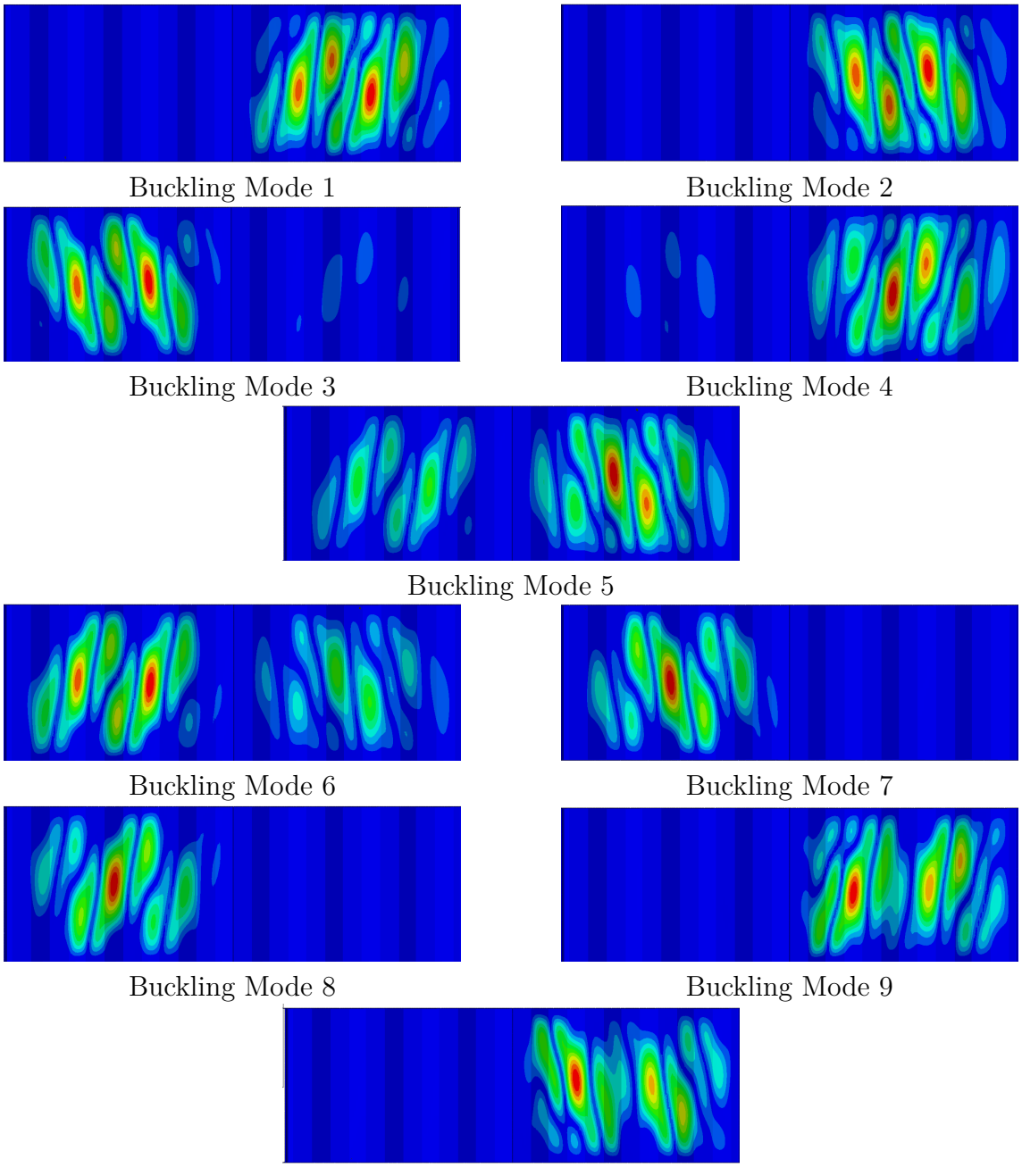

Figure 5.3: Buckling Modes of girder M12; Modes (1 to 10)

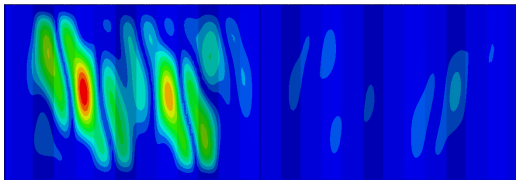

Buckling Mode 11

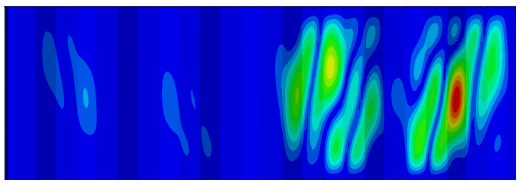

Buckling Mode 12

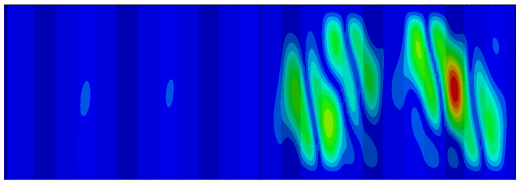

Buckling Mode 13

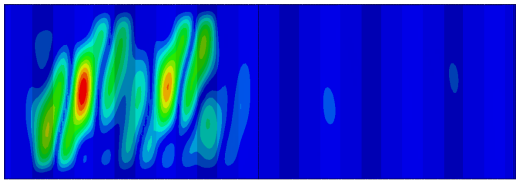

Buckling Mode 14

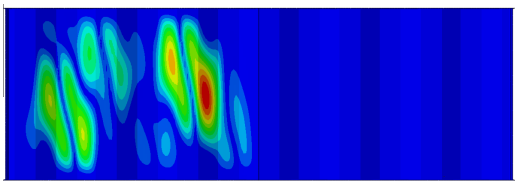

Buckling Mode 15

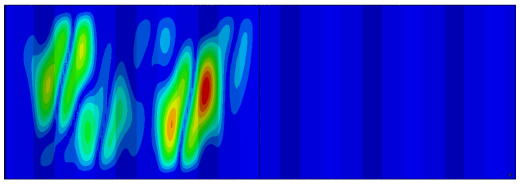

Buckling Mode 16

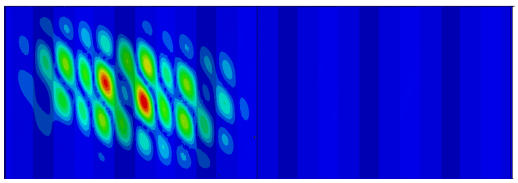

Buckling Mode 17

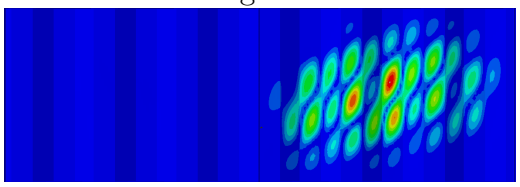

Buckling Mode 18

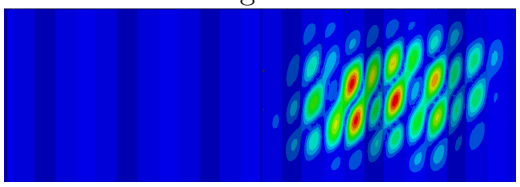

Buckling Mode 19

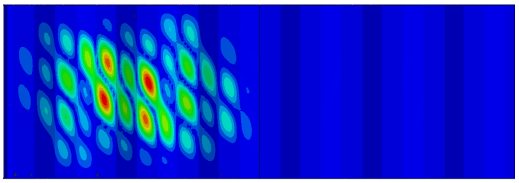

Buckling Mode 20

Figure 5.4: Buckling Modes of girder M12; Modes (10 to 20)

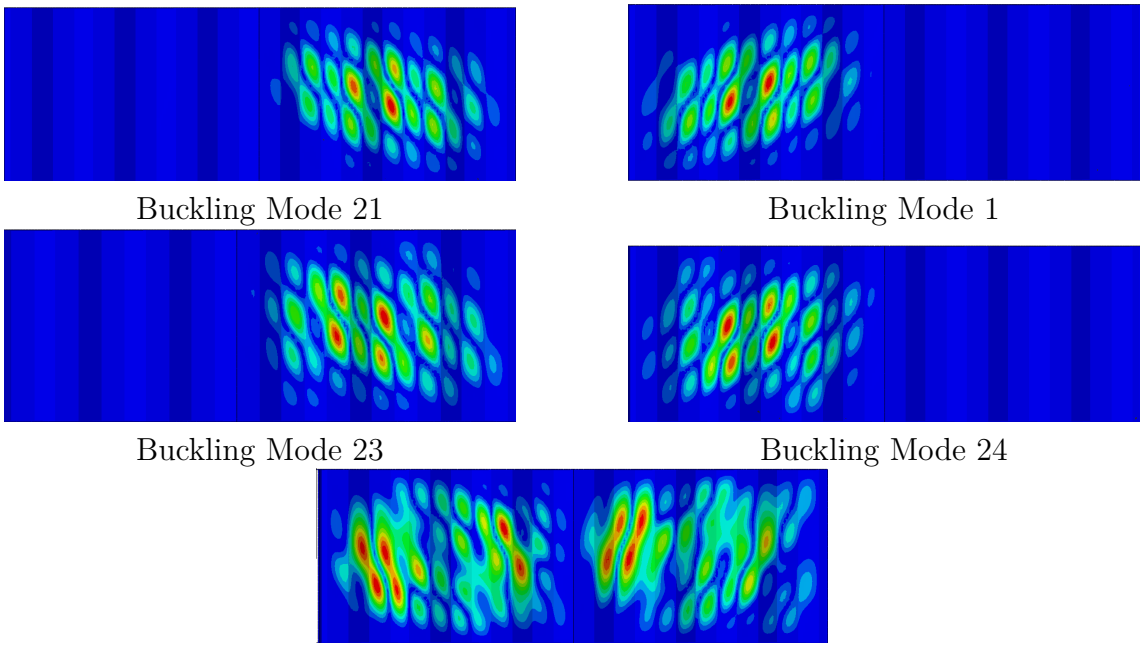

Buckling Mode 21

Buckling Mode 1

Buckling Mode 23

Buckling Mode 24

Buckling Mode 25

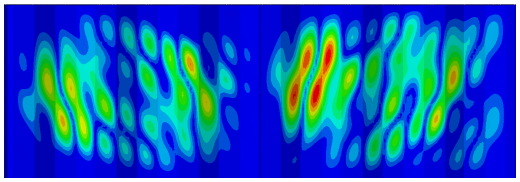

Buckling Mode 26

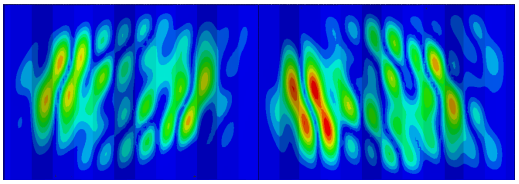

Buckling Mode 27

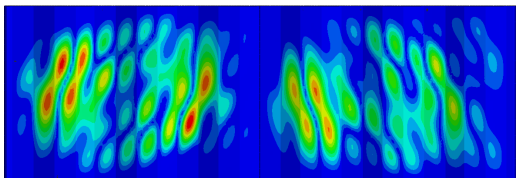

Buckling Mode 28

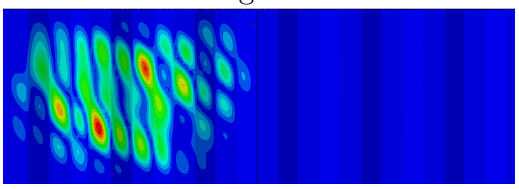

Buckling Mode 29

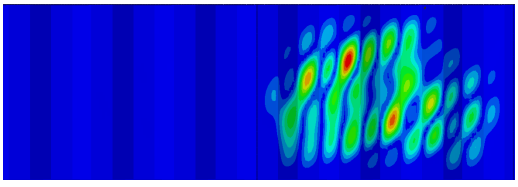

Buckling Mode 30

Figure 5.5: Buckling Modes of girder M12; Modes (20 to 30)

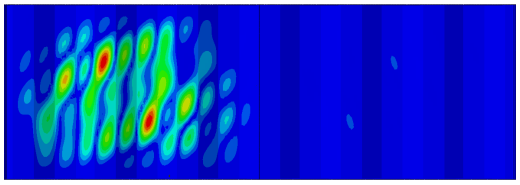

Buckling Mode 31

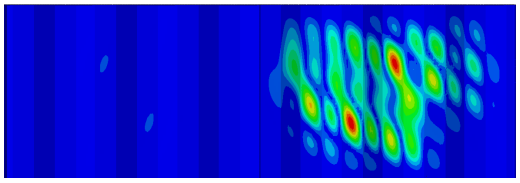

Buckling Mode 32

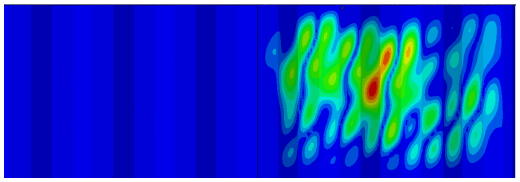

Buckling Mode 33

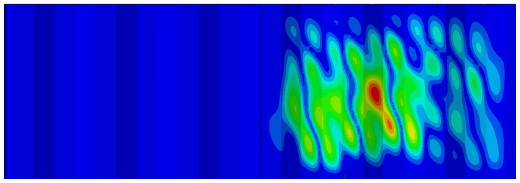

Buckling Mode 34

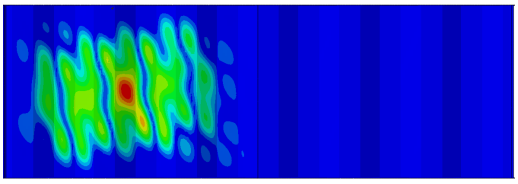

Buckling Mode 35

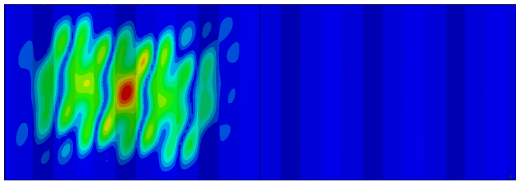

Buckling Mode 36

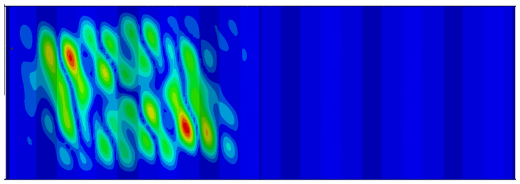

Buckling Mode 37

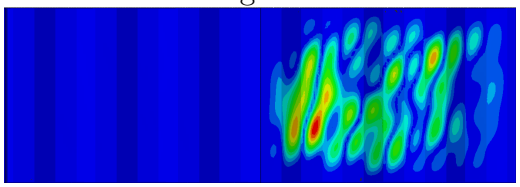

Buckling Mode 38

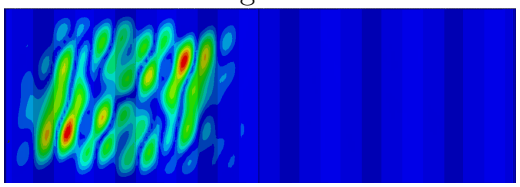

Buckling Mode 39

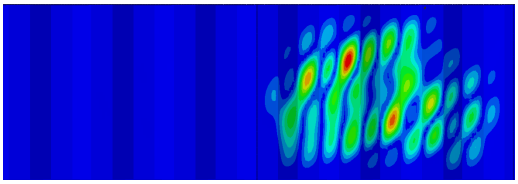

Buckling Mode 40

Figure 5.6: Buckling Modes of girder M12; Modes (30 to 40)

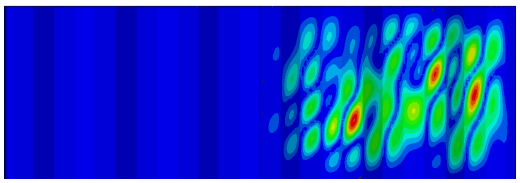

Buckling Mode 41

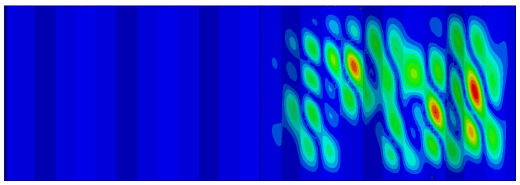

Buckling Mode 42

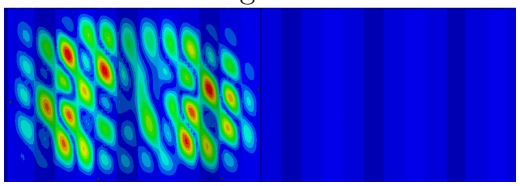

Buckling Mode 43

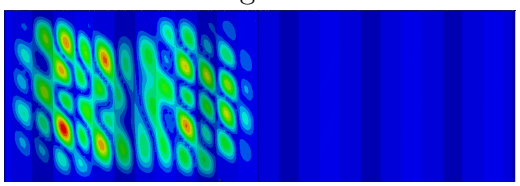

Buckling Mode 44

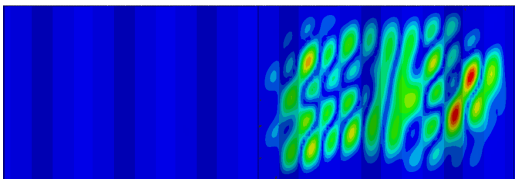

Buckling Mode 45

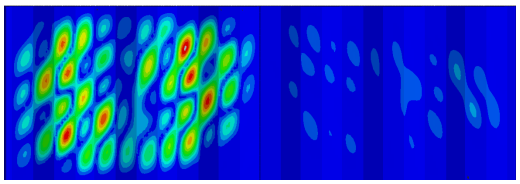

Buckling Mode 46

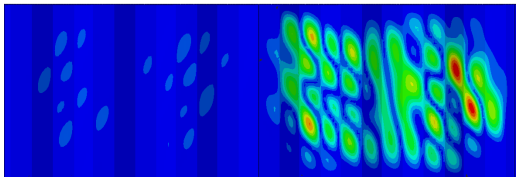

Buckling Mode 47

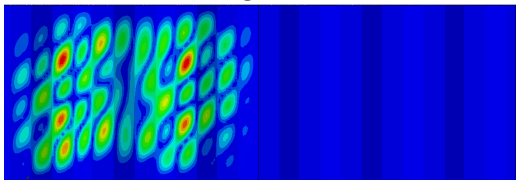

Buckling Mode 48

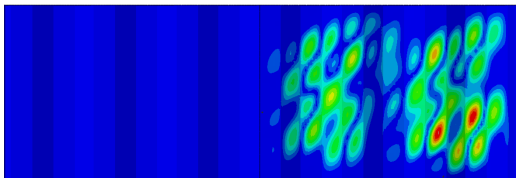

Buckling Mode 49

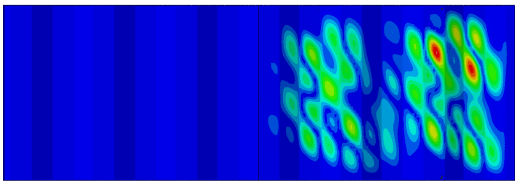

Buckling Mode 50

Figure 5.7: Buckling Modes of girder M12; Modes (40 to 50)

For each eigenvalue, a nonlinear analysis for four different amplitude (Hw/100, Hw/200, Hw/300, and Hw/400) has been performed, and the results in figures 5.8 and 5.9 show the variation of the ultimate shear capacity of the positive eigen shapes when the mode changes in range of 20% between the first mode and the last one. Figure 5.10, on the other hand, presents the variation of the ultimate shear capacity of the negative modes.

It can be seen that the shear strength is very sensitive to the shape and amplitude of the initial imperfection in this case. For example, the shear capacity drops from 184.98 MPa for the perfect shape to 59.52 MPa (around third) for amplitude Hw/100 and a shape similar to mode 4, and it drops from 184.98 MPa to 79 MPa for amplitude Hw/200.

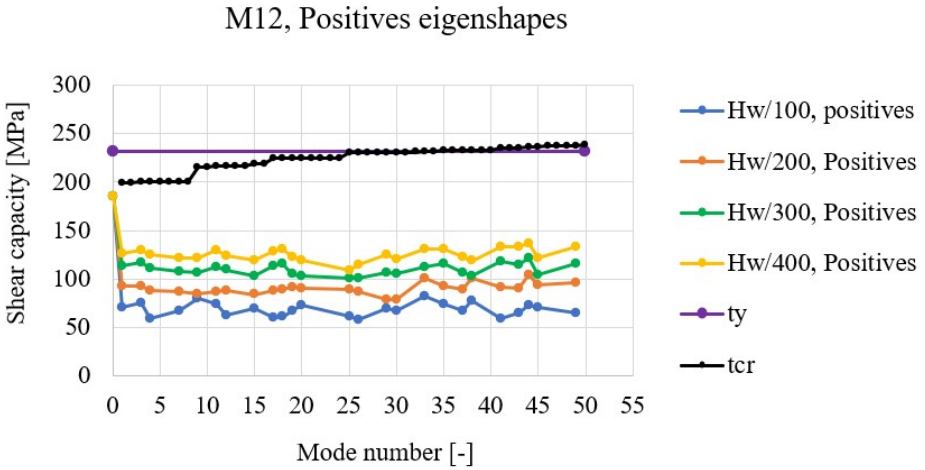

Figure 5.8: Shear capacity variation with different initial imperfection amplitude and positive mode shapes, the yield strength and the critical shear capacity, M12

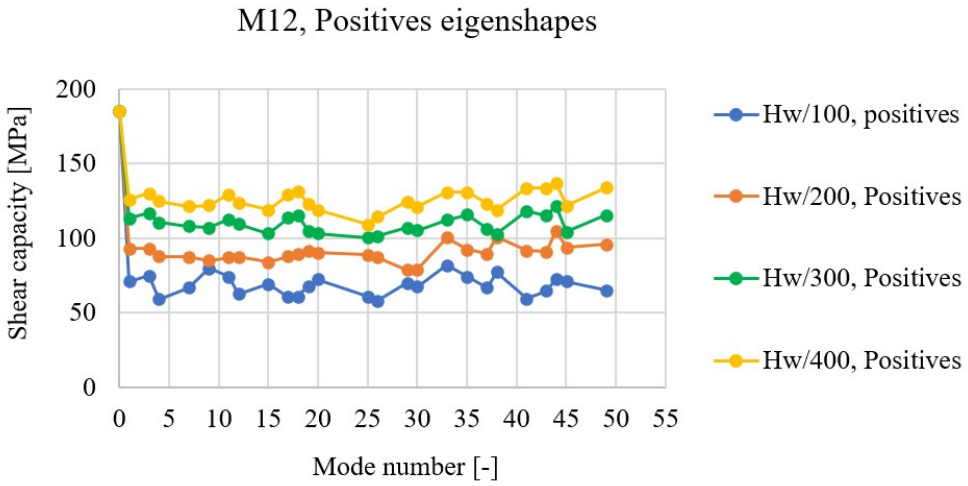

Figure 5.9: Shear capacity variation with different initial imperfection amplitude and positive mode shapes, M12

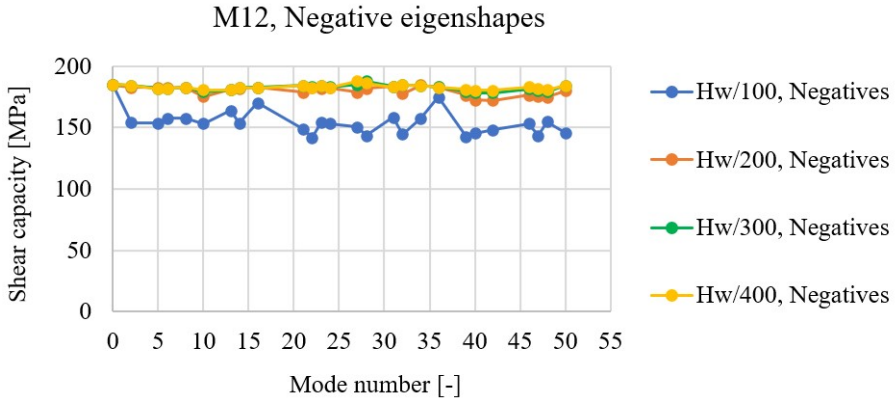

Figure 5.10: Shear capacity variation with different initial imperfection amplitude and negative mode shapes, M12

To study the effect of the eigenvalue sign, a comparison between shear capacity resulted from two different shapes with the same eigenvalues with different signs has been conducted. Mode 20 and mode 21 have eigenvalues of 4.2421 and -4.2423, respectively. The imperfection amplitude changes from H/100 to Hw/400. The change in shear capacity for the two modes with different imperfection amplitude is presented in figure 5.11. Another comparison between mode 4 and mode 5 also has the same eigenvalue and different shapes of 3,7765 and -3,7771, respectively. Figure 5.12 shows the change in shear capacity for these two modes.

Referring to figures 5.11 and 5.12 the shear capacity decreases significantly with increasing the imperfection amplitude. For instance, for mode 5, the capacity decrease from 124.878 MPa to 110.758 MPa (11.31%) by increasing the imperfection amplitude from Hw/400 to Hw/300. Additionally, the positive and negative eigenshapes result in different shear capacities, with the positive eigenshapes having a lower capacity.

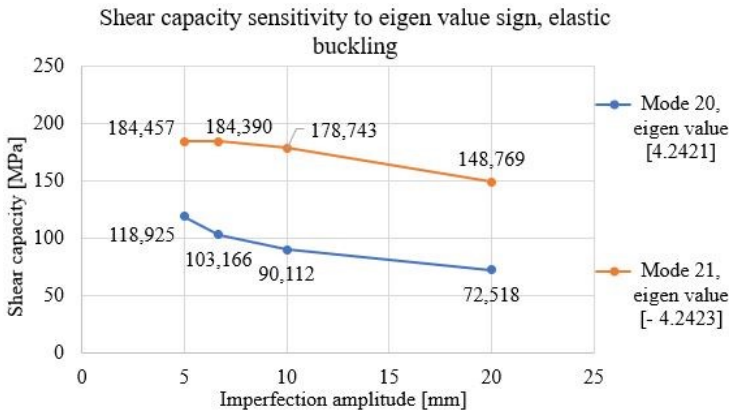

Figure 5.11: Shear capacity variation with different initial imperfection amplitude for different eigen value signs, Mode 20 and 21

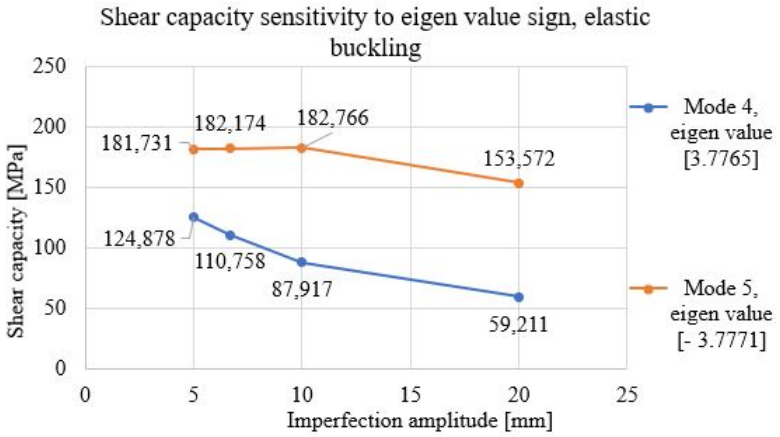

Figure 5.12: Shear capacity variation with different initial imperfection amplitude for different eigen value signs, Mode 4 and 5

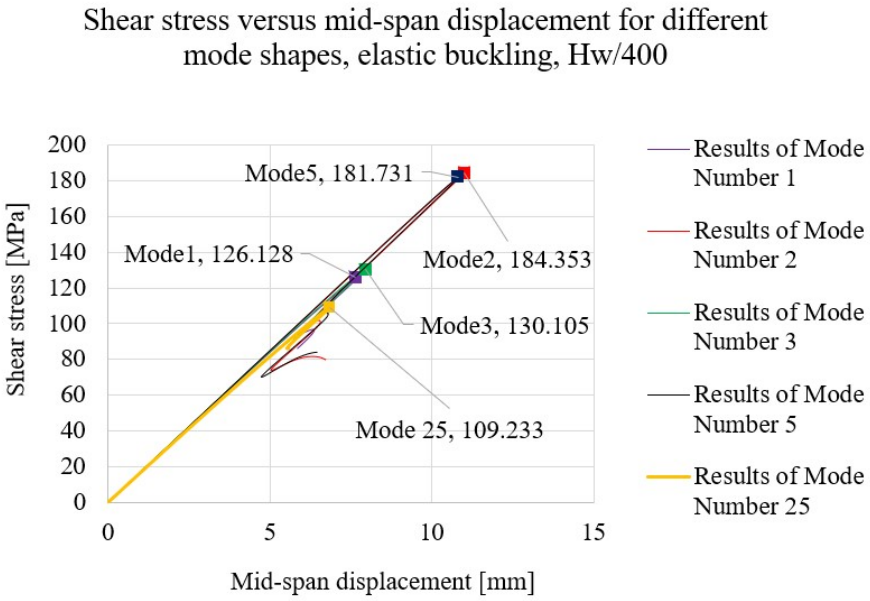

Figure 5.13: Shear behaviour for different mode shapes, M12, Imperfection amplitude Hw/400

To compare the behaviour of the girder under various imperfection shapes, a relation between shear stress and in-plane displacement has been presented in figure 5.13 for imperfection amplitude of Hw/400. It can be seen that the behavior is consistent in all shapes. However, the maximum capacity varies depending on the mode number. Initial imperfection of mode 1 shape and Hw/400 amplitude, for example, gives a capacity of 126.128 MPa, while mode 25 gives 109.233 MPa with the same amplitude.

It's worth noting that the shape of the imperfection can be of any shape. Negative modes, on the other hand, are caused by a negative shear field that reverses the real shear field. As a consequence, in figure 5.14, the negative and positive modes

are differentiated, as well as a low and high band. The upper band of capacity is determined by the negative eigenvalues, while the lower band is determined by the positive eigenvalues. As a result, as initial imperfection shapes, positive eigenvalues are more crucial.

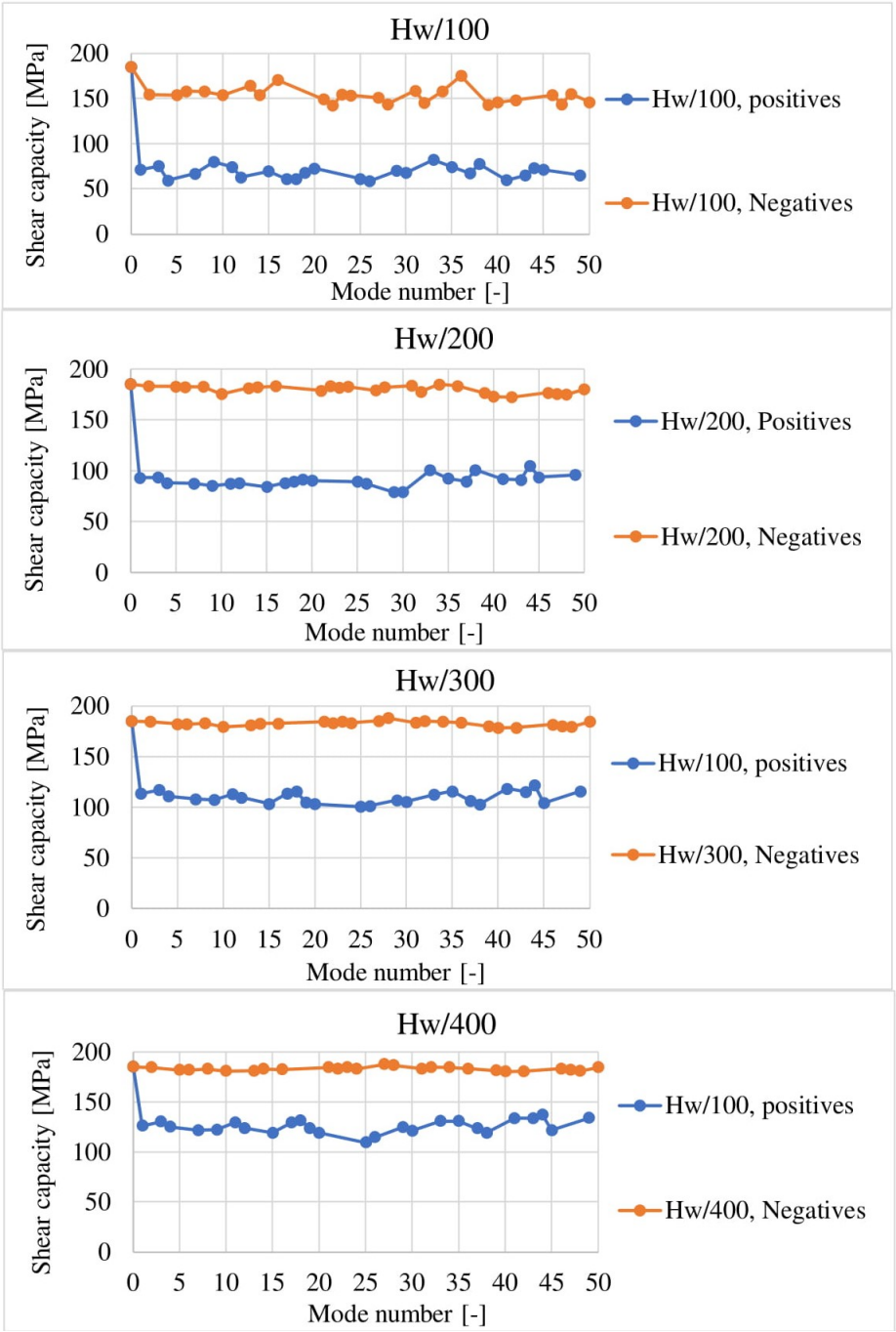

Figure 5.14: Shear capacity sensitivity to mode shape, Positive and negative eigen values, M12 , different amplitudes

5.2 Shear buckling strength higher than shear yield strength, Matsnoki girder [29]

Another case was investigated to see if imperfection sensitivity is affected when the critical shear buckling is greater than the shear yield strength ($\tau_{cr} > \tau_y$). Duplex 1.4162 was used to investigate a bridge girder (Matsnoki [29]) in this case. As in the previous specimen (M12), the beam girder is modeled in ABAQUS with a Quadratic, S8R element. The study is converging when the eigenvalue is converging. Convergence study has been done using structural element S8R and presented in Table 5.2 and in figure 5.15. The results show that an element size of Hw/20 can be used with good accuracy.

Table 5.2: Mesh Convergence study for Matsnoki

S8R		
Mesh size	Mesh size [mm]	Eigen value
Hw/60	36.833	17.518
Hw/40	55.25	17.532
Hw/20	110.5	17.975
Hw/10	221	18.309
Hw/5	442	20.237

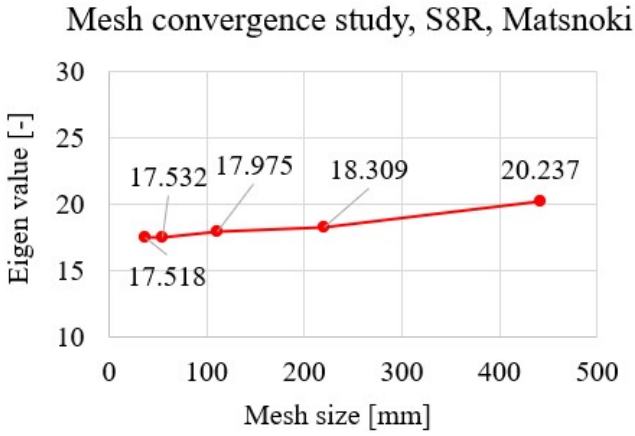

Figure 5.15: Mesh Convergence study for Matsnoki

The dimensions, mechanical properties and shear buckling strength of the girder are presented in table 5.3.

Table 5.3: Dimensions, mechanical properties and shear buckling stress of specimen Matsnoki

Dimension					
b_f **(mm)**	t_f **(mm)**	h_w **(mm)**	t_w **(mm)**	**Imperfection (mm)**	α **(degrees)**
400	60	2210	10	Variable	30
h_r **(mm)**	**b (mm)**	**c (mm)**	**d (mm)**	**a (mm)**	**Length (mm)**
150	300	300	259.85	3300	6600
Material model					
E (Gpa)	F_y **(Mpa)**	**Plastic Strain at** F_y	F_u **(Mpa)**	**Plastic Strain at** F_u	**Poisson ratio**
200	True stress-strain curve presented above				
τ_y **(MPa)**	**Eigen value**	τ_{cr} **(Mpa)**	τ_{cr_EU} **(Mpa)**	**Difference**	**Reference load (kN)**
205.45	17.518	792.67	887.05	0.11	2000

To determine the number of modes to be considered in the study, a linear buckling analysis was conducted. There are 42 buckling modes that satisfy 20% of the difference between last mode and first mode. Table 5.4 shows the eigenvalues of these modes . The buckling mode shapes are illustrated in figures 5.16 to 5.20 .

In this case also, a nonlinear study was carried out for four different amplitudes: hw/100, hw/200, hw/300, and hw/400, with the results of the positive eigenshapes seen in figures 5.21 and 5.22. Figure 5.23 presents shear capacity variation for the four different amplitudes of the negative eigenshapes.

It can be observed here that in this case of inelastic buckling, where the buckling strength is much larger than yielding strength, the shear strength is less sensitive to the initial imperfection shape than the previous case. For instance, the shear capacity decreases from 311.163 MPa for the perfect shape to 222.78 MPa (28%) for the amplitude of Hw/200 and a shape similar to mode 22. This decrease is smaller than the decrease in the case of M12 (around 33%).

Table 5.4: The modes considered in the study with range of 20% from first mode, Matsnoki

Eigen Shapes	**Eigen value**	**ABS**	τ_{cr} **[MPa]**		**Eigen Shapes**	**Eigen value**	**ABS**	τ_{cr} **[MPa]**	
1	17.518	17.518	792.67	***	23	-19.883	19.883	899.68	***
2	17.525	17.525	792.99	***	24	-19.883	19.883	899.68	***
3	-17.544	17.544	793.85	***	25	19.887	19.887	899.86	***
4	-17.549	17.549	794.07	***	26	20.297	20.297	918.42	***
5	17.586	17.586	795.75	***	27	20.306	20.306	918.82	***
6	17.587	17.587	795.79	***	28	20.31	20.31	919.00	***
7	-17.587	17.587	795.79	***	29	20.335	20.335	920.14	***
8	-17.588	17.588	795.84	***	30	-20.346	20.346	920.63	***
9	18.9	18.9	855.20	***	31	-20.351	20.351	920.86	***
10	18.977	18.977	858.69	***	32	-20.365	20.365	921.49	***
11	-19.059	19.059	862.40	***	33	-20.366	20.366	921.54	***
12	-19.072	19.072	862.99	***	34	20.772	20.772	939.91	***
13	19.26	19.26	871.49	***	35	20.778	20.778	940.18	***
14	19.262	19.262	871.58	***	36	-20.806	20.806	941.45	***
15	-19.329	19.329	874.62	***	37	-20.808	20.808	941.54	***
16	-19.329	19.329	874.62	***	38	20.817	20.817	941.95	***
17	19.65	19.65	889.14	***	39	20.819	20.819	942.04	***
18	19.815	19.815	896.61	***	40	-20.837	20.837	942.85	***
19	-19.839	19.839	897.69	***	41	-20.837	20.837	942.85	***
20	-19.841	19.841	897.78	***	42	21.018	21.018	951.04	***
21	19.855	19.855	898.42	***	43	21.043	21.043	952.17	
22	19.873	19.873	899.23	***	44	21.11	21.11	955.20	
*** Eigenvalues in the studied range, 1.2*first eigenvalue									

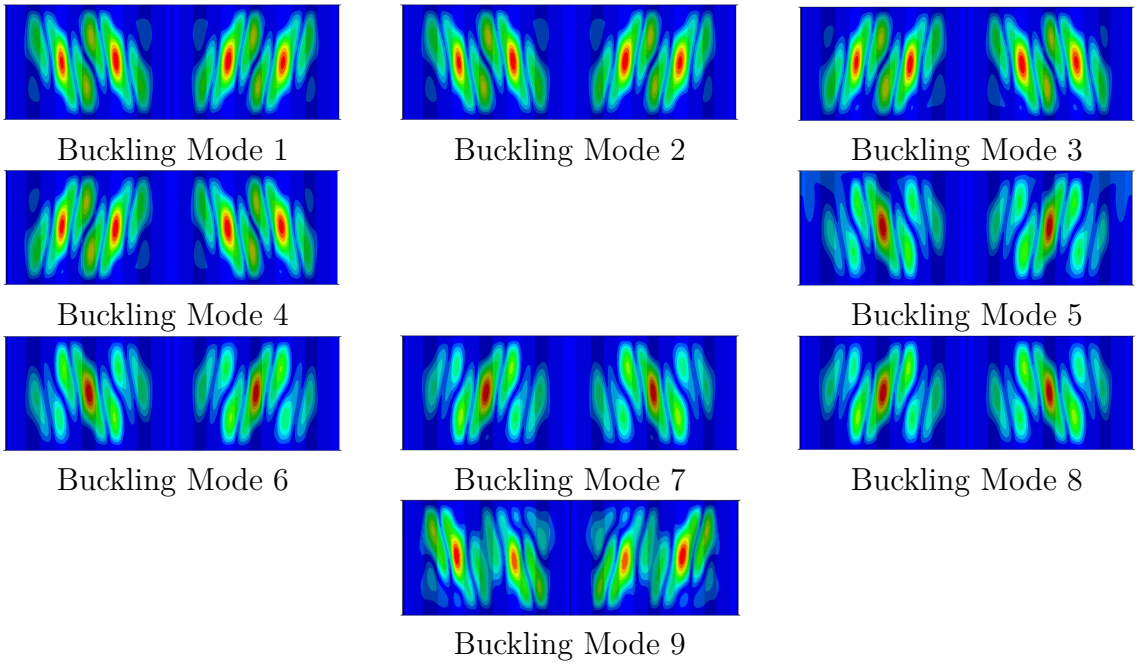

Figure 5.16: Buckling Modes of girder Matsnoki; Modes (1 to 9)

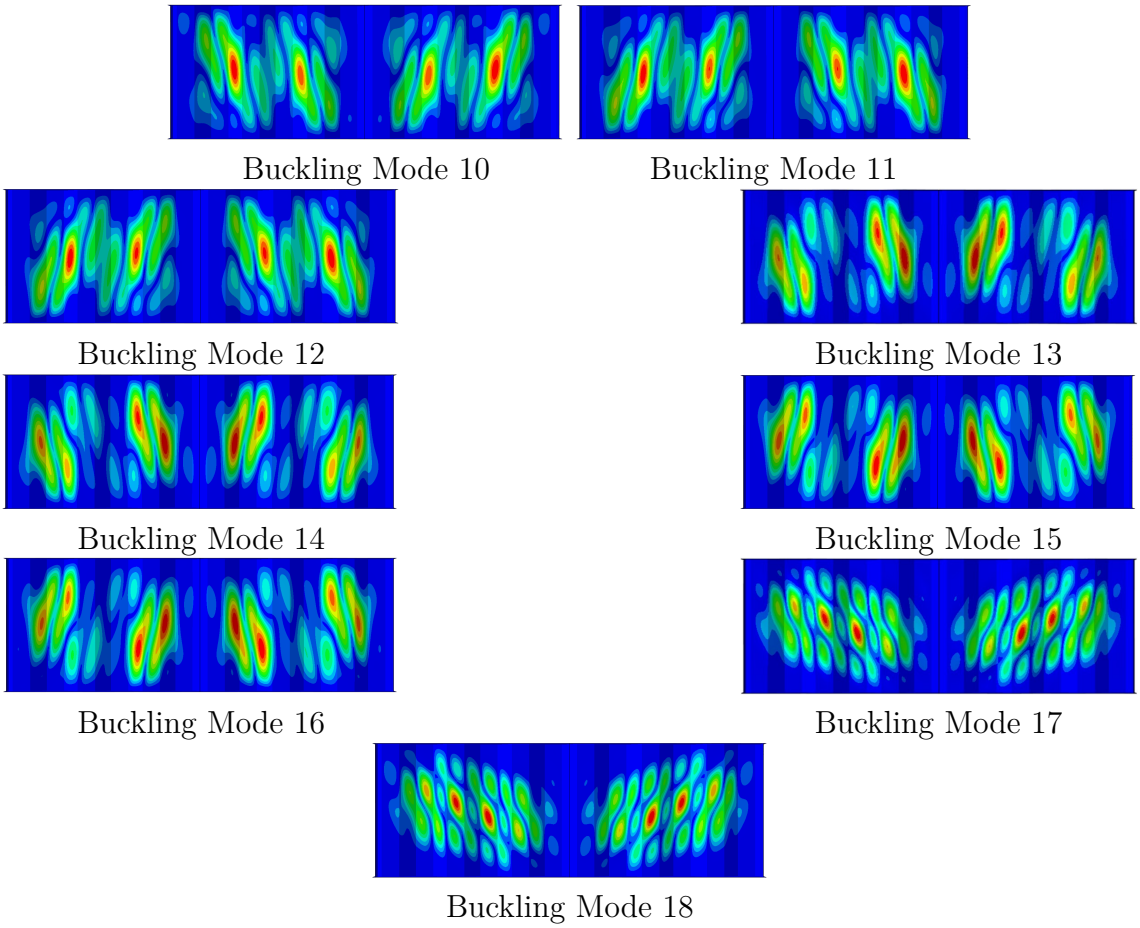

Figure 5.17: Buckling Modes of girder Matsnoki; Modes (10 to 18)

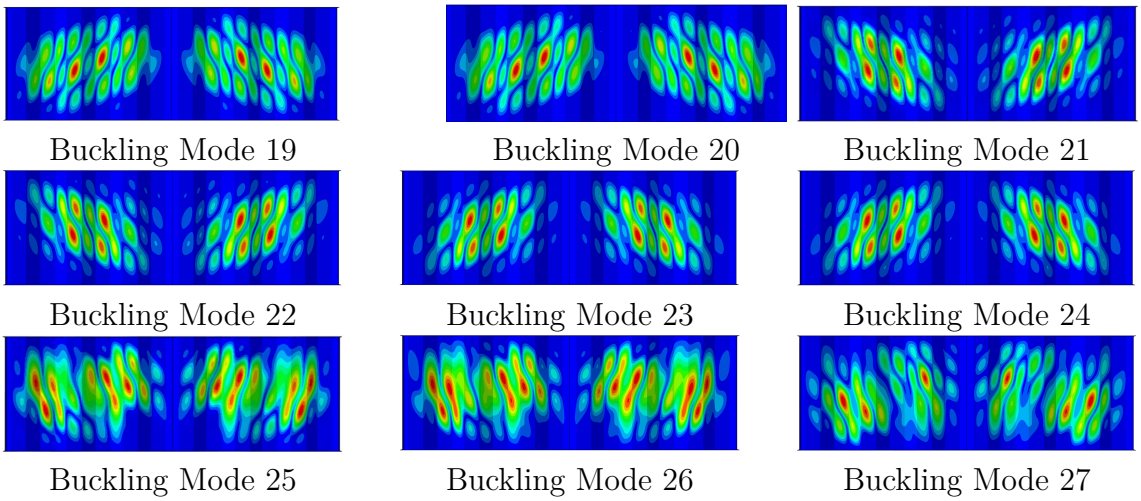

Figure 5.18: Buckling Modes of girder Matsnoki; Modes (19 to 27)

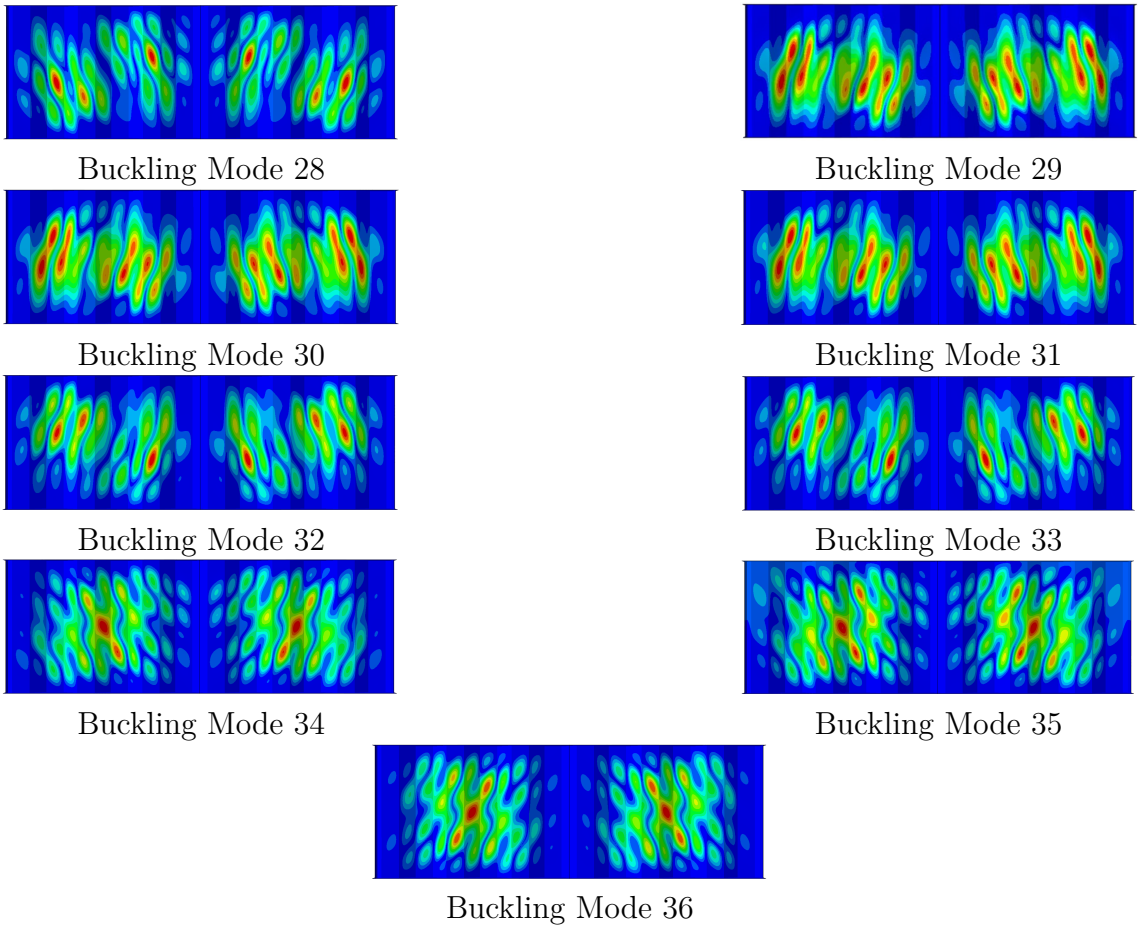

Figure 5.19: Buckling Modes of girder Matsnoki; Modes (28 to 36)

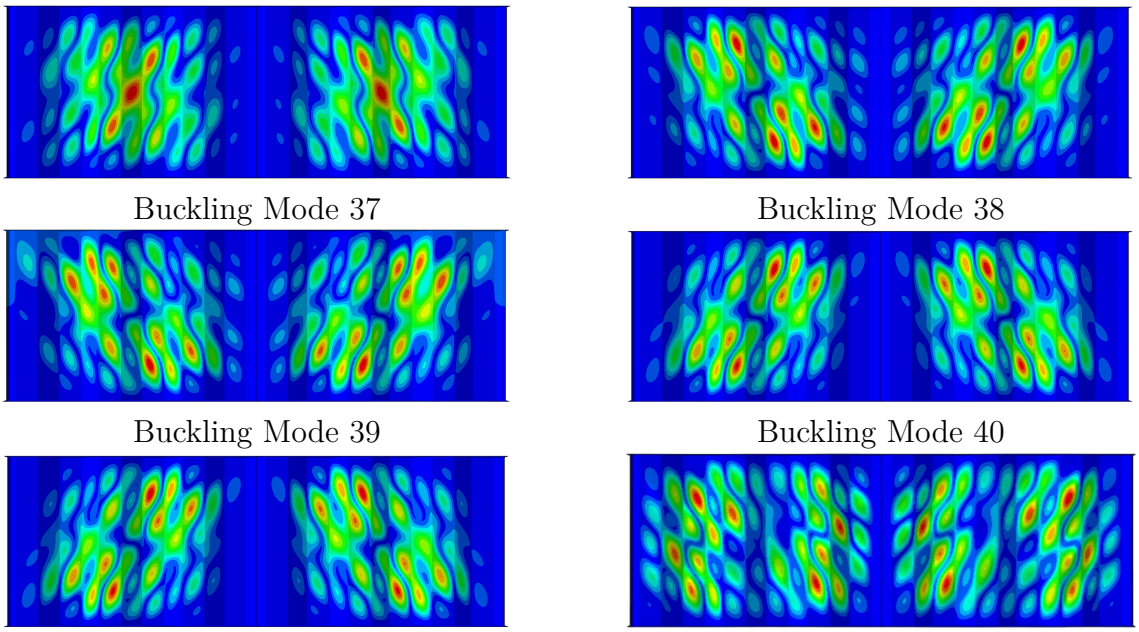

Figure 5.20: Buckling Modes of girder Matsnoki; Modes (37 to 42)

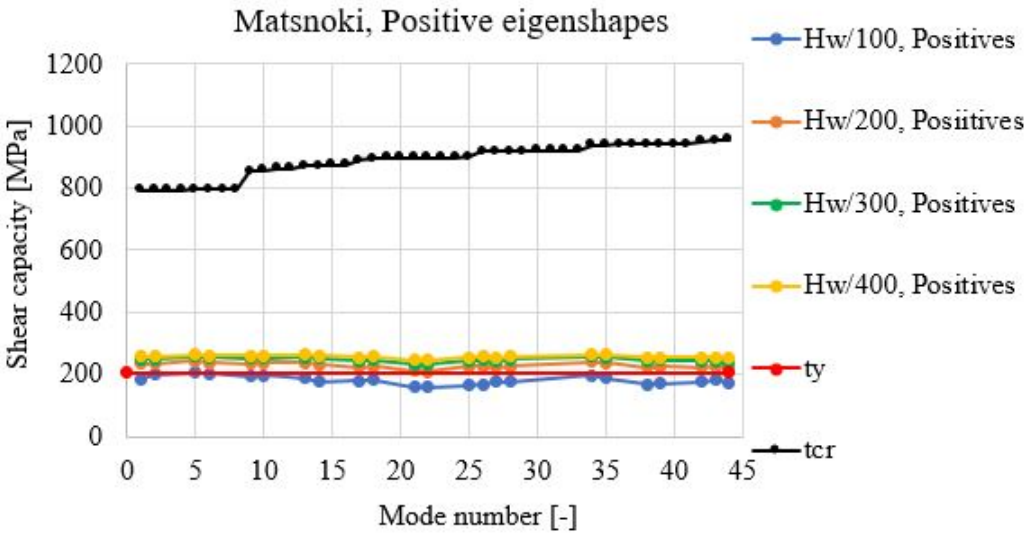

Figure 5.21: Shear capacity variation with different initial imperfection shapes, positive eigenshapes, inelastic buckling

Referring to figure 5.21, the shear yielding stress is much lower than the shear buckling stress, as can be seen. In this case, the girder reaches yielding before buckling, making the shear capacity close to yield stress.

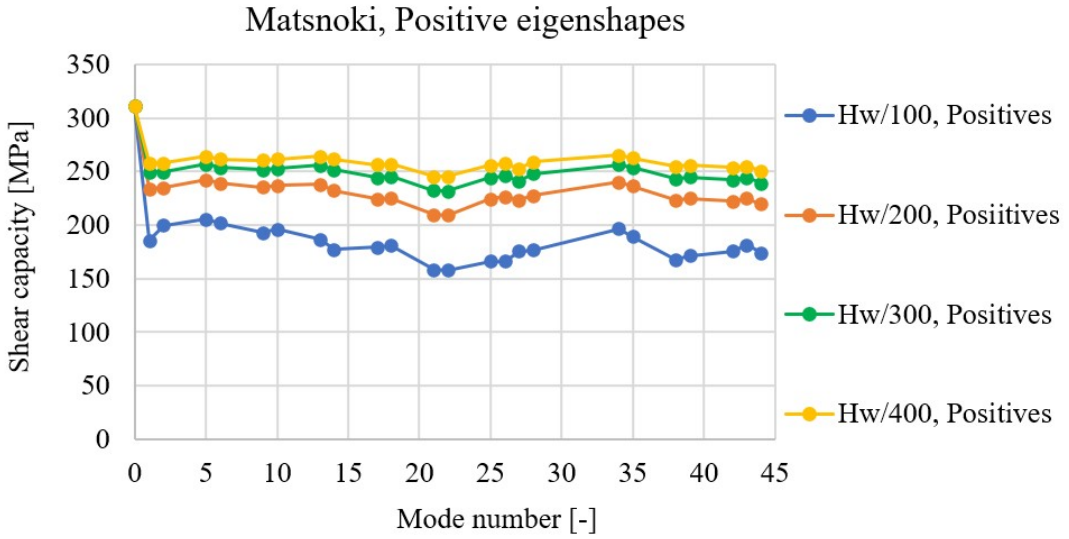

Figure 5.22: Shear capacity variation with different initial imperfection shapes and positive eigenshapes, inelastic buckling

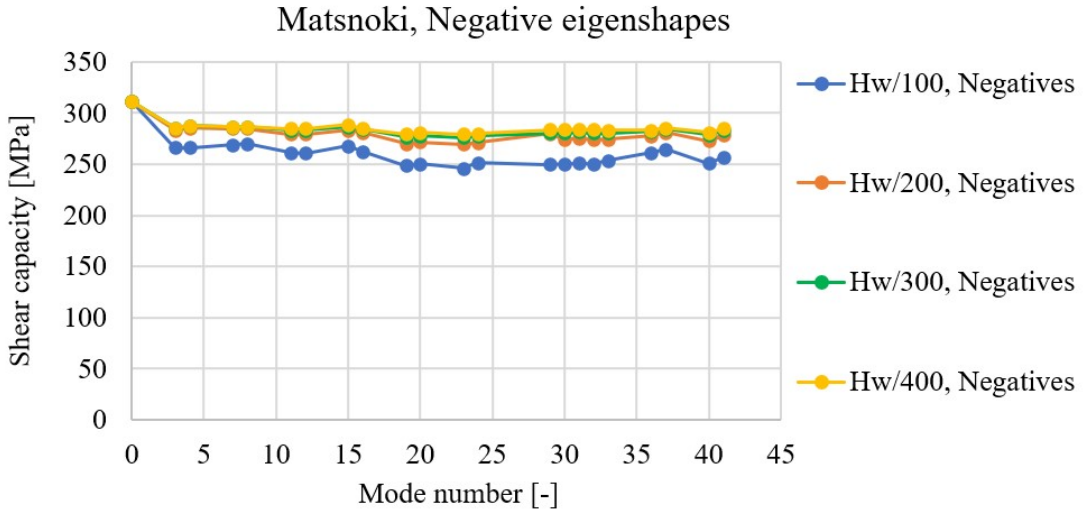

Figure 5.23: Shear capacity variation with different initial imperfection shapes and negative eigenshapes, inelastic buckling

The shear capacity resulted from negative eigenvalues and positive eigenvalues for different amplitudes are differentiated in figure 5.24. The upper band of capacity is determined by the negative eigenvalues, while the lower band is determined by the positive eigenvalues. As a result, as initial imperfection shapes, positive eigenvalues are more crucial in this case also.

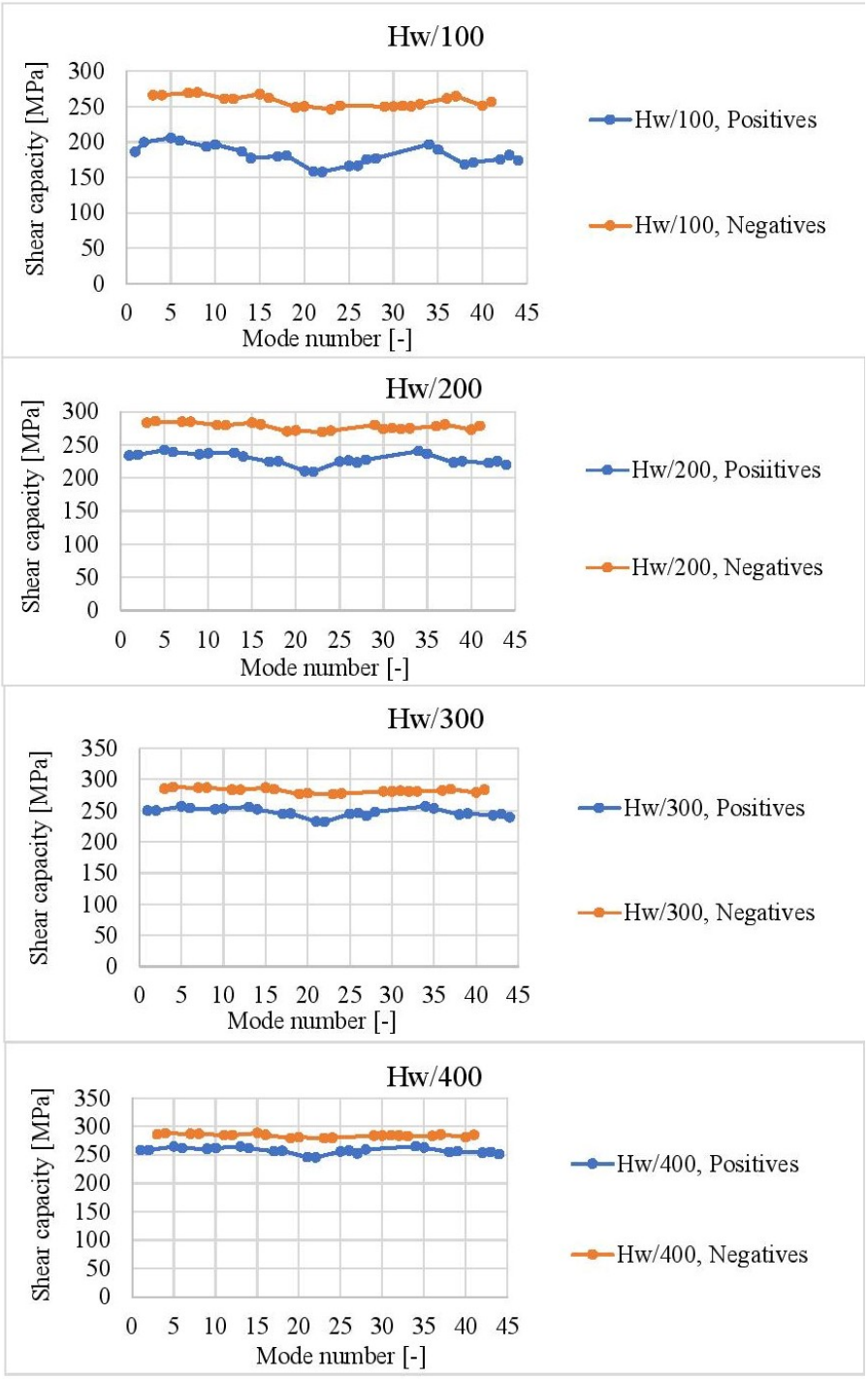

Figure 5.24: Shear capacity sensitivity to mode shape, positive and negative eigen values, inelastic buckling for different amplitudes

5.3 Shear buckling strength is smaller than shear yield strength, girder S2, [18]

Further investigation has been done to assess the sensitivity for imperfection where the shear buckling strength is lower than the shear yield strength ($\tau_{cr} < \tau_y$). Specimen (S2-2) from literature presented by Nie et al. [18] has been used.

A mesh convergence study is carried out to determine a suitable mesh size for FE simulations. In ABAQUS, several mesh sizes are tested, and the study is converging when the eigenvalue is converging. The elements are organized freely, and the element type is taken from the comparison between Quadratic S8R and Linear S4R. Results are presented in Table 5.5 and figure 5.25.

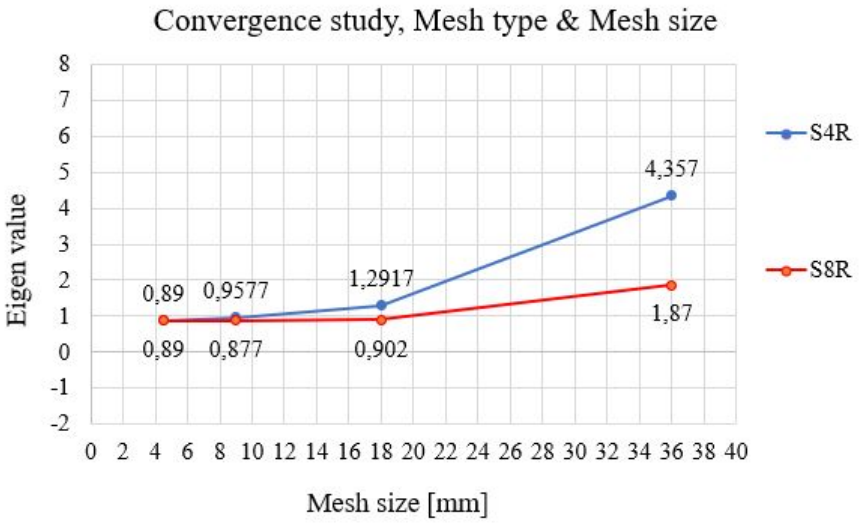

Figure 5.25: Mesh Convergence study for S2

It is concluded from the convergence study that element size of 4.5 mm, 9 mm, and 18 mm with the second-order element (S8R) or element size of 4.5 mm and 9 mm with the linear type (S4R) give close values of eigenvalues with a difference of 3%, so an element of size 18 mm (Hw/20) of S8R or element of size 9 mm (Hw/40) of S4R gives good accuracy to proceed with. The element type S8R with 18 mm (Hw/20) has been chosen for further study.

The dimensions, mechanical properties, and shear buckling strength of specimen S2 are presented in table 5.7. The load has been applied in the middle of the length.

Table 5.5: Mesh Convergence study for S2

S4R		
Mesh size	Mesh size [mm]	Eigen value
Hw/80	4.5	0.89
Hw/40	9	0.9577
Hw/20	18	1.2917
Hw/10	36	4.357
S8R		
Mesh size	Mesh size [mm]	Eigen value
Hw/80	4.5	0.89
Hw/40	9	0.877
Hw/20	18	0.902
Hw/10	36	1.87

Table 5.7: Dimensions, mechanical properties and shear buckling stress of specimen S2

Dimension					
b_f **(mm)**	t_f **(mm)**	h_w **(mm)**	t_w **(mm)**	**Imperfection (mm)**	α **(degrees)**
200	20	360	0.9	Variable	37
h_r **(mm)**	**b (mm)**	**c (mm)**	**d (mm)**	**a (mm)**	**Length (mm)**
48	80	63.74	64	1.475	2.95
Material model					
E (Gpa)	F_y **(Mpa)**	**Plastic Strain at** F_y	F_u **(Mpa)**	**Plastic Strain at** F_u	**Poisson ratio**
200	True stress-strain curve presented above				
τ_y **(MPa)**	**Eigen value**	τ_{cr} **(Mpa)**	τ_{cr_EU} **(Mpa)**	**Difference**	**Reference load (kN)**
232.12	0.902	139.273	122.26	0.12	100

A linear buckling analysis has been performed to define the number of modes to be considered in the study. The number of eigen modes that fulfill the condition of 20% are 56 Modes. The modes are illustrated in figures 5.26, 5.28, 5.29, 5.30 and 5.31. The eigen values for the fifty six modes are presented in table 5.8

Table 5.8: The modes considered in the study with range of 20% from first mode, S2

Eigen Shapes	**Eigen value**	**ABS**	τ_{cr} **[MPa]**		**Eigen Shapes**	**Eigen value**	**ABS**	τ_{cr} **[MPa]**	
1	-0.9025	0.9025	139.27	***	31	-0.9702	0.9702	149.72	***
2	-0.9025	0.9025	139.28	***	32	-0.9702	0.970	149.72	***
3	0.90255	0.9026	139.28	***	33	1.0046	1.0046	155.03	***
4	-0.90258	0.90258	139.29	***	34	1.0047	1.0047	155.05	***
5	0.9026	0.9026	139.29	***	35	1.0049	1.0049	155.08	***
6	-0.90263	0.90263	139.29	***	36	1.0049	1.0049	155.08	***
7	0.90264	0.90264	139.30	***	37	-1.0056	1.0056	155.19	***
8	0.90269	0.90269	139.30	***	38	-1.0057	1.0057	155.20	***
9	-0.91581	0.91581	141.33	***	39	-1.0058	1.0058	155.22	***
10	-0.91588	0.91588	141.34	***	40	-1.0059	1.0059	155.23	***
11	0.91591	0.91591	141.34	***	41	1.043	1.043	160.96	***
12	-0.91596	0.91596	141.35	***	42	1.0432	1.0432	160.99	***
13	0.91598	0.91598	141.35	***	43	1.0434	1.0434	161.02	***
14	-0.91603	0.91603	141.36	***	44	1.0435	1.0435	161.03	***
15	0.91605	0.91605	141.37	***	45	-1.0445	1.0445	161.19	***
16	0.91612	0.91612	141.38	***	46	-1.0446	1.0446	161.20	***
17	0.93894	0.93894	144.90	***	47	-1.0449	1.0449	161.25	***
18	0.93905	0.93905	144.92	***	48	-1.045	1.045	161.27	***
19	-0.93909	0.93909	144.92	***	49	1.0733	1.0733	165.63	***
20	0.93913	0.93913	144.93	***	50	1.0733	1.0733	165.63	***
21	-0.93919	0.93919	144.94	***	51	-1.0733	1.0733	165.63	***
22	0.93927	0.93927	144.95	***	52	-1.0733	1.0733	165.63	***
23	-0.93928	0.93928	144.95	***	53	1.0772	1.0772	166.23	***
24	-0.93941	0.93941	144.97	***	54	1.0773	1.0773	166.25	***
25	0.96945	0.96945	149.61	***	55	-1.0773	1.0773	166.25	***
26	0.96945	0.96945	149.61	***	56	-1.0774	1.0774	166.27	***
27	0.96961	0.96961	149.63	***	57	1.0855	1.0855	167.52	
28	0.96963	0.96963	149.63	***	58	1.0859	1.0859	167.58	
29	-0.96999	0.96999	149.69	***	59	1.0863	1.0863	167.64	
30	-0.97001	0.97001	149.69	***	60	1.0867	1.0867	167.70	
*** Eigenvalues in the studied range, 1.2*first eigenvalue									

For each eigenvalue, a nonlinear analysis for four different amplitudes (Hw/100, Hw/200, Hw/300, and Hw/400) has been performed. The results are illustrated in figures 5.32 and 5.33. In this case, the negative eigen shapes are disregarded since they give higher shear capacity according to the previous two investigations of M12 and Matsnoki girders. The positive eigen shapes are more critical and give lower shear capacity. It can be seen that in this case, the shear strength is less sensitive to the initial imperfection shape and amplitude than M12. For instance, the shear capacity decreases from 166.256 MPa for the perfect shape to 140.57 MPa (15.4%) for the amplitude of Hw/100 and a shape similar to mode 5. This decrease is smaller than the decrease in the case of elastic buckling in M12 (around 33%).

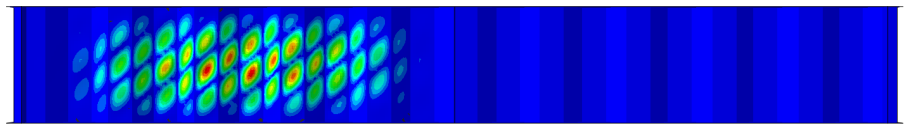

Buckling Mode 1

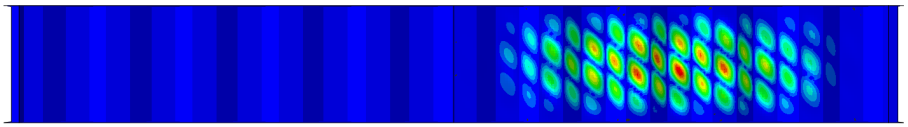

Buckling Mode 2

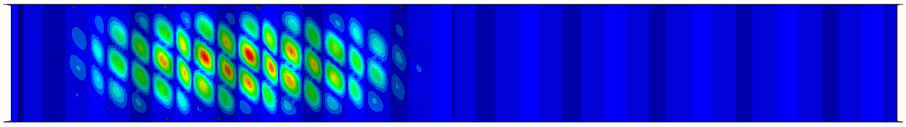

Buckling Mode 3

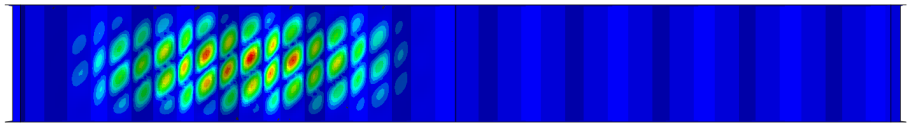

Buckling Mode 4

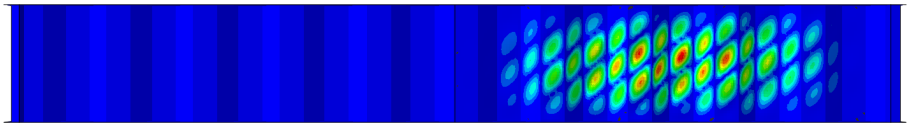

Buckling Mode 5

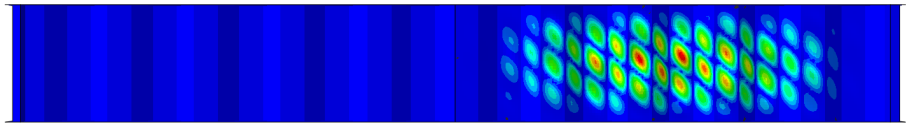

Buckling Mode 6

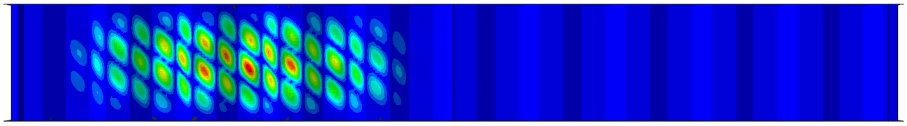

Buckling Mode 7

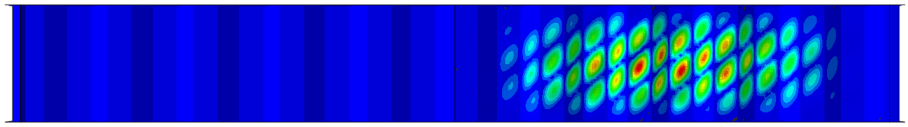

Buckling Mode 8

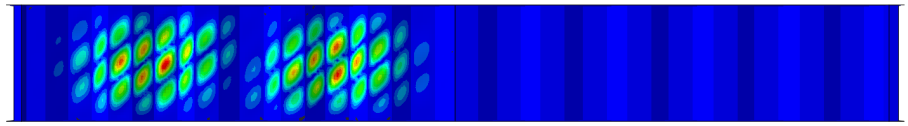

Buckling Mode 9

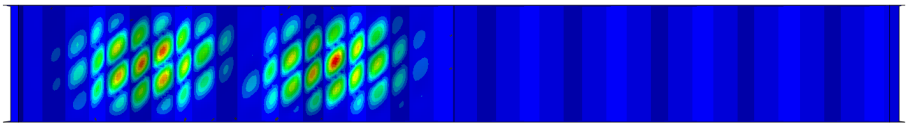

Buckling Mode 10

Figure 5.26: Buckling Modes of girder S2; Modes (1 to 10)

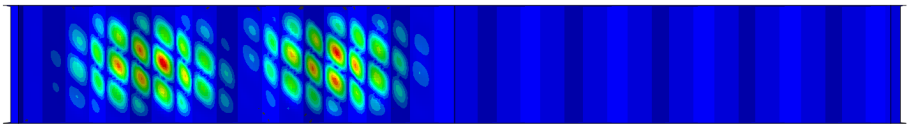

Buckling Mode 11

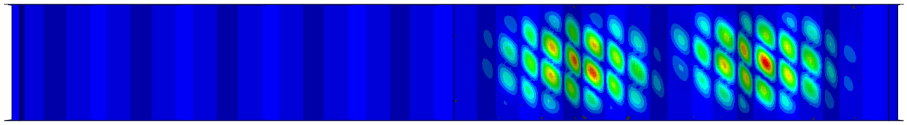

Buckling Mode 12

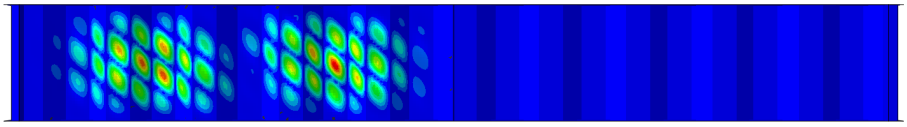

Buckling Mode 13

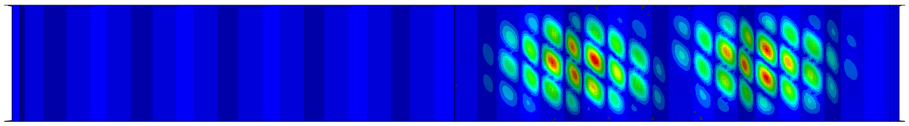

Buckling Mode 14

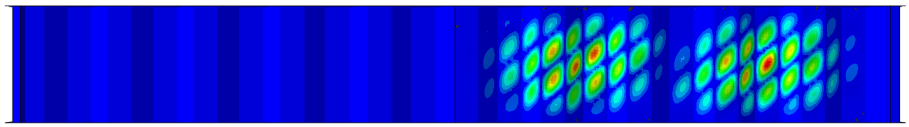

Buckling Mode 15

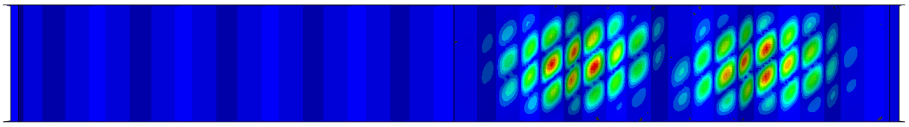

Buckling Mode 16

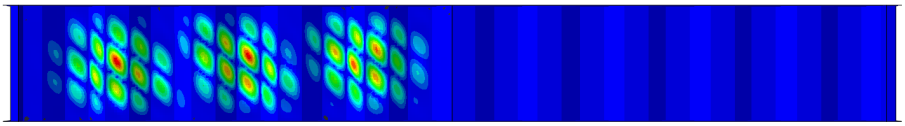

Buckling Mode 17

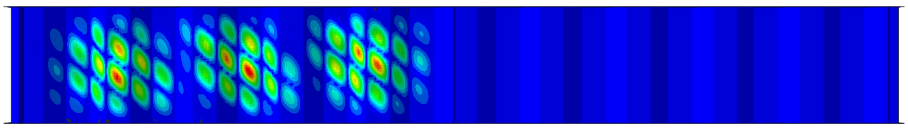

Buckling Mode 18

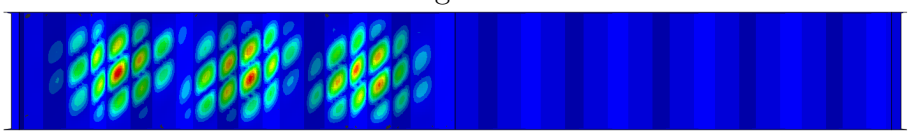

Buckling Mode 19

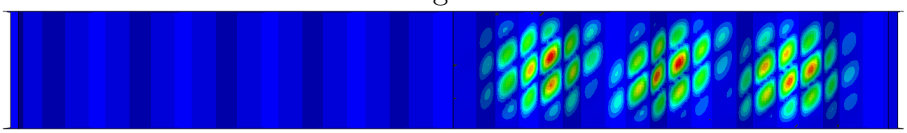

Buckling Mode 20

Figure 5.27: Buckling Modes of girder S2; Modes (11 to 20)

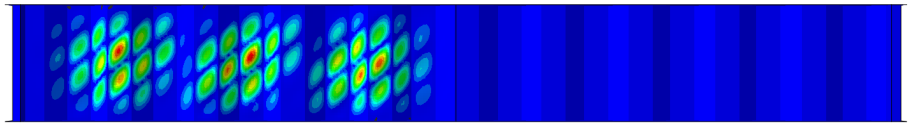

Buckling Mode 21

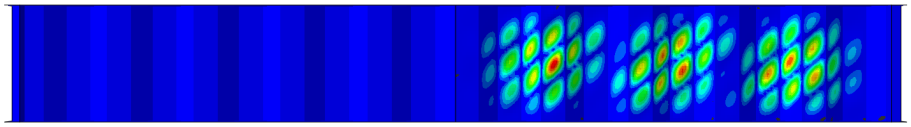

Buckling Mode 22

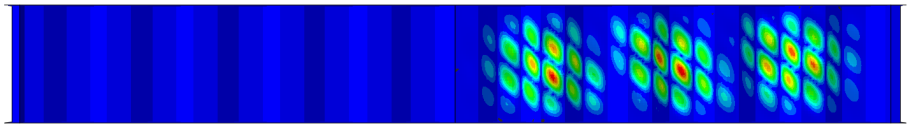

Buckling Mode 23

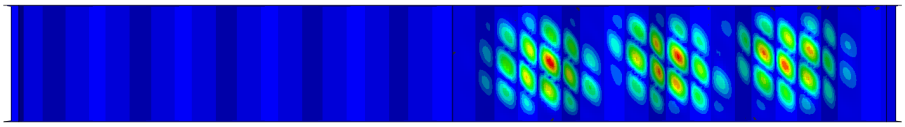

Buckling Mode 24

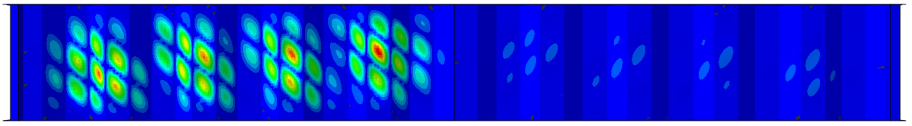

Buckling Mode 25

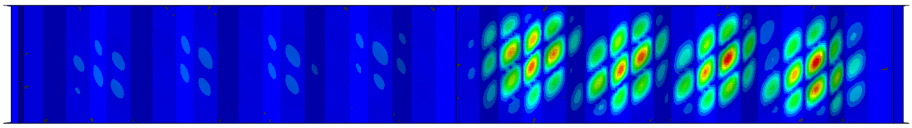

Buckling Mode 26

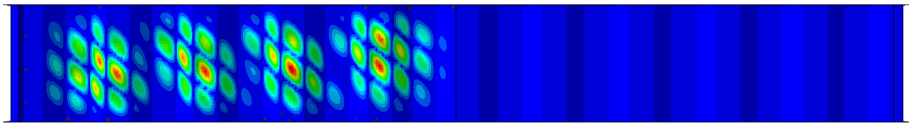

Buckling Mode 27

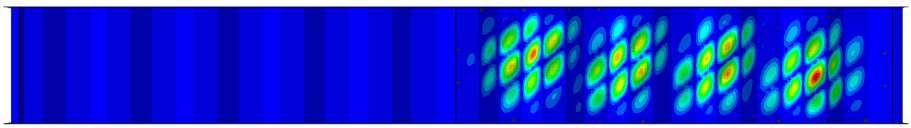

Buckling Mode 28

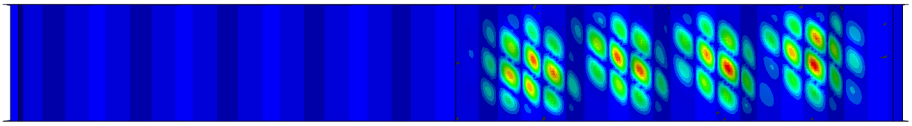

Buckling Mode 29

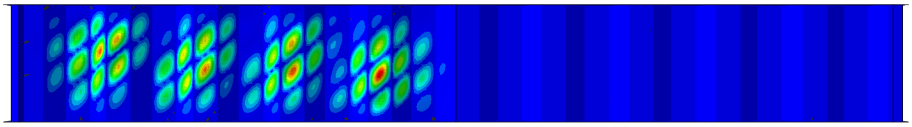

Buckling Mode 30

Figure 5.28: Buckling Modes of girder S2; Modes (21 to 30)

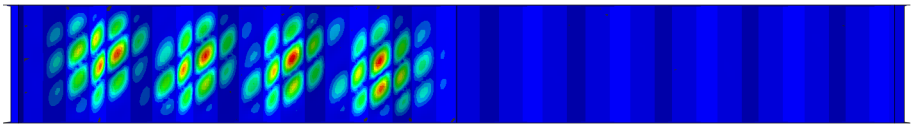

Buckling Mode 31

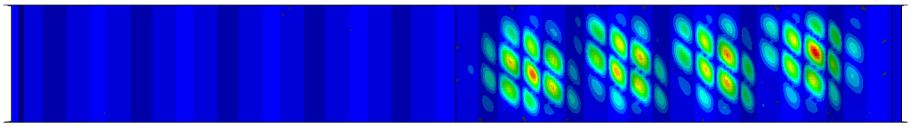

Buckling Mode 32

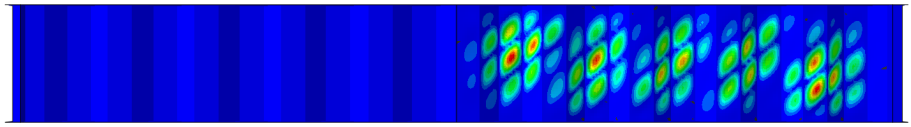

Buckling Mode 33

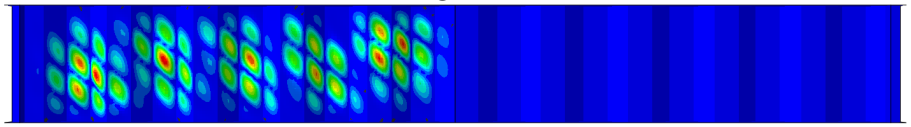

Buckling Mode 34

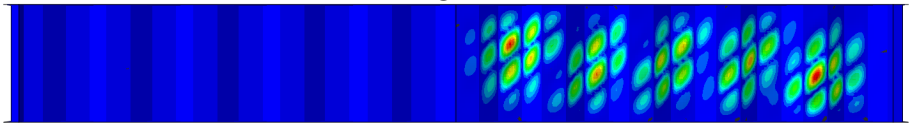

Buckling Mode 35

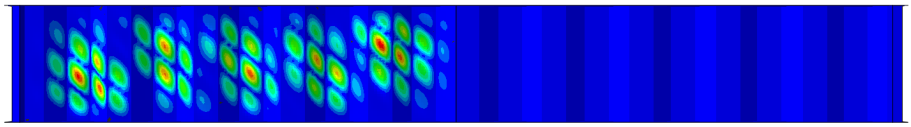

Buckling Mode 36

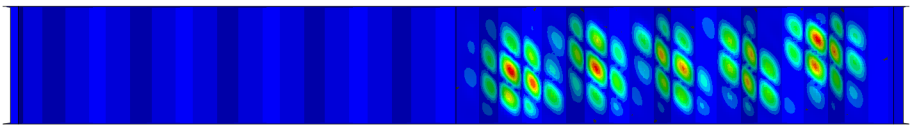

Buckling Mode 37

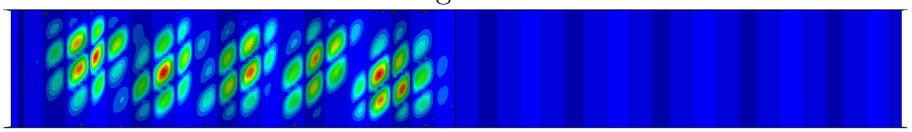

Buckling Mode 38

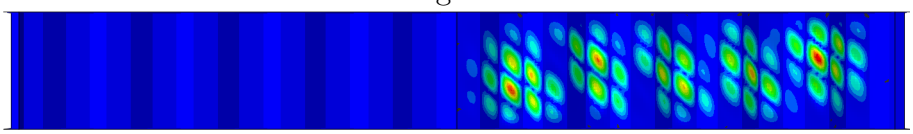

Buckling Mode 39

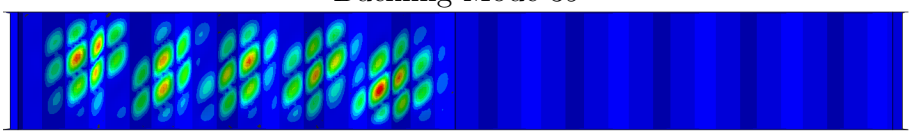

Buckling Mode 40

Figure 5.29: Buckling Modes of girder S2; Modes (31 to 40)

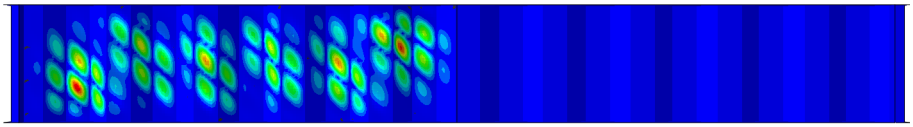

Buckling Mode 41

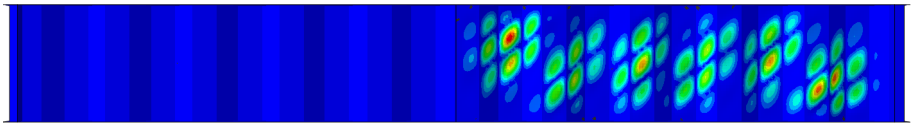

Buckling Mode 42

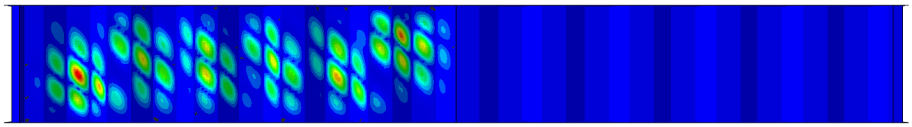

Buckling Mode 43

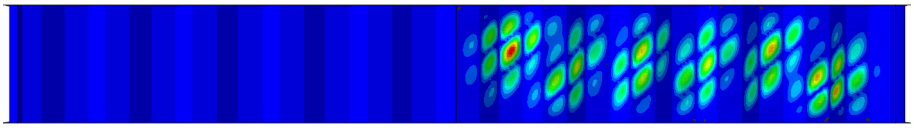

Buckling Mode 44

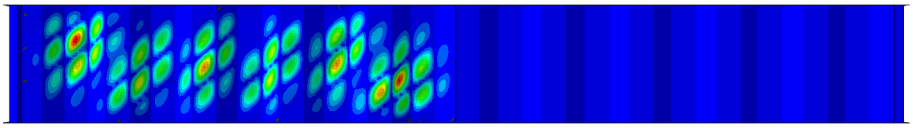

Buckling Mode 45

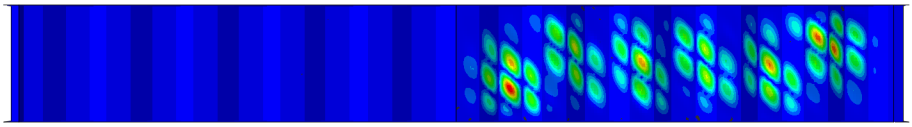

Buckling Mode 46

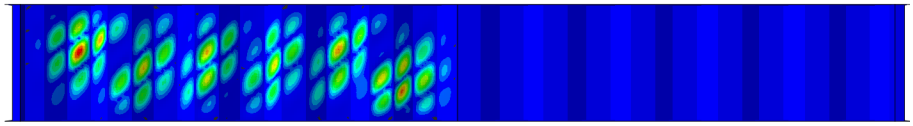

Buckling Mode 47

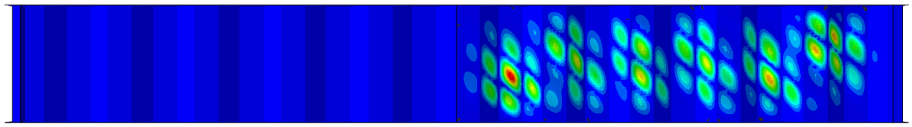

Buckling Mode 48

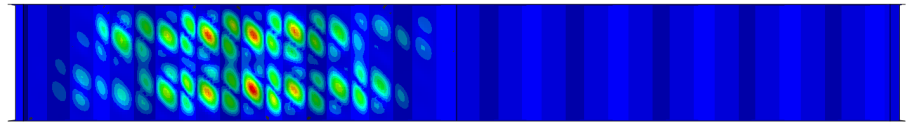

Buckling Mode 49

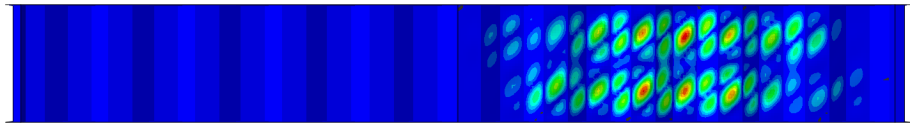

Buckling Mode 50

Figure 5.30: Buckling Modes of girder S2; Modes (41 to 50)

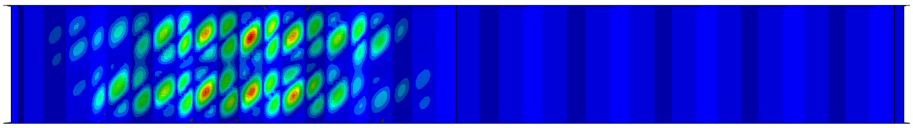

Buckling Mode 51

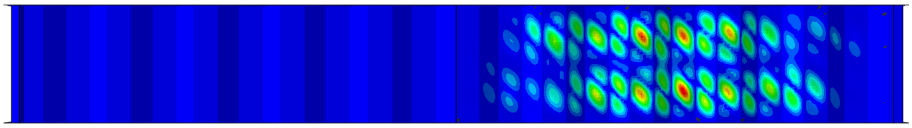

Buckling Mode 52

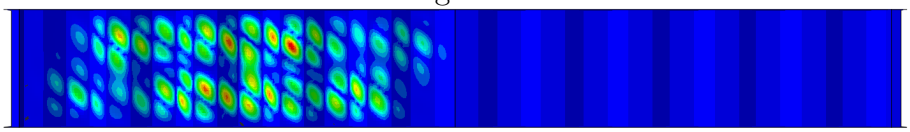

Buckling Mode 53

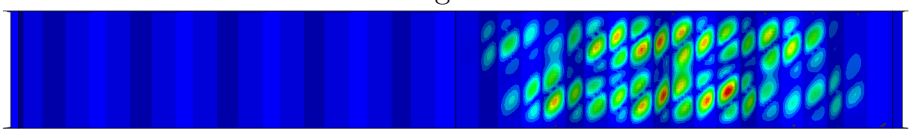

Buckling Mode 54

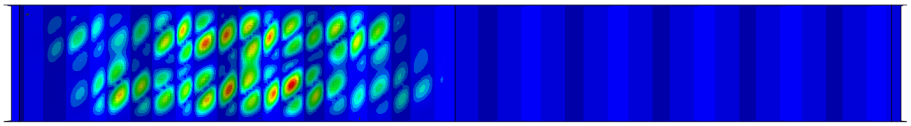

Buckling Mode 55

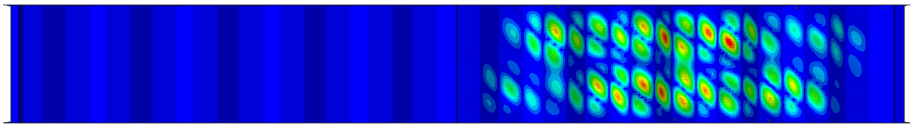

Buckling Mode 56

Figure 5.31: Buckling Modes of girder S2; Modes (51 to 56)

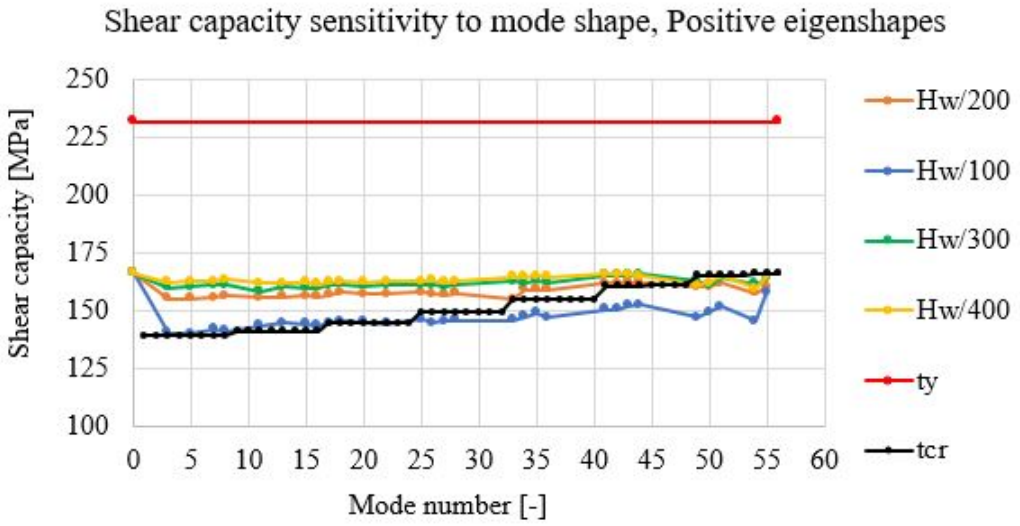

Figure 5.32: Shear capacity variation with different initial imperfection amplitude and mode shapes, the yield strength and the critical shear capacity, S2

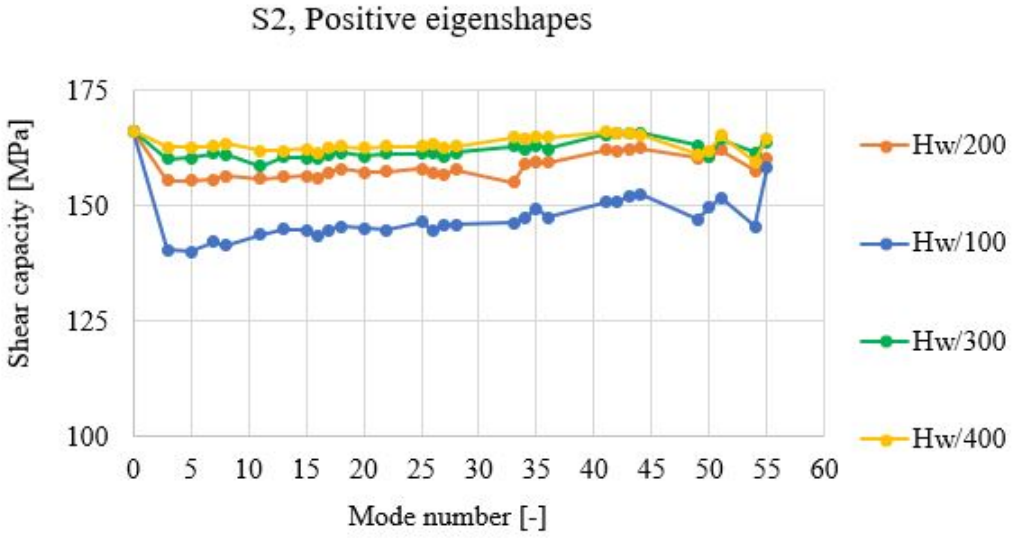

Figure 5.33: Shear capacity variation with different initial imperfection amplitude and mode shapes, S2

Referring to figure 5.34 the shear capacity in the single mode decreases with increasing the imperfection amplitude. For instance, for mode 12, the capacity decrease from 165.92 MPa to 164.17 MPa (1%) by increasing the imperfection amplitude from Hw/400 to Hw/300.

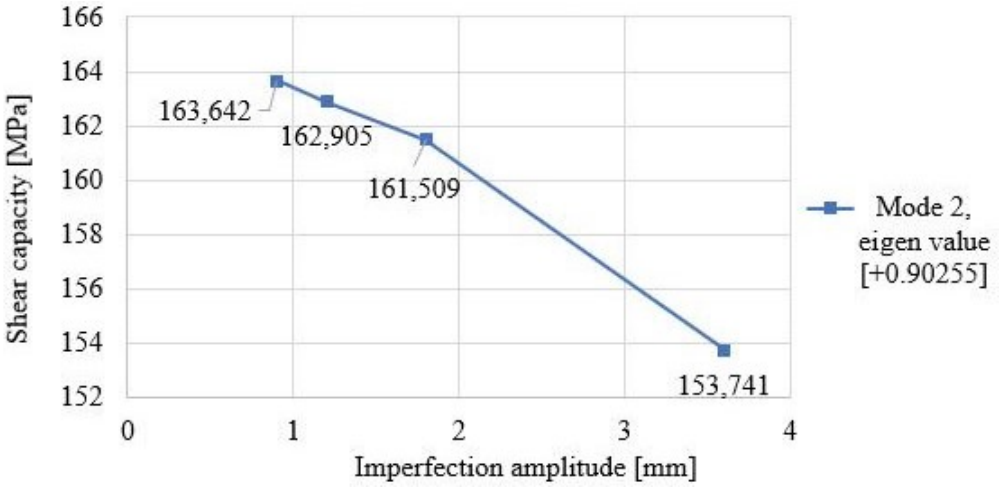

Figure 5.34: Shear capacity variation with different initial imperfection amplitude for different eigen value signs, S2, Mode 12

To compare the behavior of the girder under various imperfection shapes, a relation between shear stress and in-plane displacement has been presented in figure 5.35. For imperfection amplitude of Hw/400. It is seen that the behavior is similar for all shapes—however, the ultimate capacity changes with mode number. The first positive mode is mode number 2, and that gives a capacity of 163.64 MPa, while mode number 5 gives a capacity of 162.38 MPa.

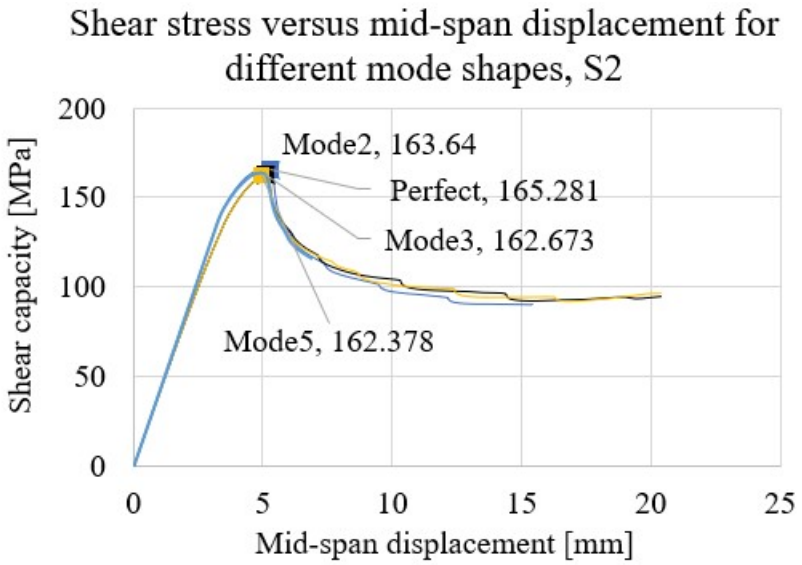

Figure 5.35: Shear behaviour for different mode shapes, S2, Imperfection amplitude Hw/400

.

5.4 Comparison of the three studied girders' shear behavior

In many previous studies on the corrugated web girders, the most critical mode shape considered in the design is the first positive mode, which gives the lowest shear capacity but in this study, after modeling the three different specimens; M12, S2, and Matsnoki, it is observed that the first mode is not the most critical shape and many other modes can give lower shear capacity.

In M12, the difference between the first positive mode (mode 1) and the most critical mode (mode 29) is around 15 %. The shear behavior of the girder with mode 29 as initial imperfection is presented in figure 5.36. A very small yielded area in the middle of the web can be seen at ultimate load. Yielding starts at out-of-displacement around 14.6 mm and continues up to 17 mm at ultimate load. The residual capacity is around 65 MPa.

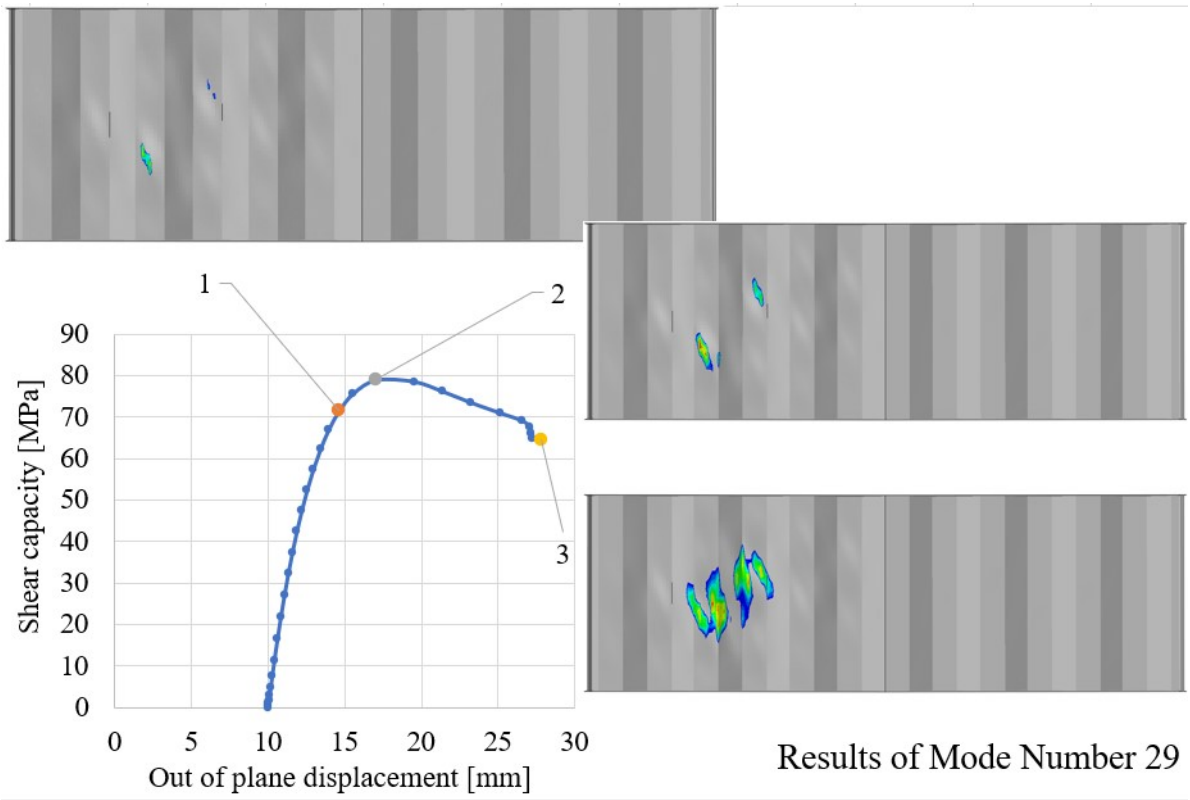

Figure 5.36: Shear behaviour, mode 29, M12

The second specimen is S2 with elastic buckling, where shear buckling strength is smaller than shear yield strength. The first positive mode is mode 3, and the mode that gives the lowest capacity is mode 33. The girder here starts yielding before it reaches the ultimate shear capacity as presented in the figures 5.37. In mode 33, yielding starts at out-of-displacement around 2.7 mm and continue up to 3.7 mm at ultimate load. The residual capacity is around 105 MPa.

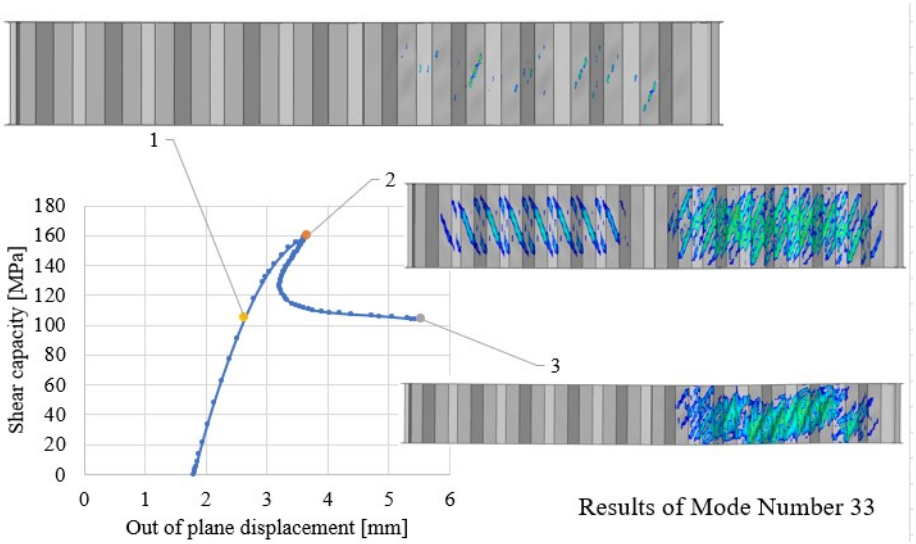

Figure 5.37: Shear behaviour, mode 33, S2

The third specimen is Matsnoki with inelastic buckling, where shear buckling strength is much higher than shear yield strength. The difference between the first positive mode (mode 1) and the most critical mode (mode 22) is 10.4%. In both cases, the girder is governed by yielding, which starts before it reaches the ultimate shear capacity and buckles as presented in the figure 5.38.In mode 22, the yielding lasts from 13 mm to 18.4 mm, and the girder shows quite ductile behavior after ultimate capacity. The residual capacity is around 165 MPa.

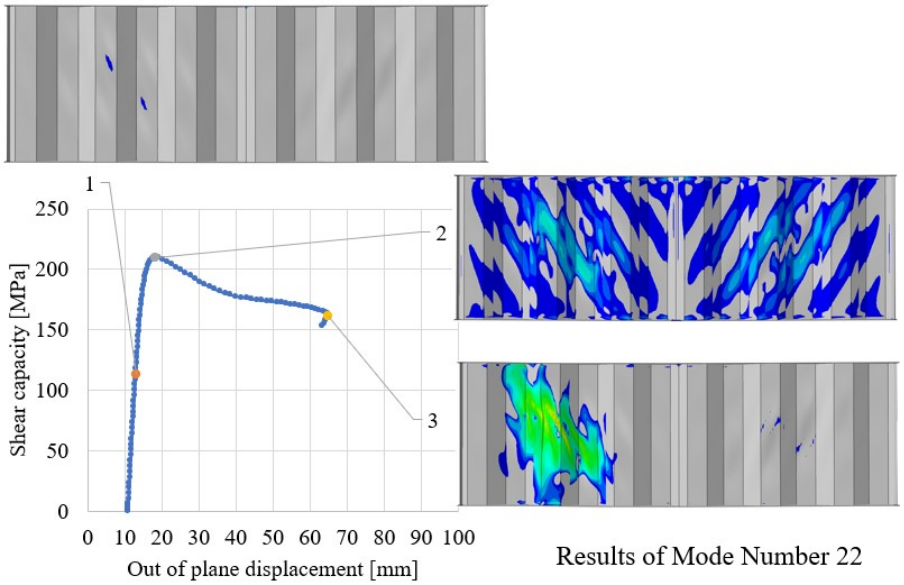

Figure 5.38: Shear behaviour, mode 22, Matsnoki

The behavior of the three girders with shear buckling stress, shear yielding stress, and shear slenderness for each case are presented in figure 5.39. In the first case, S2, the shear slenderness is quite large, and the shear behavior is governed by buckling. The shear stress reaches buckling strength, and then a bit afterward,

the capacity decreases until failure. In the second case, M12, the shear slenderness is intermediate, and the shear behavior here is very sensitive to imperfection. The girder fails before reaching the yielding or buckling strength. In the third case, Matsnoki, the shear slenderness is quite small, and the shear behavior is governed by yielding. The shear stress reaches yielding strength, and then a bit afterward, the capacity decreases until failure.

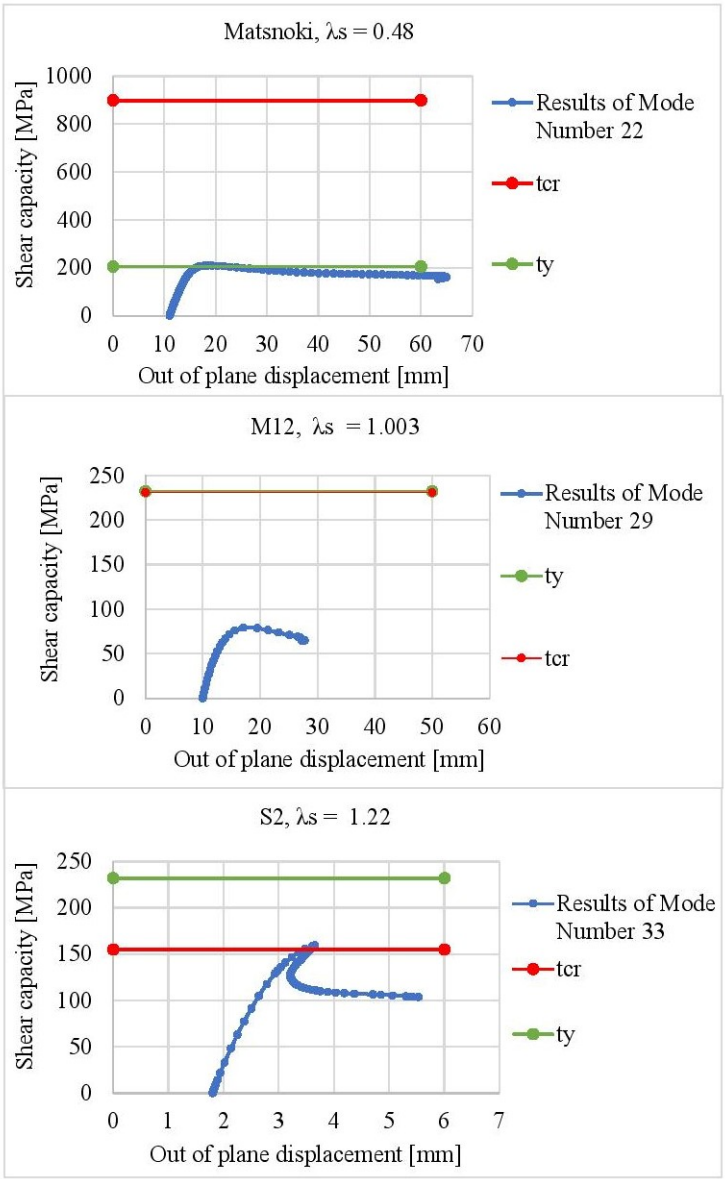

Figure 5.39: comparison of the three studied girders' shear behavior

5.5 Mode combination

This section aims to look at other shapes of initial imperfection. The initial imperfection may take any shape. In this section, the shape of a combination of eigenshapes is considered. Various combinations are investigated, and the resulting

shear capacity is compared to that of single modes as an initial imperfection.

The expression used for imperfection profile from mode combination is illustrated in equation 5.2. It is composed of three terms, i.e., imperfection shape, imperfection magnitude, and a combination factor [22]. Each mode's contribution is treated equally here, with the magnitude remaining constant.

$$G(x, y, z) = \sum_{i=1}^{n} c_i \alpha_i \varphi_i(x, y, z) \tag{5.2}$$

Where

α is the imperfection amplitude, from test measurements or equivalent imposed imperfection.

c_i is the combination factor.

$\varphi_i(x, y, z)$ is the imperfection Shape.

Due to the variation of shear capacity with mode number and the need to easily find the worst mode combination, two initial imperfection amplitudes (Hw/200, Hw/300) were considered, and five different combinations of initial imperfection shapes (All modes in the range (first mode to 1.2*first mode), Odd modes, even modes, Positive modes, and Odd-positive-modes) were considered. The results for the three cases are listed below.

5.5.1 Moon girder, M12

The number of single modes considered for M12 girder is 50 modes in the range between first mode and 1.2* first mode. Shear capacity for the different mode combination with initial imperfection amplitude of Hw/200 are illustrated in table 5.9 and figure 5.40. Mode combination shapes have same amplitude and are illustrated in figure 5.42.

Table 5.9: Shear capacity for different mode combination, M12, Imperfection of Hw/200, Range (first mode to 1.2 first mode)

Elastic buckling, M12, Hw/200					
Mode combination	**No. modes**	**Scale factor**	**Shear cpacity (MPa)**	**No. of modes that give higher capacity**	**Max decrease in capacity from single modes**
All (1 to 50)	50	0.00199441563621859	109.18	50%	-28%

Odd modes	25	0.00306842589751458	83.21	96%	-5%
Even modes	25	0.00252652854977261	96.46	56%	-18%
Positive modes	25	0.00266453503863576	85.33	92%	-7%
Positive Modes_Odds	17	0.00335570469798658	86.92	92%	-9%

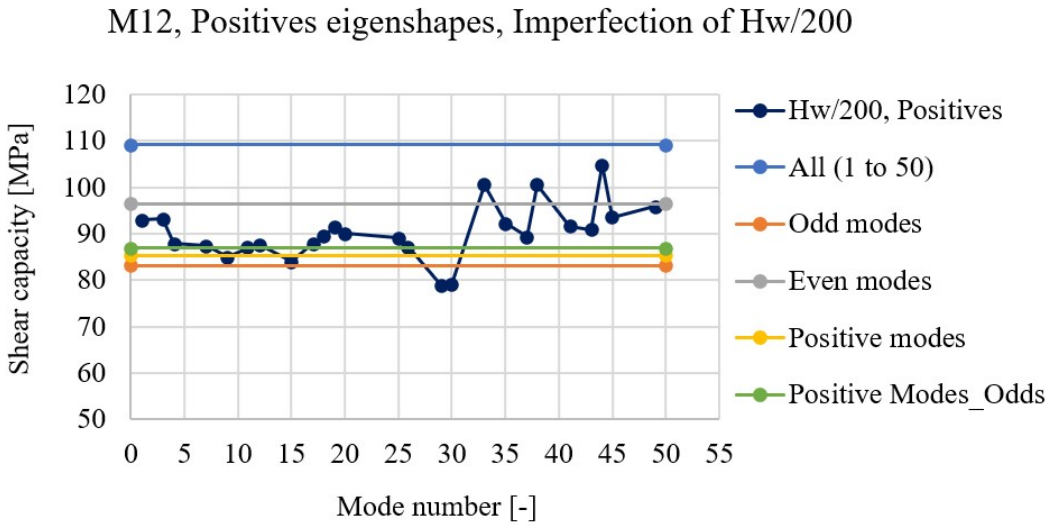

Figure 5.40: Shear capacity of different single modes and different mode combinations, M12, Hw/200

Shear capacity for the different mode combination with initial imperfection amplitude of Hw/300 are presented in table 5.10 and figure 5.41. Mode combination shapes have same amplitude and are presented in figure 5.43.

Table 5.10: Shear capacity for different mode combination, M12, Imperfection of Hw/300, Range (first mode to 1.2 first mode)

Elastic buckling, M12, Hw/300					
Mode combination	**No. modes**	**Scale factor**	**Shear capacity (MPa)**	**Number of modes that give higher capacity**	**Max decrease in capacity from single modes**
All (1 to 50)	50	0.00132961042414573	131.97	50%	-24%
Odd modes	25	0.00204561726500972	105.47	84%	-5%
Even modes	25	0.00168435236651508	117.13	54%	-14%
Positive modes	25	0.00177635669242384	111.83	72%	-10%
Positive Modes_Odds	17	0.00223713646532438	100.7	98%	-0.2%

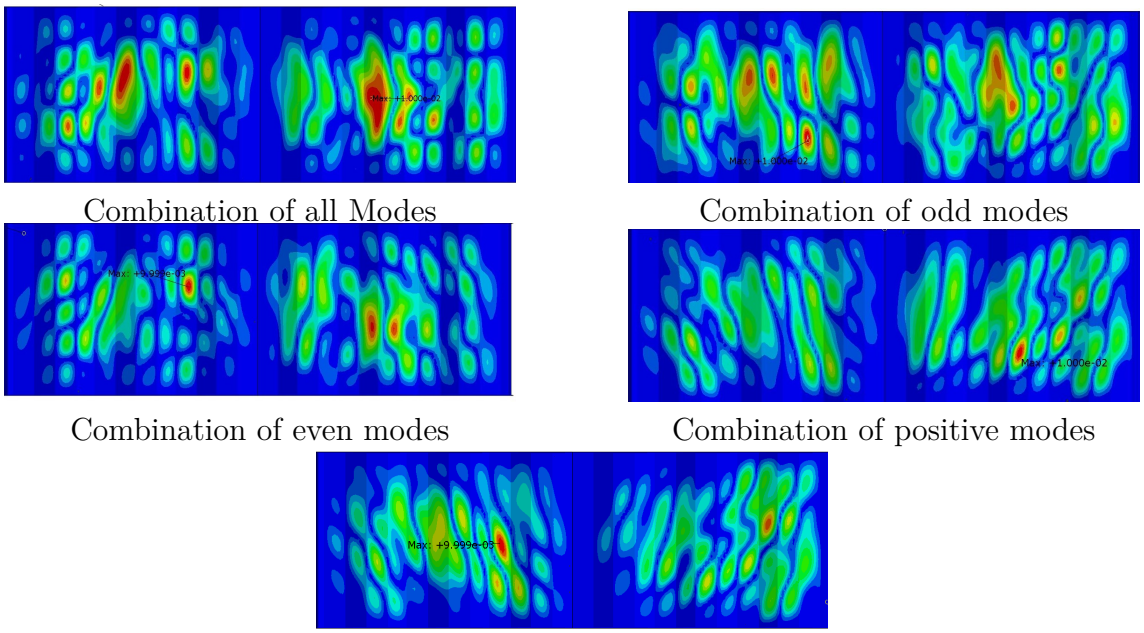

Figure 5.42: Mode combination of girder M12; Modes (1 to 50) Imperfection (hw/200)

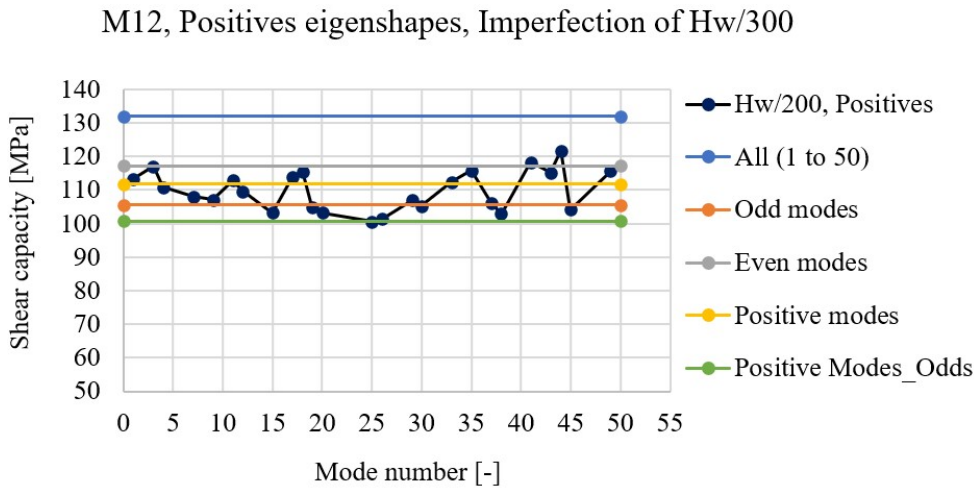

Figure 5.41: Shear capacity of different single modes and different mode combinations, M12, Hw/300

The results show that for the initial imperfection amplitude of hw/200, the combination of the odd modes gives the lowest shear capacity with a value of 83.21 MPa. This gives shear capacity less than 96% of single modes in the studied range. However, the combination of positive-odd-modes becomes the most critical with imperfection amplitude of hw/300. This combination gives shear capacity less than 98% of single modes.

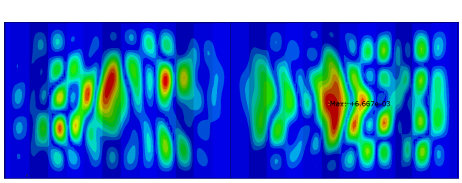

Combination of all Modes

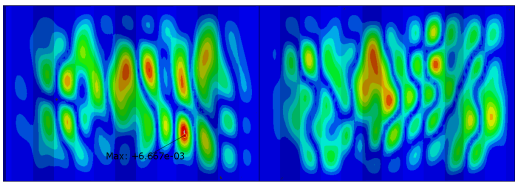

Combination of odd modes

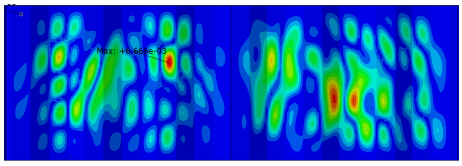

Combination of even modes

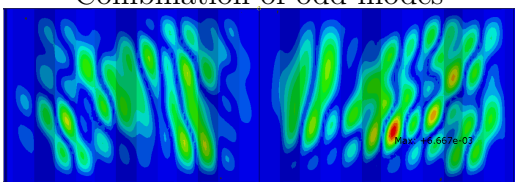

Combination of positive modes

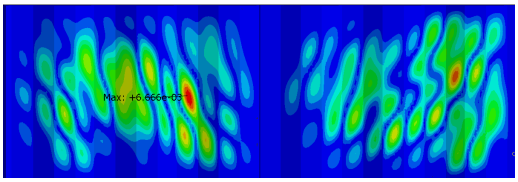

Combination of positive odd modes

Figure 5.43: Mode combination of girder M12; Modes (1 to 50) Imperfection (hw/300)

5.5.2 S2 girder

The number of single modes considered for the S2 girder is 56 modes in the range between the first mode and 1.2*first mode. Shear capacity for the different mode combination with initial imperfection amplitude of Hw/200 are presented in table 5.11 and figure 5.44. Mode combination shapes have the same amplitude and are presented in figure 5.45.

Table 5.11: Shear capacity for different mode combination, S2, Imperfection of Hw/200, Range (first mode to 1.2 first mode)

S2, Hw/200					
Mode combination	**No. modes**	**Scale factor**	**Shear capacity (MPa)**	**Number of modes that give higher capacity**	**Max decrease in capacity from single modes**
All (1 to 56)	56	0.000234100663285213	163.580	8%	-8%
Odd modes	28	0.000339814989616764	163.580	8%	-8%
Even modes	28	0.000344036697247706	162.037	32%	-7%
Positive modes	28	0.000399822301199467	160.494	36%	-6%
Positive Modes_Odds	15	0.000612873333333333	157.407	66%	-4%

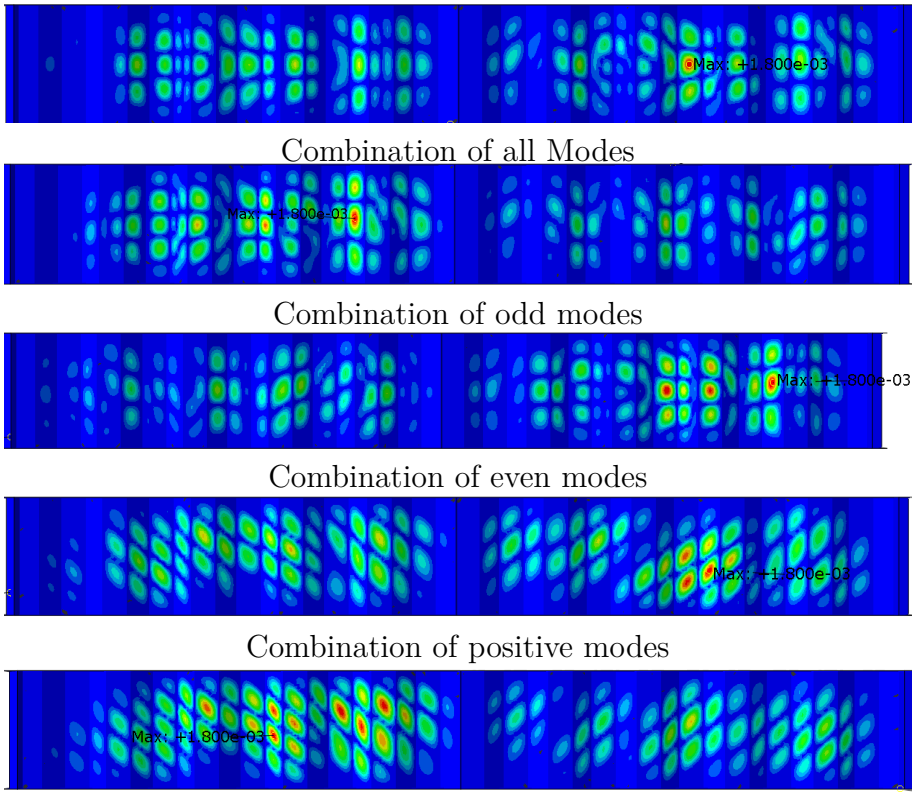

Figure 5.45: Mode combination of girder S2; Modes (1 to 56) Imperfection (hw/200)

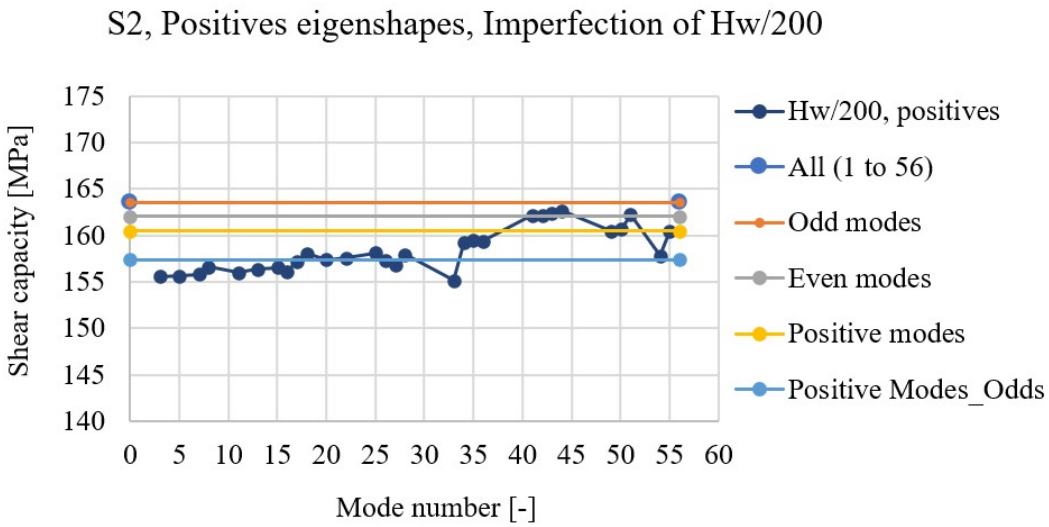

Figure 5.44: Shear capacity of different single modes and different mode combinations, S2, Hw/200

Shear capacity for the different mode combination with initial imperfection amplitude of Hw/300 are presented in table 5.12 and figure 5.46. Mode combination shapes have same amplitude and are presented in figure 5.47.

Table 5.12: Shear capacity for different mode combination, S2, Imperfection of Hw/300, Range (first mode to 1.2 first mode)

S2, Hw/300					
Mode combination	**No. modes**	**Scale factor**	**Shear capacity (MPa)**	**Number of modes that give higher capacity**	**Max decrease in capacity from single modes**
All (1 to 56)	56	0.000156067108856808	165.1235	14%	-12%
Odd modes	28	0.000226543326411176	166.6667	0%	-12%
Even modes	28	0.000229357798165138	165.1235	14%	-12%
Positive modes	28	0.000266548200799645	163.5802	52%	-11%
Positive Modes_Odds	15	0.000408580183861083	162.0370	64%	-10%

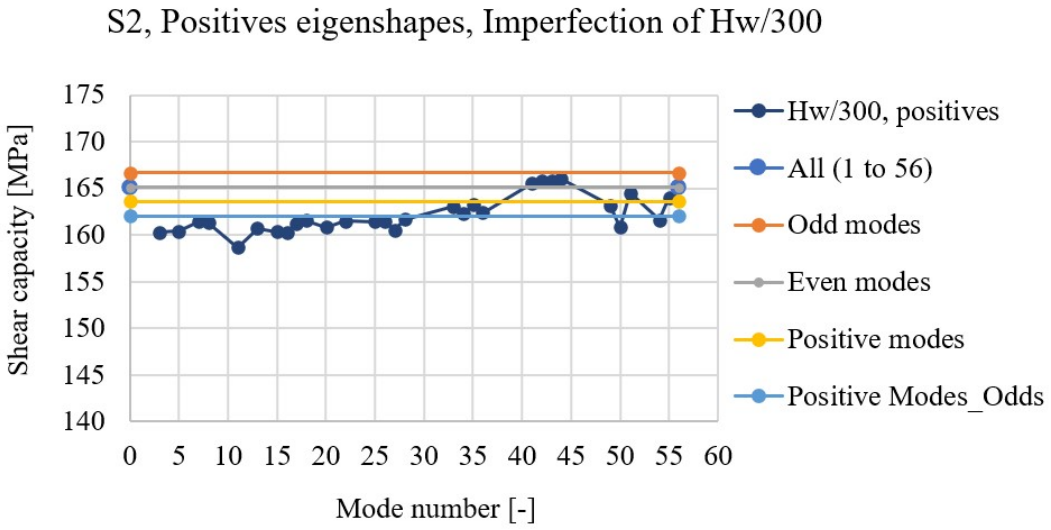

Figure 5.46: Shear capacity of different single modes and different mode combinations, S2, Hw/300

The results show that all mode combinations give close values (between 157MPa and 164 MPa). For the initial imperfection amplitude of hw/200, the combination of the positive-odd modes gives the lowest shear capacity with a value of 157.4 MPa. This gives shear capacity less than 66% of single modes in the studied range. The same combination gives the lowest capacity with an imperfection amplitude of hw/300 with a value of 162 MPa. However, this mode still gives a higher capacity than the lowest single mode.

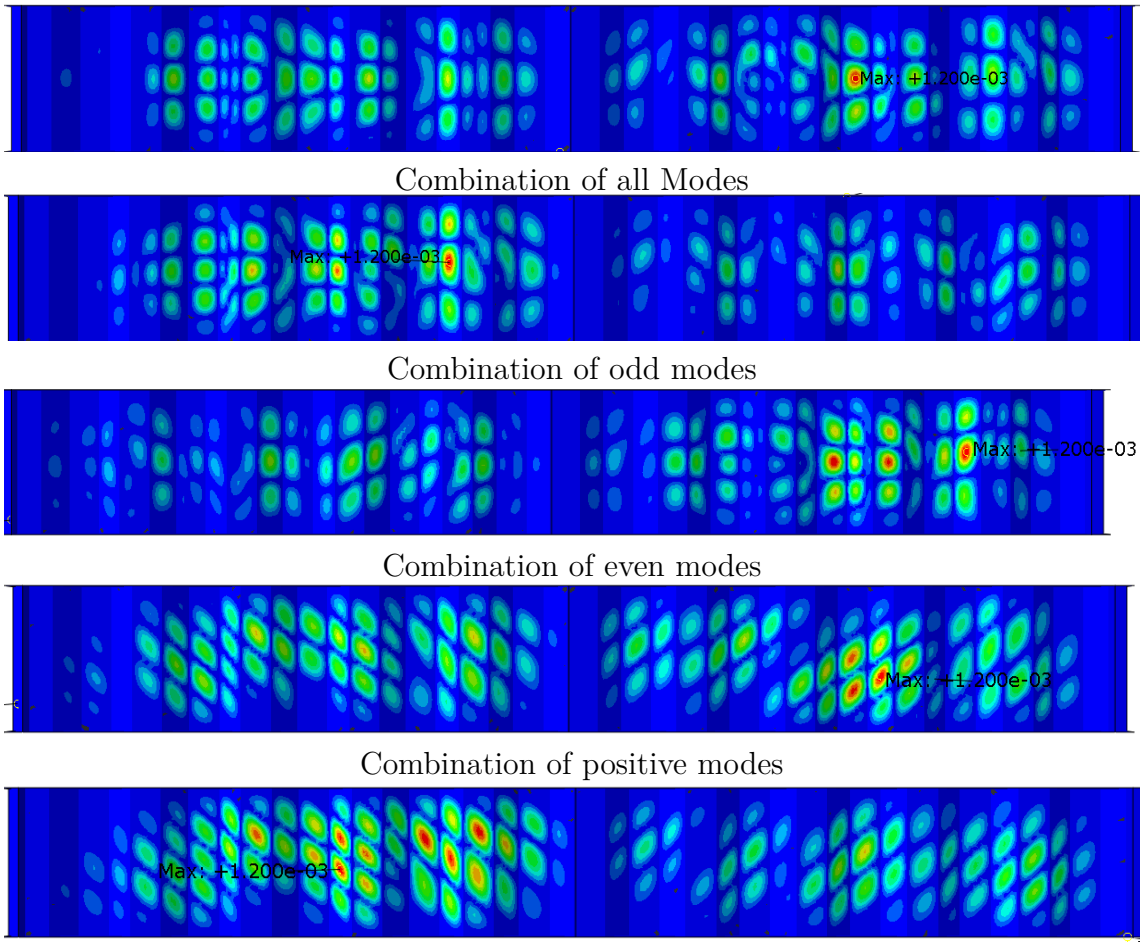

Figure 5.47: Mode combination of girder S2; Modes (1 to 56) Imperfection (hw/300)

5.5.3 Matsnoki girder

For Matsnoki girder, 42 single modes in the range of first mode to 1.2*first mode are taken into account. Table 5.13 and figure 5.48 show the shear capacity for various mode combinations with an initial imperfection amplitude of Hw/200. The amplitude of the mode combination shapes is the same, as seen in figure 5.49.

Inelastic buckling, Matsnoki, Hw/200, Range (first mode to 1.2 first mode)					
Mode combination	**No. modes**	**Scale factor**	**Shear capacity (MPa)**	**Number of modes that give higher capacity**	**Max decrease in capacity from single modes**
All (1 to 42)	42	0.00108333333333333	276.47	26%	-24%
Odd modes	21	0.00149405083829097	277.38	26%	-24%
Even modes	21	0.00190254820936639	247.059	46%	-15%
Positive modes	22	0.00261662325361118	238.46	58%	-12%
Positive Modes_Odds	11	0.00356451612903226	242.53	50%	-14%

Table 5.13: Shear capacity for different mode combination, Matsnoki, inelastic buckling, Imperfection of Hw/200, Range (first mode to 1.2 first mode)

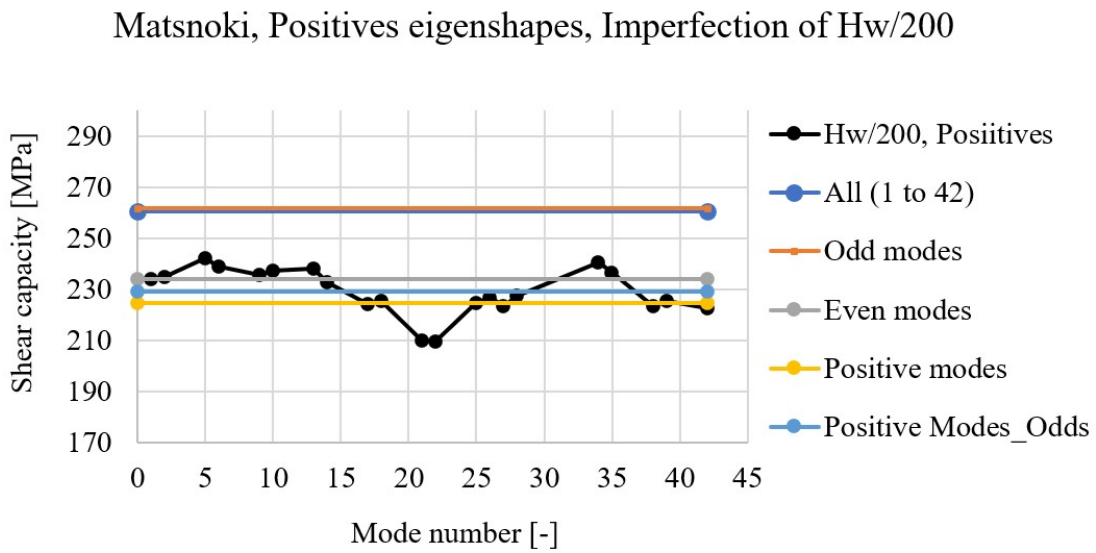

Figure 5.48: Shear capacity of different single modes and different mode combinations, inelastic buckling, Matsnoki, Hw/200

It can be observed that for the initial imperfection amplitude of hw/200, the combination of the positive modes gives the lowest shear capacity with a value of 238.46 MPa. This gives shear capacity less than 58% of single modes in the studied range. However, this capacity is still higher than the lowest capacity with mode 22, around 209 MPa.

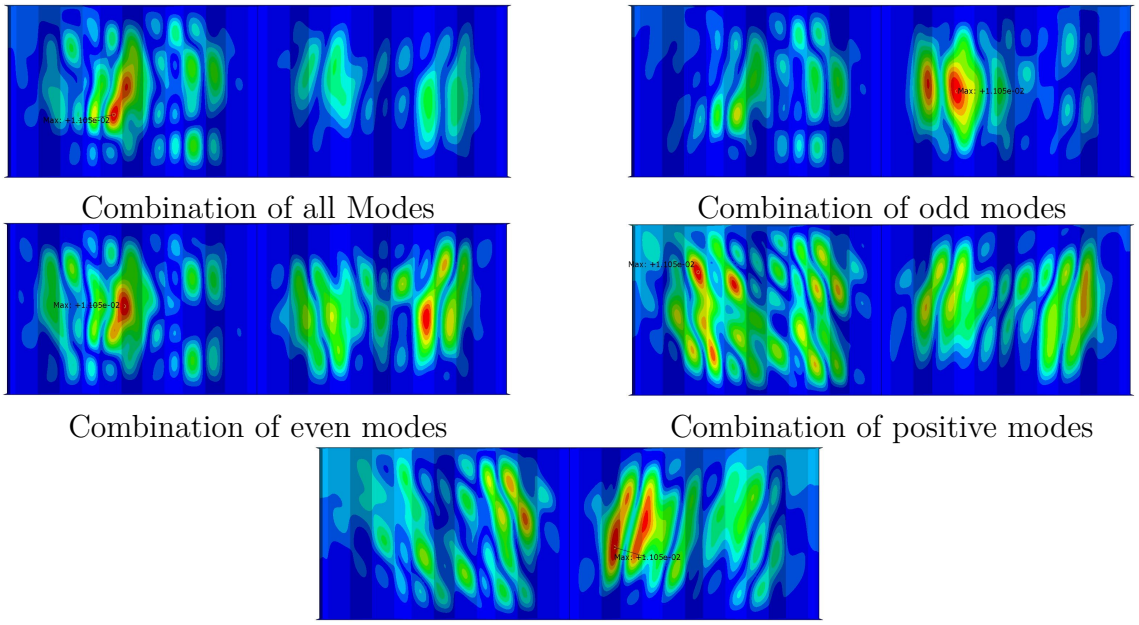

Combination of all Modes

Combination of odd modes

Combination of even modes

Combination of positive modes

Combination of positive odd modes

Figure 5.49: Mode combination of girder Matsnoki; Modes (1 to 42) Imperfection (hw/200)

5.6 Discussion

In both elastic and inelastic buckling, the combinations give lower capacity than a considerable number of single modes. However, there is no specific combination that is always critical. For instance, in elastic buckling, the combination of the odd modes gives a lower capacity than 96% of single modes, and positive modes combination gives lower capacity than 92% of single modes. On the other hand, in the case of inelastic buckling, the combination of the positive modes gives lower capacity than 58% of single modes. The combination of the positive-odds modes gives a lower capacity than 50% of single modes.

The most critical combination varies depending on the case and the amplitude of the initial imperfection, and single modes always have a lower capacity than the combination. In conclusion, no single mode combination has a lower capacity than all others and can be used as the most critical initial imperfection shape.

The shear behavior of bridge girders with the corrugated web is sensitive to initial imperfection, and the first positive mode is not always the most critical. The decrease in shear capacity between the first mode and the lowest mode in the studied range is considerable. For example, referring to table 5.14, for girder M12 and imperfection amplitude equal to hw/200, the capacity decreases by 15% between the first mode and mode 29.

M12		
Capacity, Mode 1 [MPa]	**Capacity, Mode 29 [MPa]**	**Diffrence**
92.98	78.99	15%
S2		
Capacity, Mode 1 [MPa]	**Capacity, Mode 33 [MPa]**	**Diffrence**
161.2	155.13	3.8%
Matsnoki		
Capacity, Mode 1 [MPa]	**Capacity, Mode 22 [MPa]**	**Diffrence**
233.83	209.59	10.4%

Table 5.14: Comparison between shear capacity from first mode and the most critical mode shapes

6
Parametric study

This study aims to see how several varying parameters affect shear capacity. A limited parametric study has been conducted. Five different parameters are considered, web height (hw), web thickness (tw), corrugation angle (alpha), beta ratio ($\beta = b/c$) and shear span (a). All parameters are illustrated in figure 6.1

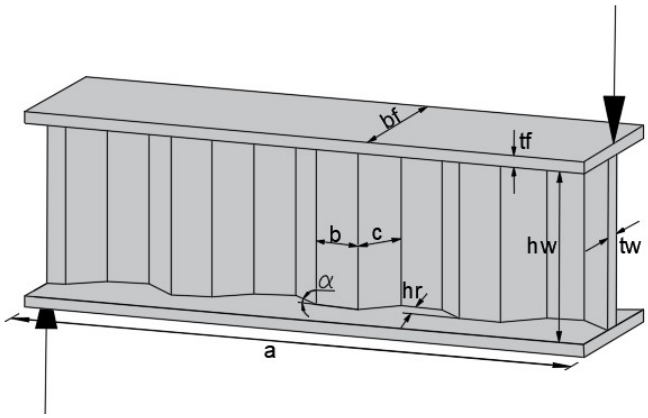

Figure 6.1: Notations of trapezoidal corrugated web girders

Due to the sensitivity of the corrugated web to the initial imperfection shape, each girder is studied with all eigenshapes that are located in range (first mode to 1.2*first mode). One-factor-at-time is used here due to the large number of analysis needed for each girder to assess the lowest shear capacity.

The Imperfection magnitude has been studied in the previous chapter and will be considered as hw/200 in this chapter. Yield strength, elastic modulus, and Poisson ratio change with the material and are also fixed in this study to the Duplex 1.4162 material.

6.1 Web height effect [hw]

To study the effect of web height on the shear capacity of stainless steel girders with corrugated web, FE-simulation for three different web heights with the same corrugation configurations and shear span has been performed. Figure 6.2 shows the shear capacity variation for the three girders with different buckling eigenshapes as initial imperfection shape and hw/200 as initial imperfection amplitude. Only

positive eigenshapes in the studied range were taken into account because they result in lower capacity, as mentioned in the previous chapter. The shear capacity for each girder is estimated to be the lowest capacity from the studied eigenshapes as imperfection, and the load-displacement curve has been presented for each case in figure 6.3.

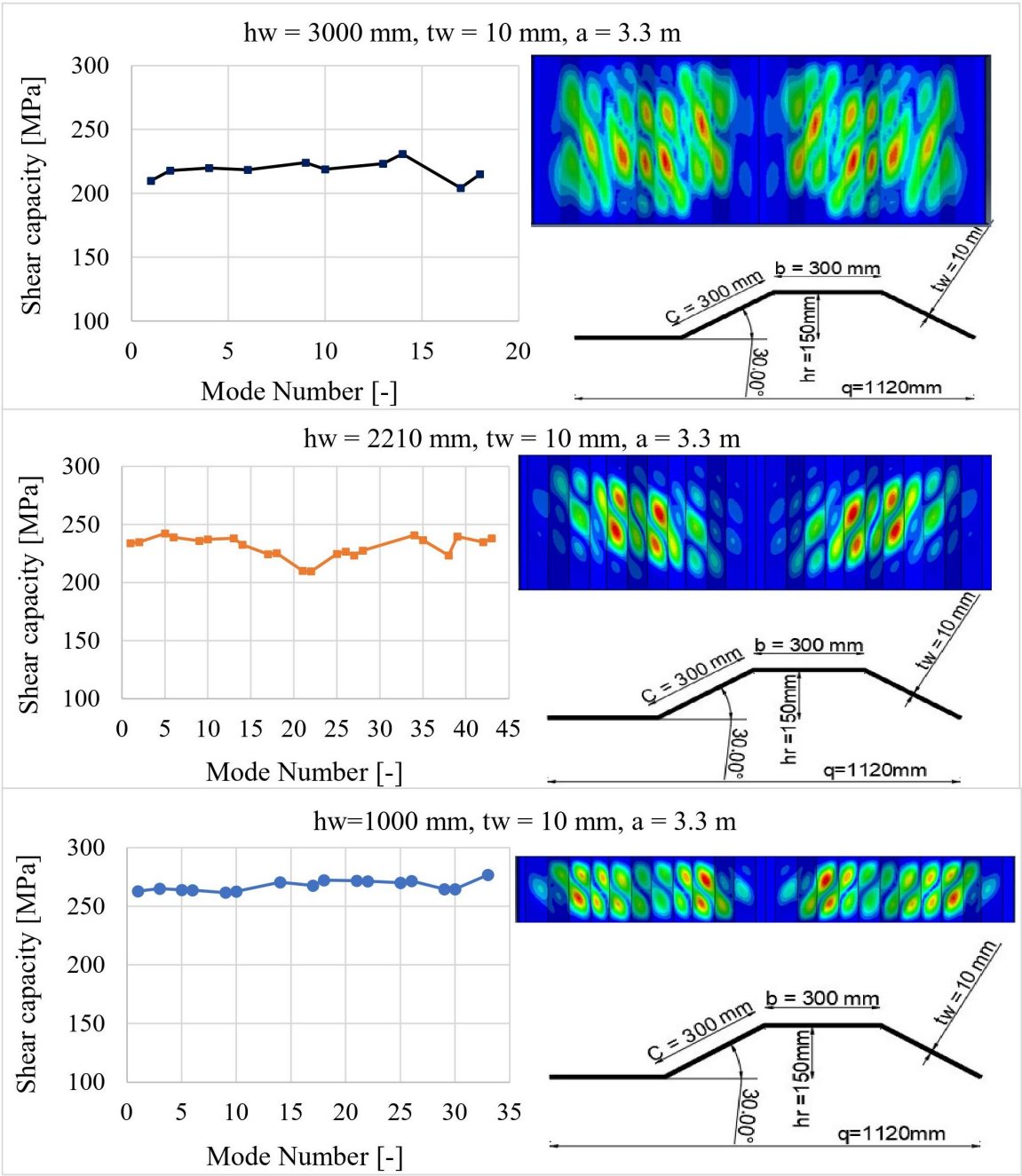

Figure 6.2: Shear capacity variation with web height and initial imperfection shape

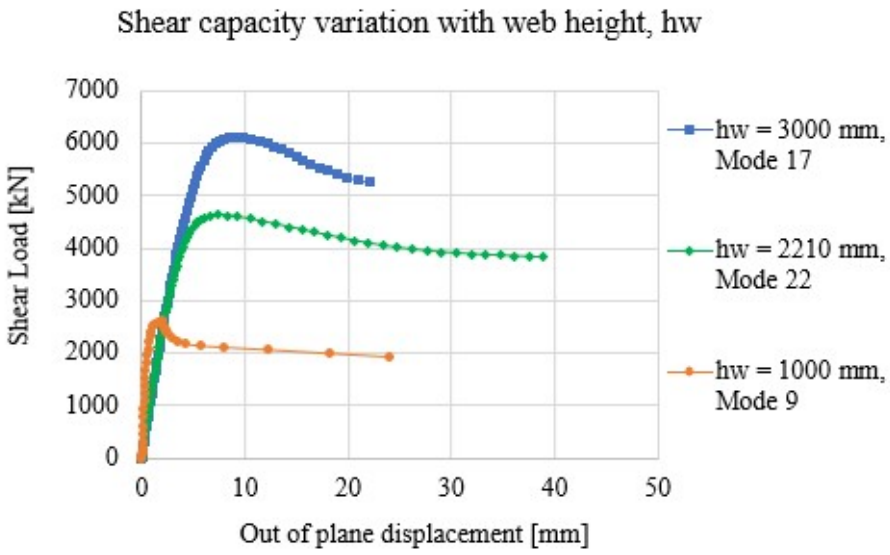

Figure 6.3: Shear capacity variation with web height, hw

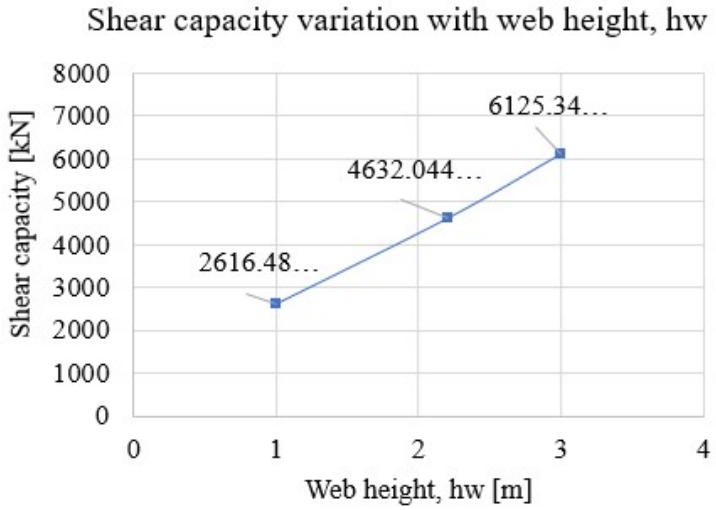

Figure 6.4: Ultimate shear capacity for different web heights

It can be observed from figure 6.3 and figure 6.4 that the shear capacity increase significantly with increasing web height. However, this increase is nonlinear since increasing web height will increase the slenderness and increase the shear resistance area at the same time. These two factors have the opposite effect on the girder shear capacity. Also, the buckling mode tends to change from global to interactive to local with decreasing the web height.

6.2 Web thickness effect [tw]

Three FE-simulations are conducted for three web thicknesses of the same corrugation geometry and shear span length to evaluate the effect of web thickness on

the ultimate shear capacity of corrugated stainless steel girders. Figure 6.5 shows the shear capacity variation for the three girders with different buckling eigenshapes as initial imperfection shape and hw/200 as initial imperfection amplitude. Only positive eigenshapes in the studied range were taken into account because they result in lower capacity, as mentioned in the previous chapter. The shear capacity for each girder is estimated to be the lowest capacity from the studied eigenshapes as imperfection, and the load-displacement curve has been presented for each case in figure 6.6.

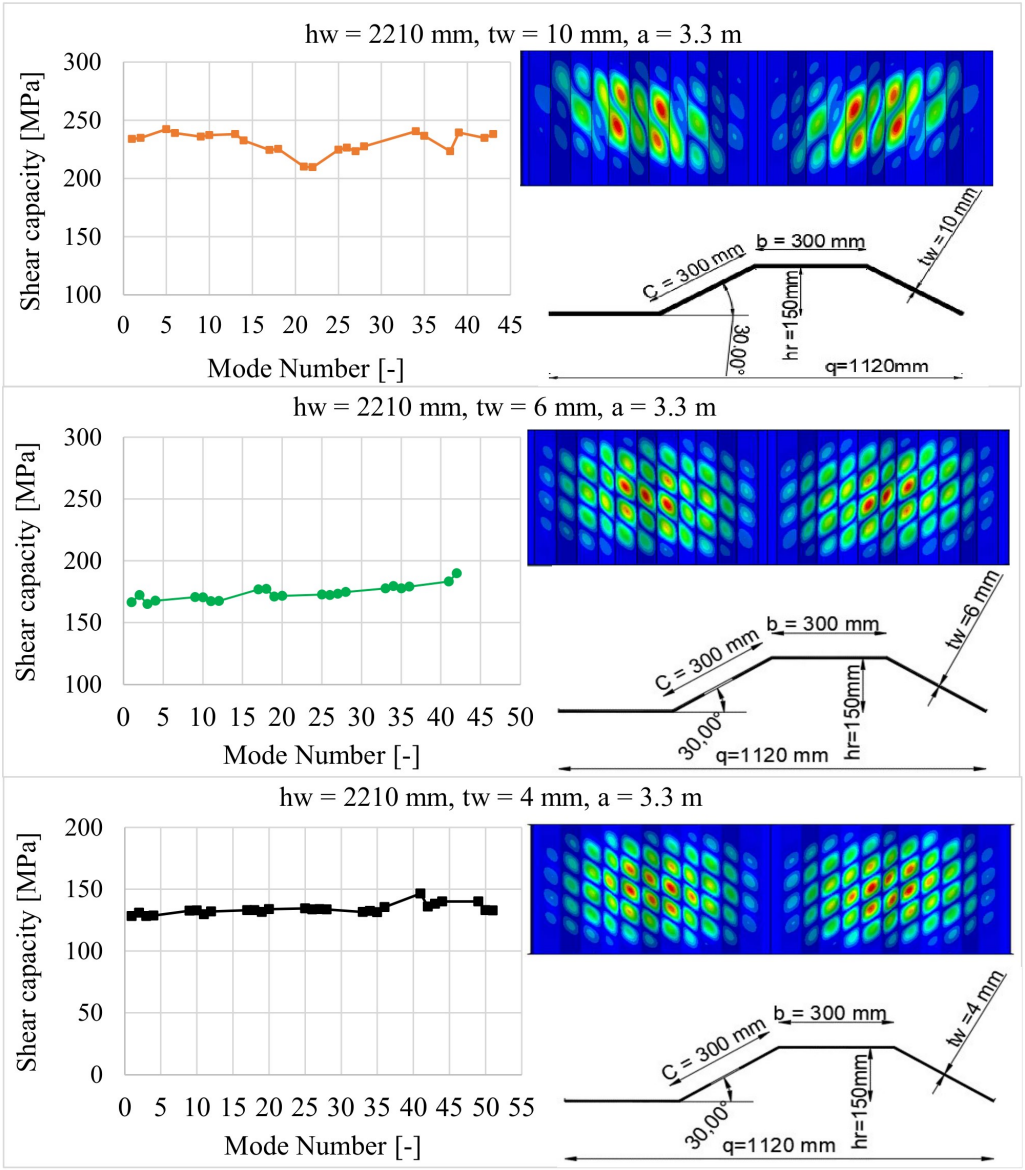

Figure 6.5: Shear capacity variation with web thickness and initial imperfection shape

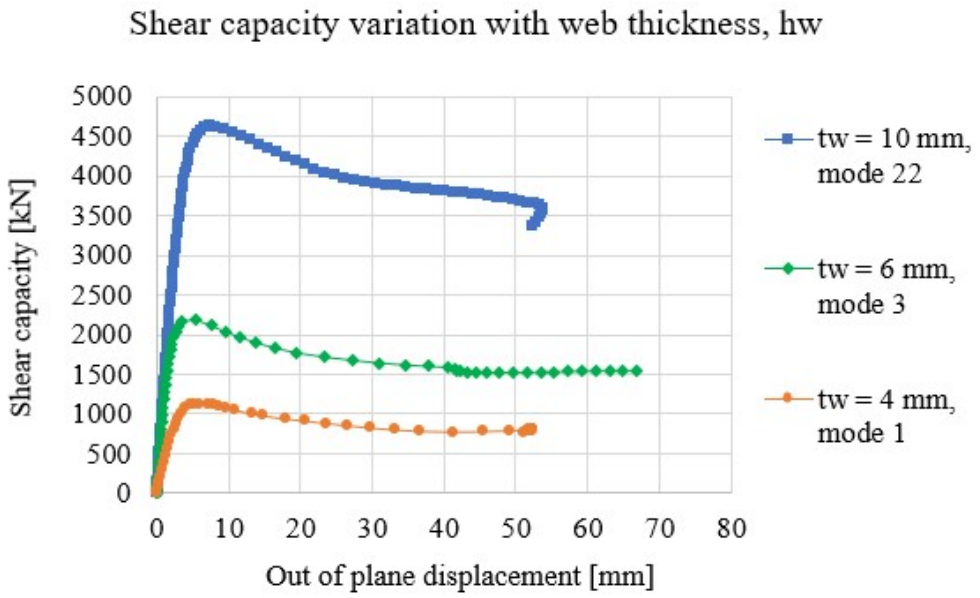

Figure 6.6: Shear capacity variation with web thickness, hw

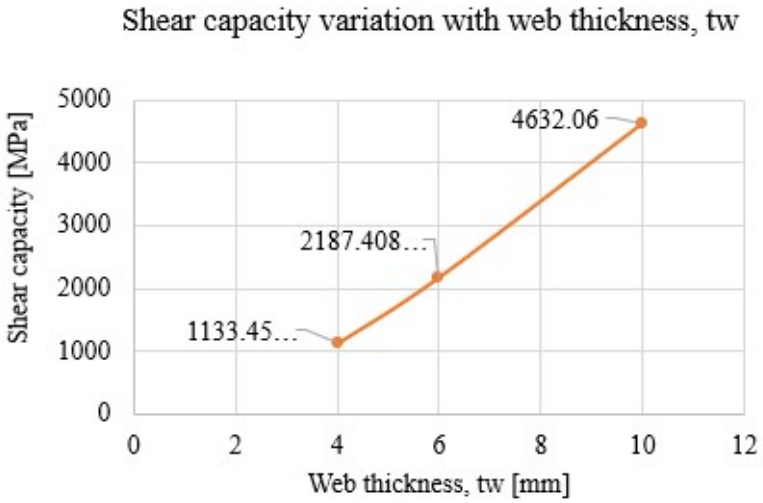

Figure 6.7: Ultimate shear capacity for different web thicknesses

It can be observed from figure 6.6 and figure 6.7 that the shear capacity increase significantly with increasing web thickness. Here, the nonlinear increase is more significant since increasing web thickness will decrease the slenderness and increase the shear resistance area at the same time. These two factors have the same effect on the girder shear capacity. Also, the buckling mode tends to change from global to interactive to local with decreasing the web thickness.

6.3 Beta ratio effect [β] or [b/c]

Three FE-simulations for three beta ratios with the same web height, thickness, and shear span are conducted to investigate the ratio between the flat fold and the

inclined fold, beta ratio, on the ultimate shear capacity of corrugated stainless steel girders. Figure 6.8 shows the shear capacity variation for the three girders with different buckling eigenshapes as initial imperfection shape and hw/200 as initial imperfection amplitude. Only positive eigenshapes in the studied range were taken into account because they result in lower capacity, as mentioned in the previous chapter. The shear capacity for each girder is estimated to be the lowest capacity from the studied eigenshapes as imperfection, and the load-displacement curve has been presented for each case in figure 6.9.

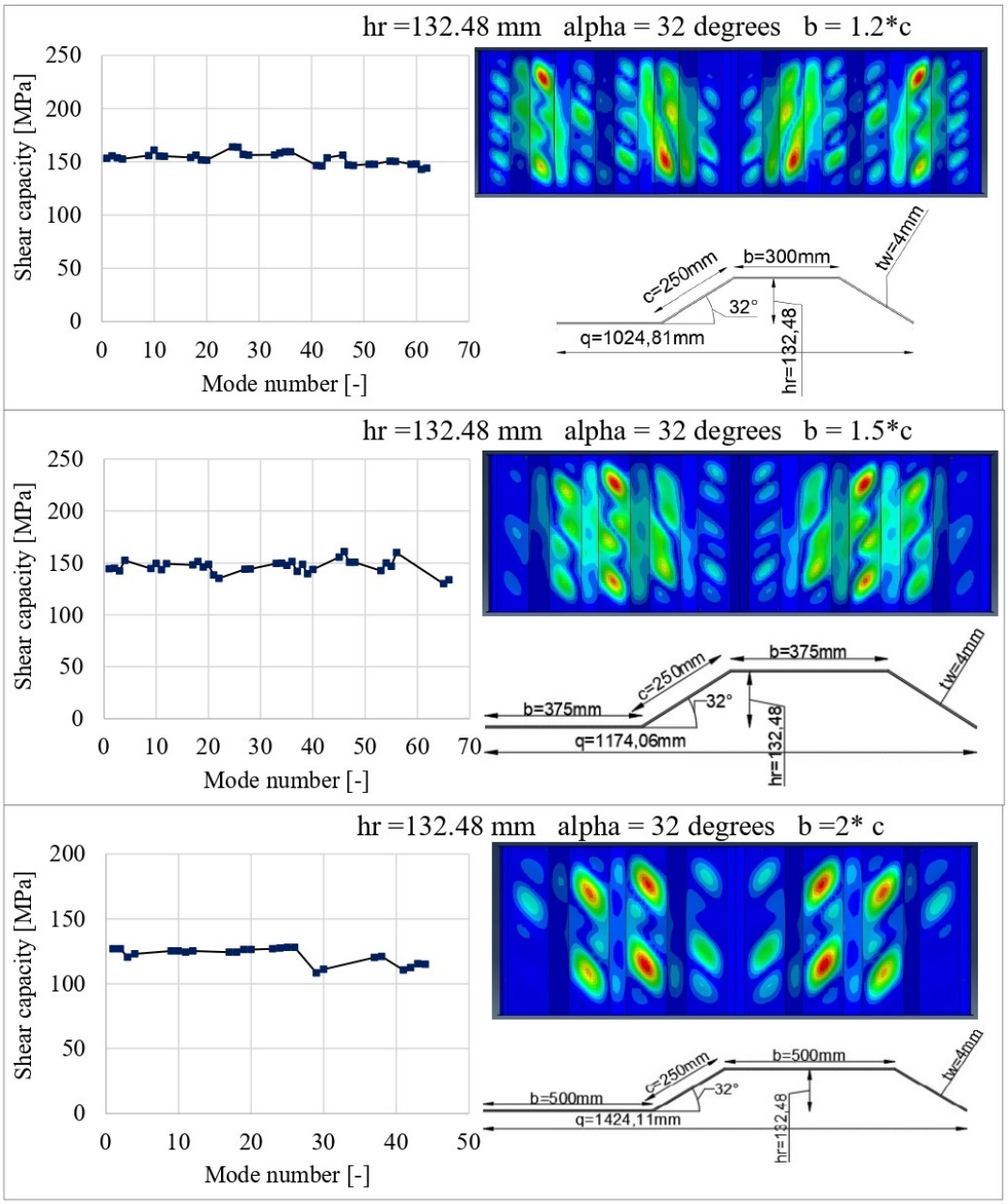

Figure 6.8: Shear capacity variation with beta ratio and initial imperfection shape

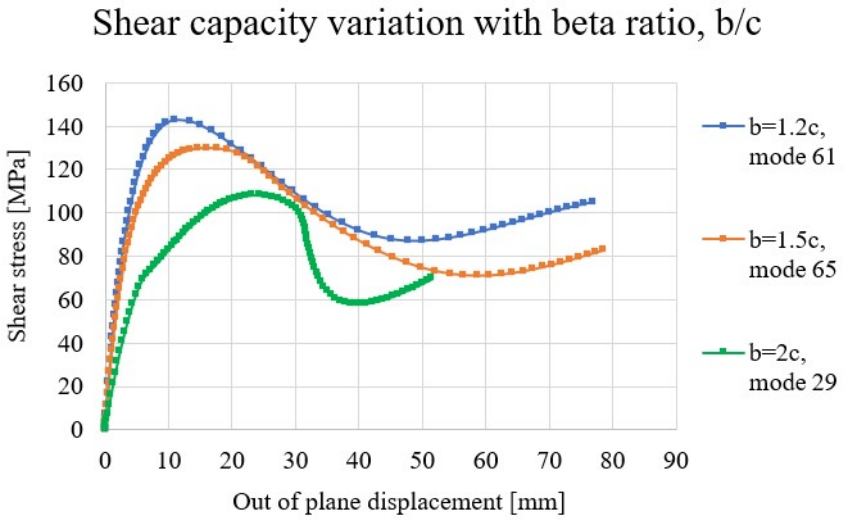

Figure 6.9: Shear capacity variation with beta ratio, β

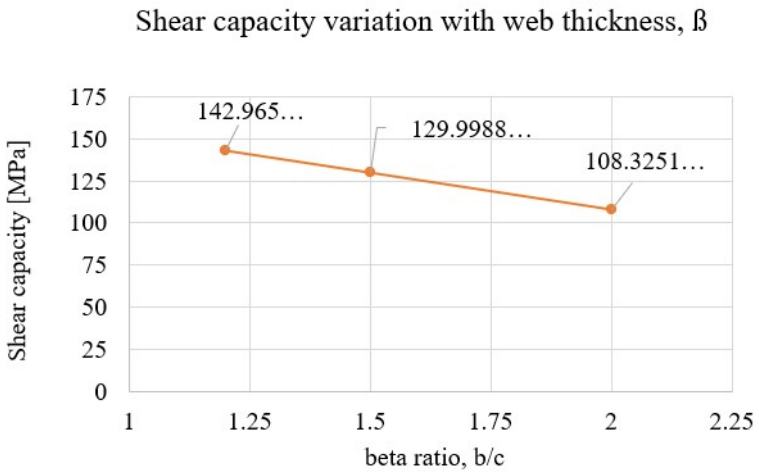

Figure 6.10: Ultimate shear capacity for different beta ratios

It can be observed from figure 6.9 and figure 6.10 that the shear capacity decreases with increasing ratio b/c. For instance, the shear capacity decreases from [142.965 MPa] to [130 MPa], around 9%, by increasing beta ratio from [1.2 to 1.5, 25%]. In addition, the buckling mode tends to change from global to interactive to local with an increasing beta ratio.

6.4 Corrugation angle [α], and corrugation depth [hr] effect

To investigate the effect of corrugation angle, alpha, of corrugated stainless steel beam on the ultimate shear capacity, three FE-simulation is performed for three corrugation angles with the same web height, thickness, and same shear span. Figure 6.11 shows the shear capacity variation for the three girders with different buck-

ling eigenshapes as initial imperfection shape and hw/200 as initial imperfection amplitude. Only positive eigenshapes in the studied range were taken into account because they result in lower capacity, as mentioned in the previous chapter. The shear capacity for each girder is estimated to be the lowest capacity from the studied eigenshapes as imperfection, and the load-displacement curve has been presented for each case in figure 6.12.

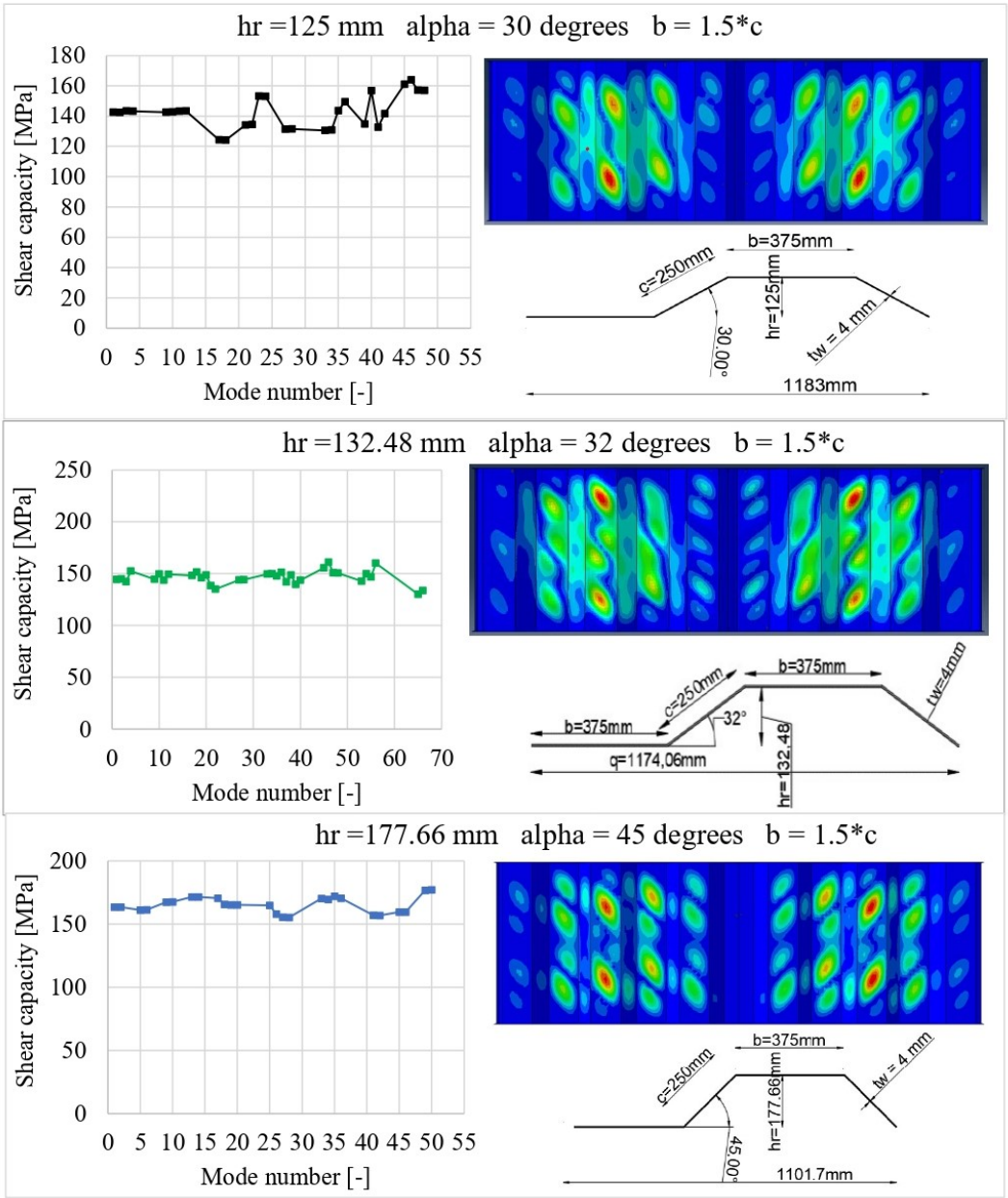

Figure 6.11: Shear capacity variation with alpha and initial imperfection shape

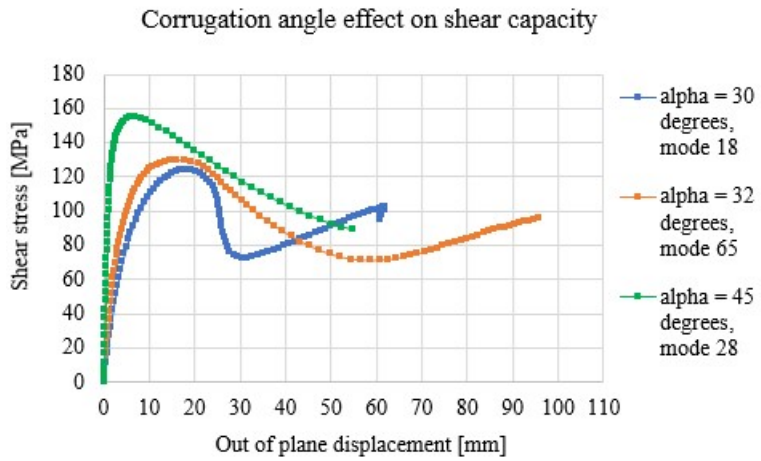

Figure 6.12: Shear capacity variation with alpha, α

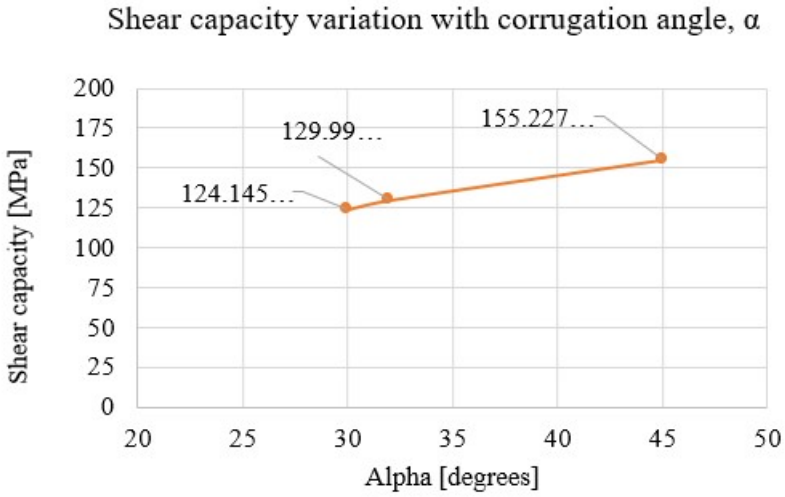

Figure 6.13: Ultimate shear capacity for different corrugation angles

Referring to figure 6.12 and figure 6.13, the shear capacity increases with increasing corrugation angle. For instance, the shear capacity increases from [124.145 MPa] to [155.23 MPa], around 24%, by increasing corrugation angle from [30 to 45, 50%]. In addition, the buckling mode tends to change from global to interactive to local with increasing corrugation angle.

6.5 Shear span effect [a]

Previous research has revealed that shear span doesn't affect the shear strength of steel beams and girders with corrugated webs [16]. A new investigation has been carried out to examine the validity of girders with stainless steel corrugated webs. FE-simulation is performed for three girders with different shear span and the same corrugation geometry, web height, and thickness. The shear capacity variation for the three girders with different buckling eigenshapes as initial imperfection shape

and hw/200 as initial imperfection amplitude is shown in Figure 6.14.

Only positive eigenshapes in the studied range were taken into account because they result in lower capacity, as stated in the previous chapter. Figure 6.15 represents the shear capacity for each girder estimated to be the lowest capacity from the studied eigenshapes as imperfection and load-displacement curve.

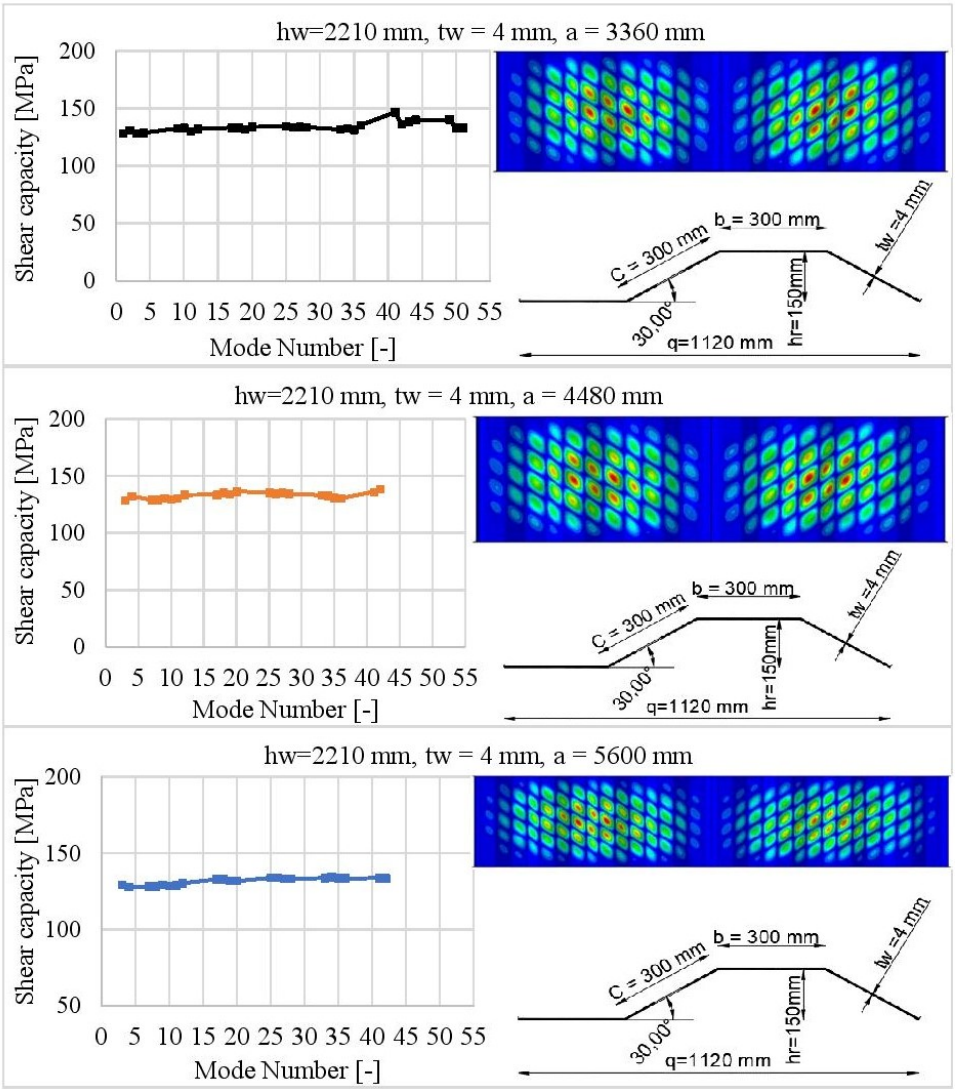

Figure 6.14: Shear capacity variation with shear span and initial imperfection shape

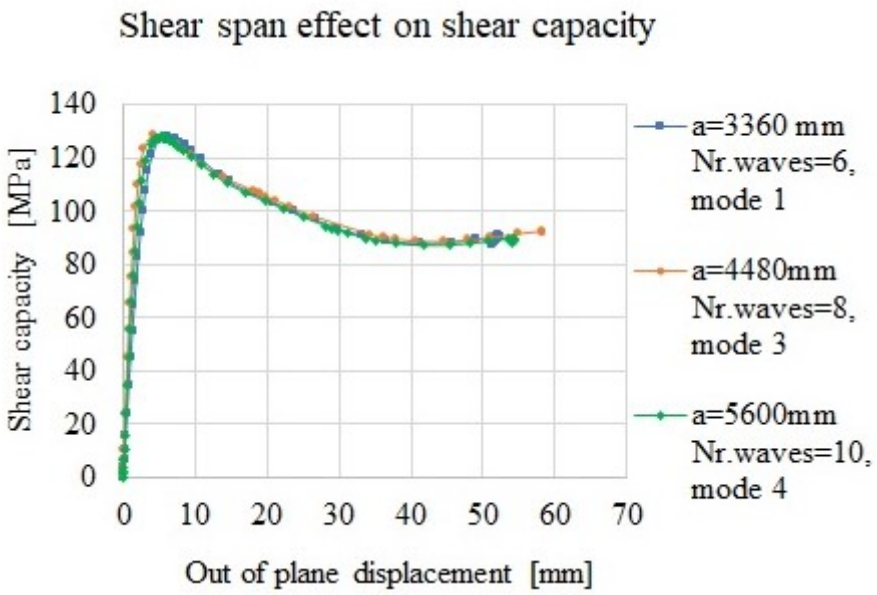

Figure 6.15: Shear capacity variation with shear span, **a**

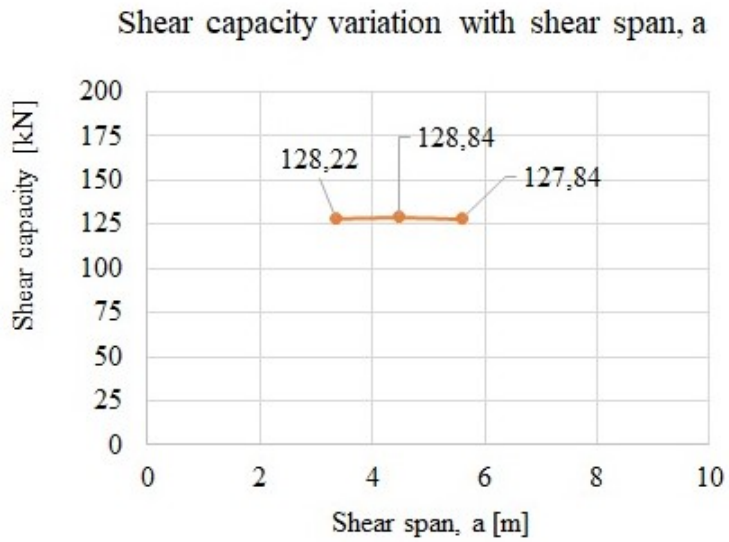

Figure 6.16: Ultimate shear capacity for different shear spans

From figure 6.15 and figure 6.16 it can be concluded that the shear span has a low or negligible effect on the ultimate shear capacity of stainless steel beams. The difference between these three specimens does not exceed 1 %.

According to FEM simulations for the tested example, there is no change in the shear buckling mode of these girders when the shear span changes.

6.6 Comparison of shear capacity from FE-simulation and Eurocode design curve

Eurocode only considers local and global buckling modes, not interactive buckling modes. For this reason, the interactive, local and global buckling modes are presented together on the design curve of Eurocode, see figure 6.17 for shear capacity results from the first mode as initial imperfection shape and imperfection amplitude of Hw/200 and figure 6.18 for shear capacity results from most critical mode as initial imperfection shape and imperfection amplitude of Hw/200. Furthermore, Eurocode assumes a corrugation angle greater than 30 degrees, so all of the girders studied previously and have a corrugation angle greater than 30 degrees are shown on the Eurocode design curve in figures 6.17 and 6.18

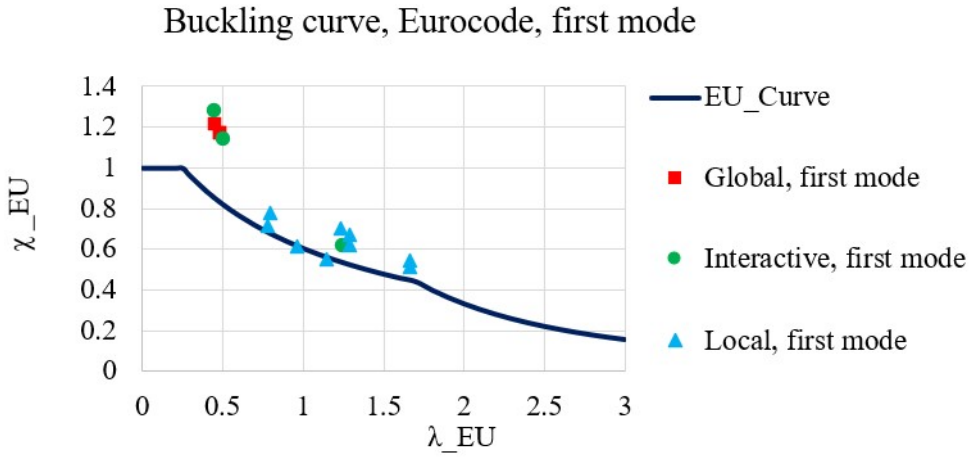

Figure 6.17: Shear capacities of studied girders, first positive buckling mode, on Eurocode design curve

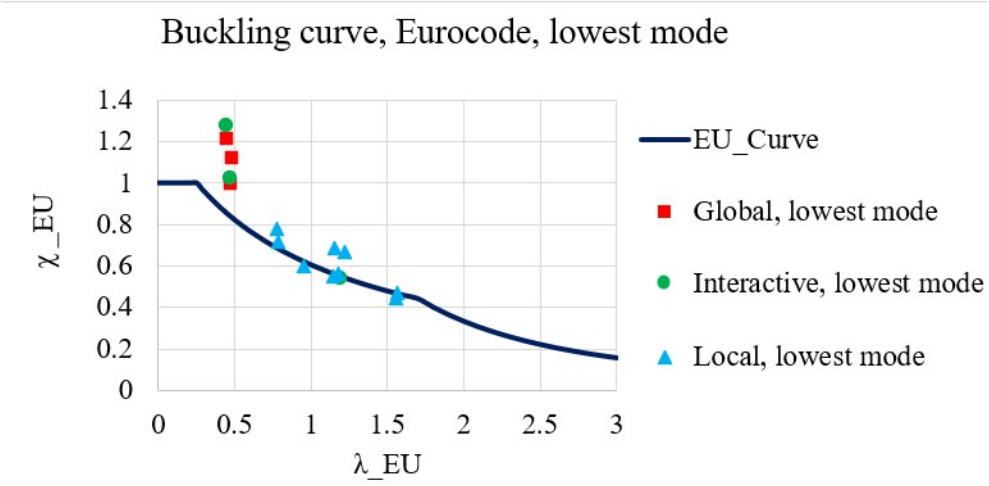

Figure 6.18: Shear capacities of studied girders, most critical positive buckling mode, on Eurocode design curve

The figures 6.17 and 6.18 show that all shear capacities for both first buckling mode and lowest buckling mode are located on or above the Eurocode design curve. In conclusion, using the Eurocode design curve with imperfection amplitude of Hw/200 and first positive eigen buckling shape can be considered as a safe estimation of the shear capacity of stainless steel bridge girders with corrugated webs.

7
Conclusion

Corrugated webs have been widely used in many countries around the world. The use of corrugated webs in bridge girders has been seen as useful in engineering, introducing the new stainless-steel material both possible and reliable.

This master thesis aims to evaluate the shear behavior of stainless steel bridge girders with corrugated webs and define the most critical parameters that influence shear behavior. Furthermore, to assess the sensitivity of stainless steel bridge girders with corrugated webs to inevitable initial imperfections. For this purpose, the ABAQUS program is used to perform nonlinear FE-analysis that includes both material and geometric nonlinearities.

The case studies used for the validation part were two different tested girders existing in literature, one of high-performance steel (G7A) tested by Driver et al. [11] and the other of normal strength steel (M12) tested by Moon et al. [17]. The ultimate load from the FEM simulation for both specimens is in good agreement with the experiment data. The same girders have been modeled using stainless steel material, Duplex 1.4162, and the shear behavior is compared. The results show that the shear capacity increases by 9% for girder G7A of high-performance steel and Duplex 1.4162. Also, the increase in the capacity in normal strength steel is much higher, around 43%.

The sensitivity of the corrugated webs' shear capacity to initial imperfection had been tested on stainless steel (Duplex 1.4162) on three different girders under different behavior, M12, and S2, where the ultimate shear strength is close or smaller than the shear yield strength and Matsnoki where the ultimate shear strength is higher than the shear yield strength. Each girder was studied using a standard of four different amplitudes: Hw/100, Hw/200, Hw/300, and Hw/400. The Eigen buckling shapes are used as initial imperfection shapes. Then, as other shapes for initial imperfection, five different combinations of these buckling modes were considered. From the findings, the following conclusions can be drawn:

1- The shear behavior of bridge girders with the corrugated web is sensitive to initial imperfection shape and amplitude, and the first positive mode is not always the most critical. The decrease in shear capacity between the first and lowest modes in the studied range is considerable.

2- Positive buckling modes give lower shear capacity than negative buckling modes.

So, the positive buckling modes are more crucial, and negative buckling modes can be disregarded.

3- In both elastic and inelastic buckling, the combinations give lower capacity than a considerable number of single modes. However, there is no specific combination that gives a smaller capacity than all single modes.

A limited parametric study then conducted with imperfection amplitude suggested by Eurocode (Hw/200) and all eigenshapes in the range of (first mode to 1.2*first mode) have been considered to assess the lowest shear capacity.

According to previous studies, five-dimensional parameters are the most influencing the shear behavior of carbon steel girders. The same parameters have been conducted on girders of stainless steel, and it has been concluded that web height, web thickness, and corrugation depth significantly increase the shear capacity. The ratio between flat fold length to inclined length decreases the shear capacity. However, the shear span has a negligible effect.

Finally, the shear capacity of all studied girders was compared to that provided by Eurocode, and it is concluded that using Eurocode design curve with the first positive buckling mode shape and initial imperfection of Hw/200 is safe, even though the first mode isn't the lowest conservative mode.

8

Suggestions for further research

The sensitivity of stainless steel bridge girders with corrugated webs is investigated in this report. It is demonstrated that the first positive eigen buckling shape as initial imperfection is not the most crucial shape for the girder's shear capacity. Furthermore, the studied range is restricted, and a more critical mode shape probably exists beyond it. On the other hand, the initial imperfection could be of any shape, and the shear capacity should be determined based on the worst shape, which is currently uncertain. In addition, to evaluate the worst mode shape, a nonlinear analysis for every mode shape needs to be conducted. So, a recommendation for future research is to investigate single modes across a broader range and try to detect a way to predict the worst buckling shape from linear buckling analysis.

Furthermore, the parametric study conducted in this study is restricted since it only considers one factor at a time. A more comprehensive parametric study that evaluates the interactions between the parameters is essential to validate the findings.

Moreover, one grade of stainless steel material has been studied. Further study needs to be performed on the other material grades.

Flange thickness and width are used to generate fixed boundary conditions. However, these variables may have a significant impact on the girder's shear behavior. Consequently, various boundary conditions should be examined before determining the ultimate shear capacity.

9

References

Bibliography

Bibliography

[1] Case Helix Bridge | Outokumpu.

[2] Outokumpu webinar series for bridge professionals.

[3] Samverkanskonstruktioner stål - betong.

[4] Soderstrom railway bridge | Outokumpu.

[5] Stainless Steel Design Innovation.

[6] Fort York bridge in Toronto, first of its kind in Canada made of UR™ 2205 Duplex stainless steel from Industeel., July 2019.

[7] Hassan H. Abbas, Richard Sause, and Robert G. Driver. Behavior of Corrugated Web I-Girders under In-Plane Loads. *Journal of Engineering Mechanics*, 132(8):806–814, August 2006.

[8] CEN. Eurocode 3: Design of steel structures - Part 1-5: Plated structural elements, upcoming draft, November 2019.

[9] Tian Chen. On Introducing Imperfection in the Non-Linear Analysis of Buckling of Thin Shell Structures. page 163.

[10] Harold M. Cobb. *History of Stainless Steel*. A S M International, Materials Park, UNITED STATES, 2010.

[11] Robert G. Driver, Hassan H. Abbas, and Richard Sause. Shear behavior of corrugated web bridge girders. *Journal of Structural Engineering*, 132(2):195–203, 2006.

[12] Robert G. Driver, Hassan H. Abbas, and Richard Sause. Shear behavior of corrugated web bridge girders. *Journal of Structural Engineering*, 132(2):195–203, 2006.

[13] Leblouba et.al. Normalized shear strength of trapezoidal corrugated steel webs. *Journal of Constructional Steel Research*, (136), 2017.

[14] Leblouba et.al. Shear buckling and stress distribution in trapezoidal web corrugated steel beams. *Thin–Walled Structures*, 113, 2017.

[15] Leblouba et.al. Shear behavior of corrugated web panels and sensitivity analysis. *Journal of Constructional Steel Research*, 151, 2018.

[16] Leblouba et.al. Normalized shear strength of trapezoidal corrugated steel webs: Improved modeling and uncertainty propagation. *Thin-Walled Structures*, 137, 2019.

[17] Moon et.al. Shear strength and design of trapezoidally corrugated steel webs. *Journal of Constructional Steel Research*, 65:1198–1205, 2009.

[18] Nie et.al. Shear strength of trapezoidal corrugated steel webs. *Journal of Constructional Steel Research*, 85, 2013.

[19] Yi et.al. Interactive shear buckling behavior of trapezoidally corrugated steel webs. *Engineering Structures*, 30, 2008.

[20] Zhang et.al. Shear behaviour of girders with trapezoidal corrugated steel webs – an experimental study. *Stahlbau*, 87, 2018.

[21] S. Farzanian, A. Louhghalam, B. W. Schafer, and M. Tootkaboni. Geometric imperfection models for CFS structural members, Part I: Comparative review of current models. 2019.

[22] Shafee Farzanian, Arghavan Louhghalam, Benjamin W Schafer, and Mazdak Tootkaboni. Geometric Imperfections in Shell Finite Element Models of CFS Members - A Review of Current State of Practice. In *Proceedings of the Annual Stability Conference*, page 18, Baltimore, Maryland, USA, 2018. Structural Stability Research Council.

[23] M. F. Hassanein and O. F. Kharoob. Behavior of bridge girders with corrugated webs: (II) Shear strength and design. *Engineering Structures*, 57:544–553, December 2013.

[24] M.F. Hassanein, A.A. Elkawas, A.M. El Hadidy, and Mohamed Elchalakani. Shear analysis and design of high-strength steel corrugated web girders for bridge design. *Engineering Structures*, 146:18–33, September 2017.

[25] M.F. Hassanein and O.F. Kharoob. Behavior of bridge girders with corrugated webs: (I) Real boundary condition at the juncture of the web and flanges. *Engineering Structures*, 57:554–564, December 2013.

[26] D Kollár and B Kövesdi. Effect of Imperfections and Residual Stresses on the Shear Buckling Strength of Corrugated Web Girders. page 20.

[27] D. Kollár and B. Kövesdi. Welding simulation of corrugated web girders - Part 2: Effect of manufacturing on shear buckling resistance. *Thin-Walled Structures*, 141, 2019.

[28] D. Kollár and B. Kövesdi. Welding simulation of corrugated web girders - Part 1: Effect of manufacturing on residual stresses and imperfections. *Thin-Walled Structures*, 146, 2020.

[29] Jiho Moon, Jongwon Yi, Byung H. Choi, and Hak-Eun Lee. Shear strength and design of trapezoidally corrugated steel webs. *Journal of Constructional Steel Research*, 65(5):1198–1205, May 2009.

[30] Richard Sause, Hassam H Abbas, Wagdy G Wassef, Robert G Driver, and Mohamed Elgaaly. Corrugated Web Girder Shape and Strength Criteria. (03):72, 2003.

[31] SCI. Design Manual for Structural Stainless Steel, 2018.

[32] Boshan Zhang, Jiangjiang Yu, Weizhen Chen, Hui Wang, and Jun Xu. Stress states and shear failure mechanisms of girders with corrugated steel webs. *Thin-Walled Structures*, 157:106858, December 2020.

A

Appendix 1: Python Script

```
# TRANSCRIPT originated by ERIK SAVE & KARL ÅKERMO and developed by FATIMA HLAL & NAHEEL MOHRA
from part import *
from material import *
from section import *
from assembly import *
from step import *
from interaction import *
from load import *
from mesh import *
from optimization import *
from job import *
from sketch import *
from visualization import *
from connectorBehavior import *
from odbAccess import *
import sys
import math
import regionToolset
import shutil

#------------------------I N P U T  D A T A--------------------------------

# Material parameters

elastic_modulus =                       # Elastic modulus [Pa]
poissons_ratio  =                       # Poissons ratio

# Nonlinear material model

Increments =                             # Number of increments for riks analysis
Modes =                                  # Number of modes to be considered

Fy =                                     # Yielding stress
strain_at_fy =                           # Platstic strain at fy

# I-section

h_w =                                    # Web height [m]
t_w =                                    # Web thickness [m]
b_f =                                    # Flange width [m]
t_f =                                    # Flange thickness [m]

# Corrugation geometry

corr_depth =                             # Corrugation depth [m]
l_par =                                  # Parallel fold length [m]
corr_ang =                               # Corrugation angle in degrees

# Model settings Linear model

num_tot_wavelengths =                    # Number of total wavelengths on the girder
point_load =                             # Point load magnitude [N]
load_position =                          # Load application, ex 5 = end of 5th wavelength from left support
global_element_size =                    # Global element size

# Stiffeners

STtiffener_th =                          #Stiffeners thickness
Initial_imperfection  =                  #Initial Imperfection

#num_tot_wavelengths = math.floor(num_tot_wavelengths*4)/4  #Round Down Wavelengths to the nearest quarter if it is not integer number of quarter wavelengths.


#-------------S T A R T  O F  S C R I P T-------------------------------------

## DEBUG MODE, when debug mode is on the analyses are not submitted

debug = 1                                                        # 1 = debug mode on, 0 = debug mode off
```

```
69  ## DEBUG MODE
70
71  #  Determining number of wavelengths for the model,
72
73  num_wavelengths = (num_tot_wavelengths)                          # Number of
    wavelengths in case of no symmetry
74  num_full_wavelengths = int(num_wavelengths)                      # Number of whole
    wavelengths, no symmetry
75  rest_wavelength = num_wavelengths-num_full_wavelengths           # Number of partial
    wavelenghts remaining, 0.25=quarter wavelength
76
77
78  # Coordinates and parameters used in script
79
80  l_par = l_par/2
81  # Angles
82  corr_ang=corr_ang*(2*pi/360)                                     # Corrugation angle
    in radians for script
83
84  # Y - coordinates
85
86  corr_amp=corr_depth/2                                            # Corrugation
    amplitude [m]
87  h_w_global=h_w+t_f                                               # Web height used in
    shell model [m]
88  half_web_thickness=t_w/2                                         # Half of web
    thickness [m]
89
90  # X - coordinates
91
92  proj_l_inc = corr_amp/math.tan(corr_ang)                         # Projected length
    of inclined fold
93  l_wavelength=4*(proj_l_inc+l_par)                                # Length of
    wavelength [m]
94  quarter_wavelength = proj_l_inc+l_par                            # Length of a
    quarter wavelength
95  load_position = load_position*l_wavelength                       # Load application,
    distance from support [m]
96
97
98  #-------------------------------LINEAR ANALYSIS---------------------------------
99
100 #----------------------------G L O B A L  M O D E L-----------------------------
101
102 # Change name of model
103
104 mdb.models.changeKey(fromName='Model-1', toName='global_model')
105 global_model = mdb.models['global_model']
106
107 ## Create quarter wavelength
108 # Create web part
109
110 global_model.ConstrainedSketch(name='web_sketch_global', sheetSize=10.0)
111 web_sketch_global = global_model.sketches['web_sketch_global']
112 web_sketch_global.Line(point1=(0.0, 0.0), point2=(proj_l_inc, -corr_amp))
113 web_sketch_global.Line(point1=(proj_l_inc, -corr_amp), point2=(quarter_wavelength, -
    corr_amp))
114 global_model.Part(dimensionality=THREE_D, name='Part1', type=DEFORMABLE_BODY)
115 global_part_1 = global_model.parts['Part1']
116 global_part_1.BaseShellExtrude(depth=h_w_global, sketch=web_sketch_global)
117
118 del web_sketch_global
119
120 # Create datum planes for flanges
121
122 global_datumpl1 = global_part_1.DatumPlaneByPrincipalPlane(offset=0.0, principalPlane
    =XYPLANE)
123 global_datumpl1 = global_part_1.datums[global_datumpl1.id]
124
125 global_datumpl2 = global_part_1.DatumPlaneByPrincipalPlane(offset=h_w_global,
    principalPlane=XYPLANE)
126 global_datumpl2 = global_part_1.datums[global_datumpl2.id]
```

```
127
128 # Create bottom flange
129
130 global_model.ConstrainedSketch(gridSpacing=0.02, name='bot_flange_sketch_global',
131     sheetSize=1.05, transform=global_part_1.MakeSketchTransform(
132     sketchPlane=global_datumpl1,
133     sketchPlaneSide=SIDE1,
134     sketchUpEdge=global_part_1.edges.findAt((proj_l_inc+l_par/2,-corr_amp,h_w_global
    ),),),
135     sketchOrientation=BOTTOM, origin=(0.0, 0.0, 0.0)))
136 bot_flange_sketch_global = global_model.sketches['bot_flange_sketch_global']
137 bot_flange_sketch_global.rectangle(point1=(0, b_f/2), point2=(quarter_wavelength, -
    b_f/2))
138 global_part_1.Shell(sketch=bot_flange_sketch_global)
139
140 del bot_flange_sketch_global
141
142 # Create top flange
143
144 global_model.ConstrainedSketch(gridSpacing=0.02, name='top_flange_sketch_global',
145     sheetSize=1.09, transform=
146     global_part_1.MakeSketchTransform(
147     sketchPlane=global_datumpl2,
148     sketchPlaneSide=SIDE1,
149     sketchUpEdge=global_part_1.edges.findAt((proj_l_inc+l_par/2,-corr_amp,h_w_global
    ),),),
150     sketchOrientation=BOTTOM, origin=(0.0, 0.0, h_w_global)))
151 top_flange_sketch_global = global_model.sketches['top_flange_sketch_global']
152 top_flange_sketch_global.rectangle(point1=(0, b_f/2), point2=(quarter_wavelength, -
    b_f/2))
153
154 global_part_1.Shell(sketch=top_flange_sketch_global,
155     sketchOrientation=BOTTOM,
156     sketchPlane=global_datumpl2,
157     sketchPlaneSide=SIDE1, sketchUpEdge=
158     global_part_1.edges.findAt((proj_l_inc+l_par/2,-corr_amp,h_w_global),))
159
160 del top_flange_sketch_global
161
162 # Create material
163
164 global_model.Material(name='Steel')
165 global_model.materials['Steel'].Elastic(table=((elastic_modulus, poissons_ratio),))
166
167 # Create Flange and web sections
168
169 global_model.HomogeneousShellSection(idealization=NO_IDEALIZATION,
170     integrationRule=SIMPSON, material='Steel', name='Flange',
171     nodalThicknessField='', numIntPts=5, poissonDefinition=DEFAULT,
172     preIntegrate=OFF, temperature=GRADIENT, thickness=t_f, thicknessField='',
173     thicknessModulus=None, thicknessType=UNIFORM, useDensity=OFF)
174 global_model.HomogeneousShellSection(idealization=NO_IDEALIZATION,
175     integrationRule=SIMPSON, material='Steel', name='Web', nodalThicknessField='',
176     numIntPts=5, poissonDefinition=DEFAULT, preIntegrate=OFF, temperature=
177     GRADIENT, thickness=t_w, thicknessField='', thicknessModulus=None,
178     thicknessType=UNIFORM, useDensity=OFF)
179
180 # Partition quarter wavelength
181
182 p1 = (proj_l_inc, 0, 0)
183 p2 = (proj_l_inc, -b_f/2, 0)
184 p3 = (proj_l_inc, 0, h_w_global)
185 p4 = (proj_l_inc, -b_f/2, h_w_global)
186
187 global_model.ConstrainedSketch(gridSpacing=0.02, name='partition_sketch_global',
188     sheetSize=1.1, transform=global_part_1.MakeSketchTransform(
189     sketchPlane=global_datumpl2,
190     sketchPlaneSide=SIDE1,
191     sketchUpEdge=global_part_1.edges.findAt((proj_l_inc,-b_f/2,h_w_global),),
192     sketchOrientation=BOTTOM, origin=(0.0, 0.0, h_w_global)))
193 partition_sketch_global = global_model.sketches['partition_sketch_global']
194 partition_sketch_global.Line(point1=(proj_l_inc, -corr_amp), point2=(proj_l_inc, b_f/
```

```
    2))
195 partition_sketch_global.Line(point1=(proj_l_inc, -corr_amp), point2=(proj_l_inc, -b_f
    /2))
196 global_part_1.PartitionFaceBySketchThruAll(
197     faces=global_part_1.faces.findAt(((p1),), ((p2),), ((p3),), ((p4),)),
198     sketch=partition_sketch_global, sketchOrientation=BOTTOM,
199     sketchPlane=global_datumpl2, sketchPlaneSide=SIDE1,
200     sketchUpEdge=global_part_1.edges.findAt((proj_l_inc,-b_f/2,h_w_global),))
201
202 del partition_sketch_global
203
204 # Copy and mirroring quarter wavelength for creation of symmetry girder
205
206 global_model.Part(compressFeatureList=ON, mirrorPlane=YZPLANE, name=
207     'global_part_2', objectToCopy=global_part_1)
208 global_part_2 = global_model.parts['global_part_2']
209
210 global_model.Part(compressFeatureList=ON, mirrorPlane=XZPLANE, name=
211     'global_part_3', objectToCopy=global_part_1)
212 global_part_3 = global_model.parts['global_part_3']
213
214 global_model.Part(compressFeatureList=ON, mirrorPlane=XZPLANE, name=
215     'global_part_4', objectToCopy=global_part_2)
216 global_part_4 = global_model.parts['global_part_4']
217
218 ## Assigning flange and web sections to parts
219
220 # Assign sections to first quarter
221 pf11 = (0, b_f/2, 0)
222 pf21 = (0, -b_f/2, 0)
223 pf31= (quarter_wavelength, b_f/2, 0)
224 pf41 = (quarter_wavelength, -b_f/2, 0)
225 pf51 = (0, b_f/2, h_w_global)
226 pf61 = (0, -b_f/2, h_w_global)
227 pf71 = (quarter_wavelength, b_f/2, h_w_global)
228 pf81 = (quarter_wavelength, -b_f/2, h_w_global)
229 pw11 = (0, 0, h_w_global/2)
230 pw21 = (quarter_wavelength, -corr_amp, h_w_global/2)
231
232 global_part_1.SectionAssignment(offset=0.0, offsetField='',
233     offsetType=MIDDLE_SURFACE, region=Region(
234     faces=global_part_1.faces.findAt(((pf11),), ((pf21),),
235     ((pf31),), ((pf41),), ((pf51),), ((pf61),), ((pf71),), ((pf81),))),
236     sectionName='Flange', thicknessAssignment=FROM_SECTION)
237 global_part_1.SectionAssignment(offset=0.0, offsetField='',
238     offsetType=MIDDLE_SURFACE, region=Region(
239     faces=global_part_1.faces.findAt(((pw11),), ((pw21),))),
240     sectionName='Web', thicknessAssignment=FROM_SECTION)
241
242 # Assign sections to second quarter
243
244 pf12 = (0, b_f/2, 0)
245 pf22 = (0, -b_f/2, 0)
246 pf32= (-proj_l_inc-l_par, b_f/2, 0)
247 pf42 = (-proj_l_inc-l_par, -b_f/2, 0)
248 pf52 = (0, b_f/2, h_w_global)
249 pf62 = (0, -b_f/2, h_w_global)
250 pf72 = (-proj_l_inc-l_par, b_f/2, h_w_global)
251 pf82 = (-proj_l_inc-l_par, -b_f/2, h_w_global)
252 pw12 = (0, 0, h_w_global/2)
253 pw22 = (-proj_l_inc-l_par, -corr_amp, h_w_global/2)
254
255 global_part_2.SectionAssignment(offset=0.0, offsetField='',
256     offsetType=MIDDLE_SURFACE, region=Region(
257     faces=global_part_2.faces.findAt(((pf12),), ((pf22),), ((pf32),),
258     ((pf42),), ((pf52),), ((pf62),), ((pf72),), ((pf82),))),
259     sectionName='Flange', thicknessAssignment=FROM_SECTION)
260 global_part_2.SectionAssignment(offset=0.0, offsetField='',
261     offsetType=MIDDLE_SURFACE, region=Region(
262     faces=global_part_2.faces.findAt(((pw12),), ((pw22),))),
263     sectionName='Web', thicknessAssignment=FROM_SECTION)
264
```

```
# Assign sections to third quarter

pf13 = (0, -b_f/2, 0)
pf23 = (0, b_f/2, 0)
pf33= (quarter_wavelength, -b_f/2, 0)
pf43 = (quarter_wavelength, b_f/2, 0)
pf53 = (0, -b_f/2, h_w_global)
pf63 = (0, +b_f/2, h_w_global)
pf73 = (quarter_wavelength, -b_f/2, h_w_global)
pf83 = (quarter_wavelength, b_f/2, h_w_global)
pw13 = (0, 0, h_w_global/2)
pw23 = (quarter_wavelength, corr_amp, h_w_global/2)

global_part_3.SectionAssignment(offset=0.0, offsetField='',
    offsetType=MIDDLE_SURFACE, region=Region(
    faces=global_part_3.faces.findAt(((pf13),), ((pf23),), ((pf33),),
    ((pf43),), ((pf53),), ((pf63),), ((pf73),), ((pf83),))),
    sectionName='Flange', thicknessAssignment=FROM_SECTION)
global_part_3.SectionAssignment(offset=0.0, offsetField='',
    offsetType=MIDDLE_SURFACE, region=Region(
    faces=global_part_3.faces.findAt(((pw13),), ((pw23),))),
    sectionName='Web', thicknessAssignment=FROM_SECTION)

# Assign sections to fourth quarter

pf14 = (0, -b_f/2, 0)
pf24 = (0, b_f/2, 0)
pf34= (-proj_l_inc-l_par, -b_f/2, 0)
pf44 = (-proj_l_inc-l_par, b_f/2, 0)
pf54 = (0, -b_f/2, h_w_global)
pf64 = (0, +b_f/2, h_w_global)
pf74 = (-proj_l_inc-l_par, -b_f/2, h_w_global)
pf84 = (-proj_l_inc-l_par, b_f/2, h_w_global)
pw14 = (0, 0, h_w_global/2)
pw24 = (-proj_l_inc-l_par, corr_amp, h_w_global/2)

global_part_4.SectionAssignment(offset=0.0, offsetField='',
    offsetType=MIDDLE_SURFACE, region=Region(
    faces=global_part_4.faces.findAt(((pf14),), ((pf24),),
    ((pf34),), ((pf44),), ((pf54),), ((pf64),), ((pf74),), ((pf84),))),
    sectionName='Flange', thicknessAssignment=FROM_SECTION)
global_part_4.SectionAssignment(offset=0.0, offsetField='',
    offsetType=MIDDLE_SURFACE, region=Region(
    faces=global_part_4.faces.findAt(((pw14),), ((pw24),))),
    sectionName='Web', thicknessAssignment=FROM_SECTION)

# Insert quarter wavelength instances

global_model.rootAssembly.DatumCsysByDefault(CARTESIAN)
global_model.rootAssembly.Instance(dependent=OFF, name='Part1-1',
    part=global_part_1)
global_model.rootAssembly.Instance(dependent=OFF, name='Part2-1',
    part=global_part_2)
global_model.rootAssembly.Instance(dependent=OFF, name='Part3-1',
    part=global_part_3)
global_model.rootAssembly.Instance(dependent=OFF, name='Part4-1',
    part=global_part_4)
global_model.rootAssembly.translate(instanceList=('Part2-1', ),
    vector=(l_wavelength/2, 0.0, 0.0))
global_model.rootAssembly.translate(instanceList=('Part3-1', ),
    vector=(l_wavelength/2, 0.0, 0.0))
global_model.rootAssembly.translate(instanceList=('Part4-1', ),
    vector=(l_wavelength, 0.0, 0.0))

# Considering partial wavelengths

if rest_wavelength == 0.25:
    w1 = int(num_full_wavelengths)+1
    w2 = int(num_full_wavelengths)
    w3 = int(num_full_wavelengths)
    w4 = int(num_full_wavelengths)
elif rest_wavelength == 0.5:
```

```
337         w1 = int(num_full_wavelengths)+1
338         w2 = int(num_full_wavelengths)+1
339         w3 = int(num_full_wavelengths)
340         w4 = int(num_full_wavelengths)
341     elif rest_wavelength == 0.75:
342         w1 = int(num_full_wavelengths)+1
343         w2 = int(num_full_wavelengths)+1
344         w3 = int(num_full_wavelengths)+1
345         w4 = int(num_full_wavelengths)
346     else:
347         w1 = int(num_full_wavelengths)
348         w2 = int(num_full_wavelengths)
349         w3 = int(num_full_wavelengths)
350         w4 = int(num_full_wavelengths)
351 
352     # Linear pattern of quarter wavelengths
353 
354     global_model.rootAssembly.LinearInstancePattern(direction1=(1.0, 0.0,
355         0.0), direction2=(0.0, 1.0, 0.0), instanceList=('Part1-1', ), number1=w1,
356         number2=1, spacing1=l_wavelength, spacing2=0.15)
357     global_model.rootAssembly.LinearInstancePattern(direction1=(1.0, 0.0,
358         0.0), direction2=(0.0, 1.0, 0.0), instanceList=('Part2-1', ), number1=(w2),
359         number2=1, spacing1=l_wavelength, spacing2=0.15)
360     global_model.rootAssembly.LinearInstancePattern(direction1=(1.0, 0.0,
361         0.0), direction2=(0.0, 1.0, 0.0), instanceList=('Part3-1', ), number1=(w3),
362         number2=1, spacing1=l_wavelength, spacing2=0.15)
363     global_model.rootAssembly.LinearInstancePattern(direction1=(1.0, 0.0,
364         0.0), direction2=(0.0, 1.0, 0.0), instanceList=('Part4-1', ), number1=(w4),
365         number2=1, spacing1=l_wavelength, spacing2=0.15)
366 
367     # Rotate instances for correct coordinate system
368 
369     all_instances=global_model.rootAssembly.instances
370     global_model.rootAssembly.rotate(angle=-90.0, axisDirection=(1.0, 0.0, 0.0),
371         axisPoint=(0.0, 0.0, 0.0), instanceList=(all_instances.keys()))
372 
373     # Merge instances into CWG and delete quarter instances
374 
375     global_model.rootAssembly.InstanceFromBooleanMerge(domain=GEOMETRY,
376         instances=all_instances.values(),
377         keepIntersections=ON, name='global_model_cwg', originalInstances=DELETE)
378 
379     # Name CWG instance and part
380 
381     global_model_instance = global_model.rootAssembly.instances['global_model_cwg-1']
382     global_model_cwg = global_model.parts['global_model_cwg']
383 
384     # Create load step
385 
386     global_model.StaticStep(name='load_step', previous='Initial')
387 
388     # Create support constraint
389 
390     origo = (0,0,0)
391     L = (num_wavelengths*l_wavelength)
392     end = (L,0,-corr_amp)
393 
394 
395     # Flip positive - negative normal of shell elements so that faces that share common
    plane have the same normal
396 
397     p_normal1 = [0] * num_full_wavelengths
398     p_normal2 = [0] * num_full_wavelengths
399     p_normal3 = [0] * num_full_wavelengths
400     p_normal4 = [0] * num_full_wavelengths
401     for i in range(0,num_full_wavelengths,1):
402         p_normal1[i] = (i*l_wavelength+3*l_wavelength/4-l_par/2,h_w_global/2,-corr_amp)
403         p_normal2[i] = (i*l_wavelength+l_wavelength/2+proj_l_inc/2,h_w_global/2,-corr_amp
        /2)
404         p_normal3[i]= (i*l_wavelength+l_wavelength-proj_l_inc/2,h_w_global/2,-corr_amp/2)
405         p_normal4[i] = (i*l_wavelength+3*l_wavelength/4+l_par/2,h_w_global/2,-corr_amp)
406 
```

```
407 p_normal1=tuple(p_normal1)
408 p_normal2=tuple(p_normal2)
409 p_normal3=tuple(p_normal3)
410 p_normal4=tuple(p_normal4)
411 p_normal_tot=p_normal1+p_normal2+p_normal3+p_normal4
412
413 # Flip normal for  ev. additional partial wavelength
414
415 if rest_wavelength == 0.75:
416     p_normal_end=[0]*2
417     p_normal_end[0]= (num_full_wavelengths*l_wavelength+l_wavelength/2+proj_l_inc/2,
        h_w_global/2,-corr_amp/2)
418     p_normal_end[1] = (num_full_wavelengths*l_wavelength+3*l_wavelength/4-l_par/2,
        h_w_global/2,-corr_amp)
419     p_normal_tot=p_normal_tot+tuple(p_normal_end)
420
421 global_model_cwg.flipNormal(regions=Region(
422     faces=global_model_cwg.faces.findAt(coordinates=p_normal_tot),))
423 global_model.rootAssembly.regenerate()
424
425 # Create global job
426
427 linear_analysis = mdb.Job(atTime=None, contactPrint=OFF, description='', echoPrint=
    OFF,
428     explicitPrecision=SINGLE, getMemoryFromAnalysis=True, historyPrint=OFF,
429     memory=90, memoryUnits=PERCENTAGE, model='global_model', modelPrint=OFF,
430     multiprocessingMode=DEFAULT, name='linear_analysis', nodalOutputPrecision=
431     SINGLE, numCpus=1, numGPUs=0, queue=None, resultsFormat=ODB, scratch='',
432     type=ANALYSIS, userSubroutine='', waitHours=0, waitMinutes=0)
433
434 # Submit global job
435
436 if debug == 0:
437     linear_analysis.submit(consistencyChecking=OFF)
438
439 #------------------------Start Modification-------------------------
440
441 ## Stifferners Creation
442
443 # Creation of Stiffener in Parts
444
445 mdb.models['global_model'].ConstrainedSketch(name='__profile__', sheetSize=
446     400.0)
447 mdb.models['global_model'].sketches['__profile__'].Line(point1=(0, 0),
448     point2=(0, h_w+t_f))
449 mdb.models['global_model'].sketches['__profile__'].VerticalConstraint(
450     addUndoState=False, entity=
451     mdb.models['global_model'].sketches['__profile__'].geometry[2])
452
453 mdb.models['global_model'].sketches['__profile__'].ObliqueDimension(textPoint=(
454     0, 0), value=h_w+t_f, vertex1=
455     mdb.models['global_model'].sketches['__profile__'].vertices[0], vertex2=
456     mdb.models['global_model'].sketches['__profile__'].vertices[1])
457 mdb.models['global_model'].Part(dimensionality=THREE_D, name='Stiffener', type=
458     DEFORMABLE_BODY)
459
460 mdb.models['global_model'].parts['Stiffener'].BaseShellExtrude(depth=b_f, sketch=
461     mdb.models['global_model'].sketches['__profile__'])
462 del mdb.models['global_model'].sketches['__profile__']
463
464 # Partiotion
465
466 mdb.models['global_model'].parts['Stiffener'].PartitionFaceByShortestPath(
467     faces=
468     mdb.models['global_model'].parts['Stiffener'].faces.getSequenceFromMask((
469     '[#1 ]', ), ), point1=
470     mdb.models['global_model'].parts['Stiffener'].InterestingPoint(
471     mdb.models['global_model'].parts['Stiffener'].edges[3], MIDDLE), point2=
472     mdb.models['global_model'].parts['Stiffener'].InterestingPoint(
473     mdb.models['global_model'].parts['Stiffener'].edges[1], MIDDLE))
474
475
```

```
476
477 # Assemble Stiffener 1 on load position
478
479 mdb.models['global_model'].rootAssembly.Instance(dependent=ON, name=
480     'Stiffener-1', part=mdb.models['global_model'].parts['Stiffener'])
481     # Final Location of stiffener, if we want to put it in the same location of the
        Load, then the final coordinates is: (load_position,h_w_global,0)
482 mdb.models['global_model'].rootAssembly.translate(instanceList=('Stiffener-1',
483     ), vector=(load_position,0,-b_f/2))
484
485 # Assemble Stiffener 2 on left side
486
487 mdb.models['global_model'].rootAssembly.Instance(dependent=ON, name=
488     'Stiffener-2', part=mdb.models['global_model'].parts['Stiffener'])
489     # Final Location of stiffener, if we want to put it in the same location of the
        Load, then the final coordinates is: (load_position,h_w_global,0)
490 mdb.models['global_model'].rootAssembly.translate(instanceList=('Stiffener-2',
491     ), vector=(0.05,0,-b_f/2))
492
493 # Assemble Stiffener 3 on right side
494
495 mdb.models['global_model'].rootAssembly.Instance(dependent=ON, name=
496     'Stiffener-3', part=mdb.models['global_model'].parts['Stiffener'])
497 # Final Location of stiffener, if we want to put it in the same location of the
    Load, then the final coordinates is: (load_position,h_w_global,0)
498 mdb.models['global_model'].rootAssembly.translate(instanceList=('Stiffener-3',
499     ), vector=(l_wavelength*num_wavelengths-0.05,0,-b_f/2))
500
501
502
503 # Assigning Stiffener Section
504
505 mdb.models['global_model'].HomogeneousShellSection(idealization=NO_IDEALIZATION
506     , integrationRule=SIMPSON, material='Steel', name='Stiffener Section',
507     nodalThicknessField='', numIntPts=5, poissonDefinition=DEFAULT,
508     preIntegrate=OFF, temperature=GRADIENT, thickness=STtiffener_th, thicknessField=
        '',
509     thicknessModulus=None, thicknessType=UNIFORM, useDensity=OFF)
510 #
511
512 mdb.models['global_model'].parts['Stiffener'].SectionAssignment(offset=0.0,
513     offsetField='', offsetType=MIDDLE_SURFACE, region=Region(
514     faces=mdb.models['global_model'].parts['Stiffener'].faces.getSequenceFromMask(
515     mask=('[#3 ]', ), )), sectionName='Stiffener Section', thicknessAssignment=
516     FROM_SECTION)
517
518 # Merge stiffeners with the beam
519
520 mdb.models['global_model'].rootAssembly.regenerate()
521 mdb.models['global_model'].rootAssembly.InstanceFromBooleanMerge(domain=
522     GEOMETRY, instances=(
523     mdb.models['global_model'].rootAssembly.instances['global_model_cwg-1'],
524     mdb.models['global_model'].rootAssembly.instances['Stiffener-1'],
525     mdb.models['global_model'].rootAssembly.instances['Stiffener-2'],
526     mdb.models['global_model'].rootAssembly.instances['Stiffener-3']),
527     keepIntersections=ON, name='CWG', originalInstances=SUPPRESS)
528 mdb.models['global_model'].parts['CWG'].seedPart(deviationFactor=0.1,
529     minSizeFactor=0.1, size=0.078)
530 mdb.models['global_model'].parts['CWG'].generateMesh()
531
532
533
534 # Create point load
535
536 mdb.models['global_model'].ConcentratedForce(cf2=-point_load, createStepName=
537     'load_step', distributionType=UNIFORM, field='', localCsys=None, name=
538     'Load-1', region=Region(
539     vertices=mdb.models['global_model'].rootAssembly.instances['CWG-1'].vertices.
        findAt(((load_position,h_w_global,0),))))
540
541
542
```

```
#Create Boundary Conditions

mdb.models['global_model'].DisplacementBC(amplitude=UNSET, createStepName=
    'load_step', distributionType=UNIFORM, fieldName='', fixed=OFF, localCsys=
    None, name='BC-1', region=Region(
    vertices=mdb.models['global_model'].rootAssembly.instances['CWG-1'].vertices.
    findAt(((0.05,0,0),))), u1=UNSET, u2=0.0, u3=0.0, ur1=0.0, ur2=0.0, ur3=
    UNSET)

mdb.models['global_model'].DisplacementBC(amplitude=UNSET, createStepName=
    'load_step', distributionType=UNIFORM, fieldName='', fixed=OFF, localCsys=
    None, name='BC-4', region=Region(
    vertices=mdb.models['global_model'].rootAssembly.instances['CWG-1'].vertices.
    findAt(((L-0.05,0,0),))), u1=UNSET, u2=0.0, u3=0.0, ur1=0.0, ur2=0.0, ur3=
    UNSET)

mdb.models['global_model'].DisplacementBC(amplitude=UNSET, createStepName=
    'load_step', distributionType=UNIFORM, fieldName='', fixed=OFF, localCsys=
    None, name='BC-2', region=Region(
    vertices=mdb.models['global_model'].rootAssembly.instances['CWG-1'].vertices.
    findAt(((load_position,h_w_global,0),))), u1=UNSET, u2=UNSET, u3=0.0, ur1=UNSET,
    ur2=UNSET,
    ur3=UNSET)
mdb.models['global_model'].DisplacementBC(amplitude=UNSET, createStepName=
    'load_step', distributionType=UNIFORM, fieldName='', fixed=OFF, localCsys=
    None, name='BC-3', region=Region(
    vertices=mdb.models['global_model'].rootAssembly.instances['CWG-1'].vertices.
    findAt(((load_position,0,0),))), u1=0.0, u2=UNSET, u3=UNSET, ur1=UNSET, ur2=UNSET
    ,
    ur3=UNSET)

#Generate Mesh

mdb.models['global_model'].parts['CWG'].seedPart(deviationFactor=0.1,
    minSizeFactor=0.1, size=global_element_size)
mdb.models['global_model'].parts['CWG'].setMeshControls(elemShape=QUAD,
    regions=mdb.models['global_model'].parts['CWG'].faces,
    technique=STRUCTURED)
mdb.models['global_model'].parts['CWG'].setElementType(elemTypes=(ElemType(
    elemCode=S8R, elemLibrary=STANDARD), ElemType(elemCode=STRI65,
    elemLibrary=STANDARD)), regions=(
    mdb.models['global_model'].parts['CWG'].faces,))
mdb.models['global_model'].parts['CWG'].generateMesh()

#--------------------Linear Buckling Analysis-----------------------
# Creating buckling model

mdb.Model(name='Buckling model', objectToCopy=mdb.models['global_model'])
mdb.models['Buckling model'].rootAssembly.regenerate()
mdb.models['Buckling model'].BuckleStep(blockSize=DEFAULT, description=
    'Bucklle', eigensolver=LANCZOS, maintainAttributes=True, maxBlocks=DEFAULT,
    minEigen=None, name='load_step', numEigen=Modes, previous='Initial')

# Adding keywords

mdb.models['Buckling model'].keywordBlock.synchVersions(storeNodesAndElements= False)
keyword = '\n*node file, global=yes, last mode=' + str(Modes) + '\nU,'
mdb.models['Buckling model'].keywordBlock.insert(76, keyword)

# Creating job for linear buckling analysis

mdb.Job(atTime=None, contactPrint=OFF, description='', echoPrint=OFF,
    explicitPrecision=SINGLE, getMemoryFromAnalysis=True, historyPrint=OFF,
    memory=90, memoryUnits=PERCENTAGE, model='Buckling model', modelPrint=OFF,
    multiprocessingMode=DEFAULT, name='Buckling', nodalOutputPrecision=SINGLE,
    numCpus=1, numGPUs=0, queue=None, resultsFormat=ODB, scratch='', type=
    ANALYSIS, userSubroutine='', waitHours=0, waitMinutes=0)

#Job Submittal

mdb.jobs['Buckling'].submit(consistencyChecking=OFF)
mdb.jobs['Buckling'].waitForCompletion()
```

```
609
610 #----------------- NONLINEAR ANALYSIS --------------------------
611
612 # Creating loop to perform nonlinear analysis for each mode shape
613
614 for mode_number in range (1,Modes):
615     print ('processing mode number' + str(mode_number))
616
617     #Adding nonlinear material model
618
619     Model_Name = 'Non-linear Model-' + str(mode_number)
620     Job_Name = 'Non-linear-Job-' + str(mode_number)
621     mdb.Model(name=Model_Name, objectToCopy=mdb.models['Buckling model'])
622     mdb.models[Model_Name].materials['Steel'].Plastic(table=((Fy, strain_at_fy), ))
623
624     #Creating nonlinear model with initial imperfection
625
626     mdb.models[Model_Name].StaticRiksStep(maintainAttributes=True, name='load_step',
627         nlgeom=ON, previous='Initial')
628     mdb.models[Model_Name].steps.changeKey(fromName='load_step', toName='nonlinear')
629     mdb.models[Model_Name].keywordBlock.synchVersions(storeNodesAndElements=False)
630     mdb.models[Model_Name].keywordBlock.setValues(edited=0)
631     mdb.models[Model_Name].keywordBlock.synchVersions(storeNodesAndElements=False)
632
633     #Increments
634
635     mdb.models[Model_Name].steps['nonlinear'].setValues(initialArcInc=0.01,
636         maxArcInc=0.1, maxNumInc=Increments, minArcInc=1e-15)
637
638     #Defining Initial Imperfection
639     #Adding Keyword
640
641     text_to_find = '*Step, name=nonlinear, nlgeom=YES'           #Copy the full line
    of the text to find, only one line
642     blocks = []
643     for block in mdb.models[Model_Name].keywordBlock.sieBlocks:
644         blocks.append(block)
645     position = blocks.index(text_to_find) -1
646     mdb.models[Model_Name].keywordBlock.synchVersions()          # IMPORTANT STRINGS
    TO MAKE IT WORK
647     mdb.models[Model_Name].keywordBlock.setValues(edited = 0)    # IMPORTANT STRINGS
    TO MAKE IT WORK
648     mdb.models[Model_Name].keywordBlock.synchVersions()          # IMPORTANT STRINGS
    TO MAKE IT WORK
649
650     imperfection = '\n*imperfection, file=buckling, step=1\n' + str(mode_number) +
    ',' +str(Initial_imperfection)      # ADD Keyword Here
651     mdb.models[Model_Name].keywordBlock.insert(position, imperfection)
652
653
654     #Job Submittal
655
656     mdb.Job(atTime=None, contactPrint=OFF, description='', echoPrint=OFF,
657         explicitPrecision=SINGLE, getMemoryFromAnalysis=True, historyPrint=OFF,
658         memory=90, memoryUnits=PERCENTAGE, model=Model_Name, modelPrint=OFF,
659         multiprocessingMode=DEFAULT, name=Job_Name,
660         nodalOutputPrecision=SINGLE, numCpus=1, numGPUs=0, queue=None,
661         resultsFormat=ODB, scratch='', type=ANALYSIS, userSubroutine='', waitHours=
662         0, waitMinutes=0)
663
664     mdb.jobs[Job_Name].setValues(multiprocessingMode=THREADS, numCpus=6,     #
    Increase Processing Power
665         numDomains=6, numGPUs=6)
666
667     mdb.jobs[Job_Name].submit(consistencyChecking=OFF)
668
669     mdb.jobs[Job_Name].waitForCompletion()
670
671     # Exporting results
672
673     odbpath = 'C:\\Folder Name\\' + Job_Name + '.odb'    # CHANGE THIS  'C:\\Folder
    Name\\' TO YOUR FOLDER PATH #
```

```
674         odb = openOdb(path=odbpath)
675 
676 
677         # Exporting Load Factor.
678 
679         print('Exporting Results to Excel')
680         LoadFactor = session.XYDataFromHistory(name='LoadFactor',odb=odb,
            outputVariableName='Load proportionality factor: LPF for Whole Model',steps=(
            'nonlinear',))
681 
682         LPFs = []
683         for i in LoadFactor:
684             LPFs.append(i[1])
685 
686         # Exporting Displacement For The Node with Maximum U3 in the Model, OUT OF PLANE
            DISPLACEMENT
687 
688         Max = 0
689         Final_Increment_U_Values= odb.steps['nonlinear'].frames[1].fieldOutputs['U'].
            values
690         for v in Final_Increment_U_Values:
691             if abs(v.data[2]) > Max:
692                 Max = abs(v.data[2])
693                 MaxNode = v.nodeLabel
694 
695         Out_Off_Plane_Displacements = []
696         for x in range(0,Increments):
697             U_Values= odb.steps['nonlinear'].frames[x].fieldOutputs['U'].values
698             for v in U_Values:
699                 if v.nodeLabel == MaxNode:
700                     Out_Off_Plane_Displacements.append([x,v.data[2]])
701 
702         # Exporting Displacement For The Midspan
703 
704         Mid_Span_Displacements = []
705         midspan = mdb.models['global_model'].rootAssembly.instances['CWG-1'].vertices.
            findAt(((load_position,0,0),))[0].index
706         for x in range(0,Increments):
707             U_Values= odb.steps['nonlinear'].frames[x].fieldOutputs['U'].values
708             for v in U_Values:
709                 if v.nodeLabel == midspan:
710                     Mid_Span_Displacements.append([x,v.data[1]])
711 
712 
713         # Merging and Exporting
714 
715         Merge = zip (Mid_Span_Displacements,Out_Off_Plane_Displacements, LPFs)
716         Shear_stress_Values=[]
717         File_Name = 'Results-' + str(mode_number) +'.csv'
718         CSV_file = open(File_Name,'w')
719         CSV_file.write('Results of Mode Number %s \n \n Increment; Mid-Span Displacement
            (mm);Increment;Out-of-plane Displacement (mm);LPF;Shear load (N); Shear stress
            (MPa) \n' %(mode_number,))
720 
721         for y in Merge:
722             Increment1 = y[0][0]
723             U2 = y[0][1]*(-1000)       # CONVERT TO mm
724             Increment2 = y[1][0]
725             U3 = y[1][1]*(-1000)       # CONVERT TO mm
726             LPF = y[2]
727             Shear_load = LPF*point_load*(L-load_position)/L
728             Shear_stress = Shear_load/(t_w*h_w*1e6)
729             Shear_stress_Values.append(Shear_stress)
730             CSV_file.write('%.0f;%.15f;%.0f;%.15f;%.15f;%.15f;%.15f \n'%(Increment1, U2,
                Increment2, U3,LPF, Shear_load, Shear_stress))
731 
732         Max_shear = max(Shear_stress_Values)
733         CSV_file.write('\n Max shear is %s (MPa) \n' %(Max_shear,))
734         CSV_file.close()
735 
736         odb.close()
737         print('Exporting Done')
```

```
738
739   #End of file
```

B

Appendix 2: FE-results

Table B.1: M12, Imperfection = Hw/100, positive modes

M12, Imperfection = Hw/100, positive modes			
Mode No.	**t_ult [Mpa]**	**Eigen value [-]**	**t_cr [MPa]**
0	184.98007		
1	71.08099663	3.7667	199.6351
3	75.10197592	3.7742	200.0326
4	59.21090591	3.7765	200.1545
7	66.81384552	3.7897	200.8541
9	79.76630127	4.0661	215.5033
11	74.31129193	4.0829	216.3937
12	62.71749139	4.0853	216.5209
15	69.42355251	4.1352	219.1656
17	60.58293653	4.2389	224.6617
18	60.8973248	4.2393	224.6829
19	67.81055617	4.2411	224.7783
20	72.51769924	4.2421	224.8313
25	60.93331897	4.3423	230.1419
26	58.32692897	4.3428	230.1684
29	69.92180991	4.3554	230.8362
30	67.71824884	4.358	230.974
33	81.9877615	4.3767	231.9651
35	74.23266959	4.3892	232.6276
37	66.99202204	4.3957	232.9721
38	77.28309512	4.3993	233.1629
41	59.4244827	4.437	235.161
43	64.84047782	4.45	235.85
44	72.98043001	4.4572	236.2316
45	71.12018144	4.461	236.433
49	64.97023249	4.4894	237.9382

Table B.2: M12, positive modes, Imperfection = Hw/200, Hw/300, Hw/400

M12, positive modes, Imperfection = Hw/200, Hw/300, Hw/400				
		Hw/200	**Hw/300**	**Hw/400**
Mode No.	**t_cr [MPa]**	**t_ult [Mpa]**	**t_ult [Mpa]**	**t_ult [Mpa]**
0		184.980	184.980	184.980
1	199.6351	92.977	113.378	126.097
3	200.0326	93.271	117.086	130.105
4	200.1545	87.917	110.758	124.878
7	200.8541	87.446	108.038	121.508
9	215.5033	85.001	107.078	122.058
11	216.3937	87.065	112.795	129.385
12	216.5209	87.599	109.578	123.757
15	219.1656	84.075	103.249	118.922
17	224.6617	87.876	113.750	129.047
18	224.6829	89.449	115.464	131.467
19	224.7783	91.384	104.942	123.260
20	224.8313	90.112	103.166	118.925
25	230.1419	89.087	100.499	109.233
26	230.1684	87.069	101.350	114.472
29	230.8362	78.995	106.999	124.665
30	230.974	79.255	105.293	121.112
33	231.9651	100.588	112.294	130.807
35	232.6276	92.312	115.747	130.733
37	232.9721	89.427	106.186	123.336
38	233.1629	100.636	102.860	118.852
41	235.161	91.664	118.294	133.636
43	235.85	90.933	115.238	133.508
44	236.2316	104.863	121.644	137.008
45	236.433	93.618	104.139	121.639
49	237.9382	95.946	115.601	133.874

Table B.3: M12, Imperfection = Hw/100, negative modes

M12, Imperfection = Hw/100, negative modes			
Mode No.	**t_ult [Mpa]**	**Eigen value [-]**	**t_cr [MPa]**
0	184.98007		
2	154.1489813	-3.7694	199.7782
5	153.5719879	-3.7771	200.1863
6	157.8566527	-3.7778	200.2234
8	157.4340229	-3.79	200.87
10	153.4189637	-4.0753	215.9909
13	163.768934	-4.0898	216.7594
14	153.4718714	-4.0917	216.8601
16	170.2701626	-4.1401	219.4253

21	148.7694416	-4.2423	224.8419
22	142.0220728	-4.2432	224.8896
23	154.0827551	-4.2438	224.9214
24	153.2826571	-4.2459	225.0327
27	150.5434229	-4.3495	230.5235
28	143.5432041	-4.35	230.55
31	158.2844129	-4.3629	231.2337
32	144.7923415	-4.3638	231.2814
34	157.735219	-4.3847	232.3891
36	174.9247139	-4.3924	232.7972
39	142.9449565	-4.4011	233.2583
40	145.421674	-4.4045	233.4385
42	148.025044	-4.4496	235.8288
46	153.3662961	-4.4758	237.2174
47	143.2735226	-4.4768	237.2704
48	154.8020194	-4.4837	237.6361
50	145.5953457	-4.5077	238.9081

Table B.4: M12, negative modes, Imperfection = Hw/200, Hw/300, Hw/400

M12, negative modes, Imperfection = Hw/200, Hw/300, Hw/400				
		Hw/200	**Hw/300**	**Hw/400**
Mode No.	**t_cr [MPa]**	**t_ult [Mpa]**	**t_ult [Mpa]**	**t_ult [Mpa]**
0		184.98007	184.98007	184.98007
2	199.7782	182.9690101	184.3534179	184.3534179
5	200.1863	182.7655044	182.1737139	181.7311821
6	200.2234	182.2894361	181.959897	181.8784189
8	200.87	182.6202009	182.9172397	182.8645594
10	215.9909	175.3650723	179.2440398	180.7624922
13	216.7594	181.3128359	180.9230475	180.9934437
14	216.8601	181.9342077	182.6800079	182.8200421
16	219.4253	183.0156376	182.6456375	182.3774598
21	224.8419	178.7425222	184.3896079	184.4571862
22	224.8896	182.9903526	183.0960417	182.8416753
23	224.9214	181.8022733	184.3429804	184.4154868
24	225.0327	182.3998511	183.0723867	182.8472352
27	230.5235	178.9417191	185.1326029	187.8305042
28	230.55	182.1207809	188.037586	186.4460459
31	231.2337	183.6669698	183.4094696	183.1482165
32	231.2814	177.776448	184.9091446	184.7794342
34	232.3891	184.7402368	184.468066	184.5907633
36	232.7972	183.2809343	183.2647347	183.0405562
39	233.2583	176.3469543	179.7409956	181.4097176
40	233.4385	172.6645806	178.4490974	180.3812079

42	235.8288	172.4061832	178.577203	180.4599566
46	237.2174	176.5033398	181.5195513	183.1658313
47	237.2704	175.4519839	180.1407161	181.8641148
48	237.6361	174.8499455	179.1660619	180.8006155
50	238.9081	179.937501	184.3922362	184.4484546

Table B.5: S2, Imperfection = Hw/100, positive modes

S2, Imperfection = Hw/100, positive modes			
Mode No.	**t_ult [Mpa]**	**Eigen value [-]**	**t_cr [MPa]**
0	166.2561728		
3	140.5723761	0.90255	139.28241
5	140.1894162	0.9026	139.29012
7	142.2838204	0.90264	139.2963
8	141.5068905	0.90269	139.30401
11	143.9202255	0.91591	141.34414
13	144.9850698	0.91598	141.35494
15	144.7197096	0.91605	141.36574
16	143.5884815	0.91612	141.37654
17	144.8297942	0.93894	144.89815
18	145.564955	0.93905	144.91512
20	145.1732292	0.93913	144.92747
22	144.7094903	0.93927	144.94907
25	146.5821892	0.96945	149.60648
26	144.8435916	0.96945	149.60648
27	145.8648178	0.96961	149.63117
28	146.0211512	0.96963	149.63426
33	146.2840188	1.0046	155.03086
34	147.6081525	1.0047	155.0463
35	149.3963286	1.0049	155.07716
36	147.4542474	1.0049	155.07716
41	150.9251326	1.043	160.95679
42	150.8602206	1.0432	160.98765
43	152.1876933	1.0434	161.01852
44	152.6152094	1.0435	161.03395
49	147.1677772	1.0733	165.63272
50	149.6684588	1.0733	165.63272
51	151.9202818	1.0733	165.63272
54	145.5815946	1.0772	166.23457
55	158.382989	1.0773	166.25

Table B.6: S2, positive modes, Imperfection = Hw/200, Hw/300, Hw/400

S2, positive modes, Imperfection = Hw/200, Hw/300, Hw/400				
		Hw/200	**Hw/300**	**Hw/400**
Mode No.	**t_cr [MPa]**	**t_ult [Mpa]**	**t_ult [Mpa]**	**t_ult [Mpa]**
0		166.256	166.256	166.256
3	139.282	155.571	160.287	162.673
5	139.290	155.633	160.391	162.766
7	139.296	155.792	161.404	162.942
8	139.304	156.589	161.295	163.572
11	141.344	156.019	158.669	162.002
13	141.355	156.376	160.682	161.961
15	141.366	156.511	160.337	162.332
16	141.377	156.081	160.210	161.670
17	144.898	157.209	161.255	162.617
18	144.915	158.075	161.552	162.904
20	144.927	157.385	160.818	162.638
22	144.949	157.591	161.491	162.889
25	149.606	158.082	161.408	163.052
26	149.606	157.245	161.462	163.464
27	149.631	156.870	160.557	162.679
28	149.634	157.929	161.648	162.867
33	155.031	155.131	163.057	164.883
34	155.046	159.207	162.291	164.767
35	155.077	159.529	163.233	165.207
36	155.077	159.366	162.375	164.881
41	160.957	162.133	165.504	166.034
42	160.988	162.082	165.792	165.974
43	161.019	162.432	165.781	165.973
44	161.034	162.659	165.980	165.417
49	165.633	160.489	163.158	161.251
50	165.633	160.641	160.830	161.941
51	165.633	162.232	164.488	165.269
54	166.235	157.782	161.608	159.668

Table B.7: Matsnoki, Imperfection = Hw/100, positive modes

Matsnoki, Imperfection = Hw/100, positive modes			
Mode No.	**t_ult [Mpa]**	**Eigen value [-]**	**t_cr [MPa]**
0	311.16335	-	-
1	186.08471	17.51800	792.66968
2	199.89432	17.52500	792.98643
5	205.72097	17.58600	795.74661
6	202.15145	17.58700	795.79186
9	193.44000	18.90000	855.20362

10	196.49012	18.97700	858.68778
13	186.93868	19.26000	871.49321
14	177.38141	19.26200	871.58371
17	179.52000	19.65000	889.14027
18	181.05815	19.81500	896.60633
21	158.56000	19.85500	898.41629
22	157.91656	19.87300	899.23077
25	166.34000	19.88700	899.86425
26	166.39282	20.29700	918.41629
27	175.63954	20.30600	918.82353
28	176.75215	20.31000	919.00452
34	196.65476	20.77200	939.90950
35	189.29359	20.77800	940.18100
38	168.28411	20.81700	941.94570
39	171.56398	20.81900	942.03620
42	175.73455	21.01800	951.04072
43	181.67420	21.04300	952.17195
44	174.31505	21.11000	955.20362

Table B.8: Matsnoki, positive modes, Imperfection = Hw/200, Hw/300, Hw/400

Matsnoki, positive modes, Imperfection = Hw/200, Hw/300, Hw/400				
		Hw/200	**Hw/300**	**Hw/400**
Mode No.	**t_cr [MPa]**	**t_ult [Mpa]**	**t_ult [Mpa]**	**t_ult [Mpa]**
0	-	311.16335	311.16335	311.16335
1	792.670	233.832	249.774	258.195
2	792.986	234.806	249.761	258.305
5	795.747	242.262	256.783	264.419
6	795.792	239.016	253.735	261.665
9	855.204	235.770	251.870	260.830
10	858.688	237.112	253.072	261.820
13	871.493	238.084	255.820	264.727
14	871.584	232.532	252.057	261.734
17	889.140	224.340	244.260	256.520
18	896.606	225.260	245.275	257.229
21	898.416	210.060	232.570	245.660
22	899.231	209.595	232.076	245.377
25	899.864	224.700	244.650	255.750
26	918.416	226.496	246.064	257.625
27	918.824	223.194	241.438	252.556
28	919.005	227.421	248.125	259.375
34	939.910	240.578	256.712	265.259
35	940.181	236.483	253.697	262.909
38	941.946	223.326	243.711	254.921

39	942.036	225.276	245.108	256.321
42	951.041	222.449	242.392	253.756
43	952.172	225.278	244.238	255.027
44	955.204	219.868	239.057	250.906

Table B.9: Matsnoki, Imperfection = Hw/100, negative modes

Matsnoki, Imperfection = Hw/100, negative modes			
Mode No.	**t_ult [Mpa]**	**Eigen value [-]**	**t_cr [MPa]**
0	311.16335	-	-
3	266.3557	-17.5440	793.8462
4	266.1510	-17.5490	794.0724
7	269.3926	-17.5870	795.7919
8	270.1925	-17.5880	795.8371
11	261.2868	-19.0590	862.3982
12	260.8161	-19.0720	862.9864
15	267.8262	-19.3290	874.6154
16	262.5789	-19.3290	874.6154
19	248.8747	-19.8390	897.6923
20	250.5651	-19.8410	897.7828
23	246.3689	-19.8830	899.6833
24	251.5296	-19.8830	899.6833
29	249.9700	20.3350	-920.1357
30	250.5452	-20.3460	920.6335
31	251.0895	-20.3510	920.8597
32	250.5452	-20.3650	921.4932
33	253.5767	-20.3660	921.5385
36	261.5385	-20.8060	941.4480
37	264.9143	-20.8080	941.5385
40	251.0440	-20.8370	942.8507
41	257.1550	-20.8370	942.8507

Table B.10: Matsnoki, negative modes, Imperfection = Hw/200, Hw/300, Hw/400

Matsnoki, negative modes, Imperfection = Hw/200, Hw/300, Hw/400				
		Hw/200	**Hw/300**	**Hw/400**
Mode No.	**t_cr [MPa]**	**t_ult [Mpa]**	**t_ult [Mpa]**	**t_ult [Mpa]**
0	-	311.163	311.163	311.163
3	793.85	283.335	285.166	285.871
4	794.07	285.509	287.464	287.707
7	795.79	284.944	286.691	286.850
8	795.84	285.098	286.775	286.894
11	862.40	279.651	283.367	284.839

12	862.99	279.566	283.427	284.850
15	874.62	283.259	286.639	288.668
16	874.62	280.957	284.102	285.063
19	897.69	270.181	276.564	279.371
20	897.78	271.635	277.999	280.899
23	899.68	269.514	276.410	279.517
24	899.68	271.240	277.459	280.039
29	920.14	279.970	280.600	283.950
30	920.63	274.067	280.666	283.856
31	920.86	275.618	281.798	284.348
32	921.49	274.067	280.666	283.856
33	921.54	274.856	280.737	283.142
36	941.45	278.158	282.173	283.600
37	941.54	280.855	284.305	285.693
40	942.85	273.006	278.921	281.270
41	942.85	278.437	283.460	285.036

Table B.11: FE-results of shear capacity for positive buckling eigenvalues ID1

Results of parametric study		
ID	**1**	**b = c**
b = 250 mm	**c = 250 mm**	**d = 176.85 mm**
hr =176,8 mm	**alpha = 45 degrees**	**Imperfection = Hw/200**
Mode No.	**Eigen value [-]**	**Shear capacity [Mpa]**
1	6.99	181.24
2	6.9904	181.18
5	7.0002	188.63
6	7.0004	188.30
9	7.2905	181.03
10	7.2926	180.94
13	7.3372	190.61
14	7.3377	190.44
17	7.6209	180.97
18	7.6216	181.06
21	7.687	197.59
22	7.688	197.19
25	7.7427	201.08
26	7.7434	200.95
29	7.9079	193.53
30	7.9097	203.03
33	8.09	192.45
34	8.0909	193.19
37	8.2802	194.70
38	8.2822	209.12
41	8.4734	208.42
42	8.4759	208.33
45	8.9547	201.50
46	8.9577	219.49
49	9.0678	204.30
50	9.0706	209.36

Table B.12: FE-results of shear capacity for positive buckling eigenvalues ID2

Results of parametric study		
ID	**2**	**b = 1.5*c**
b = 375 mm	**c = 250 mm**	**d = 176.85 mm**
hr =176,8 mm	**alpha = 45 degrees**	**Imperfection = Hw/200**
Mode No.	**Eigen value [-]**	**Shear capacity [Mpa]**
1	2.8768	163.40
2	2.8768	163.37
5	2.8776	161.11
6	2.8776	161.19
9	2.9926	167.23
10	2.9926	167.59
13	2.9962	171.43
14	2.9962	171.49
17	3.1568	170.46
18	3.1568	165.54
19	3.1599	165.16
20	3.1599	165.17
25	3.2842	164.80
26	3.2843	157.93
27	3.2851	155.48
28	3.2851	155.23
33	3.3175	170.15
34	3.3175	169.52
35	3.3208	171.89
36	3.3208	170.36
41	3.4147	156.95
42	3.4148	156.77
45	3.4254	159.47
46	3.4254	159.46
49	3.4598	176.75
50	3.4598	177.13

Table B.13: FE-results of shear capacity for positive buckling eigenvalues ID3

Results of parametric study		
ID	**3**	**hw = 1500 mm**
b = 250 mm	**c = 250 mm**	**d = 216.54 mm**
hr =125 mm	**alpha = 30 degrees**	**Imperfection = Hw/200**
Mode No.	**Eigen value [-]**	**Shear capacity [Mpa]**
1	3.5508	142.08
2	3.5508	142.54
5	3.5527	141.84
6	3.5527	151.93
9	3.6444	140.69
10	3.6445	140.70
11	3.6447	139.34
12	3.6447	144.87
17	3.776	143.18
18	3.776	143.62
19	3.7781	145.84
20	3.7782	149.43
25	3.8507	147.22
26	3.8507	147.22
29	3.8547	151.24
30	3.8547	150.95
33	3.9043	148.53
34	3.9043	148.05
35	3.9073	140.17
36	3.9074	140.27
41	3.9901	149.64
42	3.9902	149.60
43	3.9918	146.84
44	3.9919	146.79
49	4.0396	140.60
50	4.0396	140.59

Table B.14: FE-results of shear capacity for positive buckling eigenvalues ID4

Results of parametric study		
ID	**4**	**hw = 2000 mm**
b = 375 mm	**c = 250 mm**	**d = 216.54 mm**
hr =125 mm	**alpha = 30 degrees**	**Imperfection = Hw/200**
Mode No.	**Eigen value [-]**	**Shear capacity [Mpa]**
1	2.8	142.49
2	2.8001	142.44
3	2.8008	143.29
4	2.8009	143.13
9	2.9335	142.56
10	2.934	142.70
11	2.9368	143.27
12	2.9373	143.29
17	3.0799	124.24
18	3.0801	124.15
21	3.092	134.10
22	3.0926	134.40
23	3.1125	153.10
24	3.1133	153.03
27	3.1304	131.25
28	3.131	131.53
33	3.2436	130.50
34	3.2446	130.74
35	3.253	143.47
36	3.2537	149.37
39	3.2862	134.73
40	3.287	156.75
41	3.2922	132.63
42	3.2934	141.49
45	3.3544	160.87
46	3.3544	163.95
47	3.362	157.05
48	3.3621	156.84

Table B.15: FE-results of shear capacity for positive buckling eigenvalues ID5

Results of parametric study		
ID	**5**	**hw = 2000 mm**
b = 500 mm	**c = 250 mm**	**d = 216.54 mm**
hr =125 mm	**alpha = 30 degrees**	**Imperfection = Hw/200**
Mode No.	**Eigen value [-]**	**Shear capacity [Mpa]**
1	1.5854	119.77
2	1.5885	119.35
4	1.5914	119.55
7	1.5952	119.02
9	1.6515	119.81
10	1.6525	119.73
12	1.6678	119.60
15	1.6699	119.62
17	1.7299	119.76
18	1.735	119.77
20	1.7467	119.53
23	1.7522	119.55
25	1.7998	119.76
26	1.8024	119.80
27	1.8179	103.51
29	1.8208	104.12
33	1.8545	110.53
35	1.8584	110.80
37	1.9128	109.88
39	1.9256	109.19
40	1.9261	108.70
43	1.9389	114.31
45	1.9981	108.86
46	2.0138	115.74
48	2.0147	109.00
46	3.3544	163.95
47	3.362	157.05
48	3.3621	156.84

Table B.16: FE-results of shear capacity for positive buckling eigenvalues ID6

Results of parametric study		
ID	**6**	**hw = 2210 mm**
b = 300 mm	**c = 300 mm**	**tw= 10 mm**
hr =150 mm	**alpha = 30 degrees**	**Imperfection = Hw/200**
Mode No.	**Eigen value [-]**	**Shear capacity [Mpa]**
1	17.518	233.83
2	17.525	234.81
5	17.586	242.26
6	17.587	239.02
9	18.9	235.77
10	18.977	237.11
13	19.26	238.08
14	19.262	232.53
17	19.65	224.34
18	19.815	225.26
21	19.855	210.06
22	19.873	209.59
25	19.887	224.70
26	20.297	226.50
27	20.306	223.19
28	20.31	227.42
34	20.772	240.58
35	20.778	236.48
38	20.817	223.33
39	20.819	239.49
42	21.018	234.71
43	21.043	238.11
44	21.11	232.36

Table B.17: FE-results of shear capacity for positive buckling eigenvalues ID7

Results of parametric study		
ID	**7**	**hw = 2210 mm**
b = 300 mm	**c = 300 mm**	**tw= 4 mm**
hr =150 mm	**alpha = 30 degrees**	**Imperfection = Hw/200**
Mode No.	**Eigen value [-]**	**Shear capacity [Mpa]**
1	1.5603	128.22
2	1.5603	130.94
3	1.5604	128.29
4	1.5604	128.57
9	1.6036	132.54
10	1.6037	132.77
11	1.6038	129.70
12	1.6038	132.05
17	1.6488	133.09
18	1.6489	133.04
19	1.6493	131.53
20	1.6493	133.89
25	1.6625	134.34
26	1.6625	133.57
27	1.6637	133.75
28	1.6637	133.61
33	1.7095	131.47
34	1.7096	132.38
35	1.7102	131.30
36	1.7102	135.41
41	1.7433	146.56
42	1.7434	135.93

Table B.18: FE-results of shear capacity for positive buckling eigenvalues ID8

Results of parametric study		
ID	**8**	**hw = 2210 mm**
b = 300 mm	**c = 300 mm**	**tw= 6 mm**
hr =150 mm	**alpha = 30 degrees**	**Imperfection = Hw/200**
Mode No.	**Eigen value [-]**	**Shear capacity [Mpa]**
1	5.0321	166.33
2	5.0323	172.16
3	5.0324	164.96
4	5.0326	167.63
9	5.1715	170.58
10	5.1719	170.21
11	5.1735	167.29
12	5.1739	167.35
17	5.2805	176.78
18	5.2808	177.09
19	5.2863	170.94
20	5.2866	171.45
25	5.3535	172.67
26	5.354	172.16
27	5.3603	173.19
28	5.3608	174.60
33	5.4537	177.64
34	5.4543	179.50
35	5.4605	177.54
36	5.4611	179.09
41	5.5518	183.23
42	5.5523	189.89

Table B.19: FE-results of shear capacity for positive buckling eigenvalues ID9

Results of parametric study		
ID	**9**	**hw = 1500 mm**
b = 200 mm	**c = 99.3 mm**	**tw= 8 mm**
hr = 50 mm	**alpha = 30 degrees**	**Imperfection = Hw/200**
Mode No.	**Eigen value [-]**	**Shear capacity [Mpa]**
1	12.098	248.88
2	12.098	249.11
5	12.107	248.99
6	12.107	273.12
9	12.166	266.91
10	12.166	266.92
13	12.181	267.04
14	12.181	267.00
17	12.311	250.64
18	12.311	250.98
21	12.516	268.23
22	12.518	276.53
25	12.954	260.67
26	12.955	260.45
29	13.044	270.24
30	13.047	273.53
33	13.312	255.35
34	13.312	254.55
37	13.365	255.28
38	13.37	259.85
41	13.46	264.05
42	13.461	265.09
45	13.738	269.97
46	13.739	269.96
49	14.43	288.50
50	14.437	291.21
51	14.512	272.33
52	14.515	285.36

Table B.20: FE-results of shear capacity for positive buckling eigenvalues ID10

Results of parametric study		
ID	**10**	**hw = 1000 mm**
b = 300 mm	**c = 300 mm**	**tw= 10 mm**
hr =150 mm	**alpha = 30 degrees**	**Imperfection = Hw/200**
Mode No.	**Eigen value [-]**	**Shear capacity [Mpa]**
1	6.6825	262.75
3	6.6833	264.97
5	6.7002	263.87
6	6.7006	263.61
9	6.8286	261.65
10	6.8292	262.60
13	6.8845	270.48
14	6.8857	267.60
17	7.2976	272.21
18	7.3022	271.69
21	7.4772	271.34
22	7.4823	269.98
25	7.7689	269.98
26	7.7747	271.47
29	7.881	264.67
30	7.8822	264.61
33	8.1421	276.85

Table B.21: FE-results of shear capacity for positive buckling eigenvalues ID11

Results of parametric study		
ID	**11**	**hw = 3000 mm**
b = 300 mm	**c = 300 mm**	**tw= 10 mm**
hr =150 mm	**alpha = 30 degrees**	**Imperfection = Hw/200**
Mode No.	**Eigen value [-]**	**Shear capacity [Mpa]**
1	14.01	209.68
2	14.031	217.82
4	14.069	219.75
6	14.083	218.37
9	15.992	224.04
10	16.073	218.75
13	16.325	223.15
14	16.362	230.85
17	18.363	204.18
18	18.377	214.93

Table B.22: FE-results of shear capacity for positive buckling eigenvalues ID12

Results of parametric study		
ID	**12**	**hw = 1500 mm**
b = 100 mm	**c = 81.18 mm**	**tw= 4 mm**
hr = 43 mm	**alpha = 32 degrees**	**Imperfection = Hw/200**
Mode No.	**Eigen value [-]**	**Shear capacity [Mpa]**
1	12.386	239.73
2	12.386	233.24
3	12.386	229.81
4	12.386	236.14
9	12.914	269.75
10	12.914	269.50
13	12.976	266.47
14	12.976	265.98
17	13.441	268.70
18	13.441	268.68
19	13.466	272.45
20	13.466	273.66
25	14.736	248.86
26	14.736	252.25
27	14.766	241.83

Table B.23: FE-results of shear capacity for positive buckling eigenvalues ID13

Results of parametric study		
ID	**13**	**b = 1.2*c**
b = 300 mm	**c = 250 mm**	**d = 212.05 mm**
hr =132.48 mm	**alpha = 32 degrees**	**Imperfection = Hw/200**
Mode No.	**Eigen value [-]**	**Shear capacity [Mpa]**
1	4.0031	153.54
2	4.0032	155.63
3	4.0039	153.83
4	4.004	152.76
9	4.1457	155.94
10	4.146	161.05
11	4.148	155.39
12	4.1483	155.26
17	4.2844	154.10
18	4.2845	156.42
19	4.2869	151.91
20	4.287	151.62
25	4.3482	164.21
26	4.3489	163.79
27	4.3498	157.04
28	4.3504	156.46
33	4.4463	156.54
34	4.4468	158.40
35	4.4482	159.50
36	4.4487	159.67
41	4.5535	146.64
42	4.554	146.30
43	4.5681	153.86
46	4.5688	156.48
47	4.5784	147.09
48	4.5787	146.59
51	4.5805	147.72
52	4.5809	147.88
55	4.6636	150.79
56	4.6647	150.51
59	4.6699	147.71
60	4.6706	148.05
61	4.6868	142.97
62	4.6878	144.16

Table B.24: FE-results of shear capacity for positive buckling eigenvalues ID14

Results of parametric study		
ID	**14**	**b = 1.5*c**
b = 375 mm	**c = 250 mm**	**d = 212.05 mm**
hr =132.48 mm	**alpha = 32 degrees**	**Imperfection = Hw/200**
Mode No.	**Eigen value [-]**	**Shear capacity [Mpa]**
1	2.6435	144.29
2	2.6436	144.75
3	2.6472	142.22
4	2.6473	152.47
9	2.7333	144.60
10	2.7335	149.53
11	2.7353	143.46
12	2.7356	149.24
17	2.8375	148.14
18	2.8379	151.37
19	2.8452	145.94
20	2.8456	148.59
21	2.8783	138.29
22	2.8784	134.95
27	2.8856	143.82
28	2.8858	144.11
33	2.9353	149.48
34	2.9357	149.70
35	2.9404	147.71
36	2.9407	151.25
37	2.9814	141.89
38	2.9819	148.50
39	2.9871	139.49
40	2.9875	143.64
45	3.0213	155.40
46	3.0214	160.91
47	3.0256	150.69
48	3.0257	150.58
53	3.0838	142.53
54	3.0845	149.86
55	3.1014	146.64
56	3.1022	159.94
65	3.1679	130.00
66	3.1681	133.61

Table B.25: FE-results of shear capacity for positive buckling eigenvalues ID15

Results of parametric study		
ID	**15**	**b = 2*c**
b = 500 mm	**c = 250 mm**	**d = 212.05 mm**
hr =132.48 mm	**alpha = 32 degrees**	**Imperfection = Hw/200**
Mode No.	**Eigen value [-]**	**Shear capacity [Mpa]**
1	1.5777	126.96
2	1.5778	126.90
3	1.582	120.41
4	1.5821	122.98
9	1.6426	125.24
10	1.6429	125.30
11	1.6482	124.23
12	1.6485	125.22
17	1.7073	124.31
18	1.7077	124.23
19	1.7146	126.27
20	1.7149	126.28
23	1.7695	126.85
24	1.7696	127.42
25	1.7717	128.08
26	1.7717	128.02
29	1.7952	108.33
30	1.7954	111.03
37	1.8201	120.20
38	1.8204	121.01
41	1.8707	110.56
42	1.8715	112.31
43	1.8855	115.32
44	1.8865	115.05

Table B.26: Results of shear capacity from FEM-simulation and Eurocode equations

Dimensions of the I_girder										
ID	**b [mm]**	**d [mm]**	**c [mm]**	**Alpha [o]**	**hr [mm]**	**t_w [mm]**	**h_w [mm]**	**a [m]**	**bf [mm]**	**tf [mm]**
1	250	176.8	250	45	176.8	4	2000	3	300	30
2	375	176.8	250	45	177.66	4	2000	3	300	30
3	250	216.5	250	30	125	4	1500	3	300	30
4	375	216.5	250	30	125	4	2000	3	300	30
5	500	216.5	250	30	125	4	2000	3	300	30
6	300	259.8	300	30	150	10	2210	3.3	400	60
7	300	259.8	300	30	150	4	2210	3.3	400	60
8	300	259.8	300	30	150	6	2210	3.3	400	60
9	200	86.01	99.3	30	50	8	1500	3.3	500	45
10	300	259.8	300	30	150	10	1000	3.3	400	60
11	300	259.8	300	30	150	10	3000	3.3	400	60
12	100	68.86	81.18	32	43	4	1500	1.857	500	45
13	300	212	250	32	132.48	4	2000	3	300	30
14	375	212	250	32	132.48	4	2000	3	300	30
15	500	212	250	32	132.48	4	2000	3	300	30
16	80	64	63.74	37	48	0.9	360	1.475	200	20

Mechanical properties					Results					
ID	**γ_{m1} Safety factor**	**f_yw [MPa]**	**E [MPa]**	**v Poisson ratio**	**tult_EU**	**Mode**	**First mode**	**tult _FEM _Lowest mode**	**Difference from lowest mode**	**Difference from first mode**
1	1	402.1	2E+05	0.3	142.84	Local	181.24	180.94	-27%	-27%
2	1	402.1	2E+05	0.3	113.44	Local	163.39	159.46	-41%	-44%
3	1	402.1	2E+05	0.3	142.84	Local	142.08	139.34	2%	1%
4	1	402.1	2E+05	0.3	113.44	Interactive	142.49	124.14	-9%	-26%
5	1	402.1	2E+05	0.3	94.072	Local	119.77	103.5	-10%	-27%
6	1	355.9	2E+05	0.3	176.65	Interactive	233.83	209.59	-19%	-32%
7	1	402.1	2E+05	0.3	129.42	Local	128.2	128.2	1%	1%
8	1	402.1	2E+05	0.3	159.36	Local	166.33	166.33	-4%	-4%
9	1	355.9	2E+05	0.3	186.83	Global	248.88	248.88	-33%	-33%
10	1	355.9	2E+05	0.3	176.65	Interactive	262.74	261.64	-48%	-49%
11	1	355.9	2E+05	0.3	176.65	Global	209.68	204.18	-16%	-19%
12	1	355.9	2E+05	0.3	186.83	Global	239.73	229.81	-23%	-28%
13	1	402.1	2E+05	0.3	129.42	Local	156.31	143.178	-10.6%	-20.77%
14	1	402.1	2E+05	0.3	113.44	Local	144.29	130	-15%	-27%
15	1	402.1	2E+05	0.3	94.072	Local	126.96	108.325	-15%	-35%
16	1	402.1	2E+05	0.3	117.19	Local	155.57	155.13	-32%	-33%

Results										
ID	**Ref -load [kN]**	**Eigenvalue _first mode**	**Eigenvalue _Lowest mode**	**tcr_First mode**	**tcr _FEM _lowest mode**	**t_y**	**Lamda _first _mode**	**Lamda _FEM _Lowest mode**	**X_FEM _First mode**	**X_FEM _lowest mode**
1	848	6.99	7.293	370.47	386.51	232.13	0.792	0.775	0.781	0.779
2	848	2.877	3.285	152.47	174.11	232.13	1.234	1.155	0.704	0.687
3	848	3.551	3.645	250.92	257.56	232.13	0.962	0.949	0.612	0.600
4	848	2.8	3.081	148.4	163.29	232.13	1.251	1.192	0.614	0.535
5	848	1.585	1.817	84.005	96.301	232.13	1.662	1.553	0.516	0.446
6	2000	17.52	19.87	792.67	899.23	205.45	0.509	0.478	1.138	1.020
7	2000	1.56	1.56	176.5	176.5	232.13	1.147	1.147	0.552	0.552
8	2000	5.032	5.032	379.49	379.52	232.13	0.782	0.782	0.717	0.717
9	2000	12.1	12.1	1008.2	1008.2	205.45	0.451	0.451	1.211	1.211
10	3000	6.683	6.829	1002.4	1024.3	205.45	0.453	0.448	1.279	1.273
11	3000	14.01	18.36	700.5	918	205.45	0.542	0.473	1.021	0.994
12	848	12.39	12.39	875.28	875.28	205.45	0.484	0.484	1.167	1.119
13	848	5.323	5.769	282.13	305.78	232.13	0.907	0.871	0.673	0.617
14	848	2.644	3.168	140.11	167.9	232.13	1.287	1.176	0.622	0.560
15	848	1.578	1.795	83.618	95.146	232.13	1.666	1.562	0.547	0.467
16	100	0.903	1.005	139.28	155.03	232.13	1.291	1.224	0.670	0.668